AD-A064 828 OHIO STATE UNIV COLUMBUS ELECTROSCIENCE LAB F/G 20/3
THE SURFACE CURRENT AND CHARGE DENSITY INDUCED ON FINITE CYLIND--ETC(U)
OCT 78 E D GREER, W D BURNSIDE AFOSR-77-3324
UNCLASSIFIED ESL-784713-1 AFOSR-TR-79-0029 NL

1 OF 2
ADA
064828

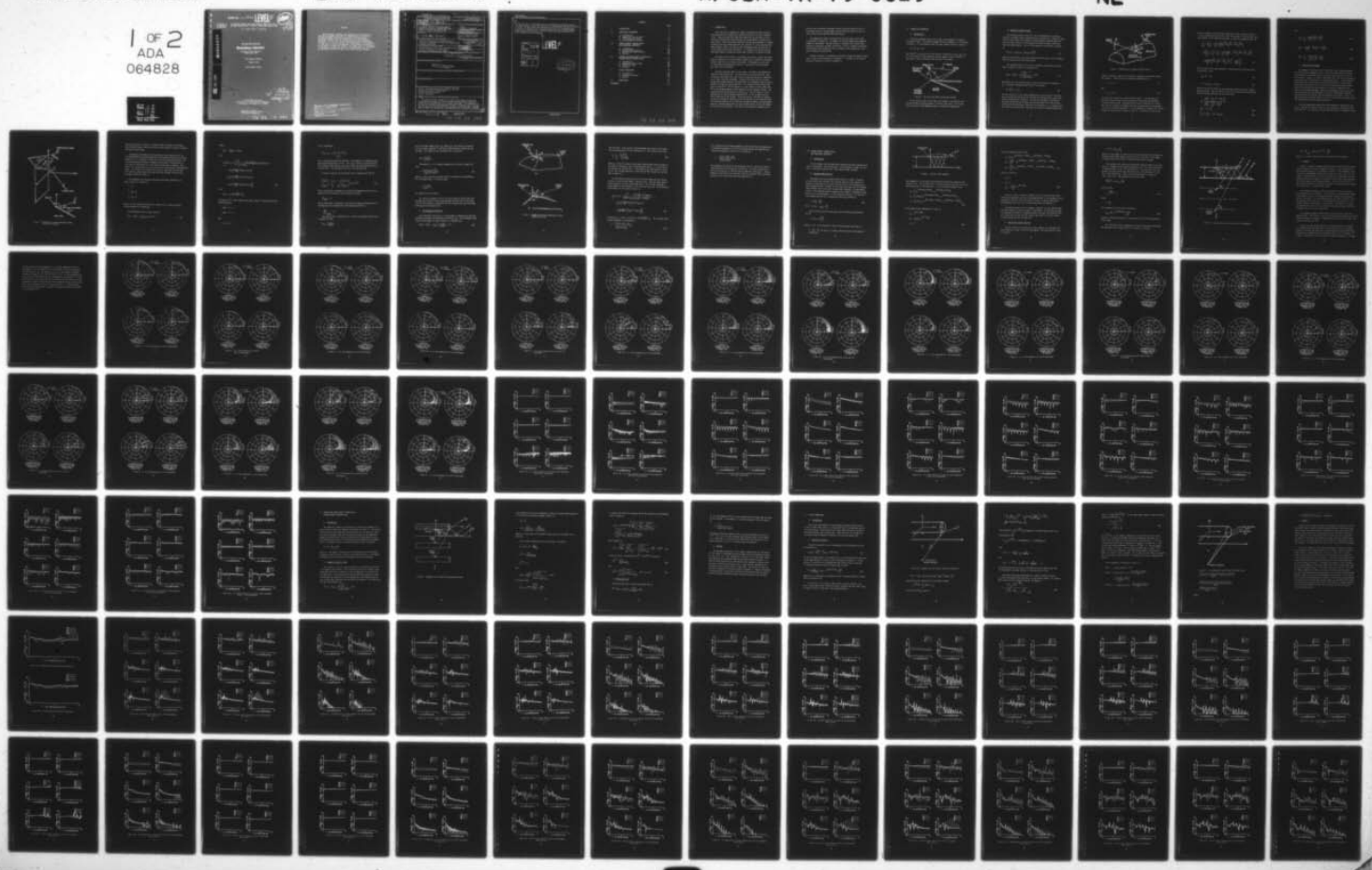

LEVEL II

OSU

THE SURFACE CURRENT AND CHARGE DENSITY INDUCED ON FINITE CYLINDER MOUNTED NEAR A PERFECTLY CONDUCTING GROUND PLANE

E. D. Greer and W. D. Burnside

The Ohio State University

ElectroScience Laboratory

Department of Electrical Engineering
Columbus, Ohio 43212

Final Report 784713-1

October 1978

Grant AFOSR 77-3324

United States Air Force
Air Force Office of Scientific Research
Bolling Air Force Base, D. C. 20332

NOTICES

When Government drawings, specifications, or other data are used for any purpose other than in connection with a definitely related Government procurement operation, the United States Government thereby incurs no responsibility nor any obligation whatsoever, and the fact that the Government may have formulated, furnished, or in any way supplied the said drawings, specifications, or other data, is not to be regarded by implication or otherwise as in any manner licensing the holder or any other person or corporation, or conveying any rights or permission to manufacture, use, or sell any patented invention that may in any way be related thereto.

UNCLASSIFIED

SECURITY CLASSIFICATION OF THIS PAGE (When Data Entered)

(9) Final rept. 1 May - 31 Jul 78

REPORT DOCUMENTATION PAGE

READ INSTRUCTIONS BEFORE COMPLETING FORM

(18) 1. REPORT NUMBER: AFOSR-TR-79-0029

2. GOVT ACCESSION NO.

3. RECIPIENT'S CATALOG NUMBER

(6) 4. TITLE (and Subtitle): THE SURFACE CURRENT AND CHARGE DENSITY INDUCED ON FINITE CYLINDER MOUNTED NEAR A PERFECTLY CONDUCTING GROUND PLANE

5. TYPE OF REPORT & PERIOD COVERED: Final 05/01/77 - 07/31/78

(14) 6. PERFORMING ORG. REPORT NUMBER: ESL-784713-1

(10) 7. AUTHOR(s): E. D. Greer and W. D. Burnside

(15) 8. CONTRACT OR GRANT NUMBER(s): AFOSR-77-3324

9. PERFORMING ORGANIZATION NAME AND ADDRESS: The Ohio State University ElectroScience Laboratory, Department of Electrical Engineering, Columbus, Ohio 43212

10. PROGRAM ELEMENT, PROJECT, TASK AREA & WORK UNIT NUMBERS: 61102F 2301/A3 (16) (17) A3

11. CONTROLLING OFFICE NAME AND ADDRESS: United States Air Force, Air Force Office of Scientific Research, Building 410/NP, Bolling Air Force Base, D.C. 20332

(11) 12. REPORT DATE: Oct 78

13. NUMBER OF PAGES: 178

(12) 183p

14. MONITORING AGENCY NAME & ADDRESS (if different from Controlling Office)

15. SECURITY CLASS. (of this report): Unclassified

15a. DECLASSIFICATION/DOWNGRADING SCHEDULE

16. DISTRIBUTION STATEMENT (of this Report)

Approved for public release; distribution unlimited.

17. DISTRIBUTION STATEMENT (of the abstract entered in Block 20, if different from Report)

18. SUPPLEMENTARY NOTES

19. KEY WORDS (Continue on reverse side if necessary and identify by block number)

Current and charge densities induced on aircraft
Geometrical Theory of Diffraction
Cylinder over ground plane
Caustic correction

20. ABSTRACT (Continue on reverse side if necessary and identify by block number)

The object of this research is to analyze the surface current and charge density induced on a finite cylinder situated above a perfectly conducting ground plane due to an incident plane wave. This geometry can be used to investigate the mechanisms involved in problems such as a plane wave incident upon a parked aircraft and other similar problems. The Geometrical Theory of Diffraction is the method used to analyze this problem. → next page

DD FORM 1 JAN 73 1473 EDITION OF 1 NOV 65 IS OBSOLETE

UNCLASSIFIED

402 251

20.

The GTD solution is first applied to a two dimensional waveguide aperture and compared with a modal type solution to indicate where the GTD ray picture is valid. The GTD solution is then applied to the finite cylinder over a ground plane problem with a procedure which partially corrects caustics which occur in the solution. Plots of current and charge densities for various geometries are presented.

LEVEL II

CONTENTS

I. INTRODUCTION

Since the 1970's, Geometrical Theory of Diffraction (GTD) solutions have been applied to compute the radiation patterns of aircraft antennas [1-7]. These solutions have been used along with the principle of reciprocity to analyze the surface current and charge density induced on aircraft [8-9]. These previously developed solutions were employed to compute surface current and charge densities for aircraft in a free space environment; however, there is a need for this information when the aircraft is closely coupled with other structures. For example, the surface current and charge density induced by a plane wave incident on a parked aircraft.

The object of this study is to analyze the surface current and charge density induced on a finite cylinder situated above a perfectly conducting ground plane due to an incident plane wave. This geometry can be used to investigate the mechanisms involved in the parked aircraft problem and other similar problems.

The basic approach taken in this study is to employ the Geometrical Theory of Diffraction (GTD). The GTD requires that the object be large in terms of wavelength such that various scattering centers are separated by at least a quarter wavelength. Therefore the solutions for surface current and charge densities are applicable for frequencies down to around 50 MHz for larger aircraft structures. The induced surface current density is given by $\vec{J} = 2\hat{n} \times \vec{H}^i$ where n is a unit normal to the surface and $\vec{H}^i$ is the incident magnetic field intensity on the cylinder surface. The induced surface charge density is given by $\rho = 2\varepsilon\hat{n} \times \vec{E}^i$ where ε is the permittivity of the surrounding medium and $\vec{E}^i$ is the incident electric field intensity on the surface. Using reciprocity, the electric surface current on a perfectly conducting aircraft surface can be determined from the radiation patterns of two mutually orthogonal magnetic current moments which are located tangentially on the aircraft surface at the point where the current is desired [8]. The electric charge density induced on the

aircraft can be similarly obtained from the radiation pattern of an infinitesimal electric current moment located along the normal to the aircraft surface at the desired observation point.

The Geometrical Theory of Diffraction solution used in this study is described in Chapter II. In Chapter III the two dimensional waveguide problem is considered. The GTD solution is compared with a modal type solution to show where the GTD ray picture is valid. Chapter IV describes the principal plane scattering from a cylinder in the presence of a perfectly conducting ground plane.

Chapter V presents a technique for partially correcting caustics which occur in the solution presented in Chapter IV. A summary of the present study and discussion is given in Chapter VI.

II. THEORETICAL BACKGROUND

A. Introduction

The basic technique used in this study is the geometrical theory of diffraction (GTD). The canonical wedge diffraction geometry is illustrated in Figure 1. In the format of GTD, the total electric field is given by

$$\vec{E} = \vec{E}^i + \vec{E}^r + \vec{E}^d \ . \qquad (1)$$

The field $\vec{E}^i$ is the electric field directly radiated by source, the field $\vec{E}^r$ is the electric field reflected from the wedge, and the field $\vec{E}^d$ is the electric field diffracted from the edge of the wedge.

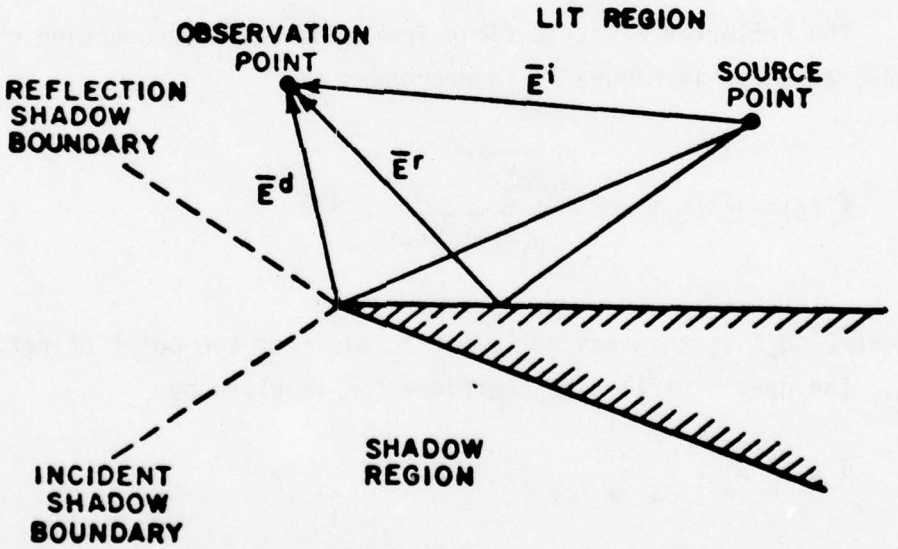

Figure 1. The basic GTD wedge diffraction problem.

The structures used in this report are assumed to be perfectly conducting and the surrounding medium is entirely free space. All fields carry an $\exp(j\omega t)$ time dependence which is assumed and suppressed.

B. Geometrical Optics Fields

The incident electric field, $\vec{E}^i$, can be generated by an arbitrary electric or magnetic source producing plane, cylindrical or spherical waves. In this study, electric or magnetic current moments producing spherical waves are used along with the reciprocity theorem to model surface current and charge density. The far field pattern of the source is written as

$$\vec{E}^i(\theta,\phi) = \left[\hat{\theta}F(\theta,\phi) + \hat{\phi}G(\theta,\phi)\right] \frac{e^{-jks}}{s} \tag{2}$$

where $F(\theta,\phi)$ and $G(\theta,\phi)$ are source pattern functions and s is the distance from the source to the observation point.

The reflected electric field from a perfectly conducting curves surface, as shown in Figure 2, is expressed as

$$\vec{E}_r(s) = \vec{E}^i(Q_r) \cdot \overline{\overline{R}} \sqrt{\frac{\rho_1^r \rho_2^r}{(\rho_1^r+s)(\rho_2^r+s)}}\ e^{-jks} \tag{3}$$

where $\vec{E}^i(Q_r)$ is the incident electric field at the point of reflection Q_r. The dyadic reflection coefficient $\overline{\overline{R}}$ is given by

$$\overline{\overline{R}} = \hat{e}_{\parallel}^i \hat{e}_{\parallel}^r - \hat{e}_{\perp} \hat{e}_{\perp} . \tag{4}$$

The unit vector $\hat{e}_{\perp}$ is the vector perpendicular to the plane of incidence and the vectors $\hat{e}_{\parallel}^i$ and $\hat{e}_{\parallel}^r$ are the incident and reflected unit vectors parallel to the plane of incidence. The plane of incidence is defined as the plane containing the incident ray and the normal $(\hat{n})$ to the surface at the point of reflection. The point of reflection, Q_r, is located using the laws of reflection which state that the angle of incidence equals the

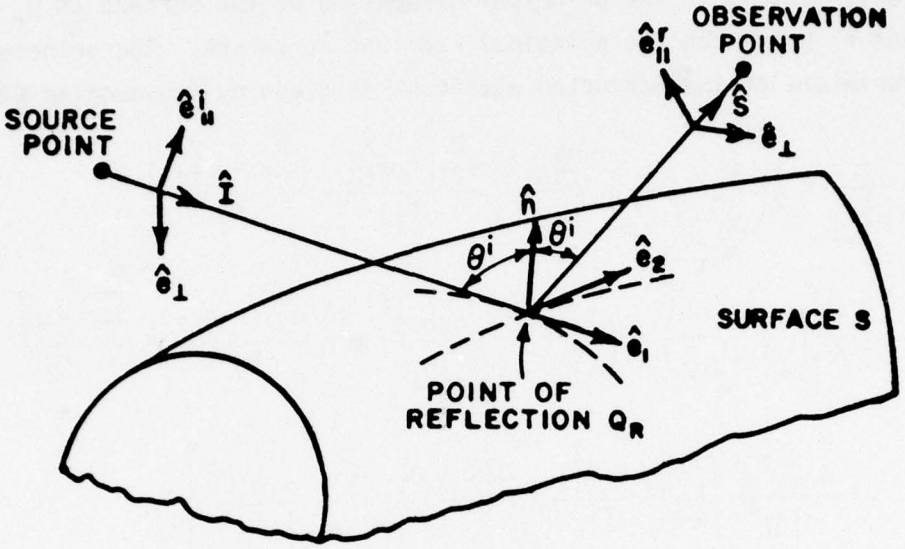

Figure 2. Reflection by a smooth convex surface.

angle of reflection and also the incident, reflected, and surface normals are coplanar. These laws can be expressed mathematically as

$$-\hat{I} \cdot \hat{n} = \hat{s} \cdot \hat{n} \tag{5}$$

and

$$\hat{I} \times \hat{n} = \hat{s} \times \hat{n} \, . \tag{6}$$

The above unit vectors are illustrated in Figure 2. The parameters ρ_1^r and ρ_2^r are the principal radii of curvature of the reflected wavefront at the reflection point. Kouyoumjian [10] gives a procedure for finding the radii of curvature by diagonalizing the curvature matrix of Deschamps [11] for the reflected wavefront. Let the wavefront be incident on a curved surface at the point Q_r as shown in Figure 2. The vectors $\hat{e}_1$ and $\hat{e}_2$ are

the unit vectors in the principal directions of the surface at Q_r with r_1 and r_2 being the two principal radii of curvature. The principal radii of curvature of the reflected wavefront as given by Kouyoumjian [10] are

$$\frac{1}{\rho^r_{1,2}} = \frac{1}{2}\left(\frac{1}{\rho^r_1} + \frac{1}{\rho^r_2}\right) + \frac{\cos\theta^i}{|\theta|^2}\left[\frac{\theta^2_{22} + \theta^2_{12}}{r_1} + \frac{\theta^2_{21} + \theta^2_{11}}{r_2}\right]$$

$$\pm \frac{1}{2}\left\{\left(\frac{1}{\rho^i_1} - \frac{1}{\rho^i_2}\right)^2 + \left(\frac{1}{\rho^i_1} - \frac{1}{\rho^i_2}\right)\frac{4\cos\theta^i}{|\theta|^2}\left[\frac{\theta^2_{22} - \theta^2_{12}}{r_1} + \frac{\theta^2_{21} - \theta^2_{11}}{r_2}\right]\right.$$

$$\left. + \frac{4\cos^2\theta^i}{|\theta|^4}\left[\left(\frac{\theta^2_{22} + \theta^2_{12}}{r_1} + \frac{\theta^2_{21} + \theta^2_{11}}{r_2}\right)^2 - \frac{4|\theta|^2}{r_1 r_2}\right]\right\} . \qquad (7)$$

The plus sign in the above equation is associated with ρ^r_1 and the minus sign with ρ^r_2. Also

$$\theta_{jk} = \hat{x}^i \cdot \hat{e}_k \qquad (8)$$

$$|\theta| = \theta_{11}\,\theta_{22} - \theta_{12}\,\theta_{21} . \qquad (9)$$

The unit vectors $\hat{x}^i_1$ and $\hat{x}^i_2$ are the principal directions of the incident wavefront at Q_r. The unit vectors $\hat{x}^r_1$ and $\hat{x}^r_2$ are the principal directions of the reflected wavefront and are found from

$$\hat{x}^r_1 = \frac{\left[\left(Q^r_{22} - \frac{1}{\rho^r_1}\right) x^r_1 - Q^r_{12}\, x^r_2\right]}{\sqrt{\left(Q^r_{22} - \frac{1}{\rho^r_1}\right)^2 + (Q^r_{12})^2}}$$

$$\hat{x}^r_2 = -\hat{s} \times \hat{x}^r_1 \qquad (10)$$

$$\hat{x}^r_{1,2} = \hat{x}^i_{1,2} - 2\,(\hat{n} \cdot \hat{x}^i_{1,2})\hat{n} \qquad (11)$$

and

$$Q^r_{11} = \frac{1}{\rho_1^i} + \frac{2\cos\theta^i}{|\theta|^2}\left[\frac{\theta_{22}^2}{r_1} + \frac{\theta_{21}^2}{r_1}\right] \tag{12}$$

$$Q^r_{12} = -\frac{2\cos\theta^i}{|\theta|^2}\left[\frac{\theta_{22}\,\theta_{12}}{r_1} + \frac{\theta_{11}\,\theta_{21}}{r_2}\right] \tag{13}$$

$$Q^r_{22} = \frac{1}{2^i} + \frac{2\cos\theta_i}{|\theta|^2}\left[\frac{\theta_{12}^2}{r_1} + \frac{\theta_{11}^2}{r_2}\right] . \tag{14}$$

C. Diffraction By a Wedge

An asymptotic solution for the diffraction from a conducting wedge was first solved by Sommerfeld [12]. Originally plane wave diffraction coefficients as presented by Keller [13] were used as the basis for the GTD solution. However, as shown in Reference [14], the use of cylindrical wave diffraction is necessary for antenna applications. Thus, different formulations for wedge diffraction were substituted for the plane wave diffraction coefficient which is the basis for wedge diffraction theory. Pauli [15] introduced the V_B function as a practical formulation for a finite angle conducting wedge. Hutchins and Kouyoumjian [16,17] have presented a formula for the diffracted field which significantly improves the accuracy of the solution over that obtained using Pauli's form. This improved solution provides superior results in the transition regions (near the incident and reflected shadow boundaries).

The three-dimensional wedge diffraction geometry is depicted in Figure 3. The source, located at $s'(\rho',\phi',z')$, generates a radiated $\vec{E}$ field given by $\vec{E}^i(s)$. The source can be an arbitrary electric or magnetic source

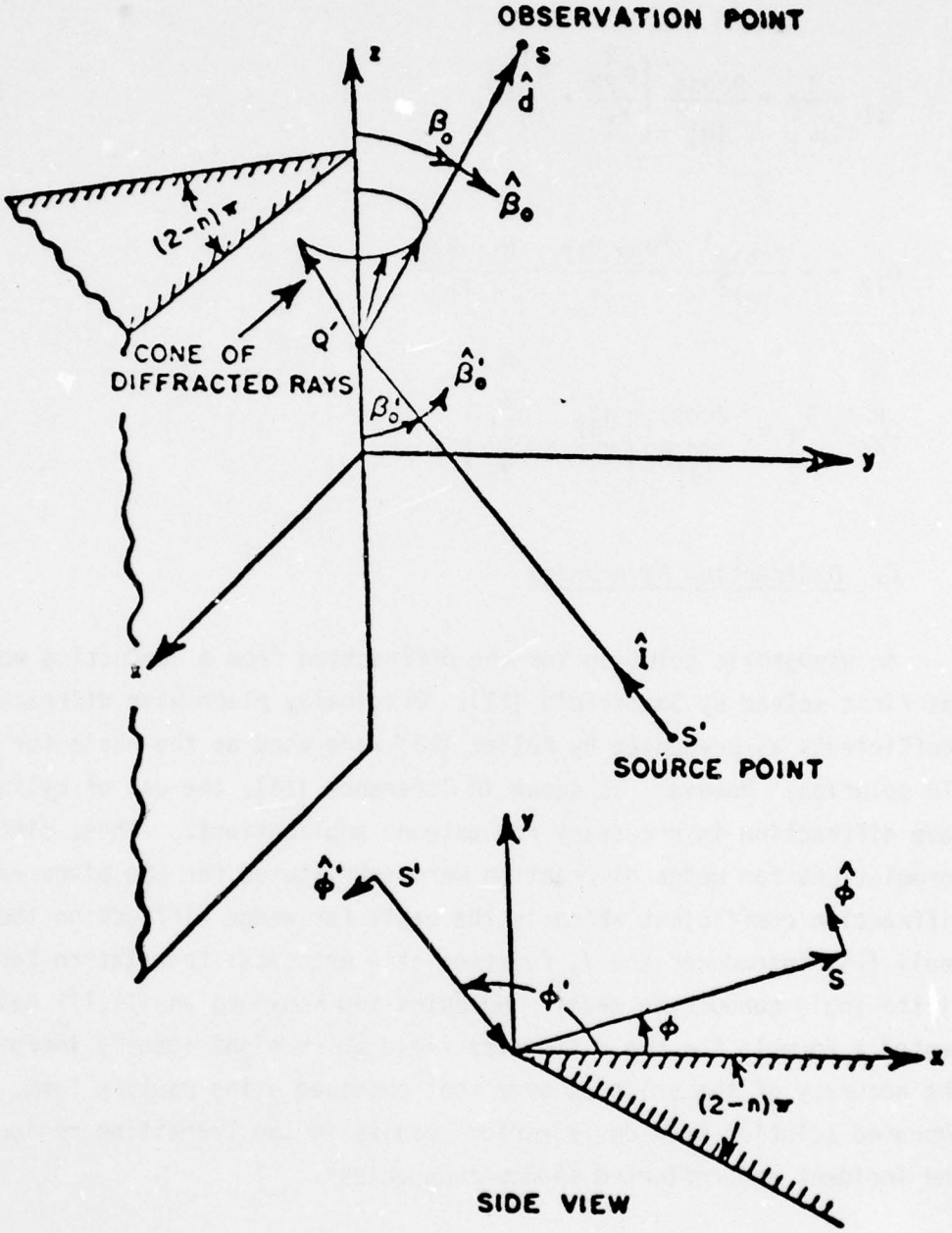

Figure 3. Geometry for three-dimensional wedge diffraction problem.

causing cylindrical, conical, or spherical wave incidence on the wedge. The diffracted vector field at $s(\rho, \phi, z)$ can be written in terms of a dyadic diffraction coefficient.

Kouyoumjian and Pathak [18] have derived a more rigorous basis for the GTD formulation and have shown that the diffracted field may be written compactly if it is defined in terms of a ray fixed coordinate system. This ray fixed coordinate system is centered at the point of diffraction Q', (or points of diffraction as in the case of plane wave incidence). Note that Q' is a unique point or set of points for a given source and observation point. The incident ray diffracts as a cone of rays such that the cone half angle (β_0) equals the angle (β_0') which the incident ray forms with the edge as shown in Figure 3.

The orthogonal unit vectors associated with these coordinates (s', $\hat{\beta}_0', \hat{\phi}', s, \hat{\beta}_0, \hat{\phi}$) are related by

$$\hat{I} = -\hat{s}$$

$$\hat{I} = \hat{\beta}_0' \times \hat{\phi}'$$

$$\hat{s} = \hat{\beta}_0 \times \hat{\phi}$$

where $\hat{I}$ is the incident direction unit vector and $\hat{s}$ is the unit vector in the direction of diffraction.

The diffracted field is, then, given by

$$\vec{E}(s) \sim \vec{E}^i(Q') \quad \bar{\bar{D}}_E(\hat{s}, \hat{I})\, A(s)\, e^{-jks} \tag{15}$$

where

$$\overline{\overline{D}}_E = - \hat{\beta}_o' \hat{\beta}_o D_s - \hat{\phi}' \hat{\phi} D_h$$

and

$$D_{\substack{s \\ h}}(\phi,\phi',\beta_o) = \frac{e^{-j\frac{\pi}{4}}}{2n\ 2\pi k \sin\beta_o} \left[\left\{ \cot\left(\frac{\pi+(\phi-\phi')}{2n}\right) F[kLa^{\pm}(\phi-\phi')] \right.\right.$$

$$\left. + \cos\left(\frac{\pi-(\phi-\phi')}{2n}\right) F[kL^{\mp}(\phi-\phi')] \right\}$$

$$\pm \left\{ \cot\left(\frac{\pi+(\phi+\phi')}{2n}\right) F[kLa^{+}(\phi+\phi')] \right.$$

$$\left.\left. + \cos\left(\frac{\pi-(\phi+\phi')}{2n}\right) F[kLa^{-}(\phi+\phi')] \right\} \right] \qquad (16)$$

with

$$a^{\pm}(\beta) = 2\cos^2\left(\frac{2n\pi N^{\mp} - \beta}{2}\right).$$

In addition, $N^{\mp}$ is the integer which comes closest to satisfying the following equations:

$$2n\pi N^{+} - \beta = +\pi$$

$$2n\pi N^{-} - \beta = -\pi$$

with

$$\beta = \phi \pm \phi' .$$

F(x) is defined by

$$F(x) = 2j\sqrt{x}\, e^{jx} \int_{|\sqrt{x}|}^{\infty} e^{-j\tau^2}\, d\tau$$

and is called the transition function. The quantity n is defined by the wedge angle WA where WA = $(2-n)\pi$. The $(\phi-\phi')$ terms are associated with the incident field; whereas, the $(\phi+\phi')$ terms are associated with the reflected field. The quantities A(s) and L are defined later.

In matrix notation the diffracted field is expressed by [16,17]

$$\begin{bmatrix} E_{\parallel}^{d}(s) \\ E_{\perp}^{d}(s) \end{bmatrix} = \begin{bmatrix} -D_s & 0 \\ 0 & -D_h \end{bmatrix} \begin{bmatrix} E_{\parallel}^{i}(Q') \\ E_{\perp}^{i}(Q') \end{bmatrix} A(s)\, e^{-jks}. \qquad (17)$$

The D_s coefficient corresponds to the $\vec{E}$-field component parallel to the edge with the (acoustically soft) boundary condition

$$\vec{E}\big|_{\text{Wedge}} = 0.$$

The D_h coefficient corresponds to the $\vec{E}$-field component perpendicular to the edge with the (acoustically hard) boundary conditions

$$\frac{\partial \vec{E}}{\partial \vec{n}}\bigg|_{\text{Wedge}} = 0.$$

The quantity A(s) in Equation (17) is the ray divergent factor given in general by [10]

$$A(s) = \sqrt{\frac{\rho}{s(\rho+s)}}\quad .$$

For the straight wedge case $\rho = \rho_e^i$, where ρ_e^i is the radius of curvature of the incident wavefront in the plane containing the incident ray and the edge. For spherical wave incidence A(s) is given by

$$A(s) = \sqrt{\frac{s'}{s(s'+s)}} \quad .$$

The quantity L is a distance parameter and is given in general by [10]

$$L = \frac{s(\rho_e+s)\rho_1\rho_2 \sin^2\beta_o}{\rho_e(\rho_1+s)(\rho_2+s)} \tag{18}$$

where ρ_1 and ρ_2 are the principal radii of curvature of the wavefront. For a straight edge, L is given by [10]

$$L = \frac{s's \sin^2\beta_o}{s+s'}$$

for spherical wave incidence.

For grazing incidence ($\phi'=0$) $D_s=0$, and D_h must be halved since the incident and reflected fields merge together and only half of the total field on the surface is associated with the incident field with the other half being the reflected field.

D. Curved Wedge Diffraction

The diffracted field due to a curved wedge is analyzed using the GTD techniques developed by Kouyoumjian and Pathak [10]. The diffracted field from a curved wedge, as seen in Figure 4 is expressed by

$$\vec{E}^d(d) \sim \vec{E}^i(Q') \cdot D_E(\hat{s},\hat{I}) \sqrt{\frac{\rho}{s(\rho+s)}}\ e^{-jks} \quad . \tag{19}$$

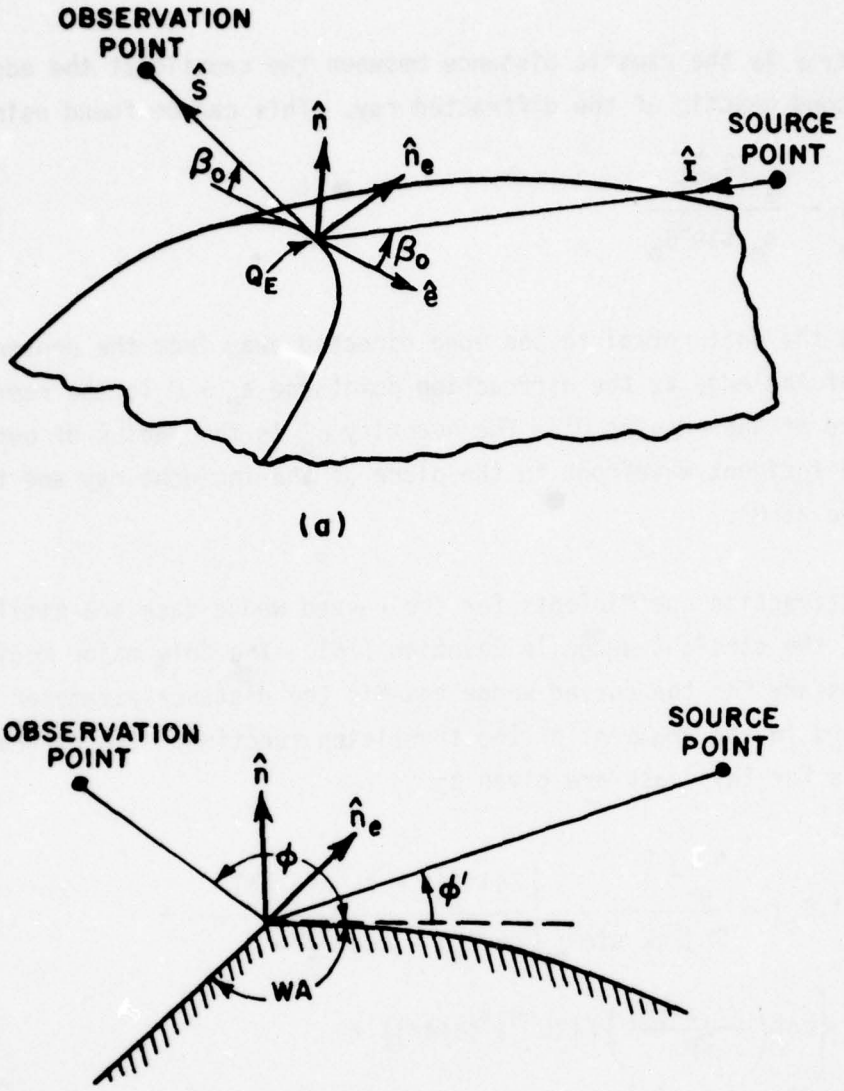

Figure 4. Geometry for three-dimensional curved wedge diffraction.

The quantity ρ is the caustic distance between the caustic at the edge and the second caustic of the diffracted ray. This can be found using

$$\frac{1}{\rho} = \frac{1}{\rho_e^i} - \frac{\hat{n}_e \cdot (\hat{i} - \hat{s})}{a_e \sin^2 \beta_o} \tag{20}$$

where $\hat{n}_e$ is the unit normal to the edge directed away from the center of curvature of the edge at the diffraction point and $a_e > 0$ is the radius of curvature of the edge at Q'. The quantity ρ_e^i is the radius of curvature of the incident wavefront in the plane of the incident ray and tangent to edge at Q'.

The diffraction coefficients for the curved wedge case are similar to those of the straight wedge in Equation (16). The only major modification necessary for the curved wedge case is the distance parameter L, which appears in the argument of the transition function. The diffraction coefficients for this case are given by

$$D_{\substack{s \\ h}}(\phi,\phi',\beta_o) = \frac{e^{-j\frac{\pi}{4}}}{2n\sqrt{2\pi k}\,\sin\beta_o}\left[\frac{2\sin(\frac{\pi}{n})\; F\; kL^i a(\phi-\phi')}{\cos(\frac{\pi}{n}) - \cos(\frac{\phi-\phi'}{n})} + \right.$$

$$\pm\left\{\cot\left(\frac{\pi+(\phi+\phi')}{2n}\right) F[kL^{rn} a^+(\phi+\phi')] + \right.$$

$$\left.\left. + \cot\left(\frac{\pi-(\phi+\phi')}{2n}\right) F[kL^{ro}\, a(\phi+\phi')]\right\}\right] \tag{21}$$

in which $a(\gamma) = 2\cos^2\gamma$ and $a^+(\gamma) = 2\cos^2\left(\frac{2\pi n-\gamma}{2}\right)$. The incident field distance parameter is expressed by

$$L^i = \frac{s(\rho_e^i+s)\,\rho_1^i\rho_2^i \sin^2\beta_o}{\rho_e^i(\rho_1^i+s)(\rho_2^i+s)} \; . \tag{22}$$

The reflected field distance parameters from the surface with superscript o (reflection boundary at $\pi-\phi'$) and from the surface with superscript n (reflection boundary at $(2n-1)\pi-\phi'$) are given by

$$L^r = \frac{s(\rho_e^r+s)\ \rho_1^r\rho_2^r\ \sin^2\beta_o}{\rho_e^r(\rho_1^r+s)(\rho_2^r+s)} \quad . \tag{23}$$

The parameters ρ_1^i and ρ_2^i are the principal radii of curvature of the incident wavefront at the point of diffraction. For plane, cylindrical, and conical waves ρ_e^i is infinite and for spherical waves $\rho_e^i=s'$. The parameters ρ_1^r and ρ_2^r are the principal radii of curvature of the reflected wavefront at Q' and can be found using Equation (7).

III. CURRENT DENSITY INDUCED UPON A TWO DIMENSIONAL WAVEGUIDE

A. Introduction

In this chapter the two dimensional waveguide and open resonator problem is investigated. The desired goal is to show where a simple ray picture is valid when compared with a more general modal solution.

B. Waveguide Mode Analysis

The geometry for the waveguide mode analysis is shown in Figure 5. In this section the radiated field from the parallel plate aperture is obtained by superposition of the diffracted fields from the edge due to each propagating mode. Rudduck and Tsai [19] have shown that this method yields answers which agree with a Wiener-Hopf technique and experimental results. The waveguide spacing determines the number of propagating modes which exist in the waveguide. If the waveguide spacing is "a" then the m-th propagating mode has a propagation angle (θ_m) defined by

$$1 > \sin\theta_m = \frac{m\lambda}{2a} \quad . \tag{24}$$

For $m = 0,1,2,\ldots,m_{max} < \frac{2a}{\lambda}$.

The diffracted field for one mode can be expressed using Equation (15) as

$$u = u^i|_{z=t} \; D \; \frac{e^{-jkr}}{\sqrt{r}}$$

where $r = |\vec{r}|$ is the distance to the far field observer and given by

$r = |\vec{d}| - |\vec{\ell} \cdot \hat{d}|$ and ℓ is a vector from the origin to the point of diffraction.

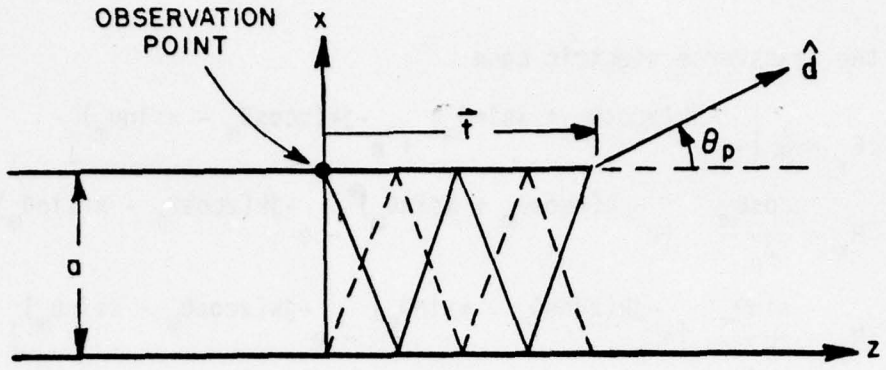

Figure 5. Parallel plate geometry.

The parameter D is the plane wave diffraction coefficient obtained from Equation (16). The incident field u^i can be written as the sum of two crossing plane waves in the waveguide. For the transverse magnetic case

$$H_y = \frac{1}{2}\left[e^{-jk(z\cos\theta_m + x\sin\theta_m)} + e^{-jk(z\cos\theta_m - x\sin\theta_m)}\right]$$

$$E_x = \frac{1}{2} z_o \cos\theta_m \left[e^{-jk(z\cos\theta_m + x\sin\theta_m)} + e^{-jk(z\cos\theta_m - x\sin\theta_m)}\right]$$

$$E_z = \frac{1}{2} z_o \sin\theta_m \left[-e^{-jk(z\cos\theta_m + x\sin\theta_m)} + e^{-jk(z\cos\theta_m - x\sin\theta_m)}\right] \tag{25}$$

At the edge of this waveguide, z=t and z=a,

$$H_y = e^{-jkt\cos\theta_m}$$

$$E_x = z_o \cos\theta_m \, e^{-jkt\cos\theta_m}$$

$$E_z = 0. \tag{26}$$

For the transverse electric case

$$E_y = \frac{1}{2}\left[-e^{-jk(z\cos\theta_m + x\sin\theta_m)} + e^{-jk(z\cos\theta_m - x\sin\theta_m)}\right]$$

$$H_x = \frac{\cos\theta_m}{z_o}\left[e^{-jk(z\cos\theta_m + x\sin\theta_m)} - e^{-jk(z\cos\theta_m - x\sin\theta_m)}\right]$$

$$H_z = \frac{\sin\theta_m}{z_o}\left[e^{-jk(z\cos\theta_m + x\sin\theta_m)} - e^{-jk(z\cos\theta_m - x\sin\theta_m)}\right] \qquad (27)$$

and at z=t and x=a,

$$E_y = 0$$

$$H_x = 0$$

$$H_z = -\frac{\sin\theta_m}{z_o} e^{-jkt\cos\theta_m} . \qquad (28)$$

The total field is found by summing in the far field the individual diffraction components due to each propagating mode in the waveguide. Using reciprocity this will yield the surface current or charge induced upon the waveguide walls due to an incident plane wave (see Chapter I).

The waveguide mode analysis becomes a numerical accuracy problem when the plate spacing is large in terms of wavelengths. As the plate spacing is increased the number of propagating modes increases (see Equation (24)). For large plate spacings the GTD solution described in the next section is more accurate as will be seen later.

C. GTD Parallel Plate Solution

The GTD solution for the parallel plate geometry is valid when this plate spacing is large in terms of wavelengths. The total electric field is given by

$$\vec{E} = \vec{E}^{i} + E_{m}^{r} + \sum_{n} \vec{E}_{n}^{d}$$

where m is the number of bounces off of the ground plane the reflected ray from the source makes before reaching the far field and n is the number of bounces which occur before a reflected ray strikes the edge.

The incident field from the infinitesimal source located in the waveguide is shadowed by the waveguide geometry for all far field observation directions except for $\theta_p = 0^o$ (see Figure 5). The reflected field components are found using image theory with only one image being visible for a given range of θ_p. Given θ_p the desired image is located at $-2a(n - \frac{1}{2})x + 0.z$. The integer n can be found from

$$\frac{2a(n-1)}{t} < \tan \theta_p \leq \frac{2an}{t}$$

which implies

$$n \leq \frac{\tan\theta_p}{r} + 1 \qquad (29)$$

where

$$r = \frac{2a}{t} .$$

The reflected field can then be written as

$$\vec{E}_m = R^{2m-1} e^{-jk2am\sin\theta_p} \frac{e^{-jkr}}{\sqrt{r}} \qquad (30)$$

where R=1 for $\vec{H}$-field parallel to the edge and R=-1 for $\vec{E}$-field parallel to the edge.

The diffracted field is composed of a sum of diffraction terms which are generated by the image sources as in Figure 6. Given by

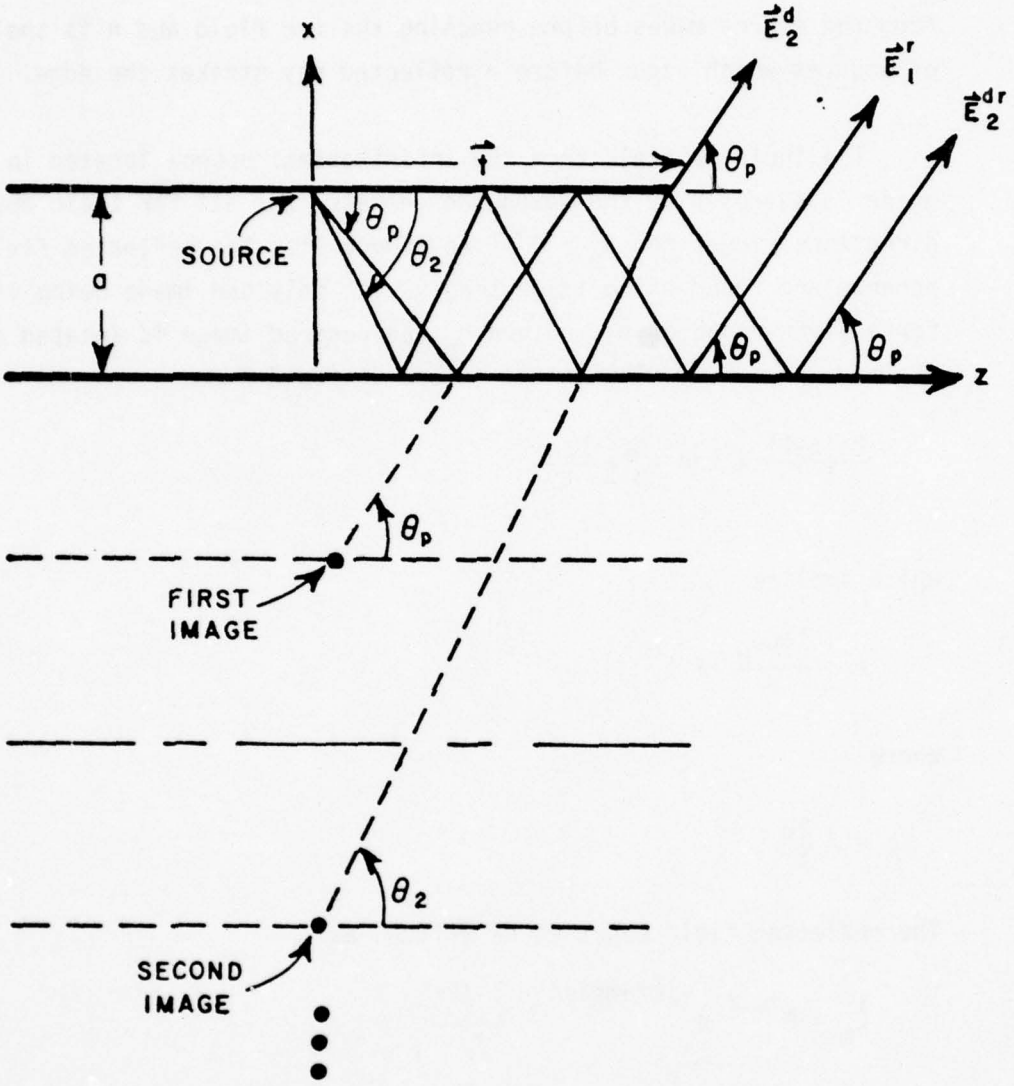

Figure 6. Image locations for the parallel plate geometry.

$$\vec{E}_n^d = \vec{E}_n^r\Big|_{edge} \cdot \bar{\bar{D}}_E(\hat{s},\hat{I})\, e^{-jk\hat{d}\cdot\hat{\ell}}\, \frac{e^{-jkr}}{\sqrt{r}} \qquad (31)$$

where ℓ is a vector from the origin to the point of diffraction.

D. Results

Figures 7 through 24 compare the GTD current solution with the modal current solution for various waveguide spacings, a, and distances from the waveguide aperture, t, as defined in Figure 5. The parameters a and t are varied independently from 0.25λ, 0.50λ, 1.0λ, 2.0λ, 5.0λ, to 10.0λ. Figures 7 through 15 are for the H-field parallel to the edge or the TM waveguide mode, while Figures 16 through 24 are for the H-field perpendicular to the edge or the TE waveguide mode. Each polar plot fixes a, t, and the polarization and varies θ_p, the angle of incidence of the incoming unit plane wave, is varied from 0^o to 90^o.

The agreement between the GTD and the modal solution increases as the waveguide spacing increases. As the spacing is increased more propagating modes can occur in the waveguide which increases the accuracy of the GTD ray picture. For the H-perpendicular case with a=0.25λ or a=0.5λ and propagating TE modes exist in the waveguide (see Equation (24)) so no modal solution is presented in these plots. The effect of no propagating modes for this case is indicated in the GTD solution by the field strength being very low for these cases.

The agreement between the GTD and the modal solution lessens as θ_p approaches 90^o. This effect is due to the GTD solution approaching a caustic since the number of ray terms is approaching infinity as can be seen using Equation (29) with $\theta_p = 90^o$.

Figures 25a through 30a show the $\hat{z}$ current magnitude in dB plotted for the H-parallel case normalized to the incident field or $|J_z|/|H^i\hat{y}|$. Figures 25b through 30b show the $\hat{y}$ current magnitude in dB for the H-perpendicular case normalized to the incident field or $|J_y|/|-H^i\cos\theta_p\hat{x} + H^i \sin\theta_p\hat{z}|$. On each plot in this section the waveguide spacing, a, is fixed

and the distance from the aperture, t, is varied continuously from 0.3 wavelengths to 10.0 wavelengths for four different values of plane wave incidence angles, θ_p. The angles, θ_p, occur in five degree increments starting at either 0^o, 15^o, 30^o, 45^o, 60^o, or 75^o. In the H-perpendicular case for a=0.25 wavelengths and a=0.5 wavelengths the waveguide is in the cutoff region. This can be seen in the plots by the low level of current indicated in Figures 43 and 44 and by the exponential decay of the current away from the aperture as seen in Figures 45 and 47. As stated before the current value presented in Figures 25 through 60 become less accurate as θ_p approaches 90^o.

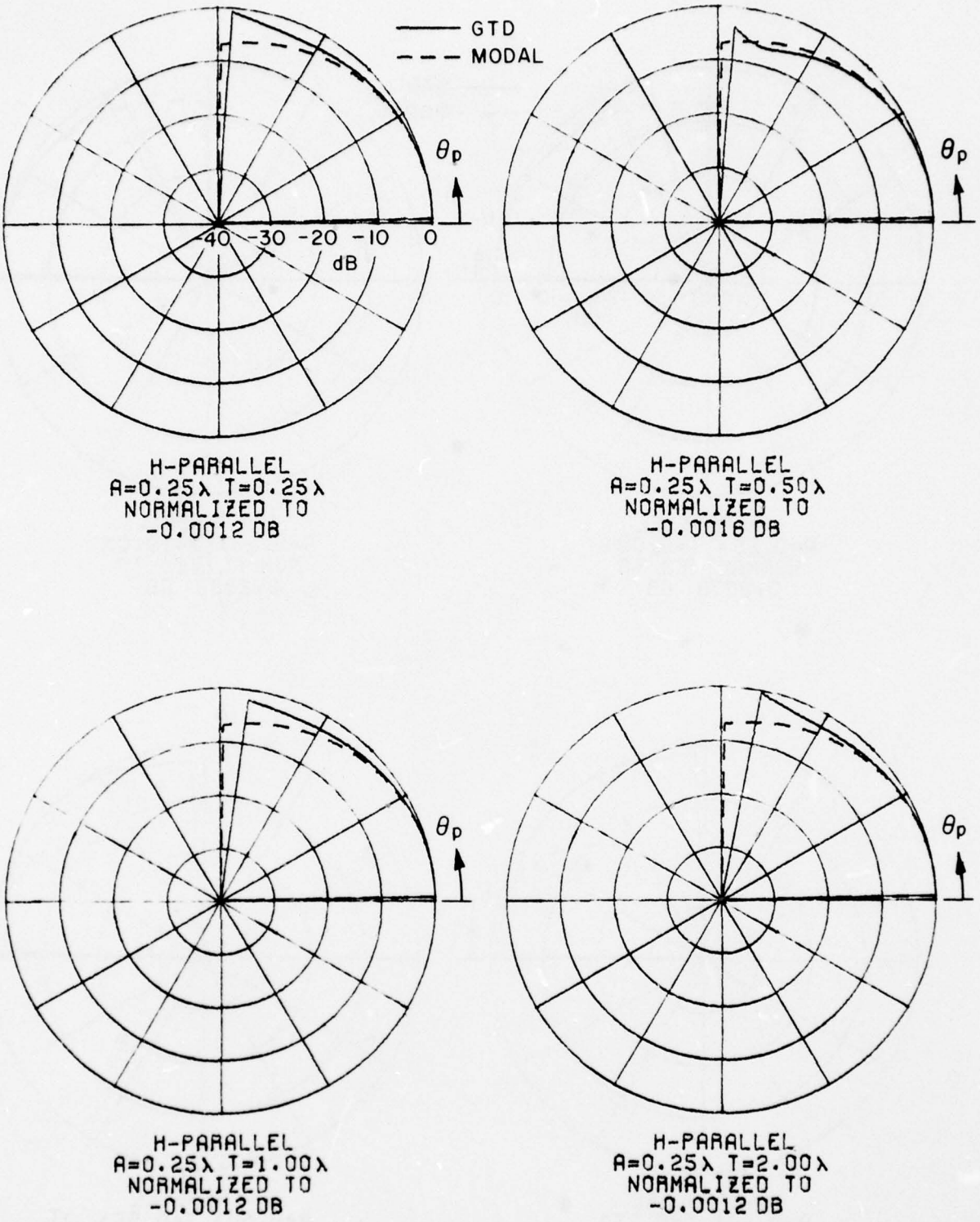

Figure 7. H_u in the waveguide for a=0.25 wavelength.

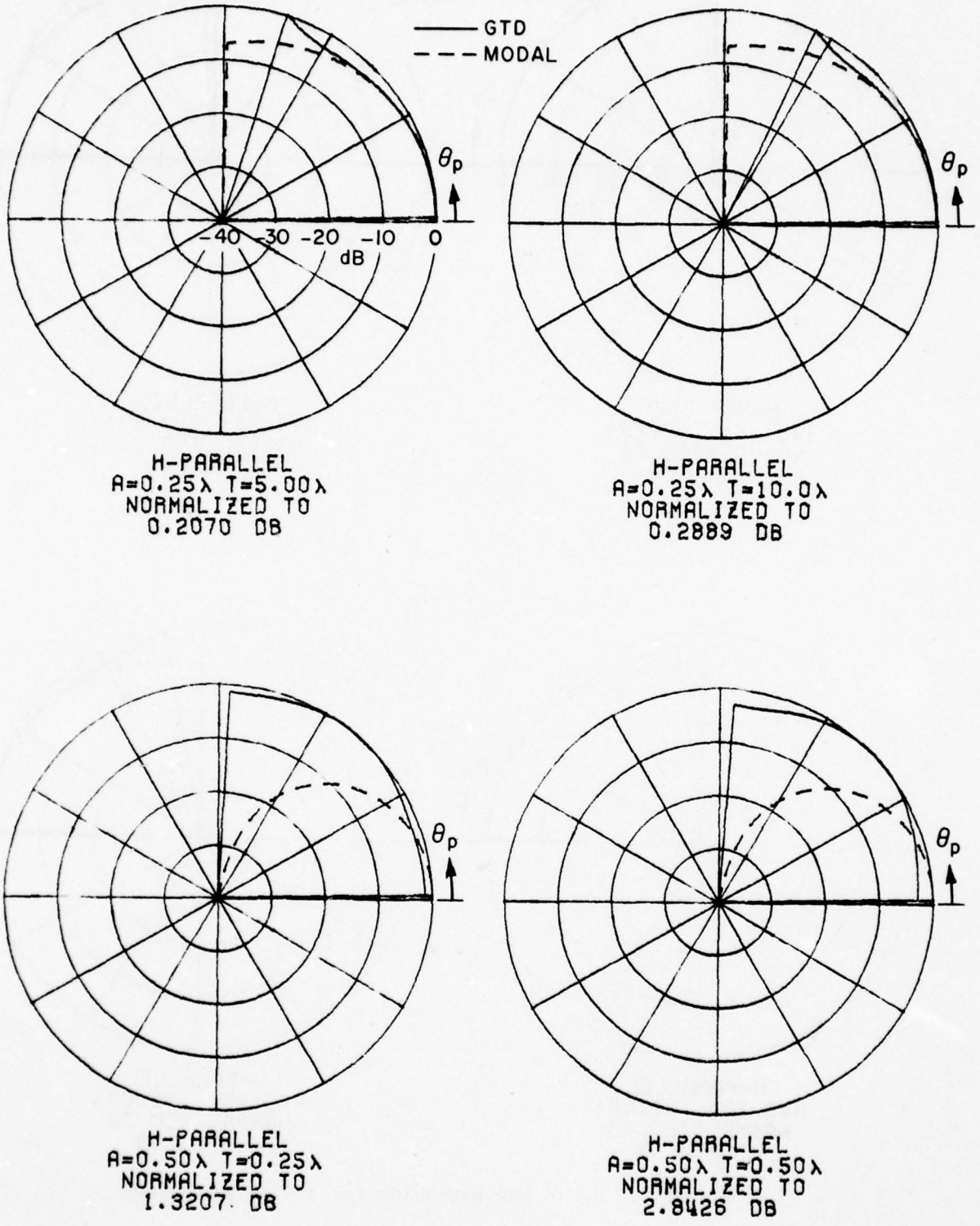

Figure 8. H_m in the waveguide for a=0.25 and 0.5 wavelength.

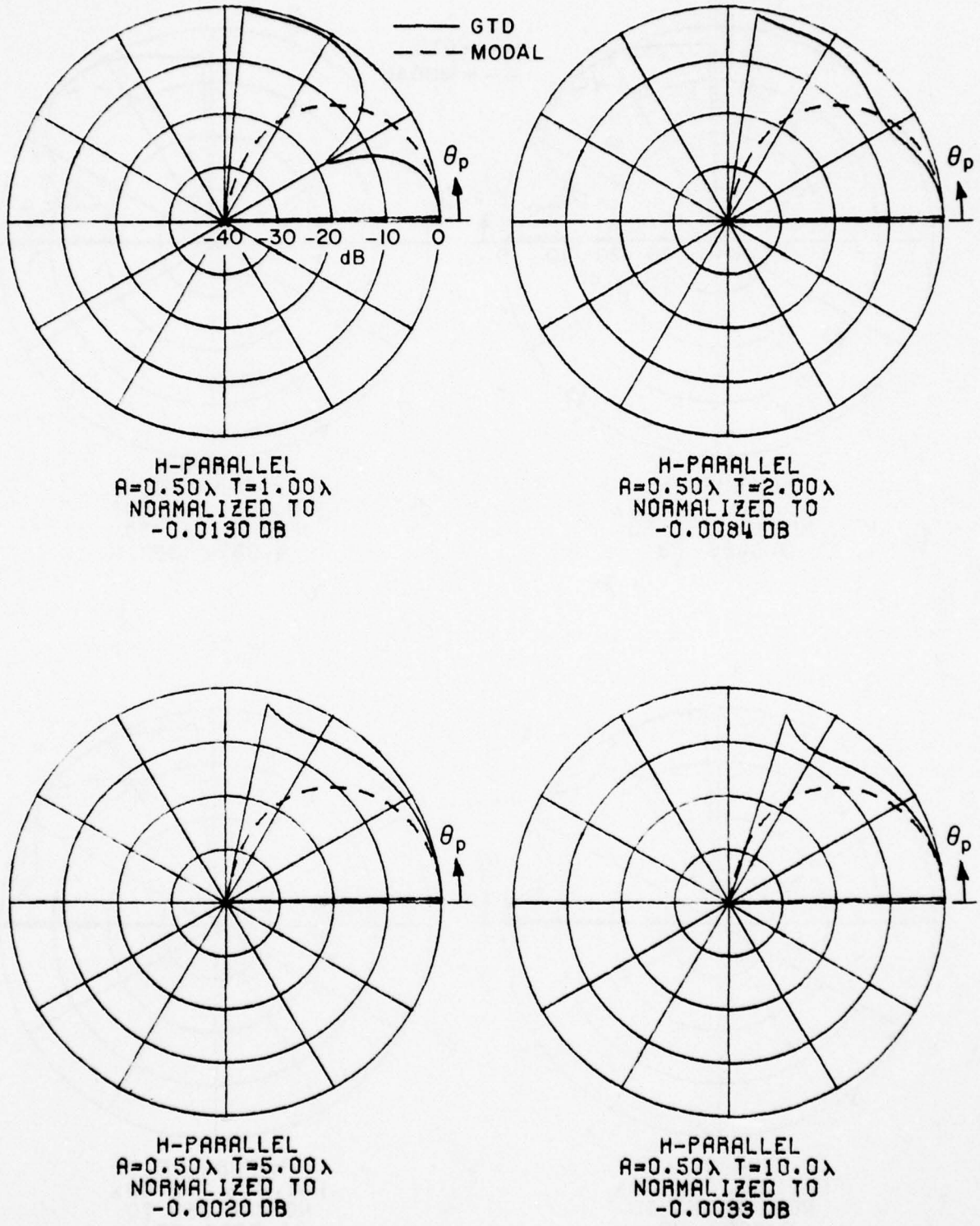

Figure 9. H_m in the waveguide for a=0.5 wavelength.

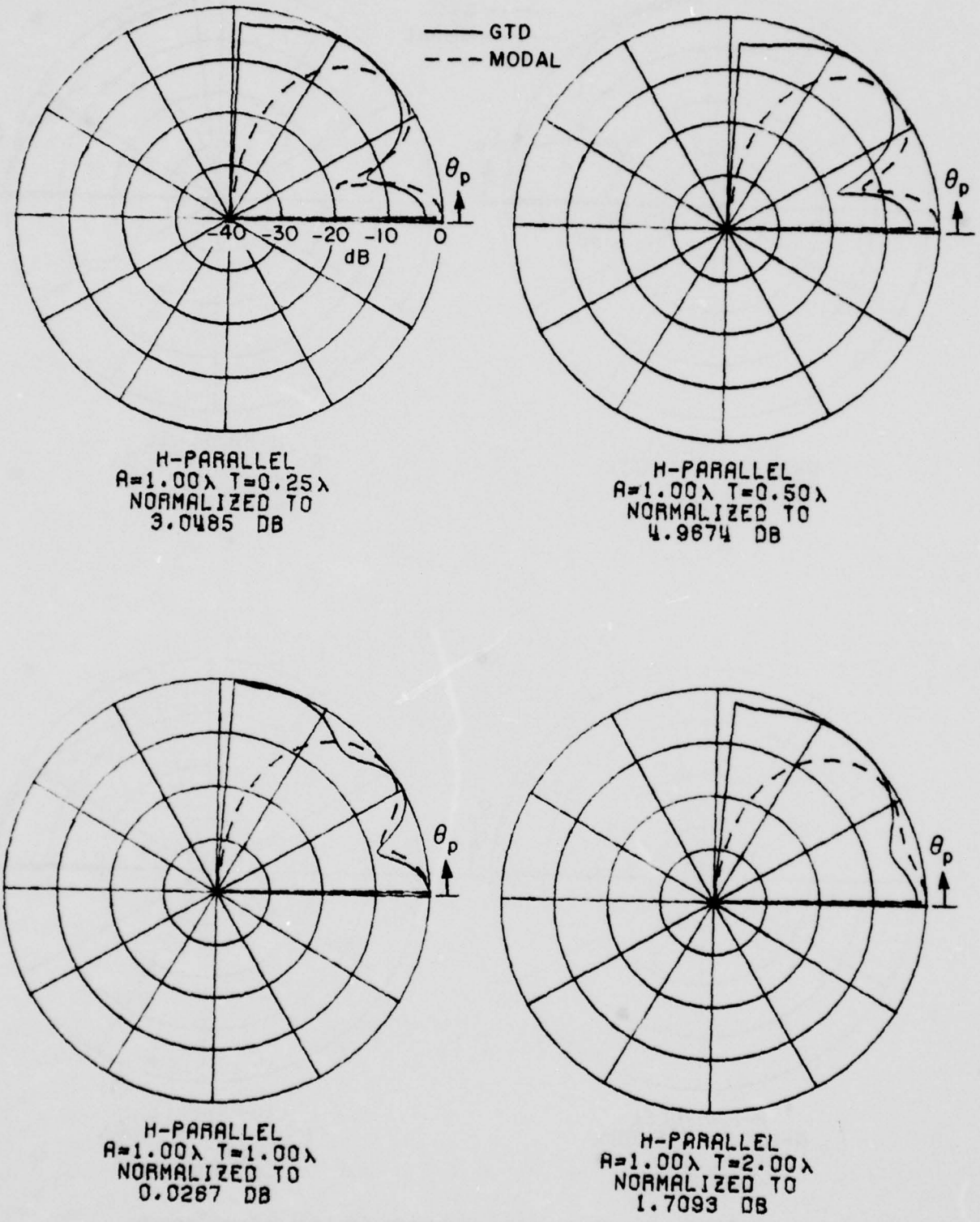

Figure 10. H_m in the waveguide for a=1.0 wavelength.

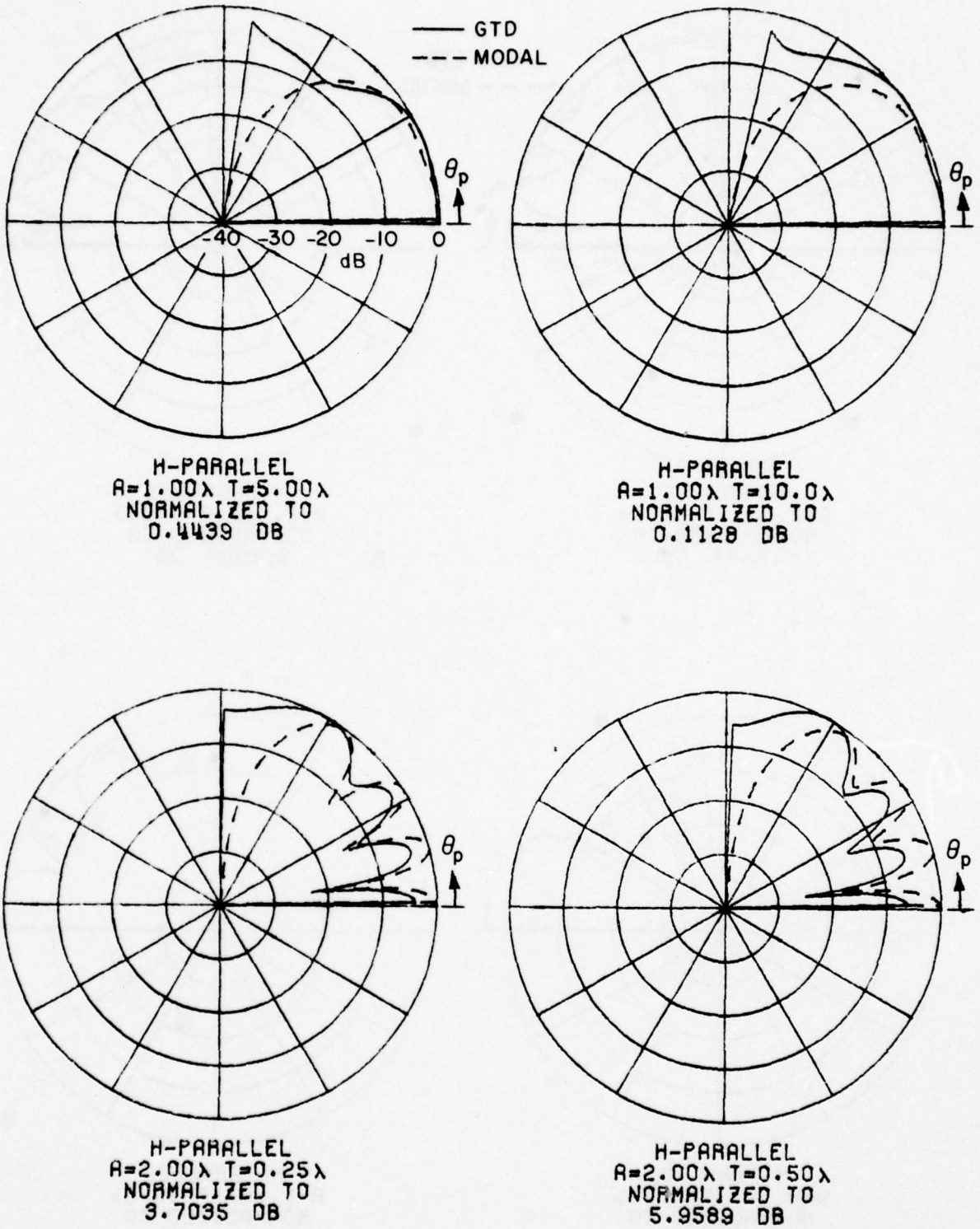

Figure 11. H_m in the waveguide for a=1.0 and 2.0 wavelength.

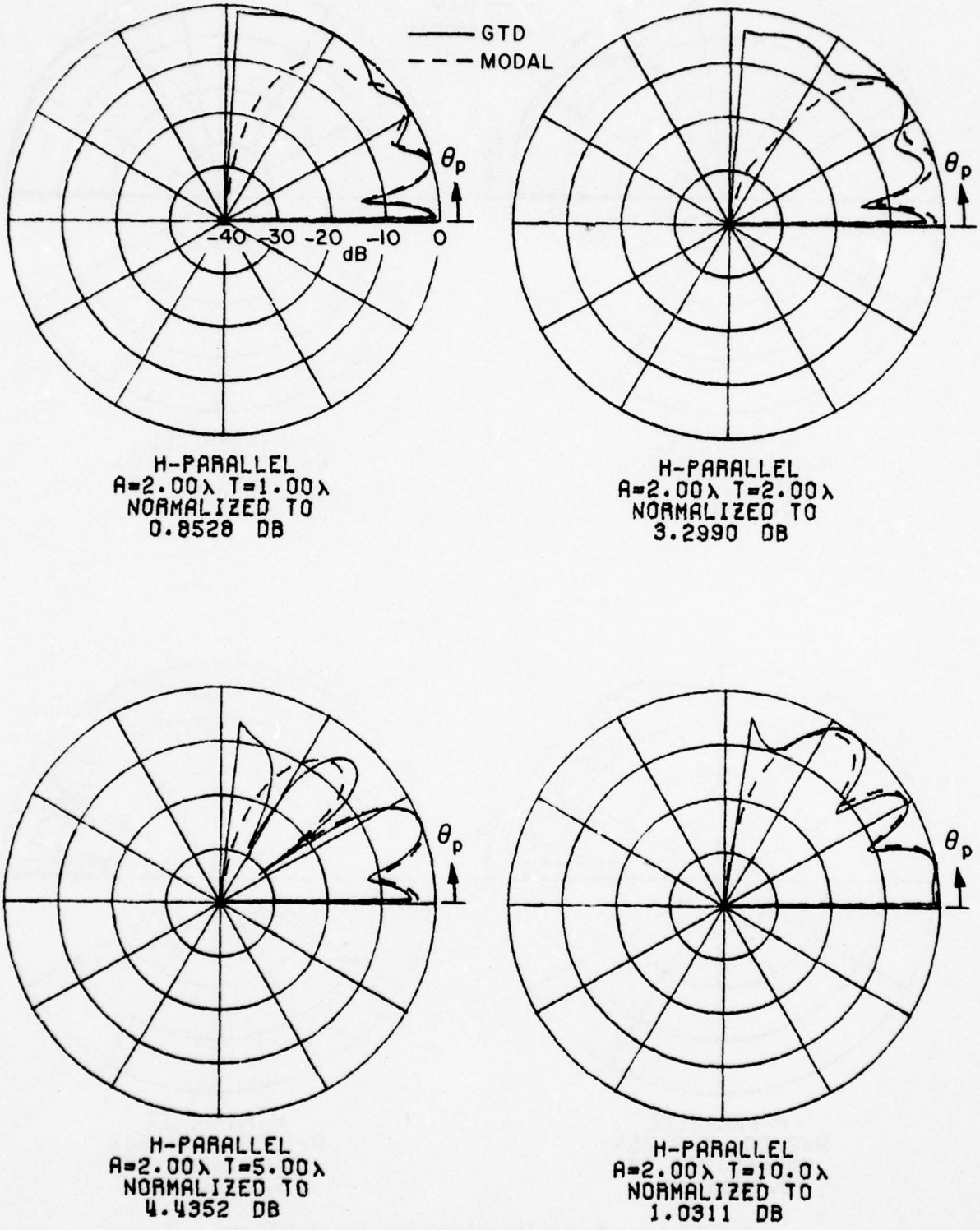

Figure 12. H_u in the waveguide for a=2.0 wavelength.

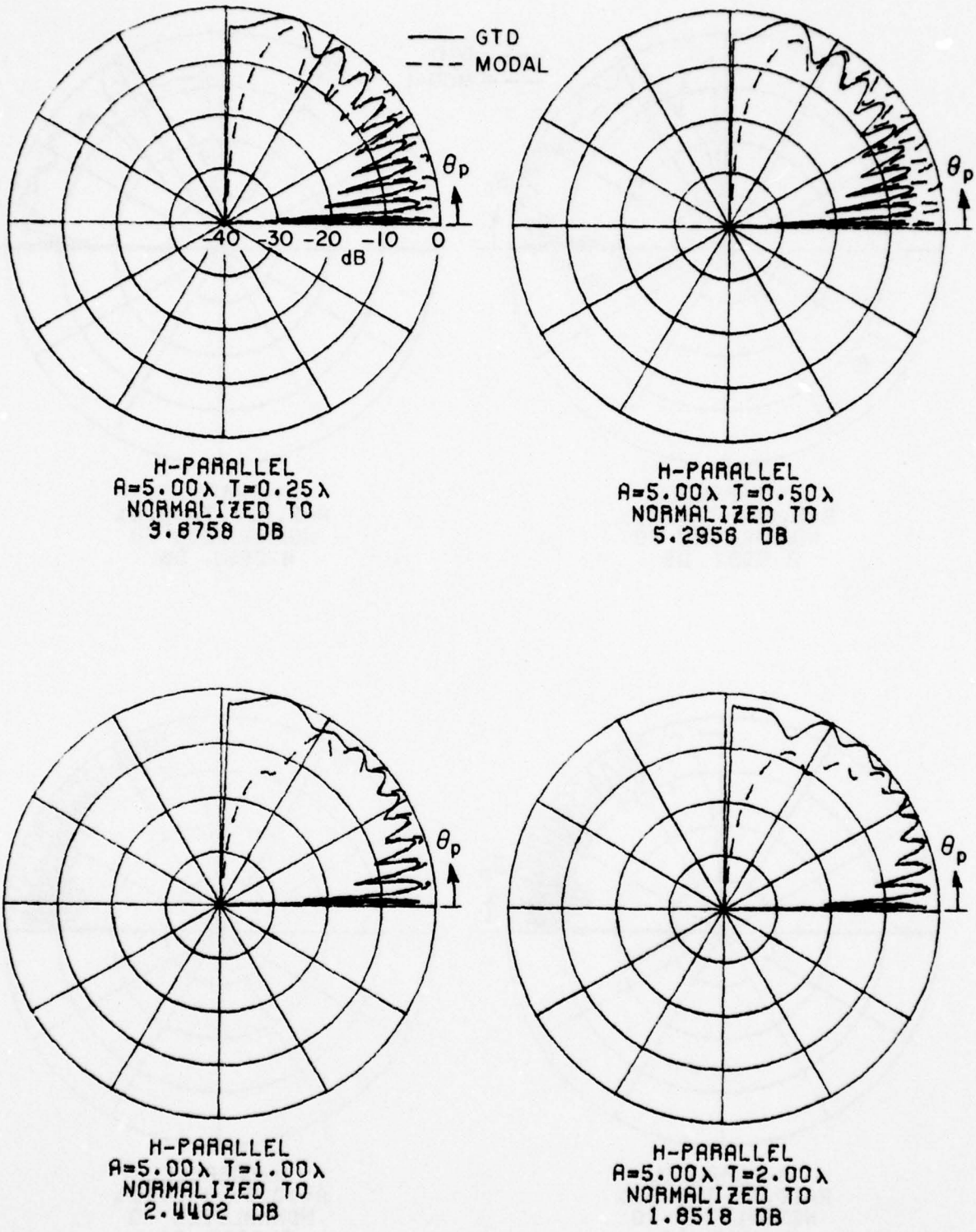

Figure 13. H_m in the waveguide for a=5.0 wavelength.

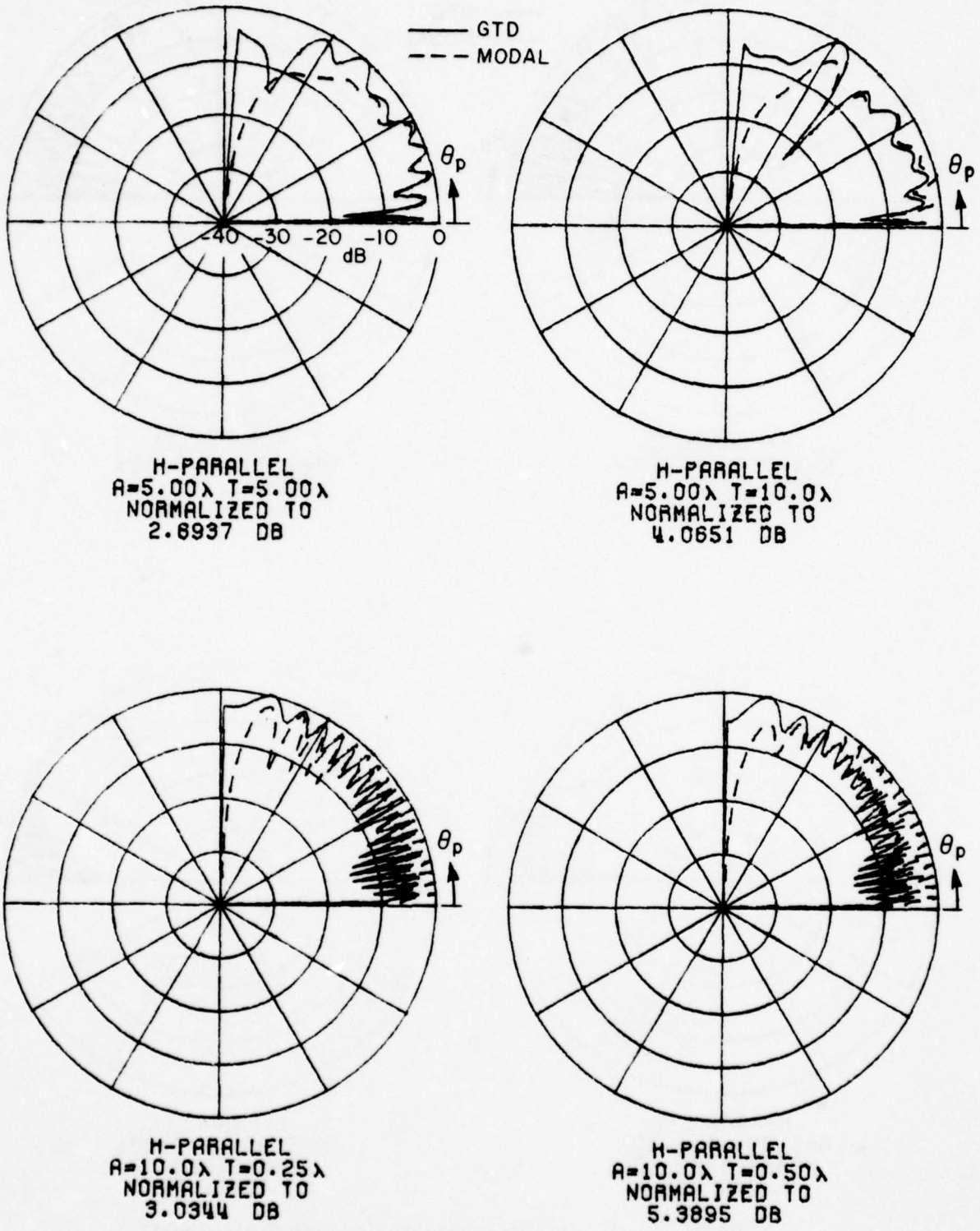

Figure 14. H_u in the waveguide for a=5.0 and 10.0 wavelengths.

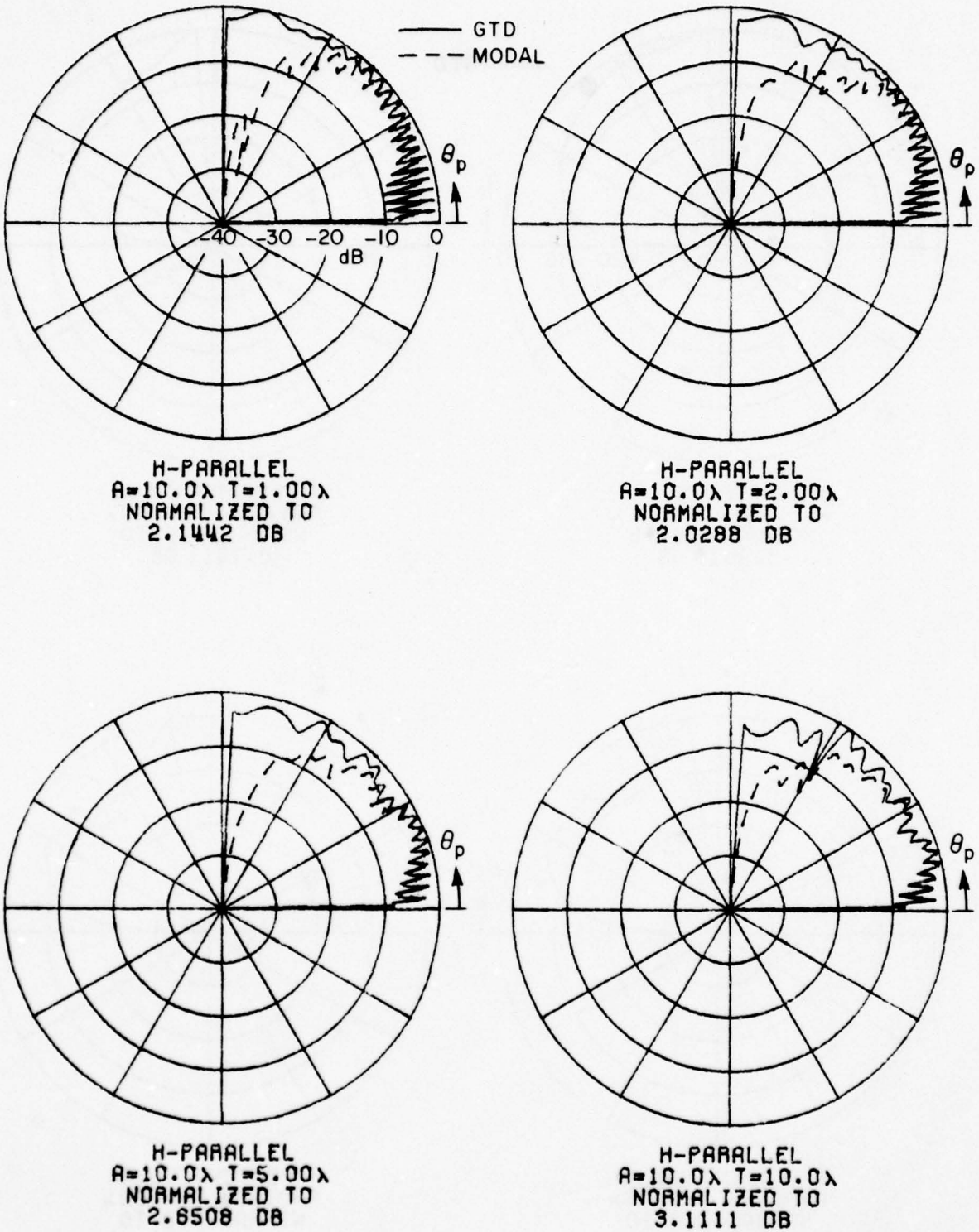

Figure 15. H_u in the waveguide for a=10.0 wavelength.

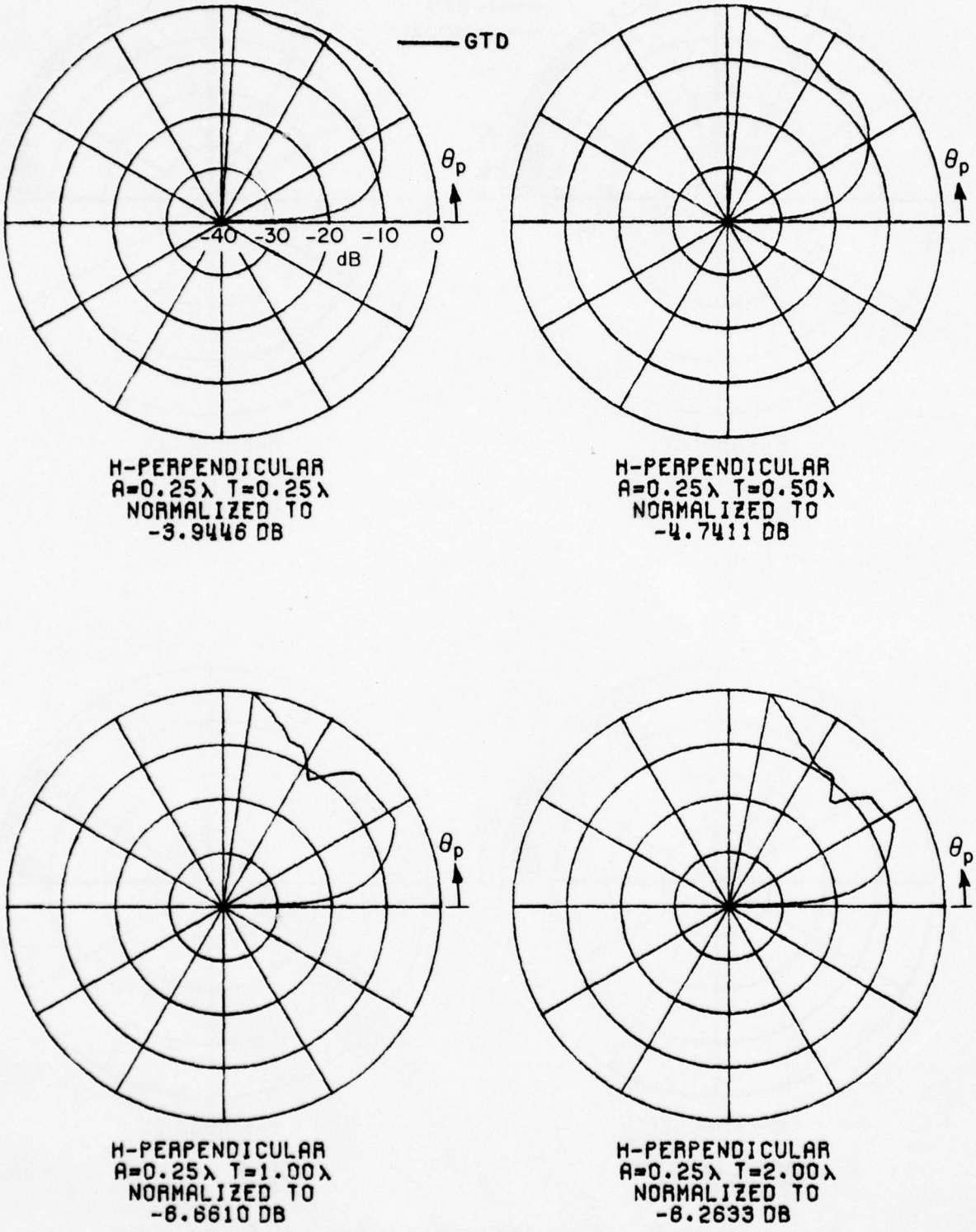

Figure 16. H_z in the waveguide for a=0.25 wavelength.

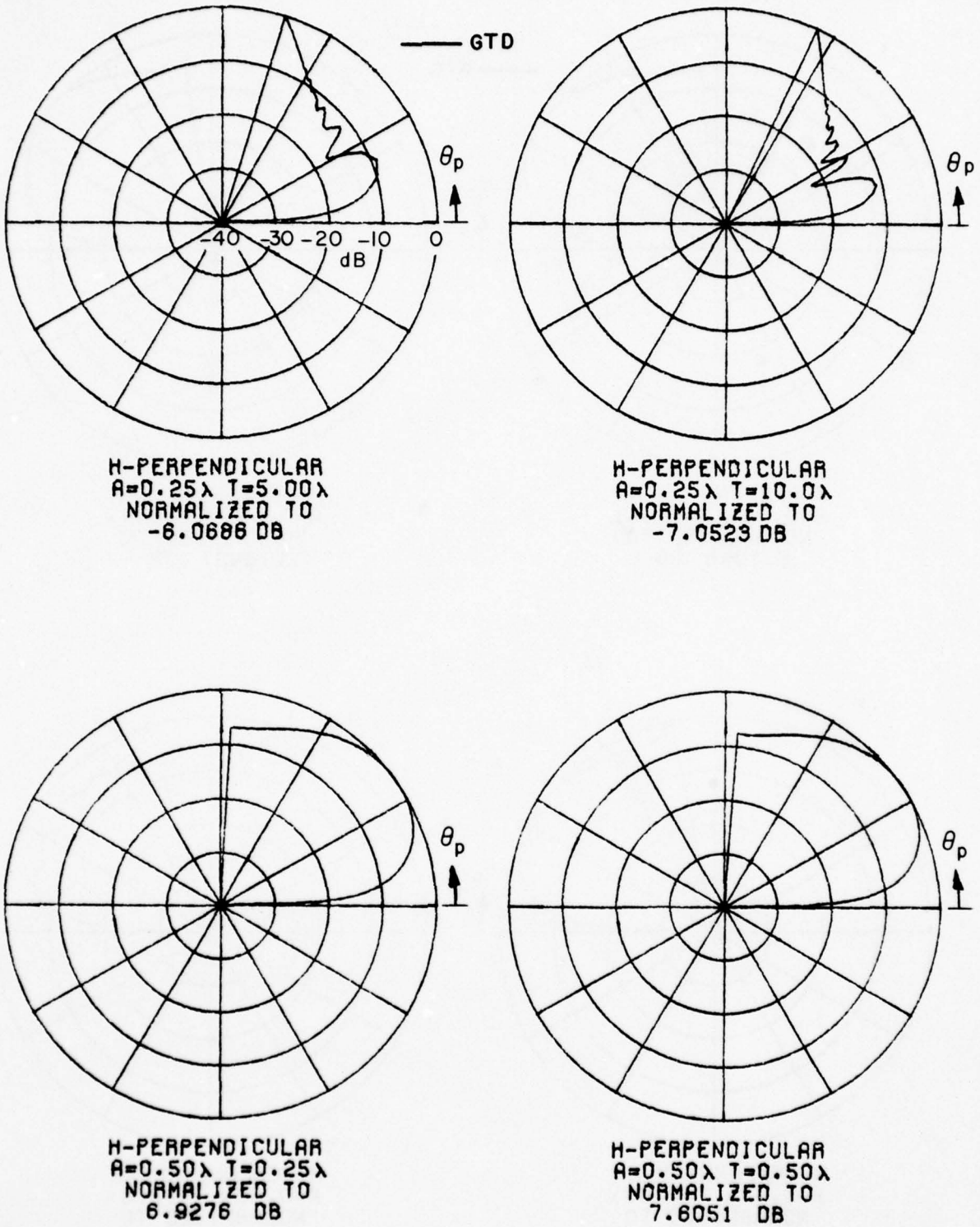

Figure 17. H_z in the waveguide for a=0.25 and 0.5 wavelength.

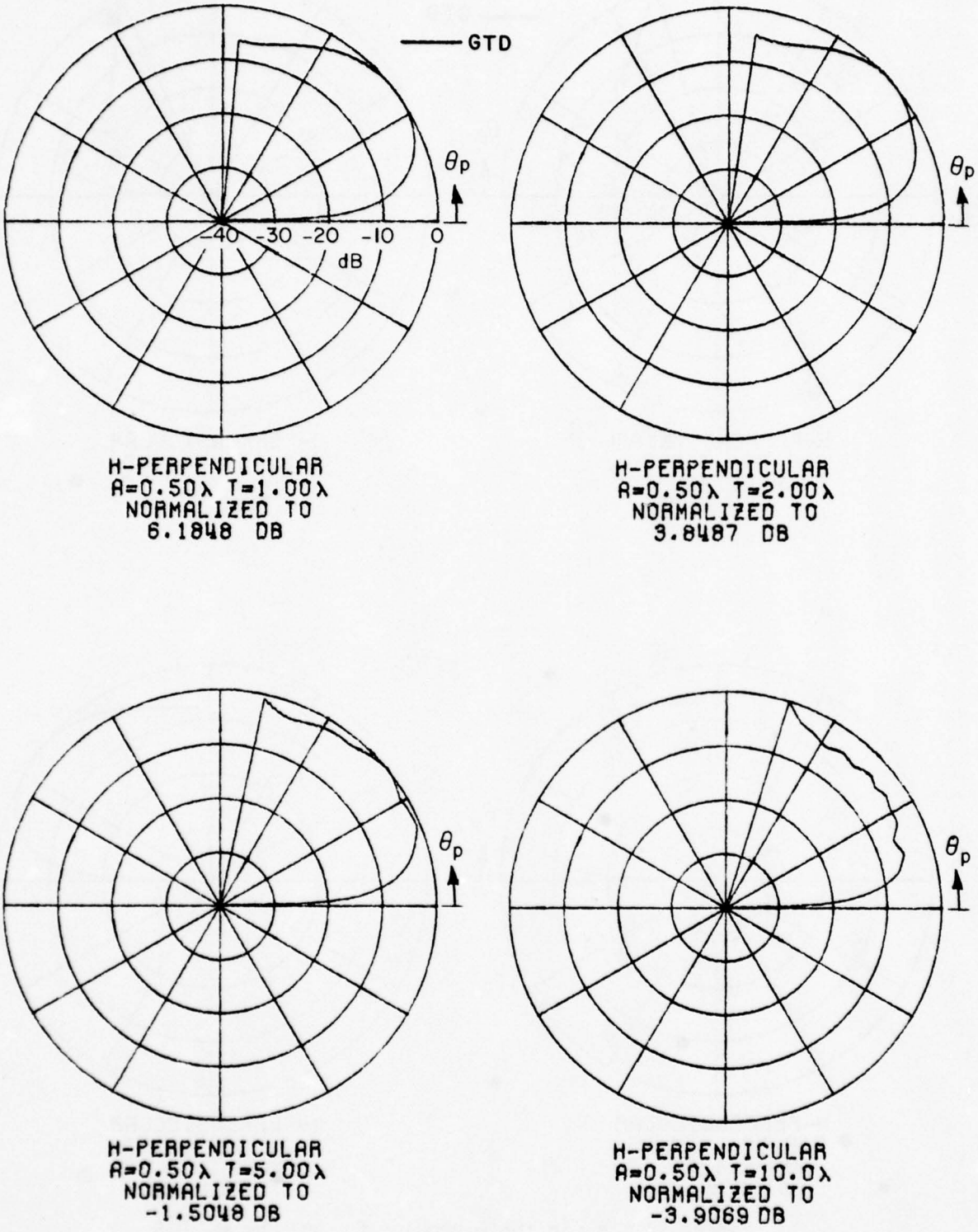

Figure 18. $H_\perp$ in the waveguide for a=0.5 wavelength.

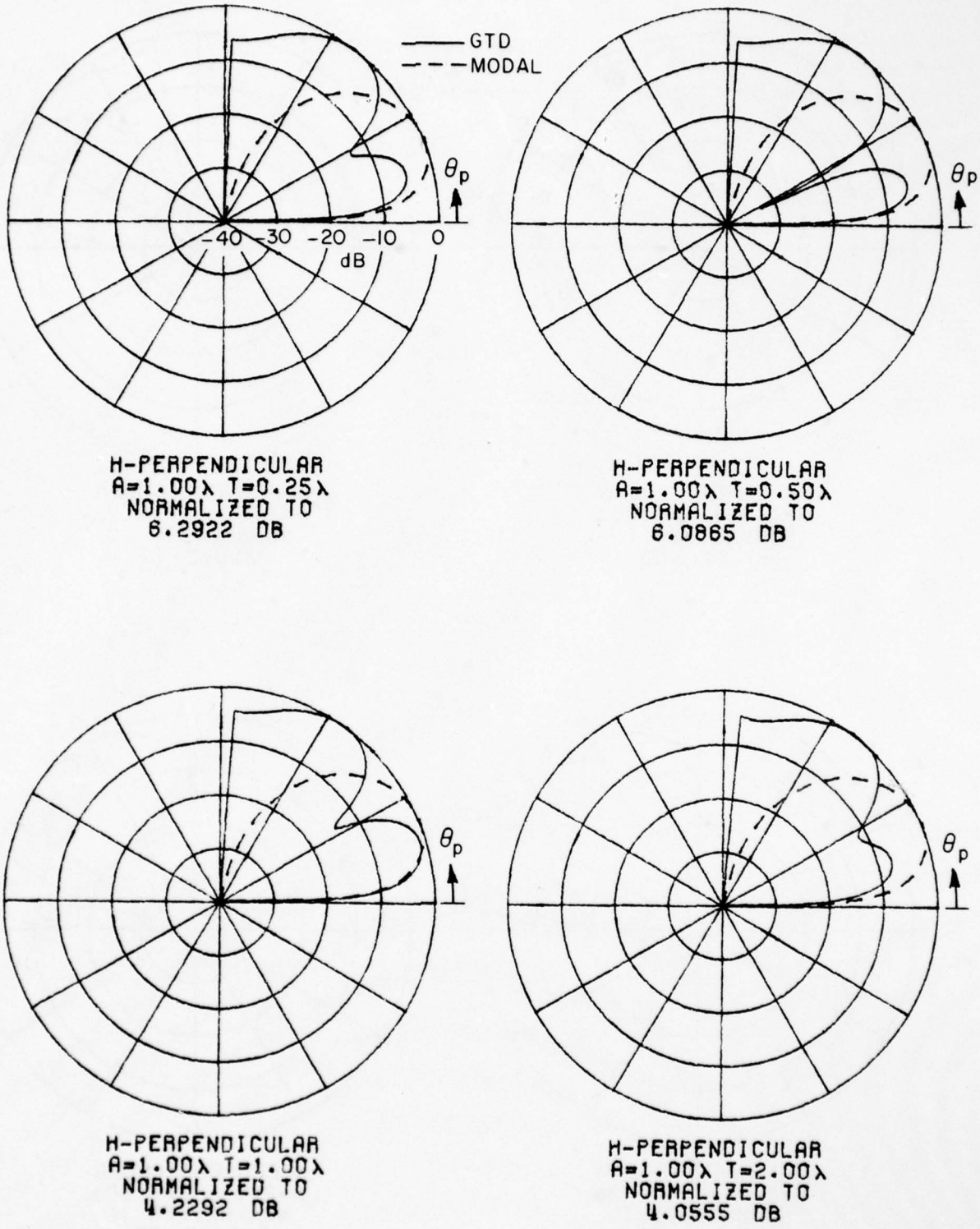

Figure 19. $H_\perp$ in the waveguide for a=1.0 wavelength.

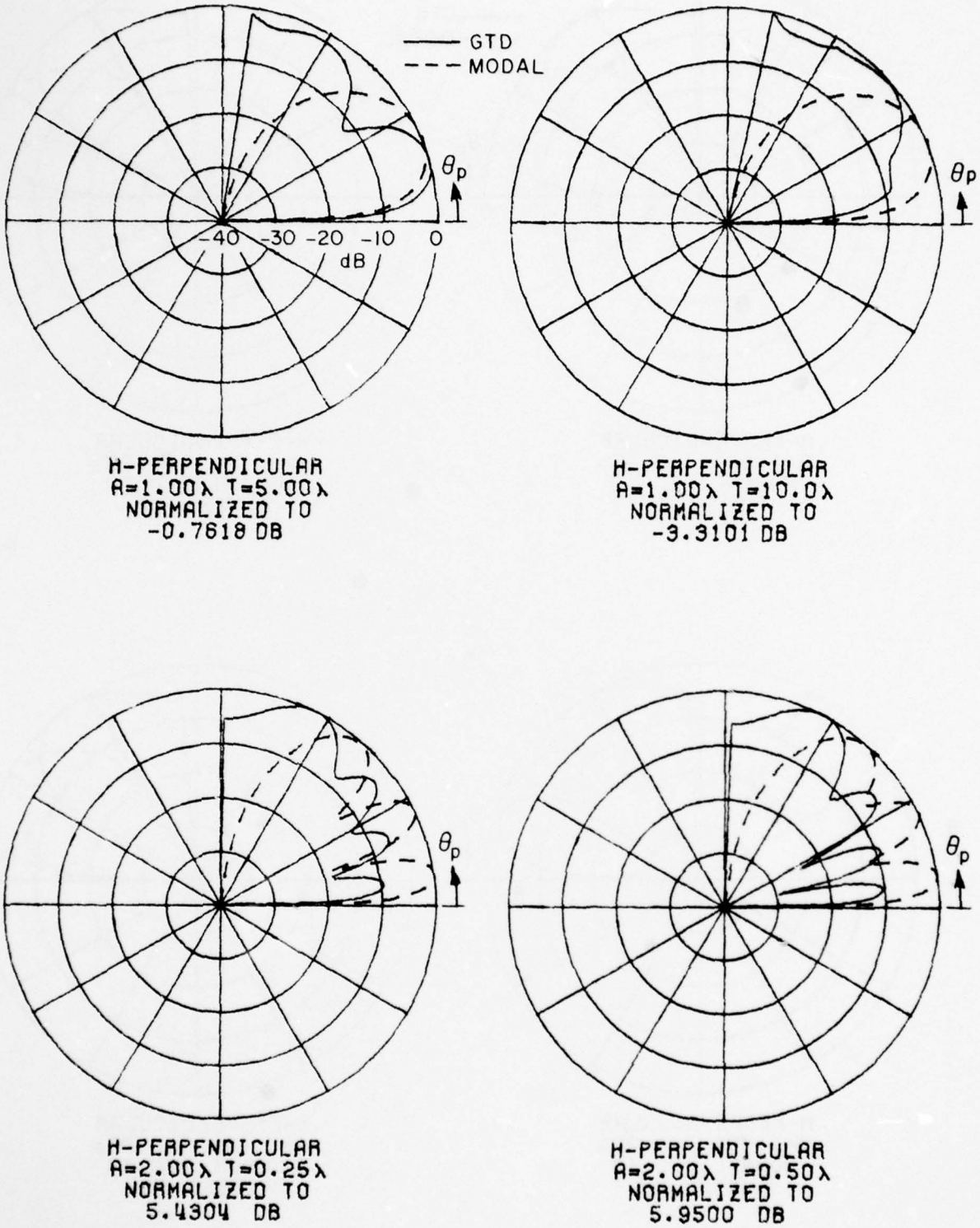

Figure 20. H in the waveguide for a=1.0 and 2.0 wavelength.

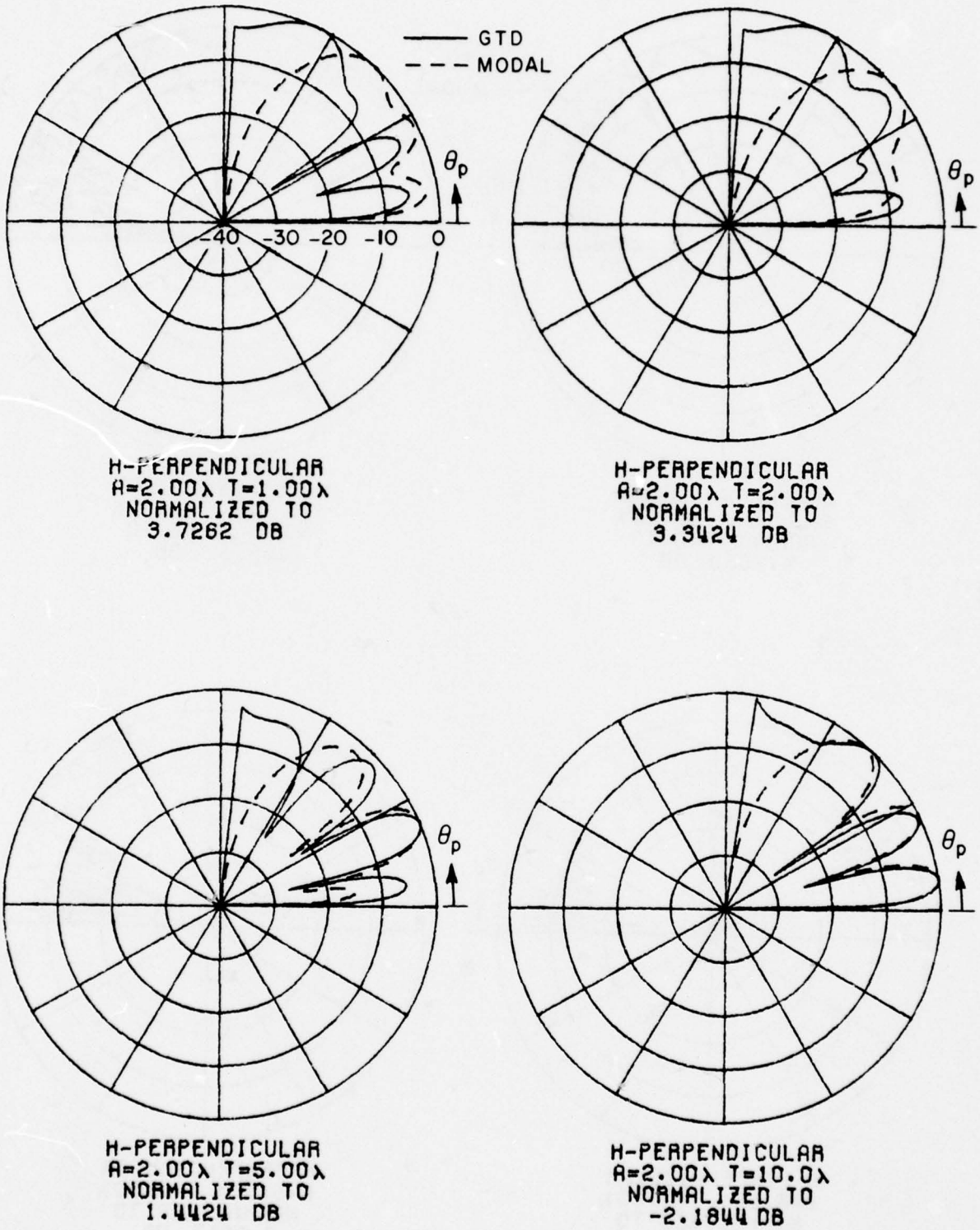

Figure 21. H_z in the waveguide for a=2.0 wavelength.

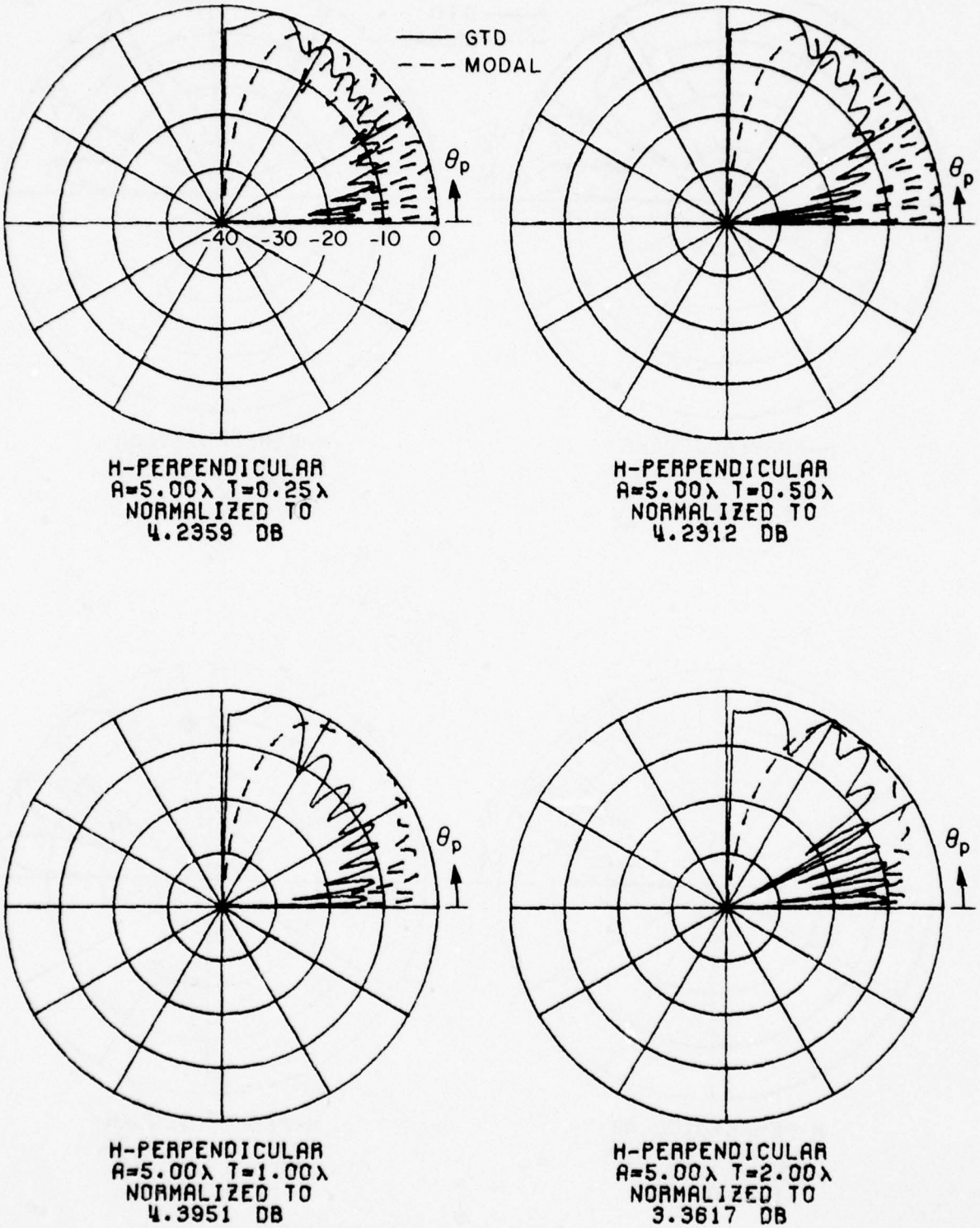

Figure 22. H_z in the waveguide for a=5.0 wavelength.

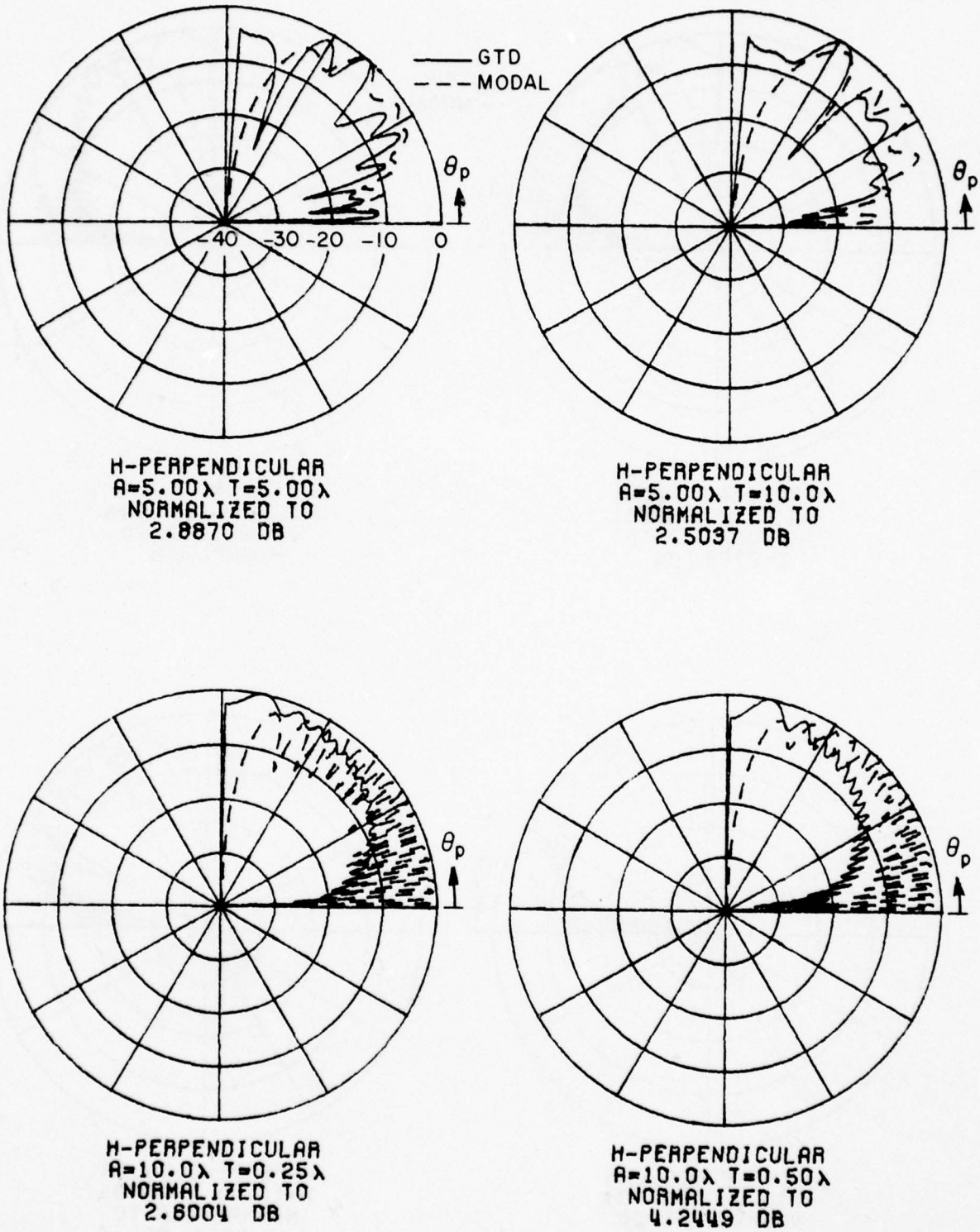

Figure 23. $H_\perp$ in the waveguide for a=5.0 and 10.0 wavelength.

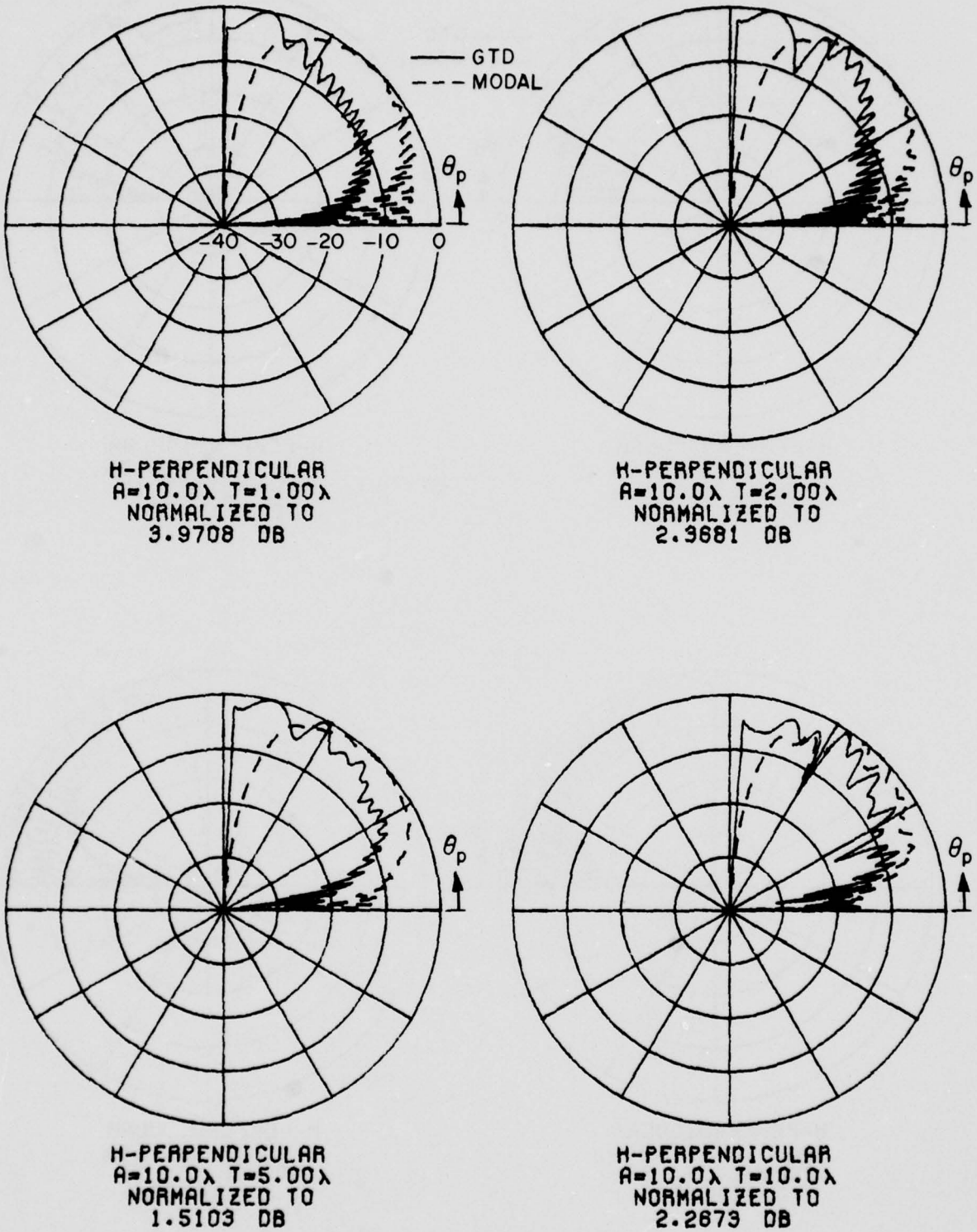

Figure 24. $H_\perp$ in the waveguide for a=10.0 wavelength.

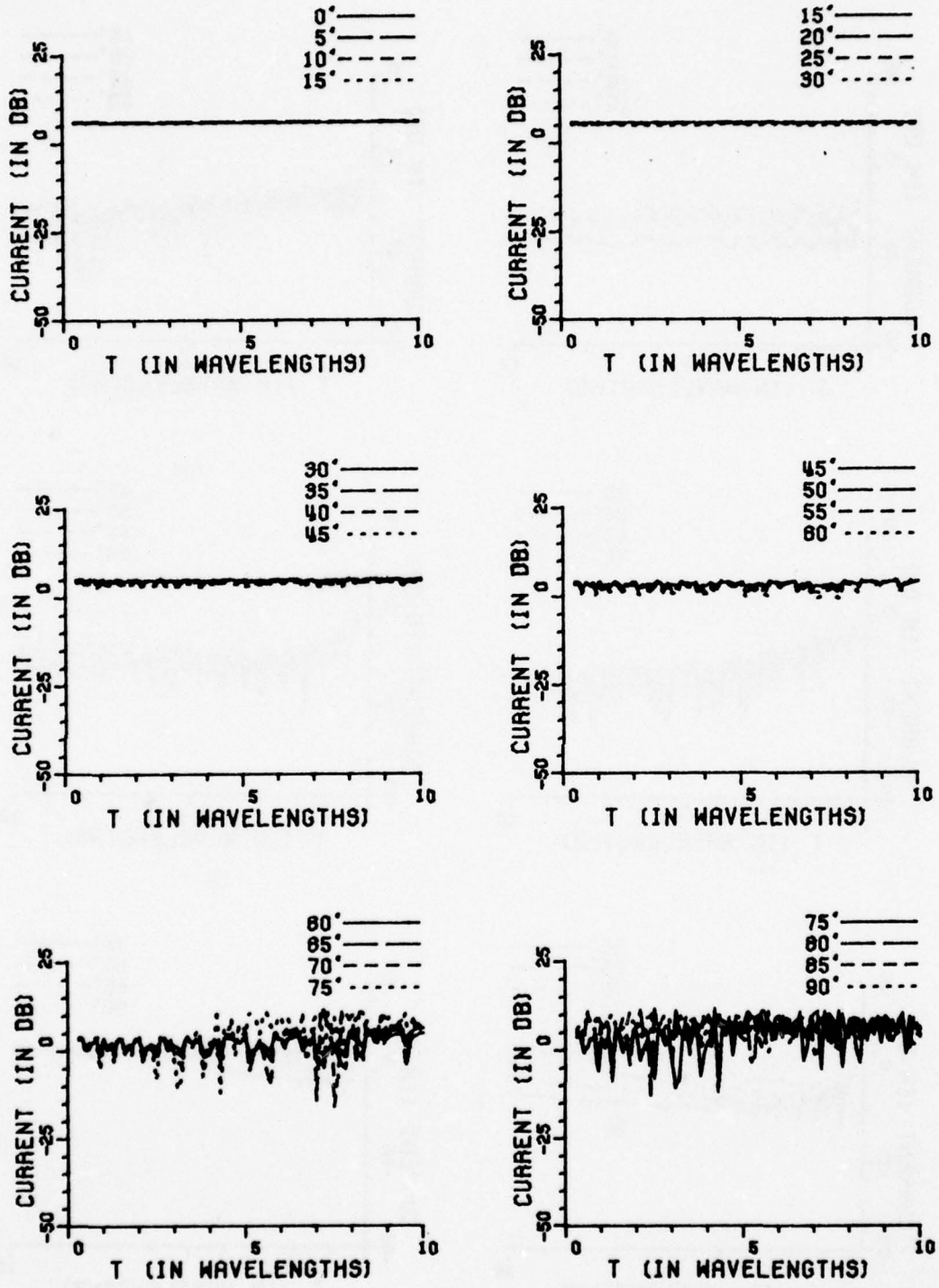

Figure 25a. H_u current density for parallel plate waveguide with a=0.25 wavelength.

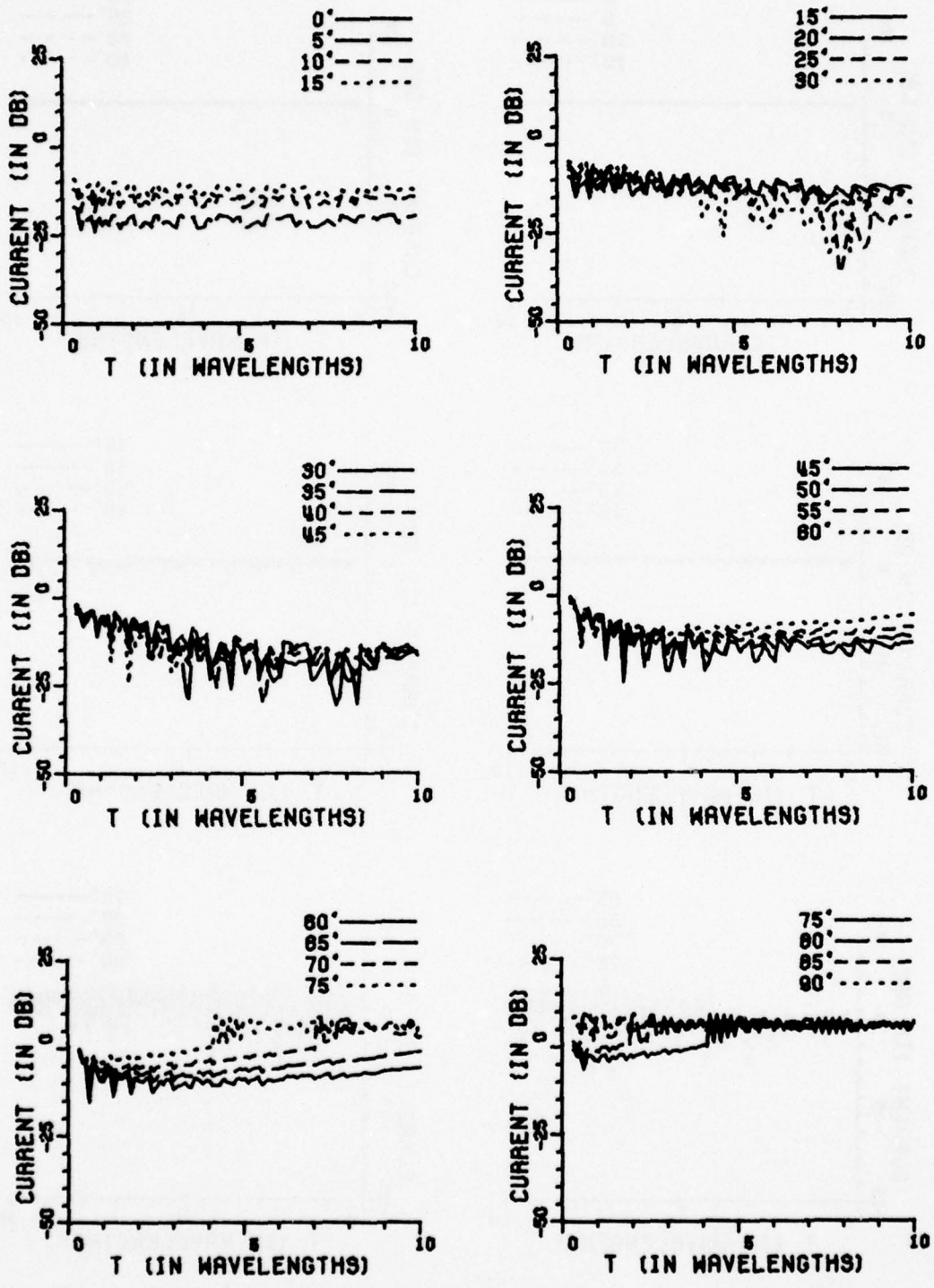

Figure 25b. $H_{\perp}$ current density for parallel plate waveguide with a=0.25 wavelength.

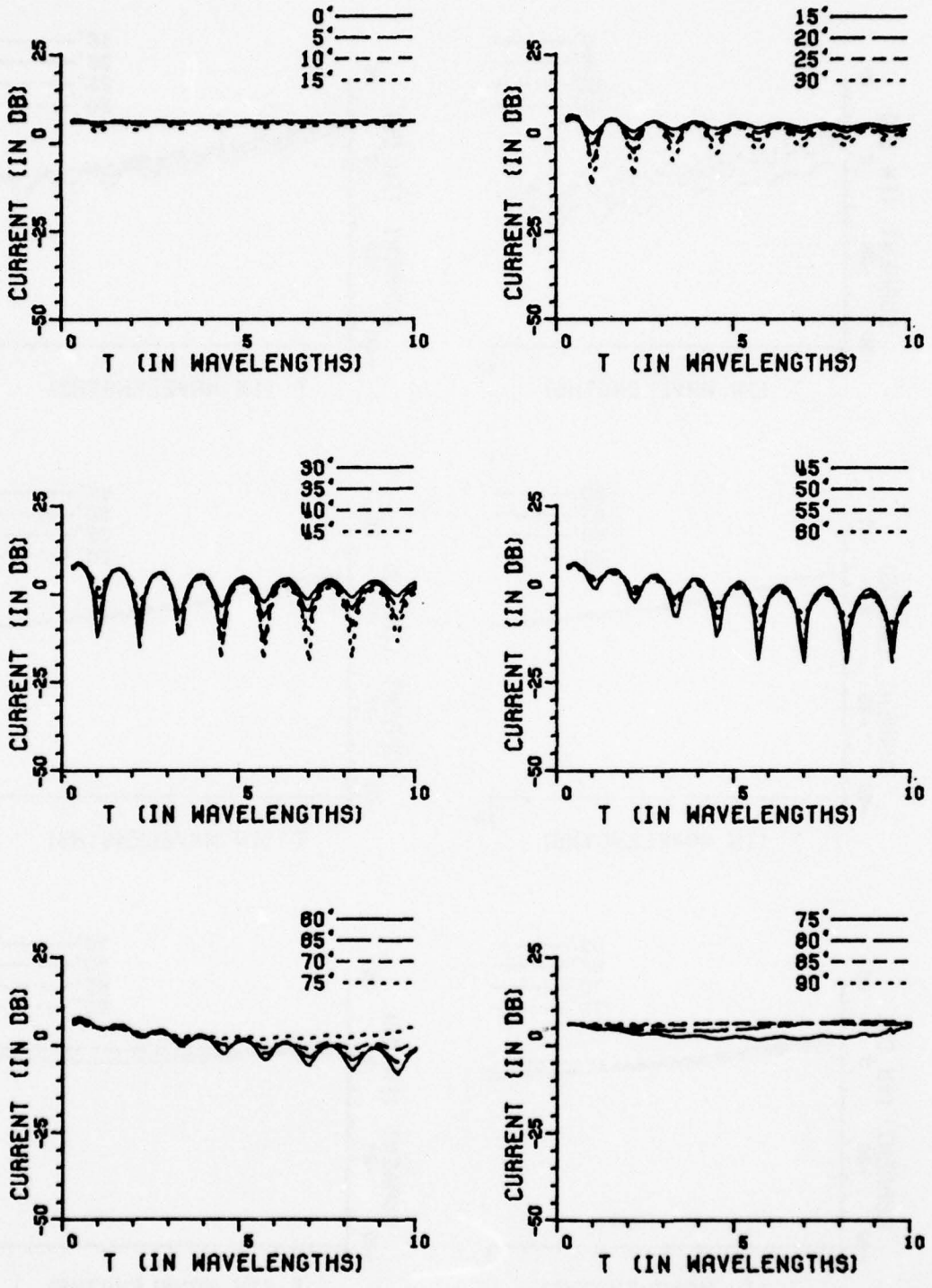

Figure 26a. H_u current density for parallel plate waveguide with a=0.5 wavelength.

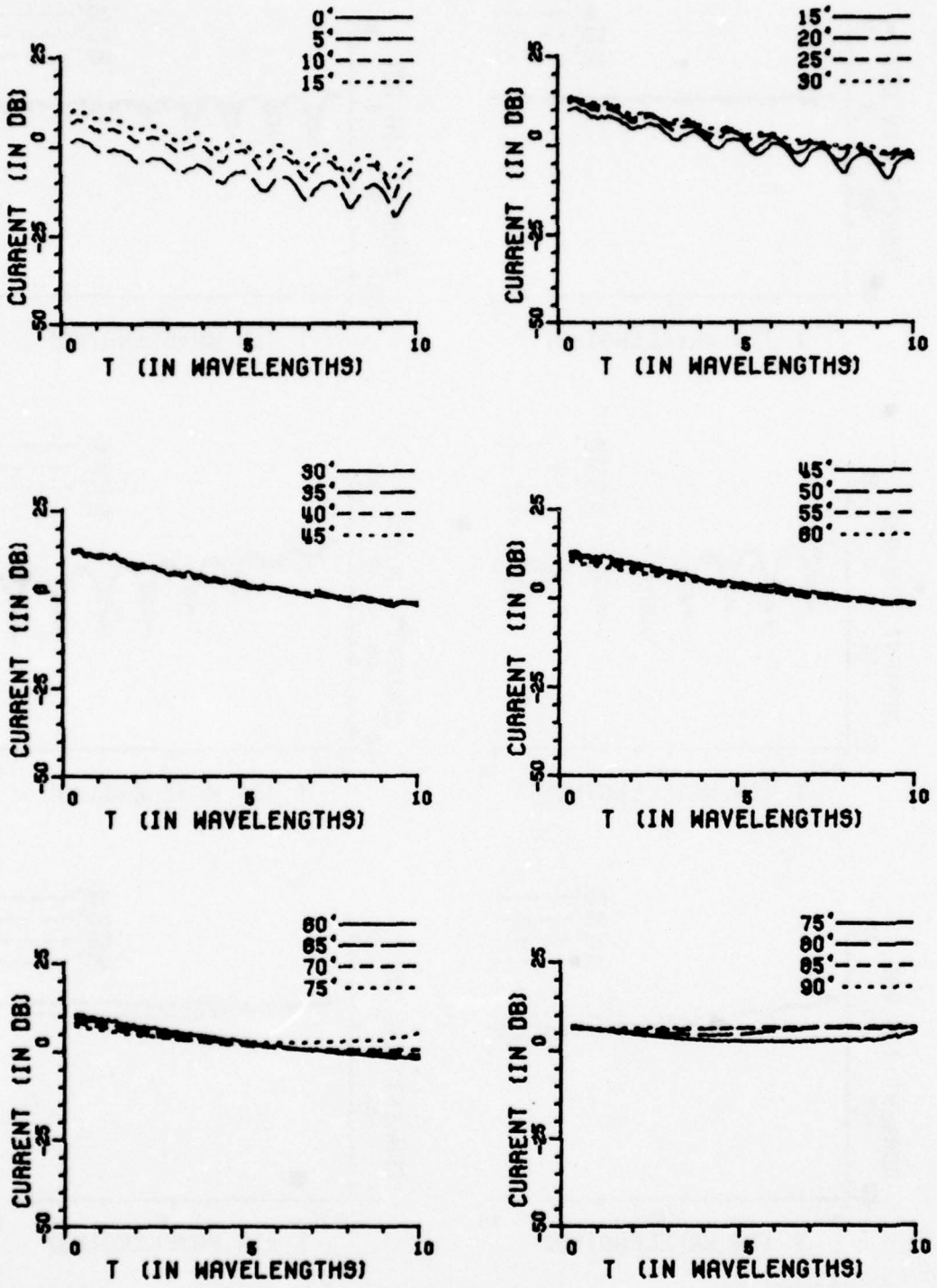

Figure 26b. H_1 current density for parallel plate waveguide with a=0.5 wavelength.

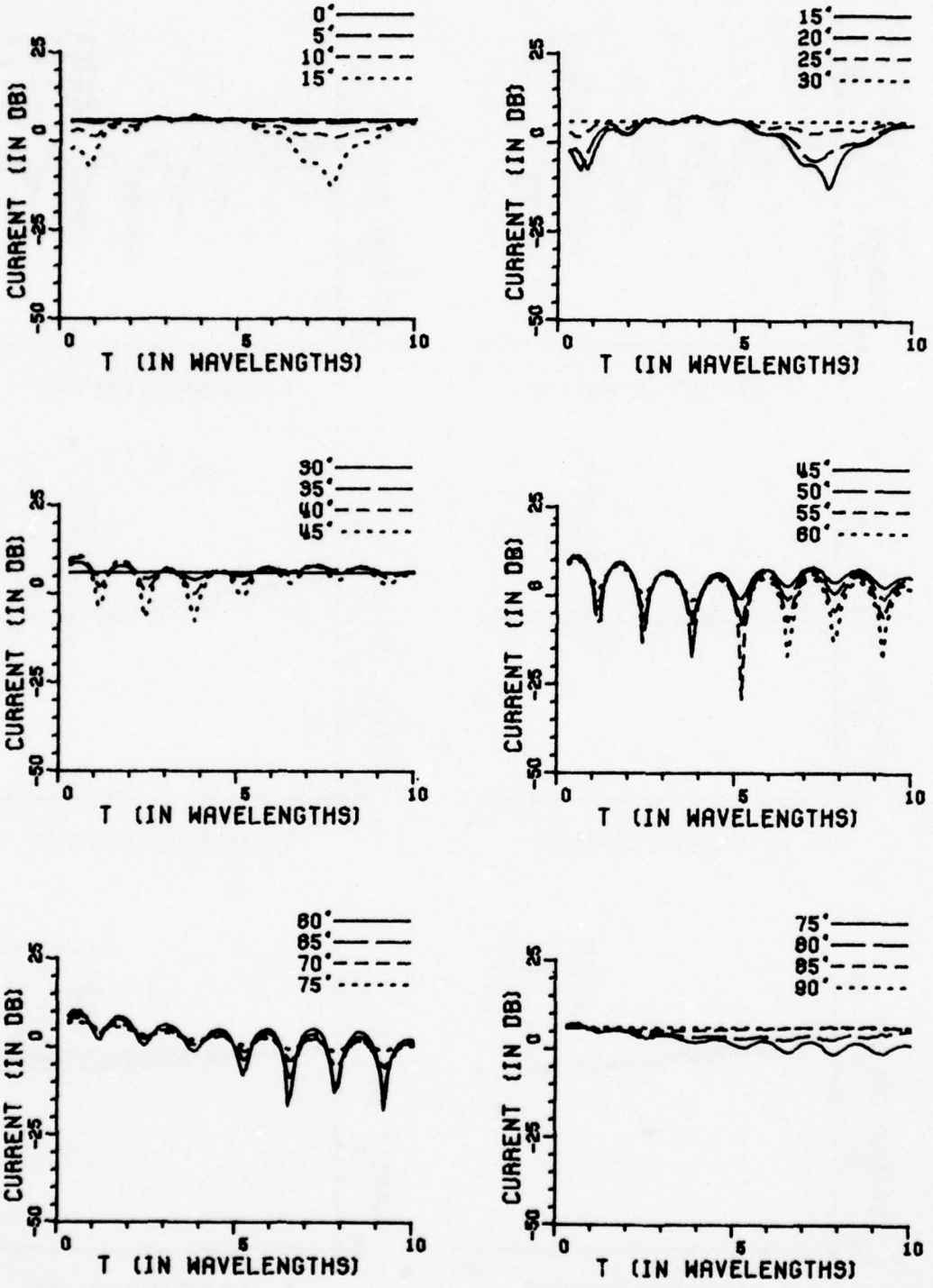

Figure 27a. H_{ϕ} current density for parallel plate waveguide with a=1.0 wavelength.

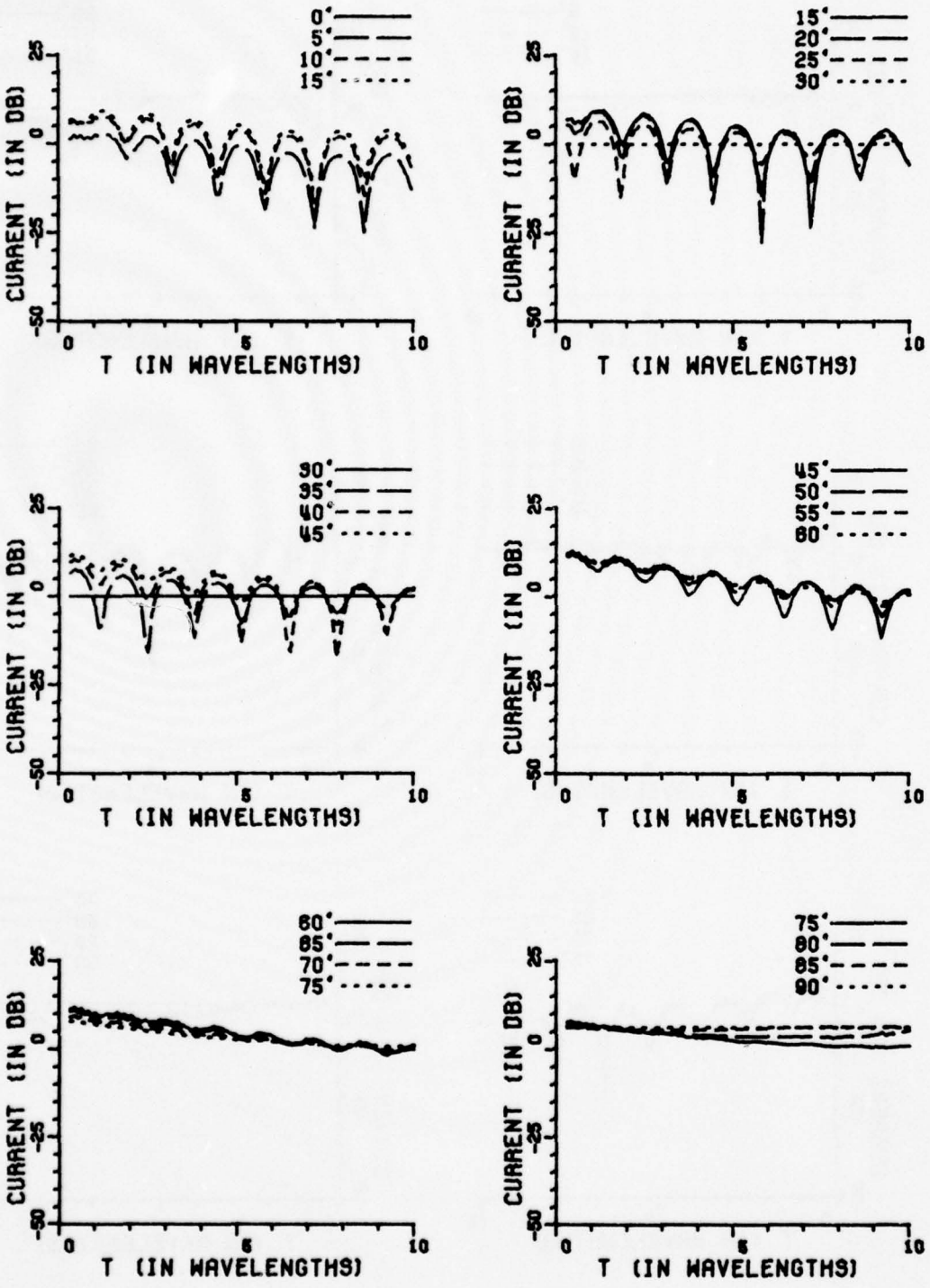

Figure 27b. $H_\perp$ current density for parallel plate waveguide with a=1.0 wavelength.

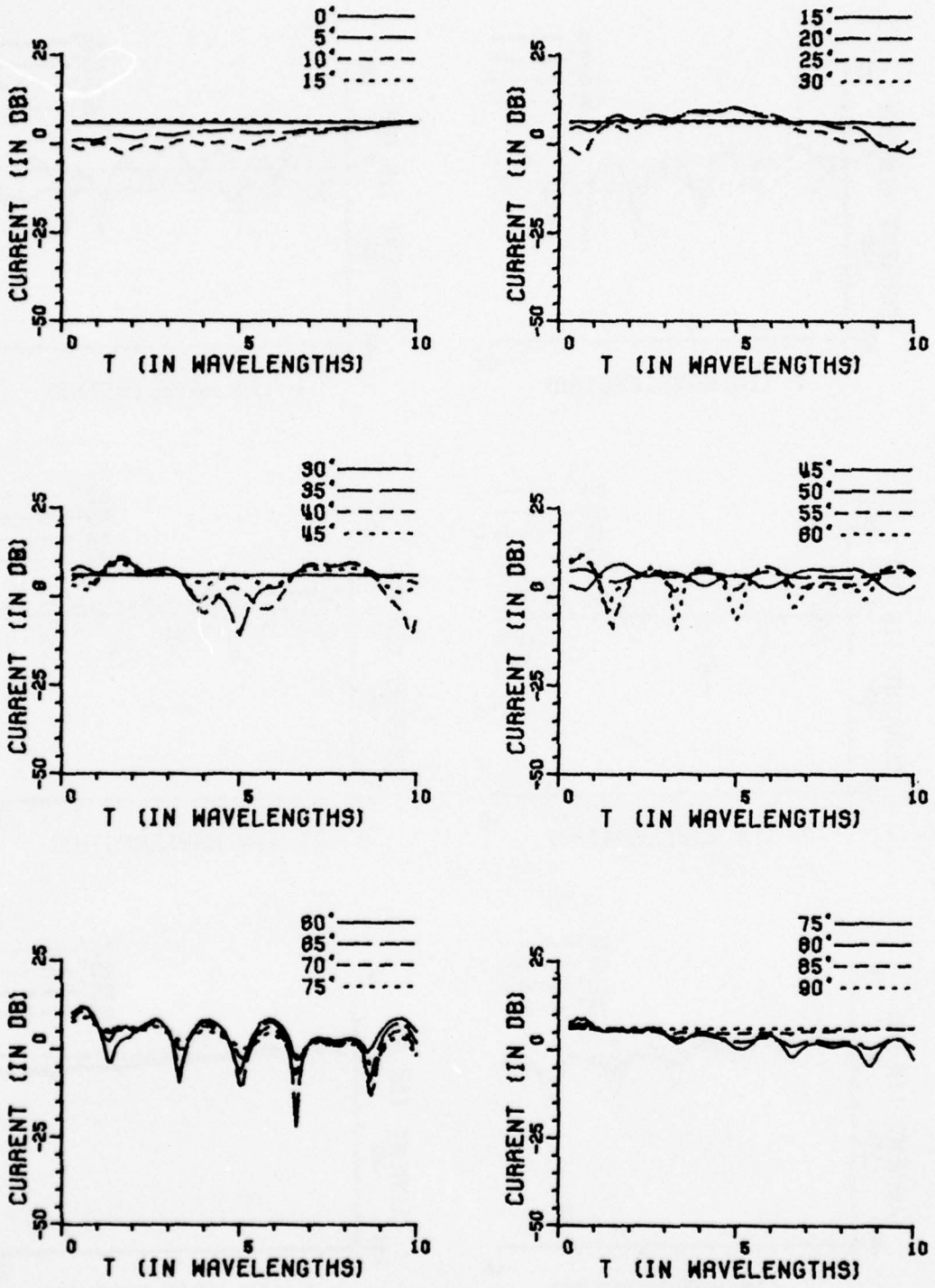

Figure 28a. H_n current density for parallel plate waveguide with a=2.0 wavelength.

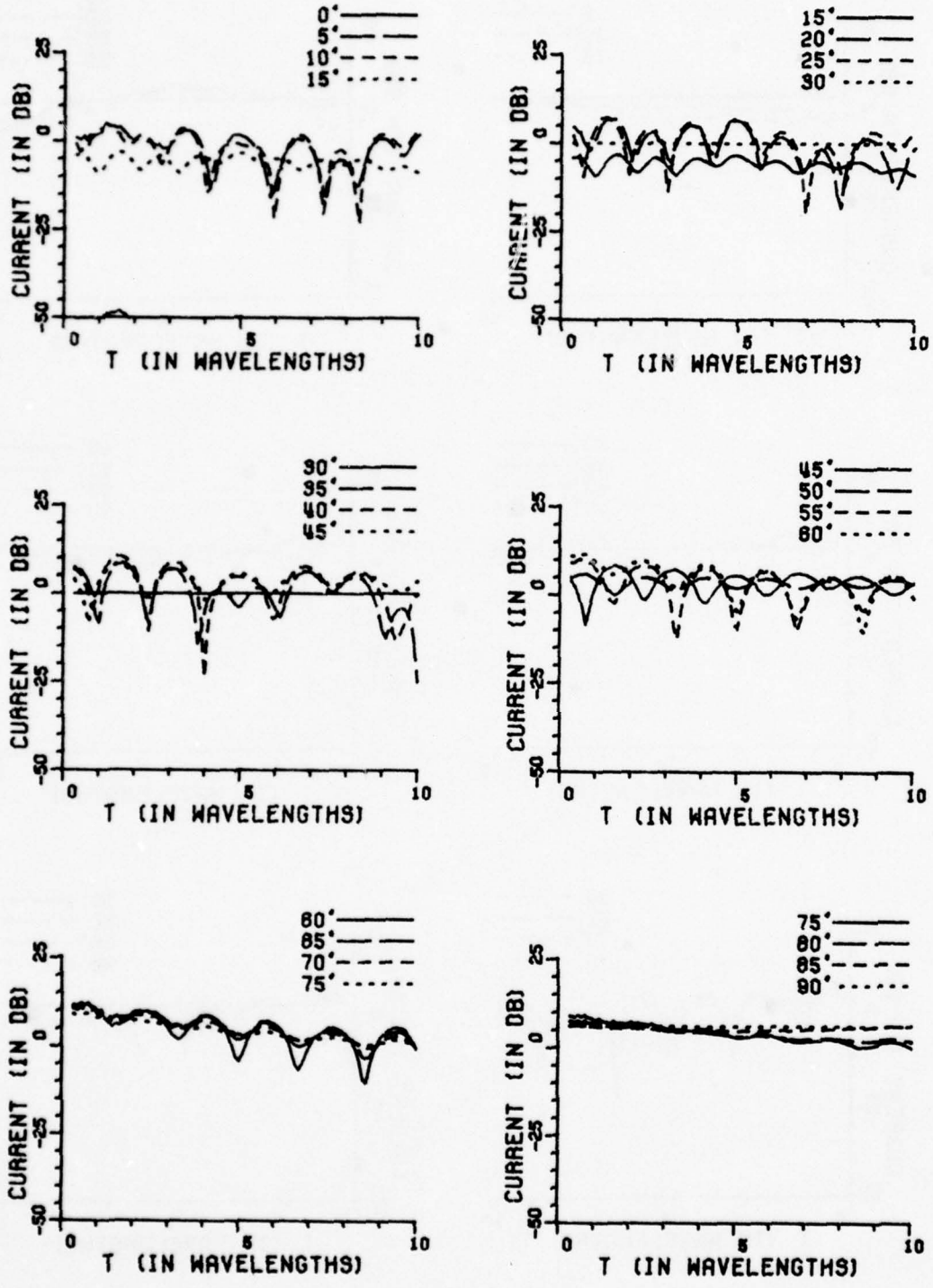

Figure 28b. H_z current density for parallel plate waveguide with a=2.0 wavelength.

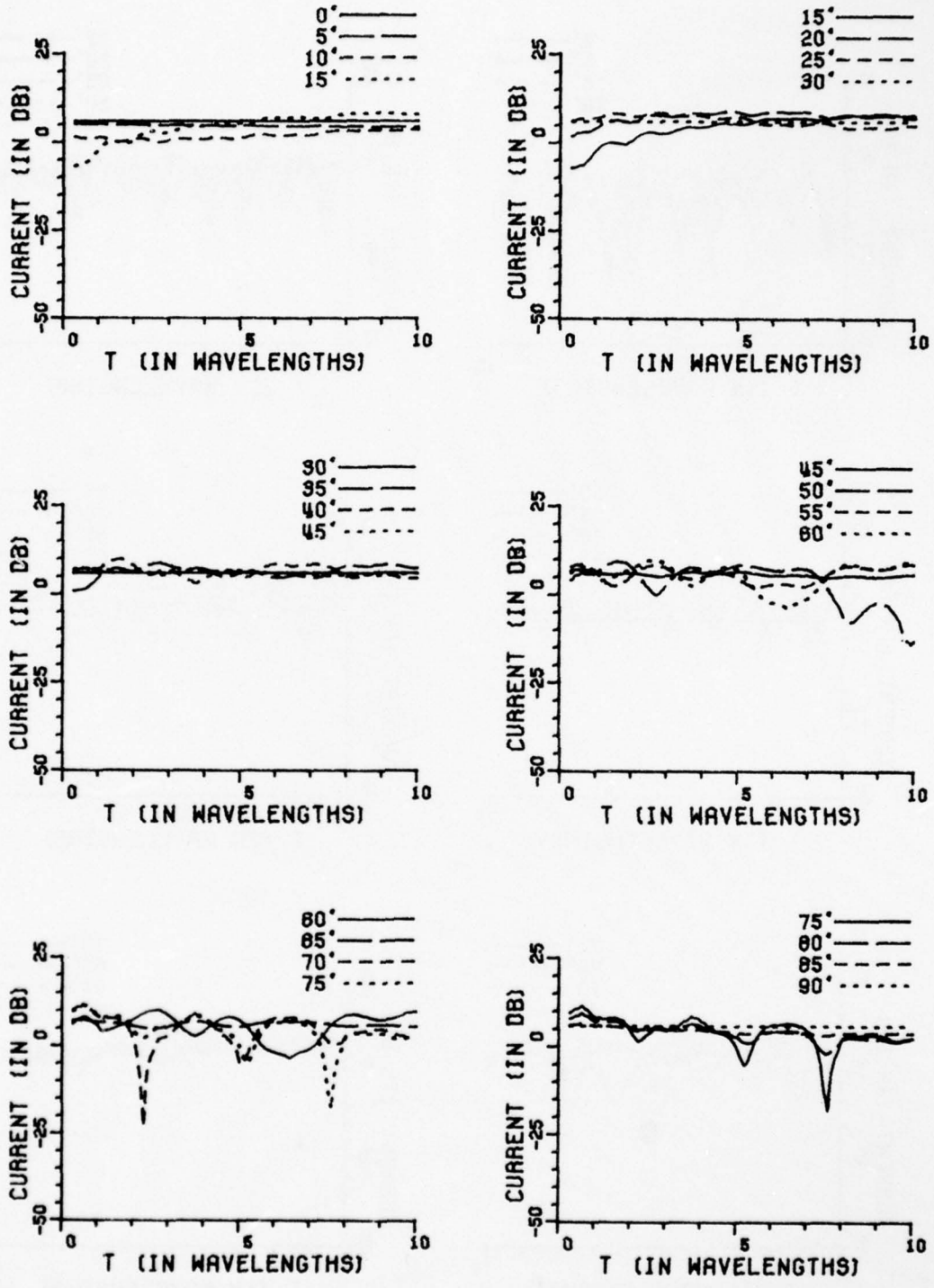

Figure 29a. H_n current density for parallel plate waveguide with a=5.0 wavelength.

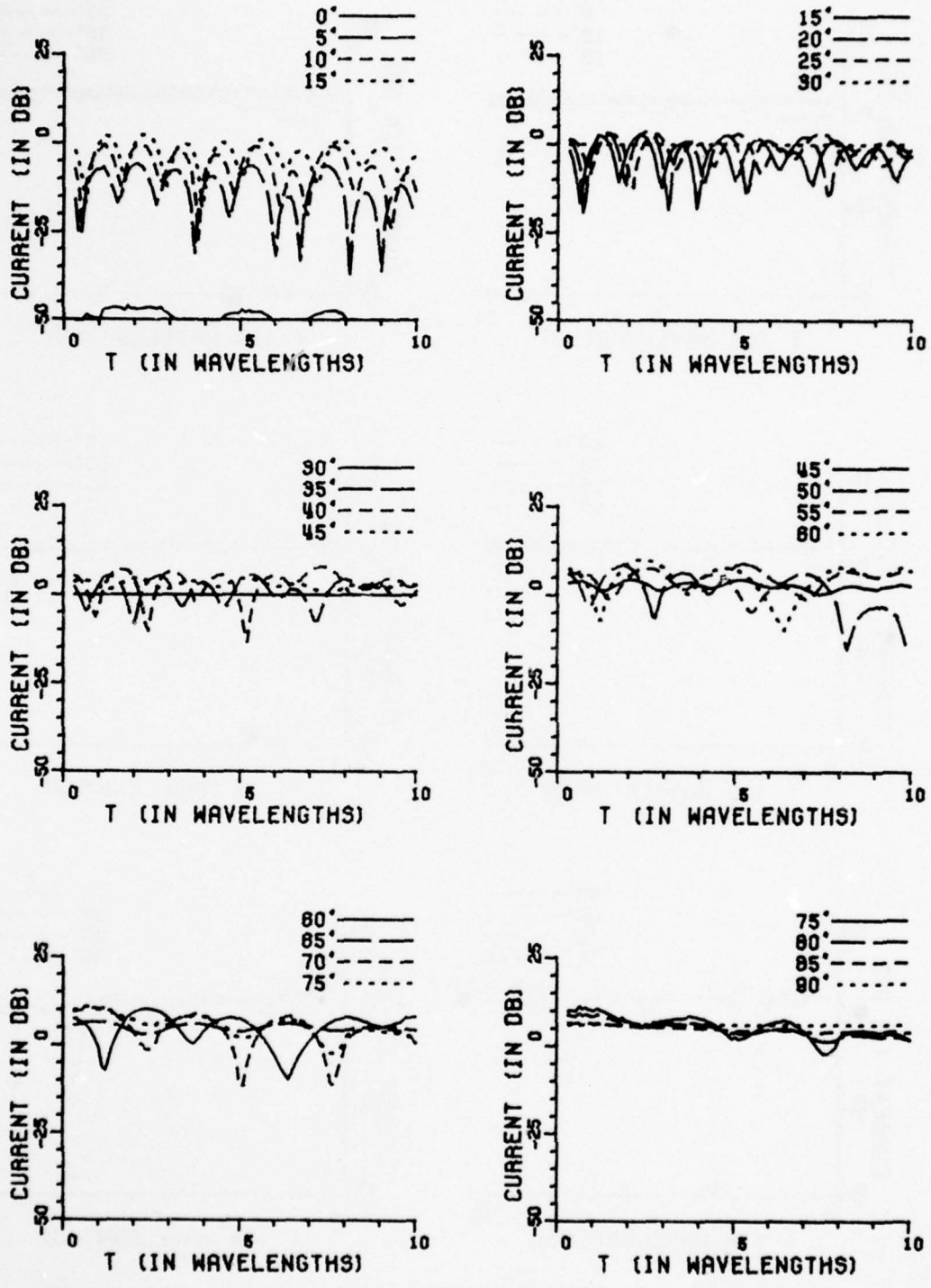

Figure 29b. $H_{\perp}$ current density for parallel plate waveguide with a=5.0 wavelength.

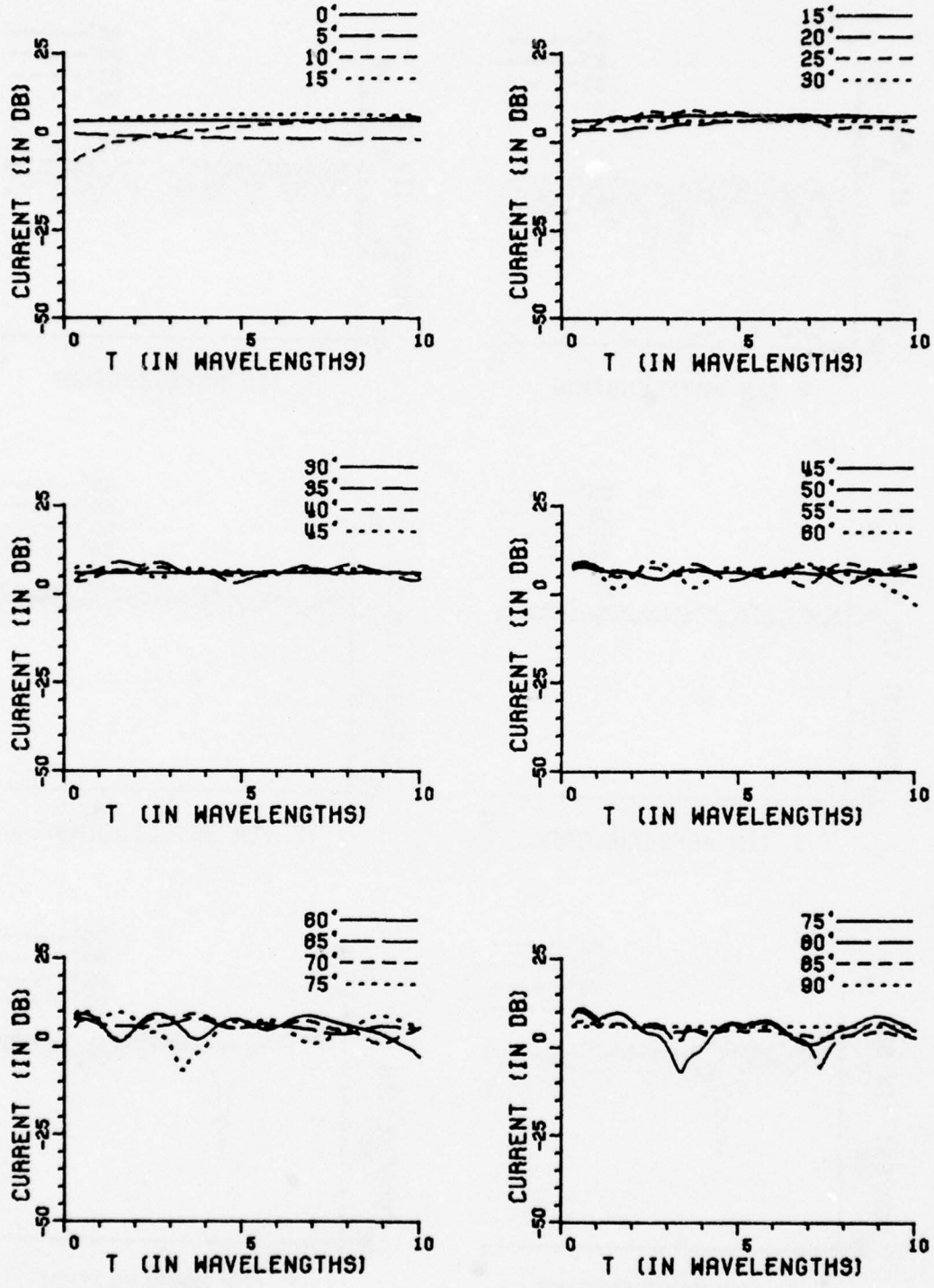

Figure 30a. H_u current density for parallel plate waveguide with a=10.0 wavelength.

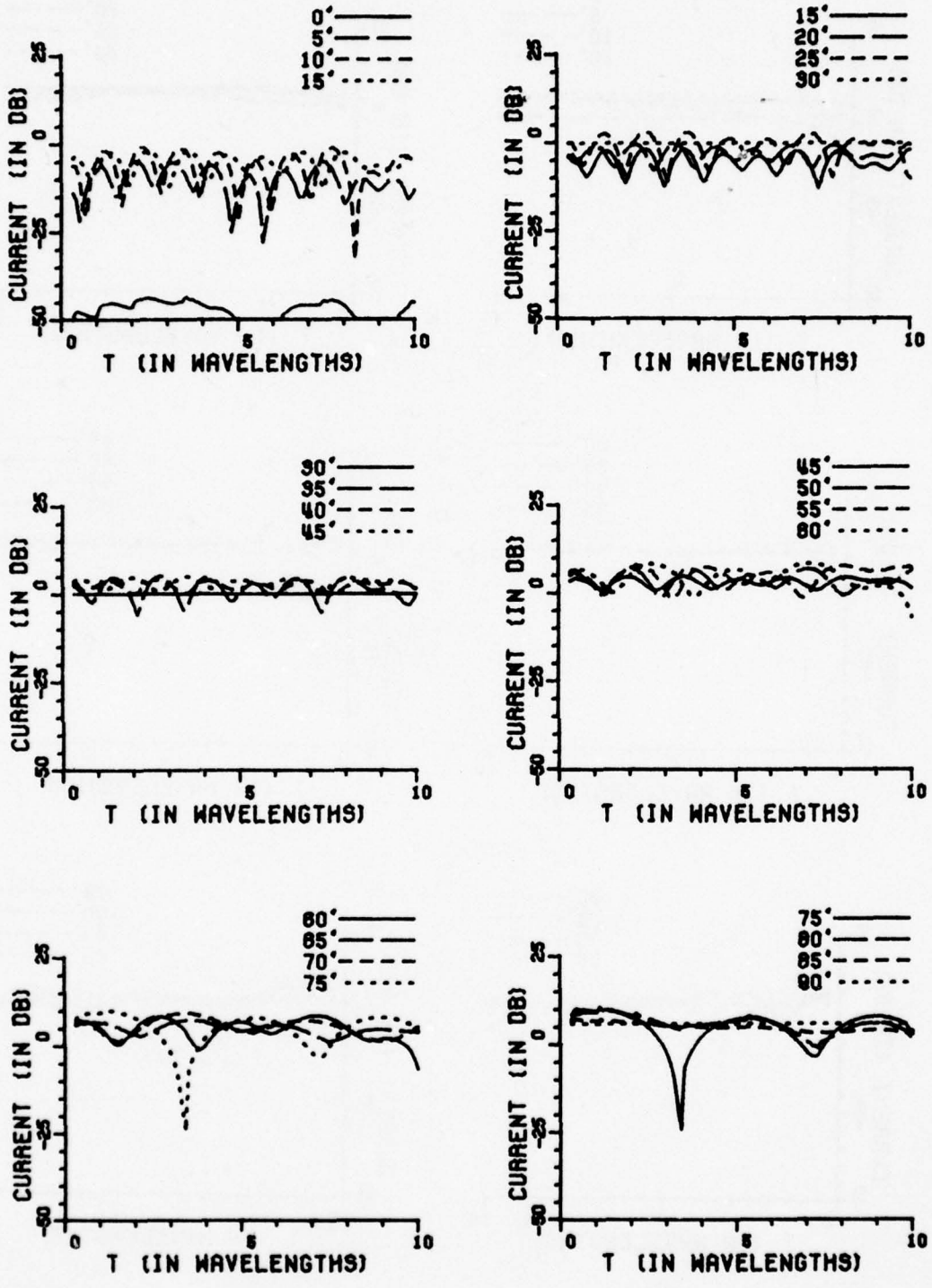

Figure 30b. $H_{\perp}$ current density for parallel plate waveguide with a = 10.0 wavelength.

IV. CURRENT AND CHARGE DENSITY INDUCED ON A CYLINDER ABOVE A GROUND PLANE

A. Introduction

The geometrical theory of diffraction as discussed in Chapter II is applied to the cylindrical geometry illustrated in Figure 31. The restrictions applied to this model are that the source must be located at least one fourth wavelength away from the cylinder endcap and the separation between the ground plane and the cylinder must be large enough so that the waveguide mode nature of the field does not predominate (see Chapter III). For patterns in the x-z plane the electric field is given by

$$\vec{E} = \vec{E}^r + \vec{E}^r_m + \sum_n \vec{E}^d_n$$

where m is the number of bounces off of the ground plane as the energy propagates from the source to the far field receiver and n is the number of bounces which occur before the reflected ray strikes the edge.

B. Geometrical Optics Terms

For patterns in the x-z plane of Figure 31 the incident field term is shadowed by the cylinder. The reflected field term is similar to the reflected field given in Chapter II in that Equations (3) through (14) are applicable. The reflected field must be modified, however, to take into account the reduction in field strength due to reflections off of the cylinder which defocuses the reflected field energy. This effect can be seen using Equation (3)

$$E^r(s) \sim E^i(Q_r) \cdot \overline{R} \sqrt{\frac{\rho^r_1 \rho^r_2}{(\rho^r_1+s)(\rho^r_2+s)}}\ e^{-jks} .$$

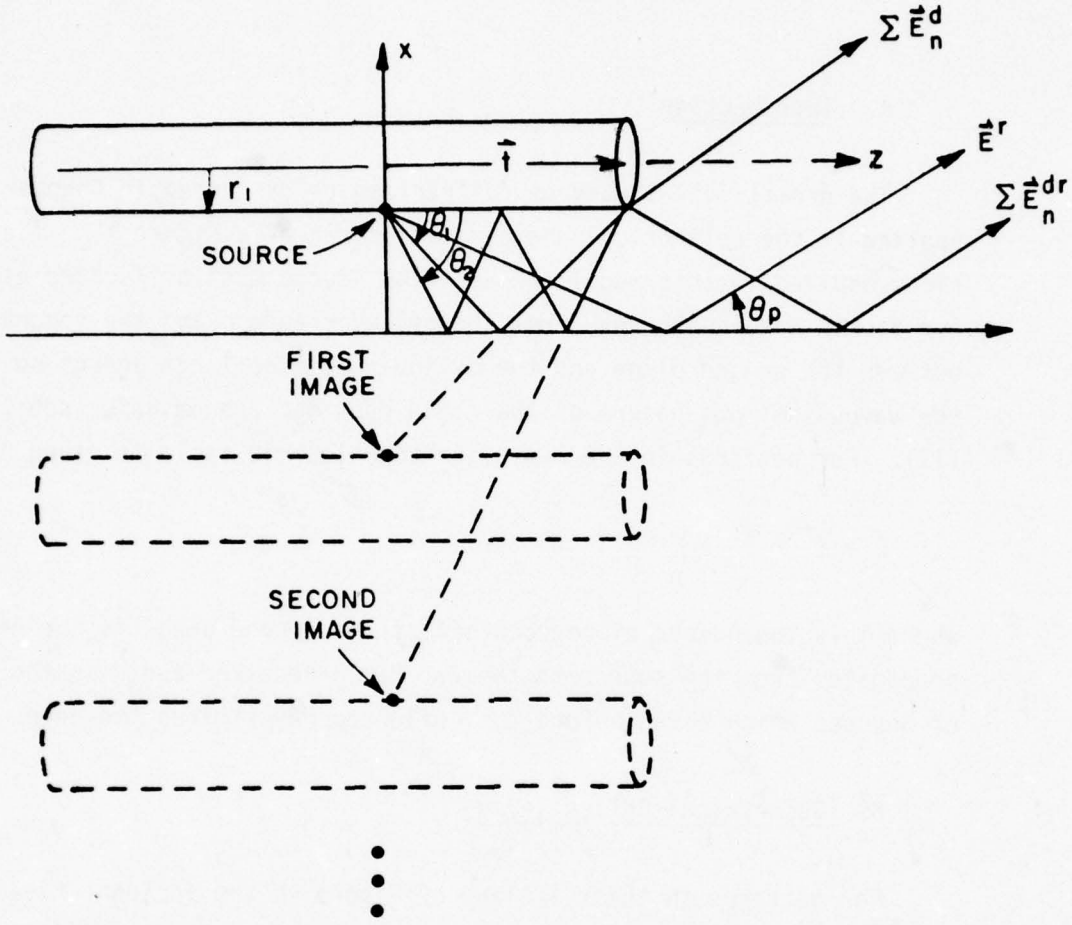

Figure 31. Geometry for cylinder over ground plane case.

The reflected field caustic parameters ρ_1^r and ρ_2^r are found using Equations (7) and for the cylindrical geometry reduce to

$$\rho_2^r = \rho_2^i$$

$$\rho_1^r = \frac{r_1\rho_1^i}{r_1+2\rho_1^i\cos\theta_i} = \frac{r_1\rho_1^i}{r_1+2\rho_1^i\sin\theta_p}$$

where r_1 is the radius of curvature of the cylinder at the point of reflection.

For a single reflection off of the cylinder, one obtains

$$\rho_1^i = \rho_2^i = 2s' = \frac{2a}{\sin\theta_p}$$

$$\rho_1^{r(1)} = \frac{2s'r_1}{r_1+4s'\sin\theta_p}$$

$$\rho_2^{r(1)} = 2s'$$

and

$$E^r(s) = \frac{e^{-jk2s'}}{2s'}\sqrt{\frac{2s'\rho_1^{r(1)}}{(2s'+s)(\rho_1^r(1)_{+s})}}\ e^{-jks}\ .$$

In the far field

$$E^r(s) = e^{-jk2s'}\sqrt{\frac{\rho_1^{r(1)}}{2s'}}\ \frac{e^{-jks}}{s}\ .$$

In general the effect of m bounces off of the cylinder on the reflected field is given by

$$E^r(s) = e^{-jk(s+2ms')}\sqrt{\frac{\rho_1^{r(1)}}{2s'}}\sqrt{\frac{\rho_1^{r(2)}}{\rho_1^{r(1)}+2'}}\sqrt{\frac{\rho_1^{r(3)}}{\rho_1^{r(2)}+2s'}} * \cdots \sqrt{\frac{\rho_1^{r(m)}}{\rho_1^{r(m-1)}+2s'}} \frac{1}{\sqrt{(s+2ms')(s+\rho_1^{r(m)})}}$$

which reduces to

$$E^r(s) = \sqrt{\frac{\rho_1^{r(1)}}{2s'}}\sqrt{\frac{\rho_2^{r(2)}}{\rho_1^{r(1)}+2s'}} \cdots \sqrt{\frac{\rho_1^{r(m)}}{\rho_1^{r(m-1)}+2s'}} \frac{e^{-jks}}{s} e^{-jk\hat{d}\cdot\hat{\ell}} \qquad (32)$$

in the far field. The quantities $\rho_1^{r(1)}$ and $\rho_1^{r(\ell)}$ are given by

$$\rho_1^{r(1)} = \frac{2s'r_1}{r_1+4s'\sin\theta_p} \qquad (33)$$

and

$$\rho_1^{r(\ell)} = \frac{r_1(\rho_1^{r(\ell-1)}+2s')}{r_1+2|\rho_1^{r(\ell-1)}+2s'|\sin\theta_p} \quad \text{for } 2 \le \ell \le m . \qquad (34)$$

C. Diffracted Field

The diffracted field is given by Equation (19) as

$$\vec{E}^d = \vec{E}_i(Q') \cdot \bar{\bar{D}}_E(\hat{s},\hat{I}) \sqrt{\frac{\rho}{s(\rho+s)}}\, e^{-jks}.$$

In the above equation $E^i(Q')$ is the reflected field incident upon the edge of the cylinder. The parameter ρ is given by Equation (20) and reduces to

$$\rho = \frac{\rho_1^i \, r_1}{r_1 + \rho_1^i(\sin\phi' + \sin\theta_p)} \quad .$$

The dyadic diffraction coefficient $\bar{D}_E$ is given by Equation (21) with $L^i = L^{rn} = L^{ro} = \rho_2^i$. For the principal plane patterns taken in this report it is sufficient to include only the diffraction from the point on the wedge located at $x=-r_1$, $z=t$ in regions away from caustics.

D. Results

The procedure described in this chapter assumes that the diffraction off the endcap is dominated by the principal point of diffraction located at $x=r_1$, $y=0.$, $z=t$. This assumption is usually valid if the other points of diffraction are separated from the principal diffraction point. If these diffraction points are sufficiently close together a caustic field can occur yielding an erroneous result. These caustics become more of a problem as the cylinder radius is decreased. The results for this section are included with the results given in Chapter V. Chapter V describes a technique which can be used to partially correct these caustics caused by closely spaced diffraction points around the endcap of the cylinder.

V. CAUSTIC CORRECTION

A. Introduction

Due to the large number of rays necessary to obtain a GTD solution to the cylinder mode, there is a good possibility of introducing caustics into the pattern. These caustics occur when three diffraction points on the endcap become close to each other. These caustics can be partially corrected using the method of Albertson, Balling, and Jenson [20].

B. Theoretical Section

Using the equivalent current technique[21] the diffracted field can be expressed as

$$E(\theta,\phi) = \frac{e^{-jkd}}{d} \int_0^{2\pi} G(\phi')\, e^{-jkh(\phi')} d\phi' \tag{35}$$

for the cylinder endcap. The function $h(\phi')$ is the distance from the source to the edge referred to the far field illustrated in Figure 32. If the points of diffraction are separated then the integral may be evaluated by standard stationary phase techniques [22] to yield

$$E_n \sim \sqrt{\frac{2\pi}{k\, h''(\phi_n)}}\; G(\phi_n)\, e^{-jkn(\phi_n) \pm j\frac{\pi}{4}}\; \frac{e^{-jkd}}{d} \tag{36}$$

where ϕ_n is a stationary or diffraction point. The above equation is equivalent to Equation (15).

If the field is in a caustic region near a cusp of caustics, i.e., near a region where three diffraction points coalesce into one, then $h'(\phi_2') \cong h''(\phi_2') \cong h'''(\phi_2') \cong 0$ and $h(\phi')$ can be approximated by

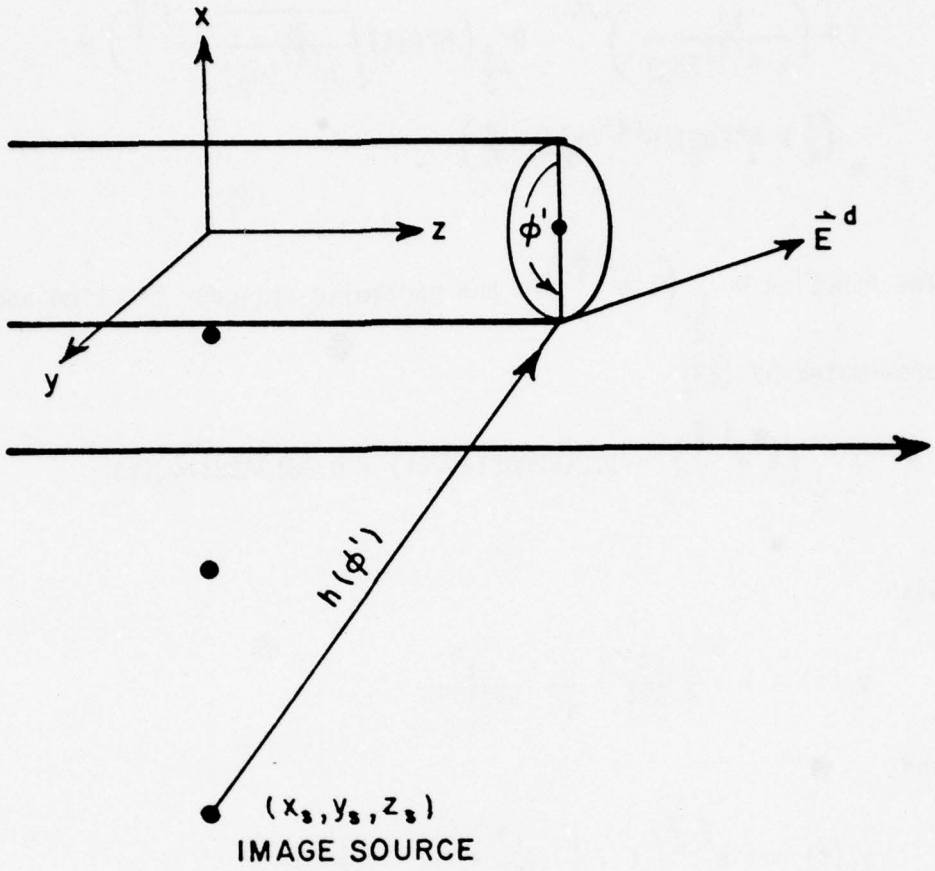

Figure 32. Geometry for the caustic correction procedure.

$$h(\phi') \cong h(\phi_2') + \frac{1}{2} h''(\phi_2')(\phi'-\phi_2') + \frac{1}{24} h^{(4)}(\phi_2')(\phi'-\phi_2')^4 .$$

Substituting this expression into the phase integral

$$I = e^{jkh(\phi_2')} \int_0^{2\pi} e^{-jkh(\phi')}\, d\phi'$$

yields for $h^{(4)}(\phi_2')$ positive

$$I \sim \left(\frac{12}{k\, h^{(4)}(\phi_2')}\right)^{1/4} D_{-\frac{1}{2}}\left(h''(\phi_2')\sqrt{\frac{3k}{h^{(4)}(\phi_2')}}\, e^{j\frac{\pi}{4}}\right) *$$

$$e^{j\left(\frac{3}{4} k\, h''(\phi_2')/h^{(4)}(\phi_2') - \frac{\pi}{8}\right)} .$$

The function $D_{-\frac{1}{2}}\left(t\, e^{j\frac{\pi}{4}}\right)$ is the parabolic cylinder function and is approximated by [23]

$$D_{-\frac{1}{2}}\left(t\, e^{j\frac{\pi}{4}}\right) = 1.215280214 y_1(t) - 0.581368317 y_2(t)$$

with

$$y_1(t) = 1 - \frac{1}{4}\frac{t^4}{3*4} + \frac{1}{4^2}\frac{t^8}{3*4*7*8} - \cdots$$

and

$$y_2(t) = t\, e^{j\frac{\pi}{4}}\left(1 - \frac{1}{4}\frac{t^4}{4*5} + \frac{1}{4^2}\frac{t^8}{4*5*8*9} - \cdots\right) .$$

The maximum possible error due to including up to the eighth order term in the parabolic cylinder function is less than 1% for $|t| < 2$.

The above result may be expressed as a caustic correction factor, c, used to multiply the GTD solution in a case caustic region. In a region where there are four diffraction points and $h^4(\phi_2') > 0$

$$c = \frac{\sqrt{\sigma} D_{-\frac{1}{2}}\left(\sigma e^{-j\frac{3\pi}{4}}\right)}{e^{-j\frac{\sigma^2}{2} + j\frac{\pi}{8}} + 2\, e^{j\frac{\sigma^2}{4} - j\frac{\pi}{8}}} \qquad (37)$$

with $\sigma = h''(\phi_2')\sqrt{3k/h^{(4)}(\phi_2')}$. In the region where there are two diffraction points and $h^{(4)}(\phi_2') > 0$

$$c = \frac{\sqrt{\sigma}\, D_{-\frac{1}{2}}\left(\sigma e^{j\frac{\pi}{4}}\right)}{e^{-j\frac{\sigma^2}{4} - h\frac{\pi}{8}}} \quad . \tag{38}$$

For $h^{(4)}(\phi_2') < 0$ the complex conjugate of the correction factors should be used. A distinction between central and noncentral rays must also be made in the case where four rays are present (see Figure 33). If the ray is noncentral then $h''(\phi_2')$ is replaced by $-2\, h''(\phi_2')$ in evaluating σ. Noncentral rays can be recognized if $h''(\phi_n') * h^{(4)}(\phi_n') > 0$. For the central ray if $h''(\phi_2') * h^{(4)}(\phi_2') < 0$ four rays are present and if $h''(\phi_2') * h^{(4)}(\phi_2) > 0$ two rays are present. Note that the parameter σ can be used to check if a caustic field is present. If $\sigma<2$ then a caustic effect is present and if $\sigma \geq 2$ then the caustic effect is negligible and c may be approximated by one.

For the geometry illustrated in Figure 32

$$h(\phi') = -r_1 \sin\theta_p \cos(\phi - \phi') + \sqrt{T}$$

$$h''(\phi') = r_1 \sin\theta_p \cos(\phi' - \phi) + \frac{r_1(x_x \cos\phi' + y_s \sin\phi')}{\sqrt{T}} - \frac{r_1(x \sin\phi' - y_s \cos\phi')}{(t)^{3/2}}$$

$$h^{(4)}(\phi') = -r_1 \sin\theta_p \cos(\phi' - \phi) - \frac{r_1(x_x \cos\phi' + y_s \sin\phi')}{\sqrt{T}}$$

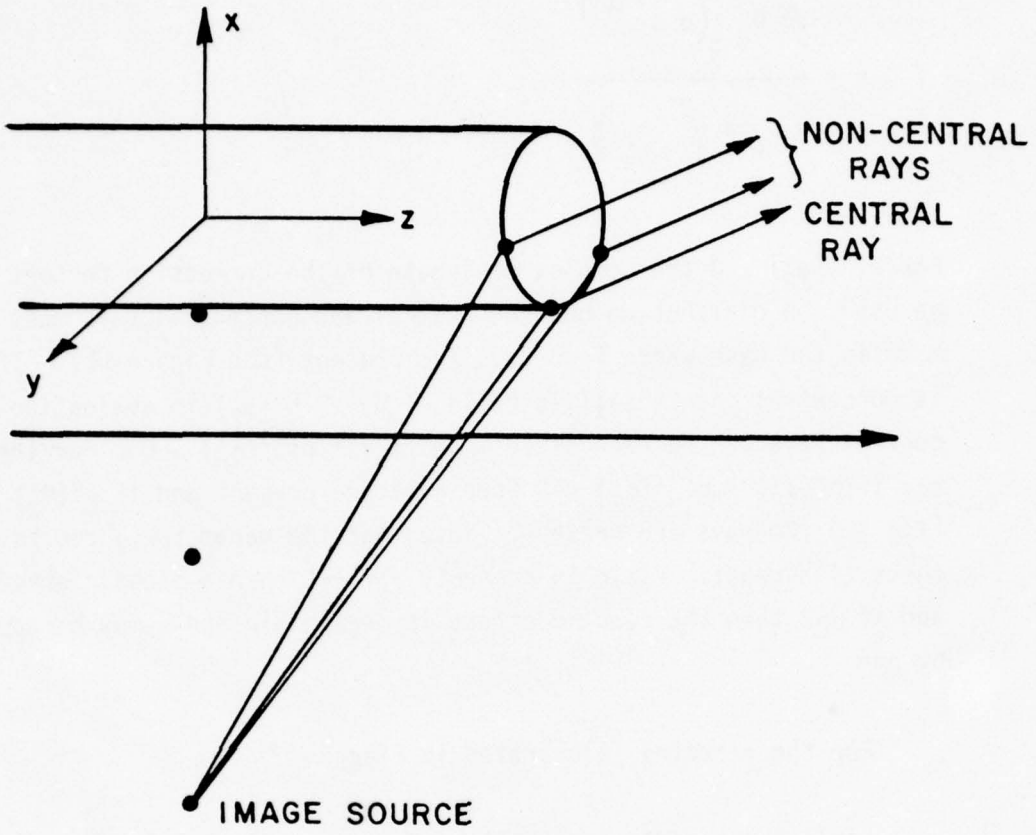

Figure 33. Illustration of central and non central rays.

$$+ \frac{r_1^2[4(x_s\sin\phi'-y_x\cos\phi')^2-3(x_s\cos\phi'+y_s\sin\phi')^2]}{T^{3/2}}$$

$$+ \frac{18r_1^3(x_s\sin\phi'-y_s\cos\phi')^2)(x_s\cos\phi'+y_x\sin\phi')}{T^{5/2}}$$

$$- \frac{15r_1^4(x_s\sin\phi'-y_s\cos\phi')^2}{T^{7/2}}$$

where

$$T = \sqrt{x_x^2+y_s^2+z_s^2+r_1^2-2r_1x_s\cos\phi' - 2r_1y_s\sin\phi'} \ .$$

C. Results

Figure 34 and 35 show the effect of the caustic correction on a five wavelength radius cylinder located one wavelength above the ground plane. Since only the principal point of diffraction is used in the caustic correction, the current level in the caustic region is slightly below the level expected in the region where three diffraction points are present. The effects of the other two diffraction points cannot be included since they would be diffracted rays which are launched as creeping waves along the cylinder. A solution for this type of ray is not currently available.

Figures 36 through 71 follow the same format as Figures 25 through 30 in presenting the induced current on the cylinder, except that the cylinder radius is varied from 0.25λ, 0.5λ, 1.0λ, 2.0λ, 5.0λ, to 10.0λ. Figures 36a through 71a show the axial current density in dB normalized to the incident plane wave or $|J_z|/|H^i y|$. In Figures 36b through 71b the surface charge density is plotted normalized to the incident plane wave or $|\rho|/|\varepsilon E^i\cos\theta_p\hat{x}-\varepsilon E^i\sin\theta_p\hat{z}|$. In Figures 36c through 71c the circumferential current density is presented normalized to the incident plane wave or $|J_y|/|-H^i\cos\theta_p\hat{x}+H^i\sin\theta_p\hat{z}|$. The caustic corrected solution is used for all these computations in that it provides the most accurate results. The caustic problems become more pronounced as the cylinder radius becomes smaller. When the radius is ten wavelengths the solution is very similar to the parallel plate waveguide as expected. The current solution becomes less accurate as the plane wave incident angle, θ_p, approaches 90^o similar to the parallel plate waveuide solution. This effect is reduced somewhat due to the reduced energy of the rays after bouncing several times off of the cylinder surface.

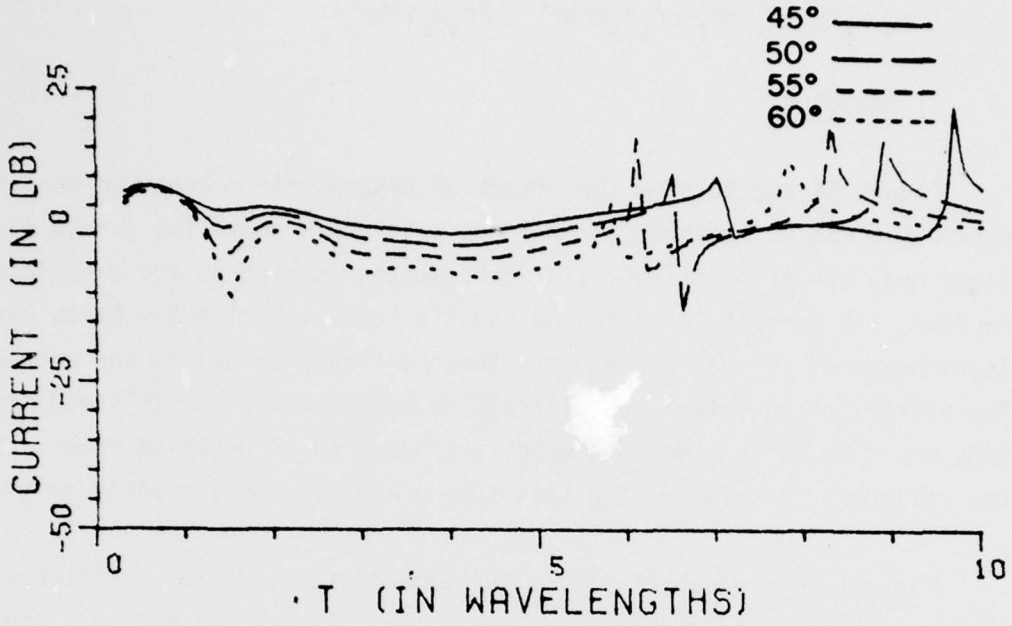

Figure 34. Current plots without caustic corrections.

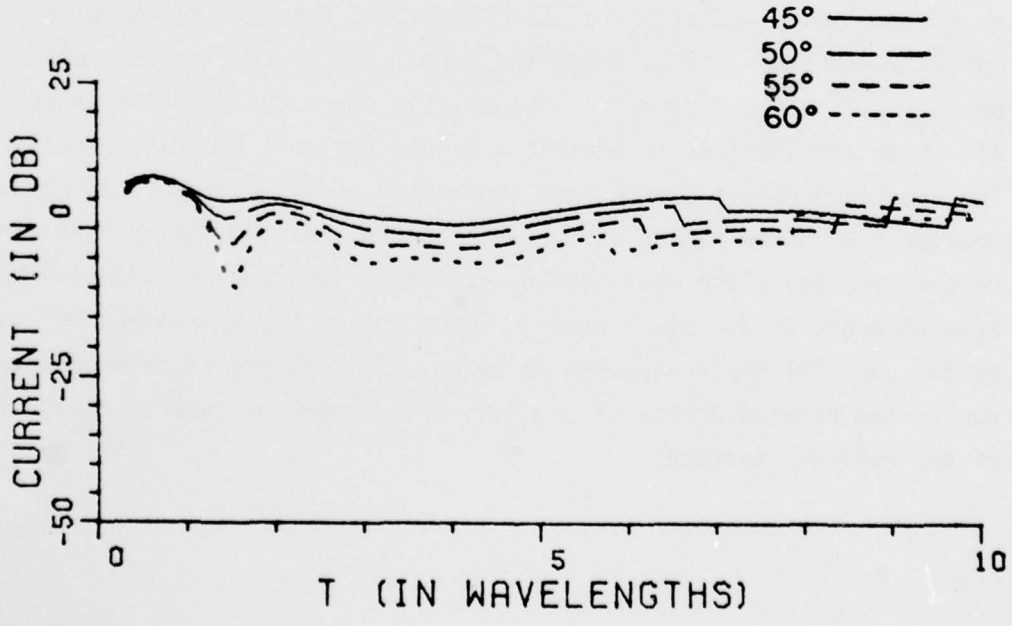

Figure 35. Current plots with caustic corrections.

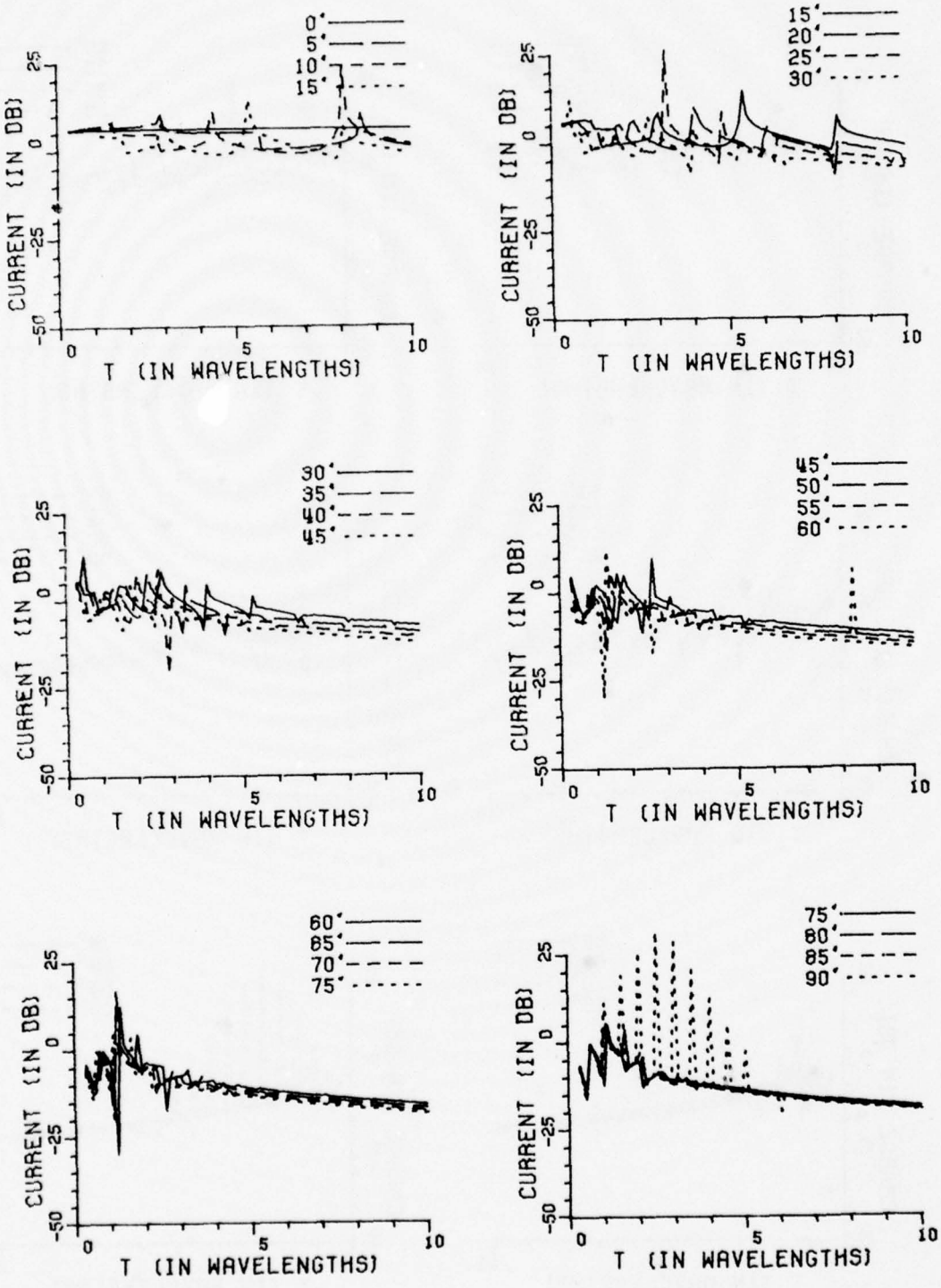

Figure 36a. Axial current density with a=0.25 wavelength and r_1/a=1.0.

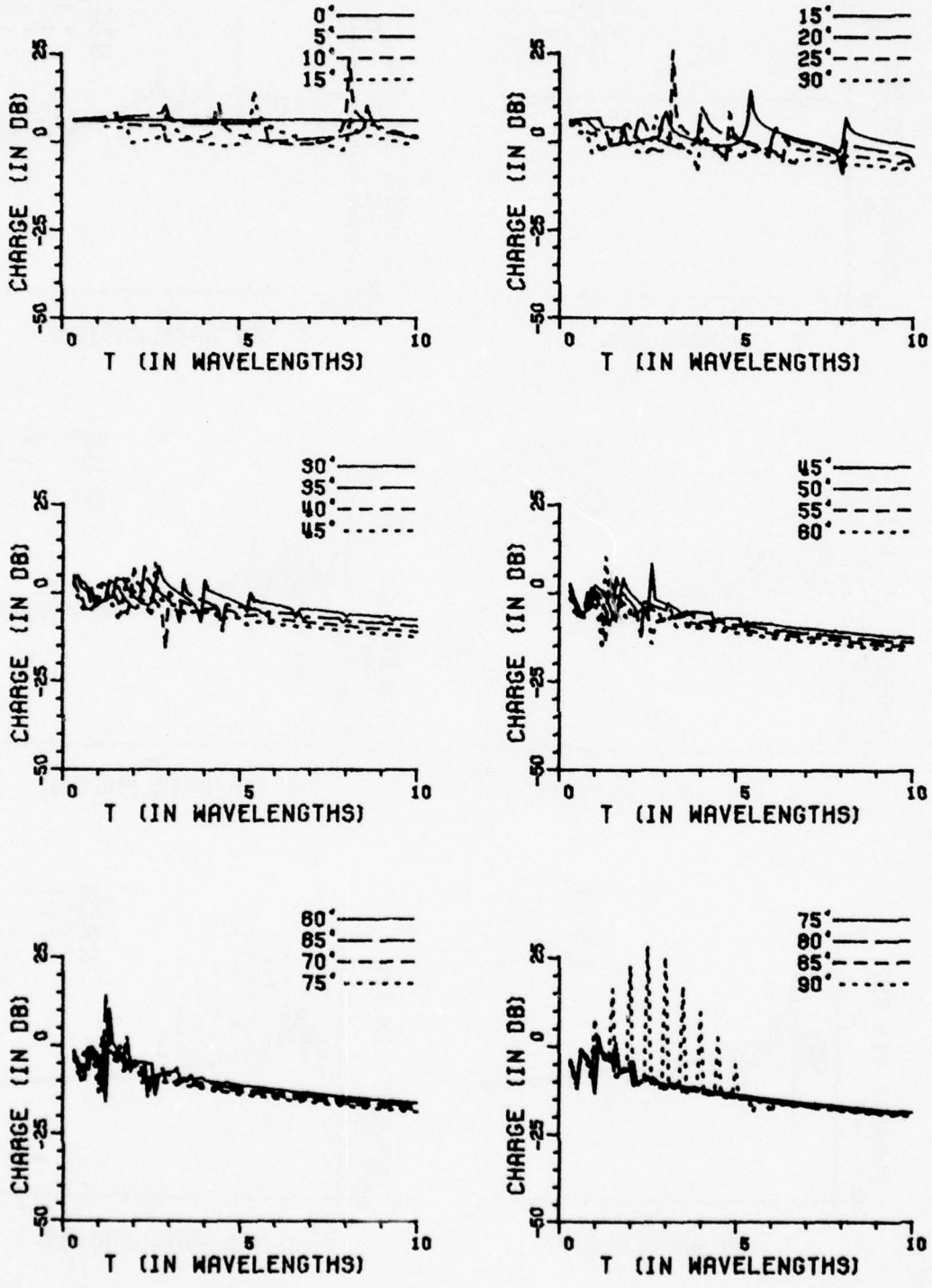

Figure 36b. Surface charge density with a=0.25 wavelength and $r_1/a=1.0$.

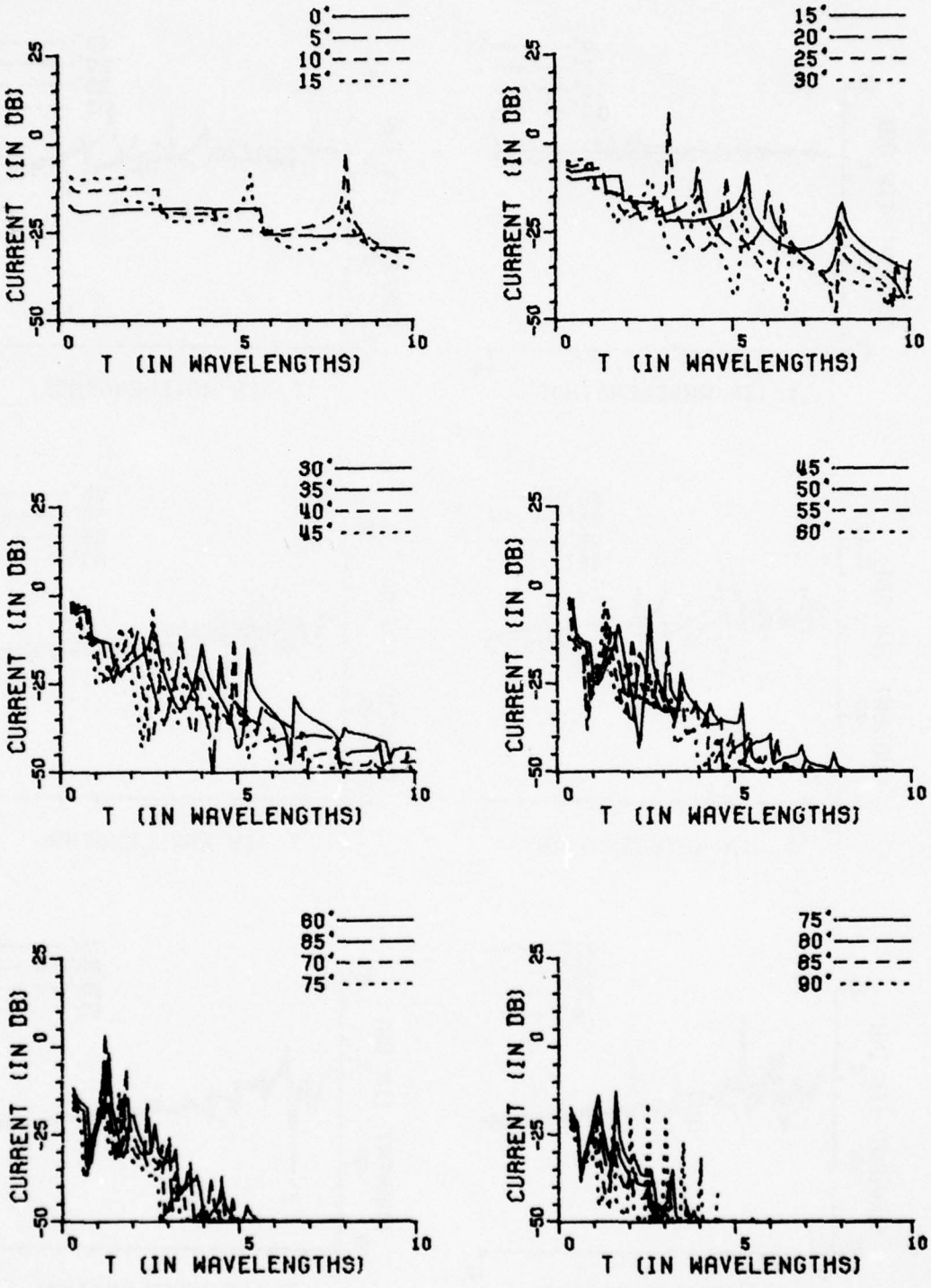

Figure 36c. Circumferential current density with a=0.25 wavelength and $r_1/a=1.0$.

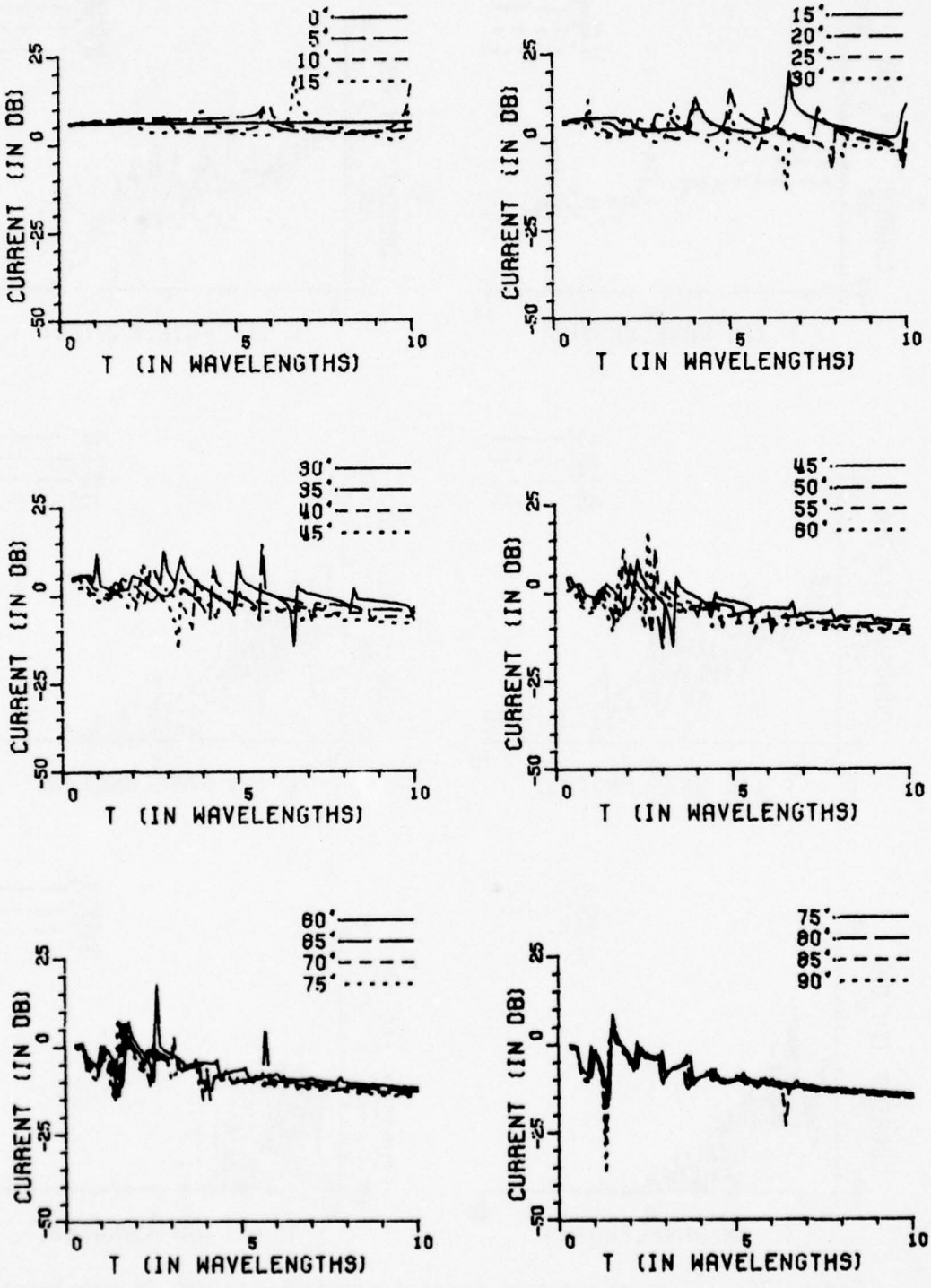

Figure 37a. Axial current density with a=0.25 wavelength and r_1/a=2.0.

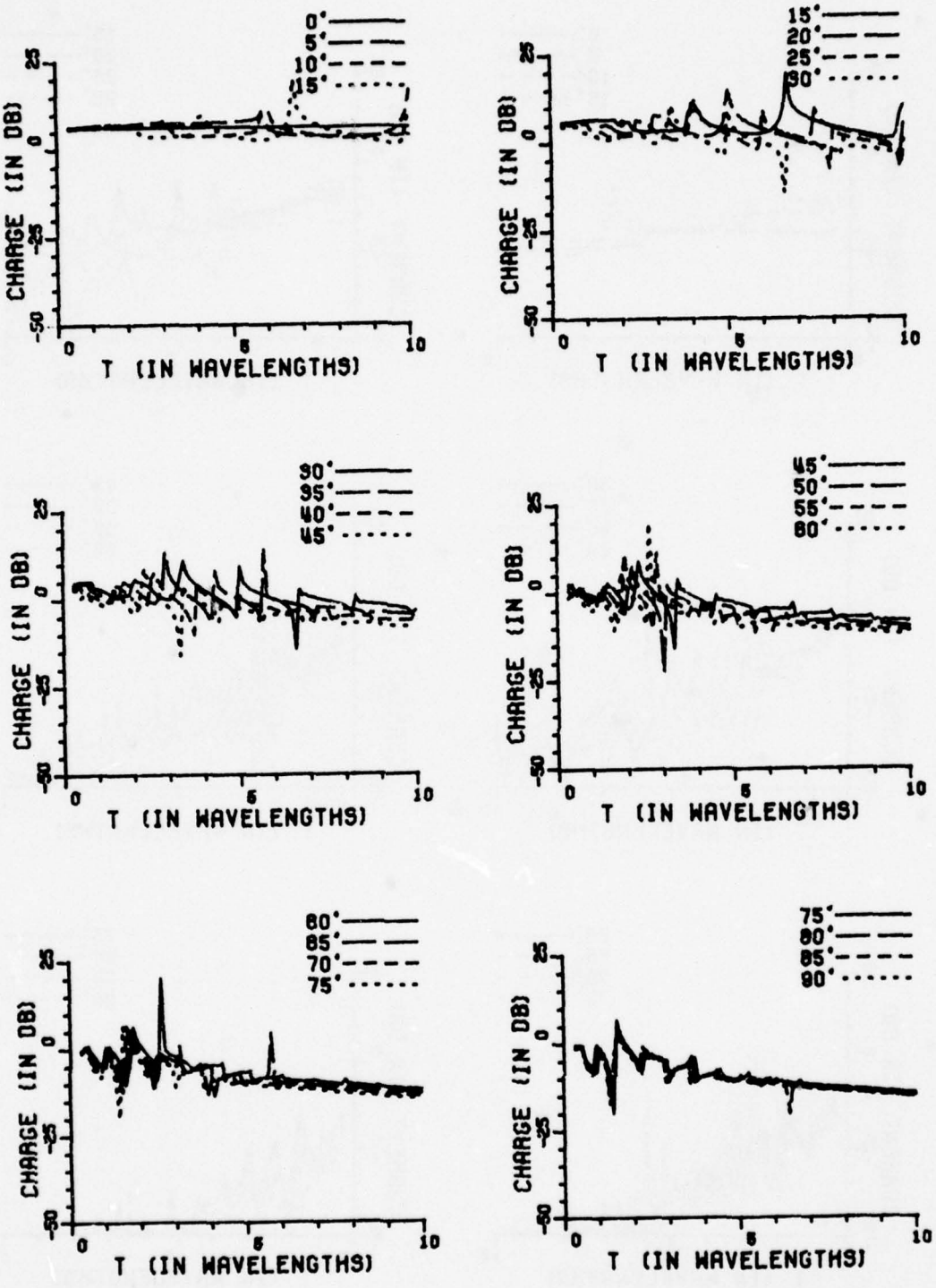

Figure 37b. Surface charge density with a=0.25 wavelength and $r_1/a=2.0$.

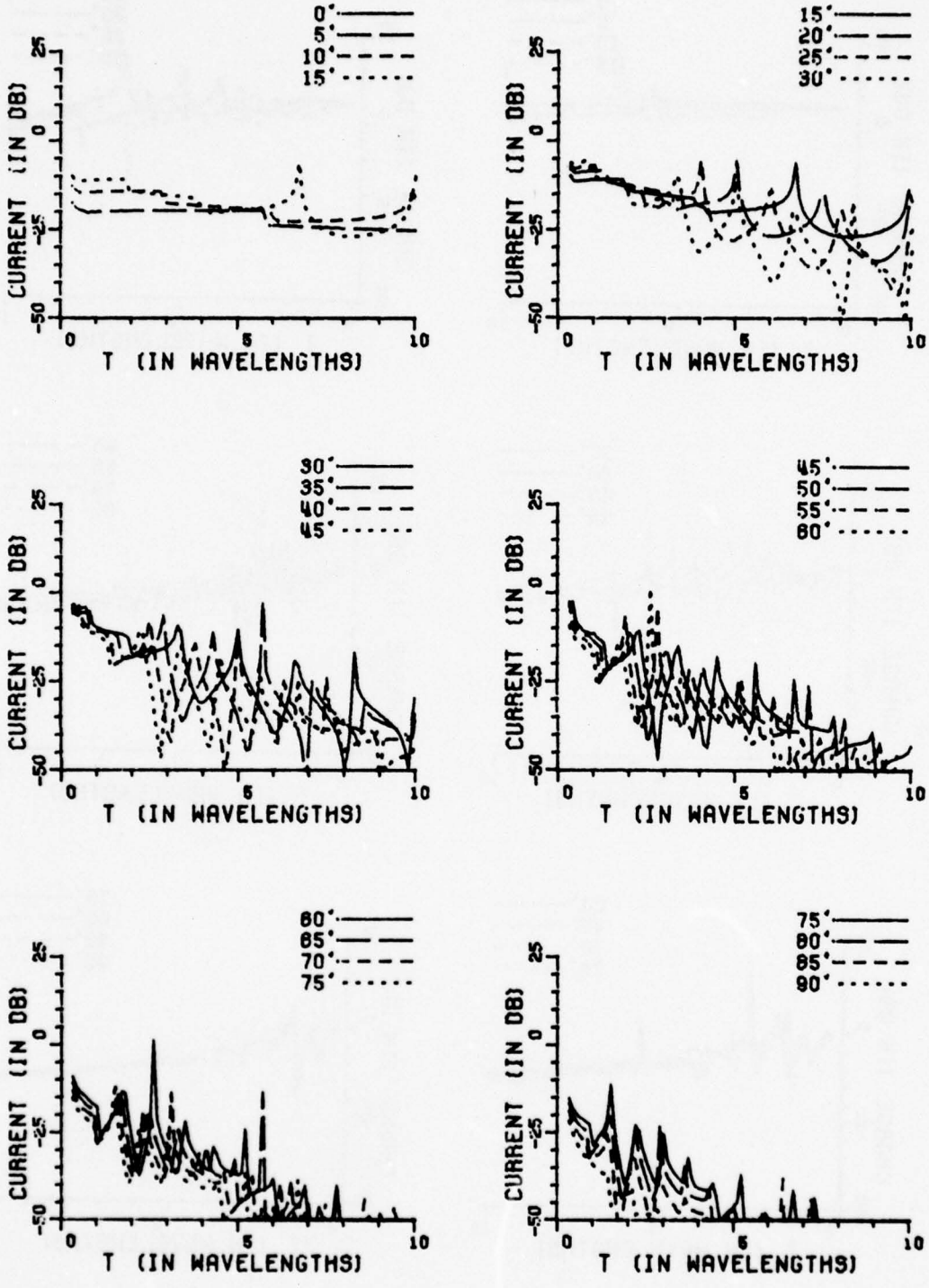

Figure 37c. Circumferential current density with a=0.25 wavelength and $r_1/a=2.0$.

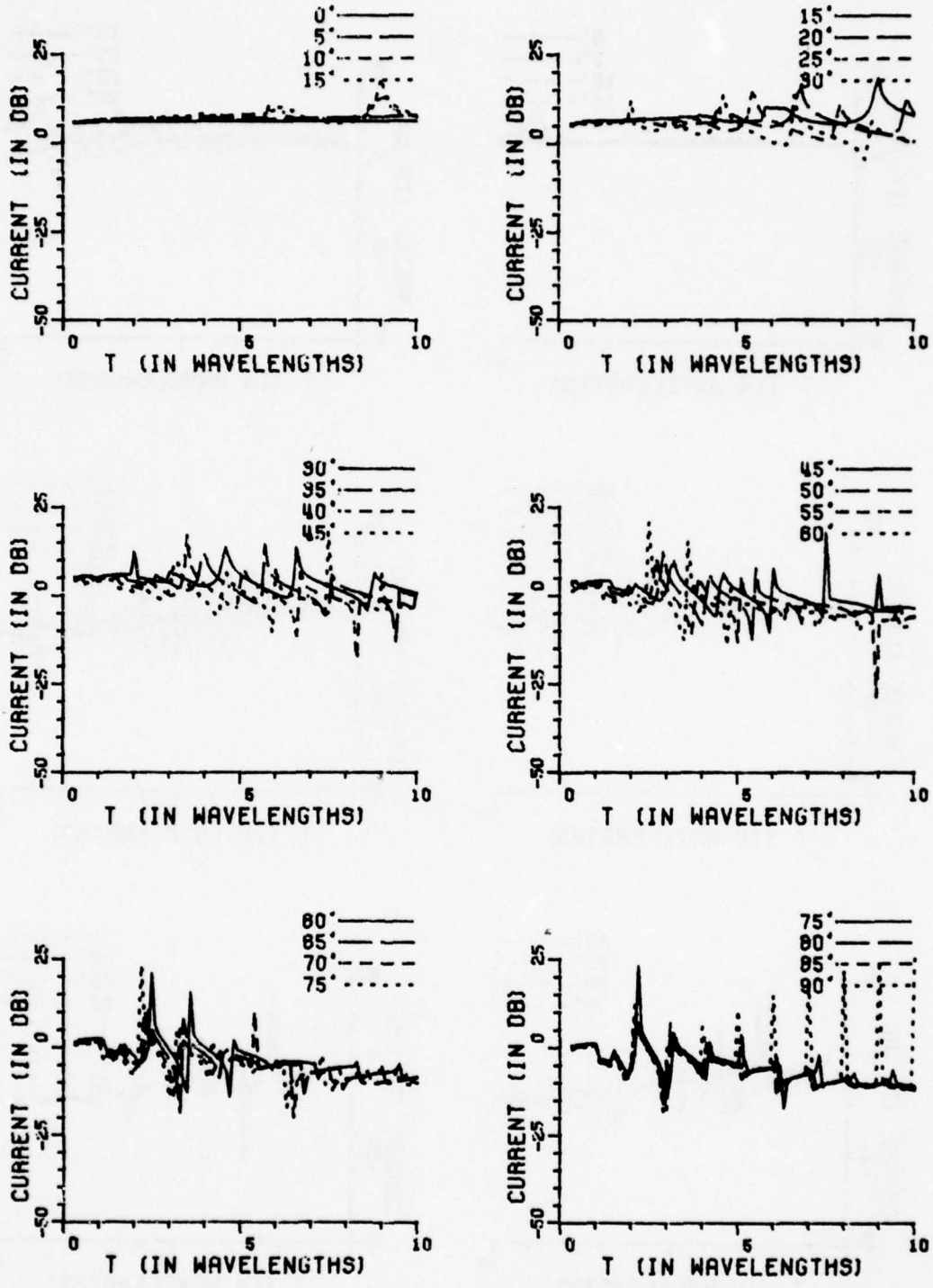

Figure 38a. Axial current density with a=0.25 wavelength and $r_1/a=4.0$.

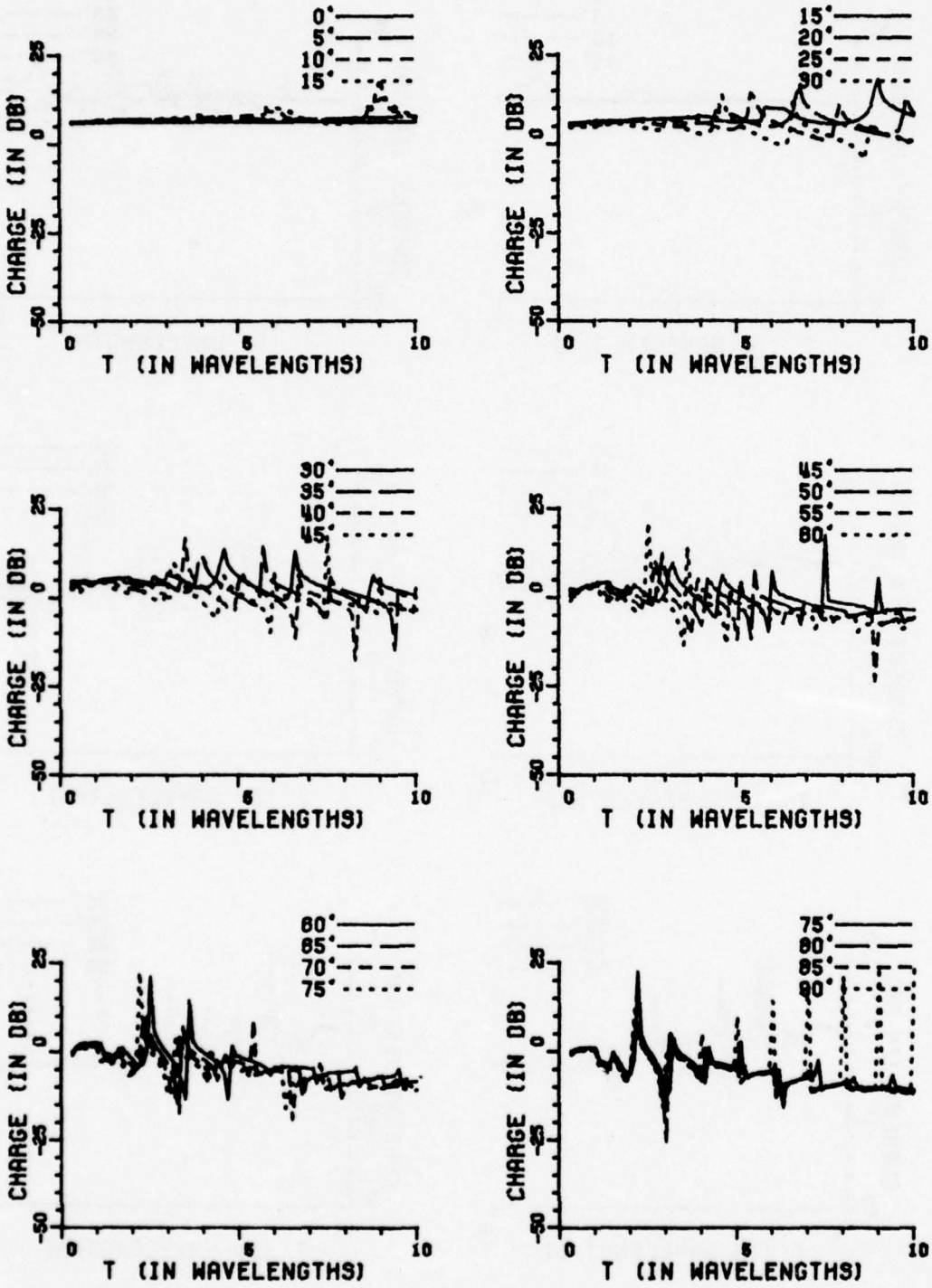

Figure 38b. Surface charge density with a=0.25 wavelength and r_1/a=4.0.

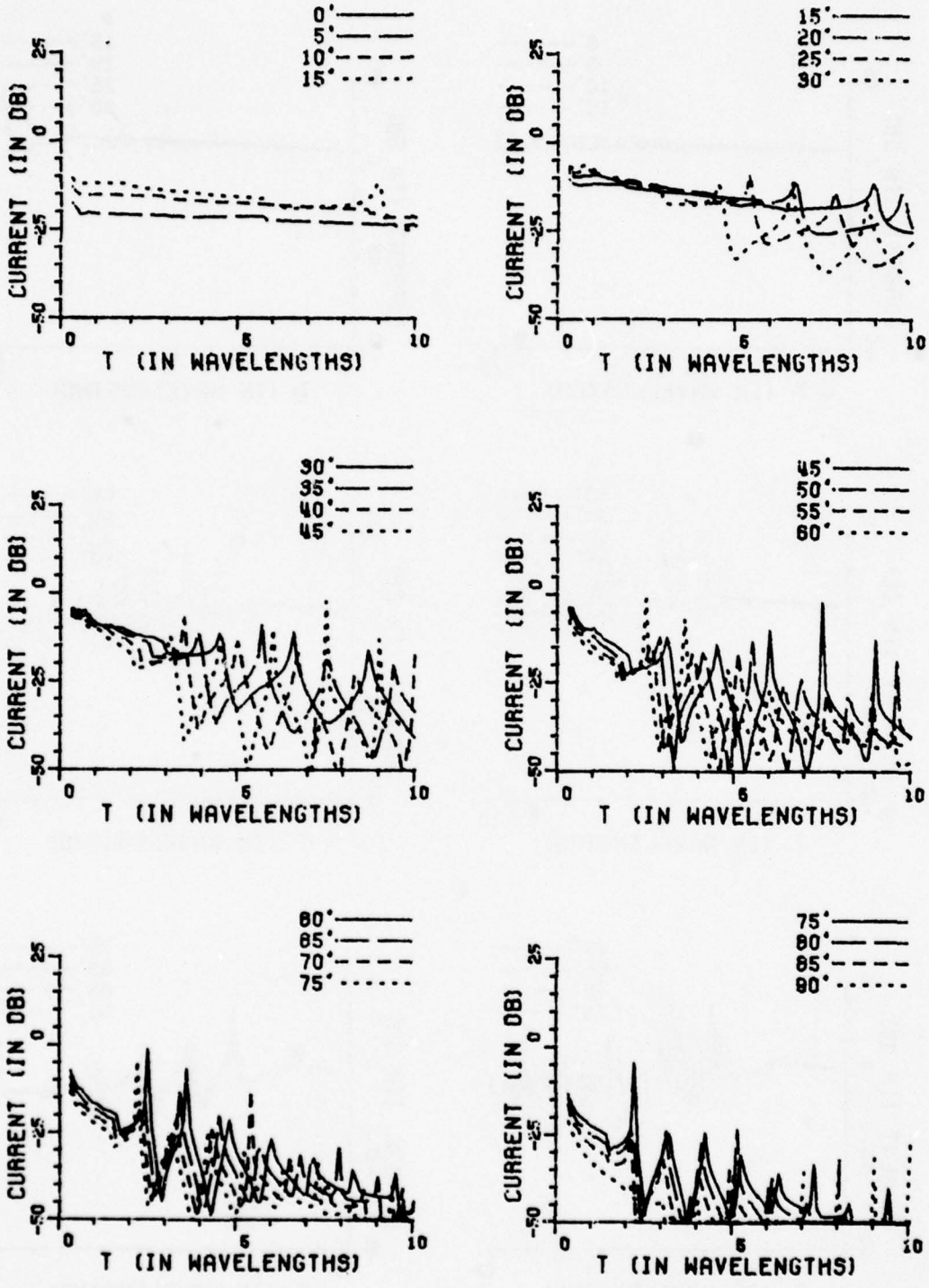

Figure 38c. Circumferential current density with a=0.25 wavelength and r_1/a=4.0.

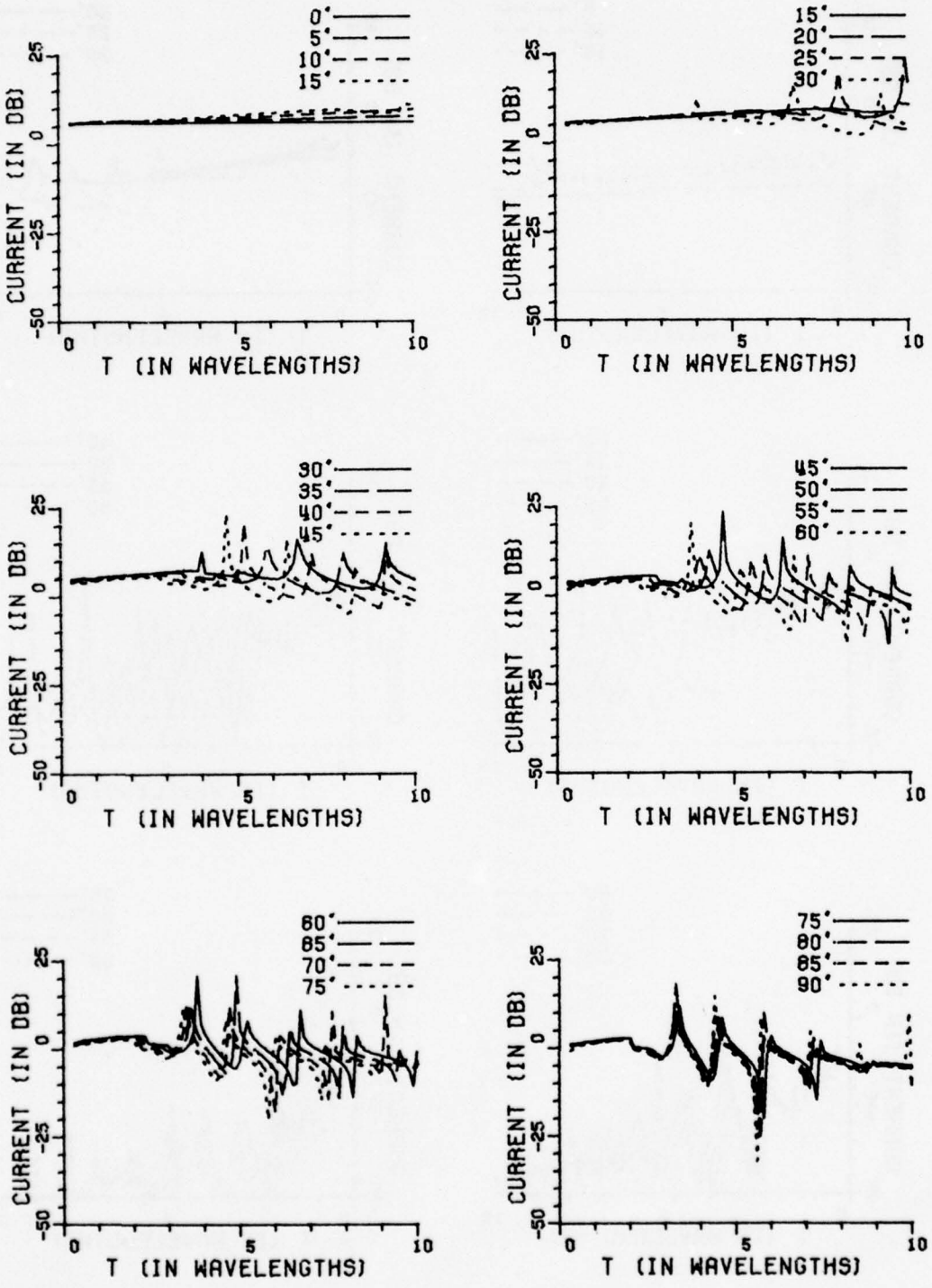

Figure 39a. Axial current density with a=0.25 wavelength and r_1/a=8.0.

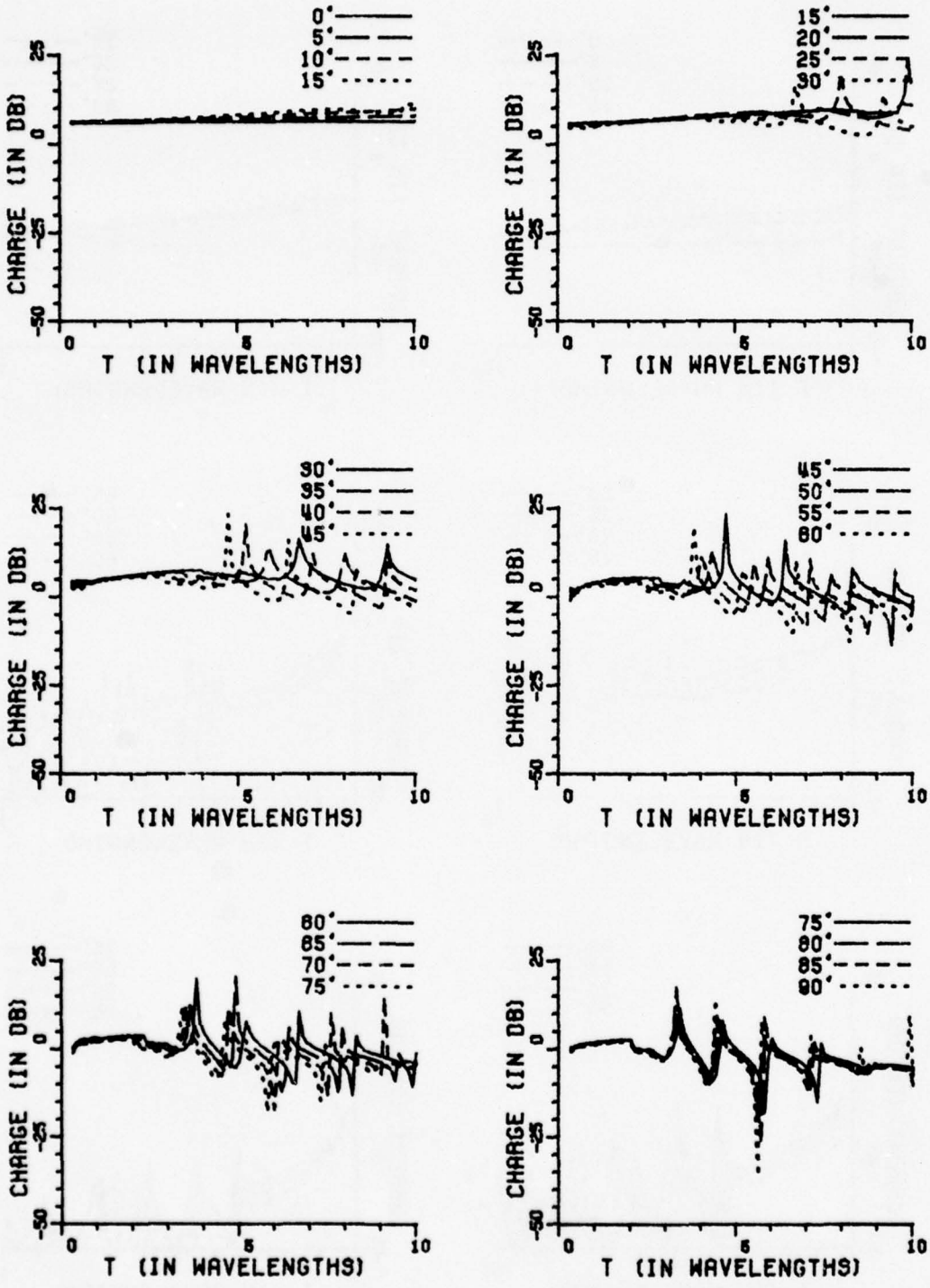

Figure 39b. Surface charge density with a=0.25 wavelength and r_1/a=8.0.

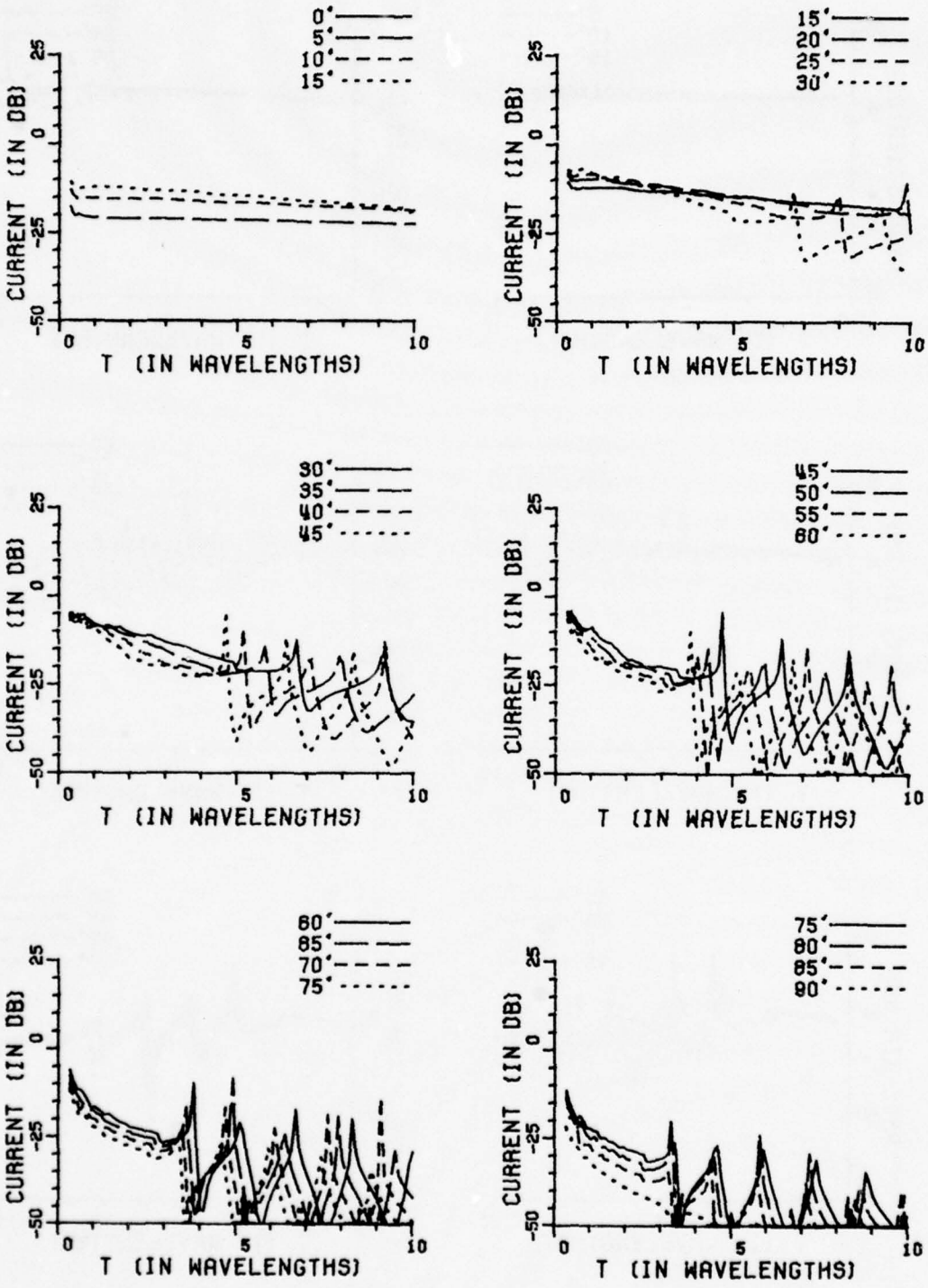

Figure 39c. Circumferential current density with a=0.25 wavelength and r_1/a=8.0.

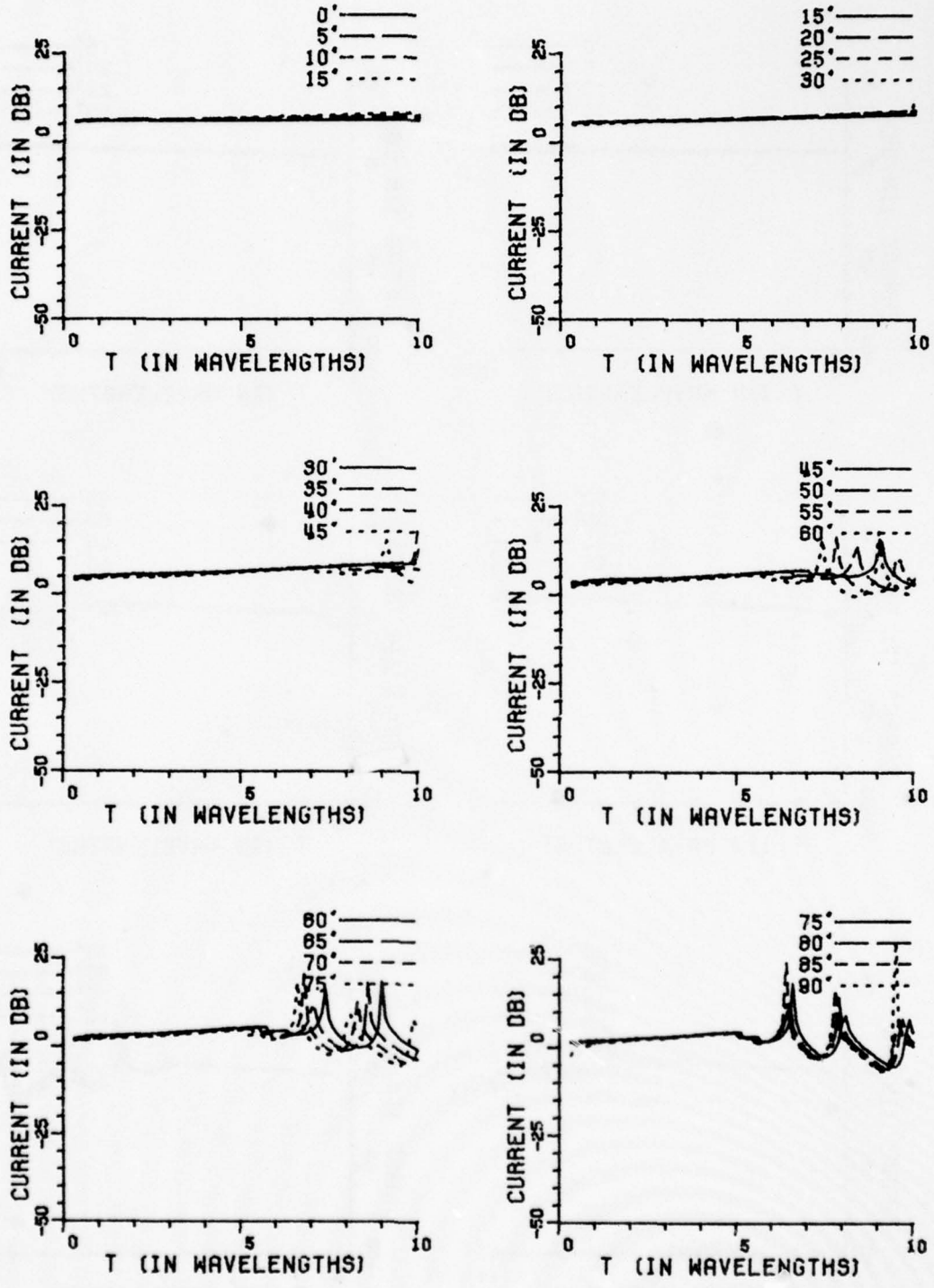

Figure 40a. Axial current density with a=0.25 wavelength and r_1/a=20.0.

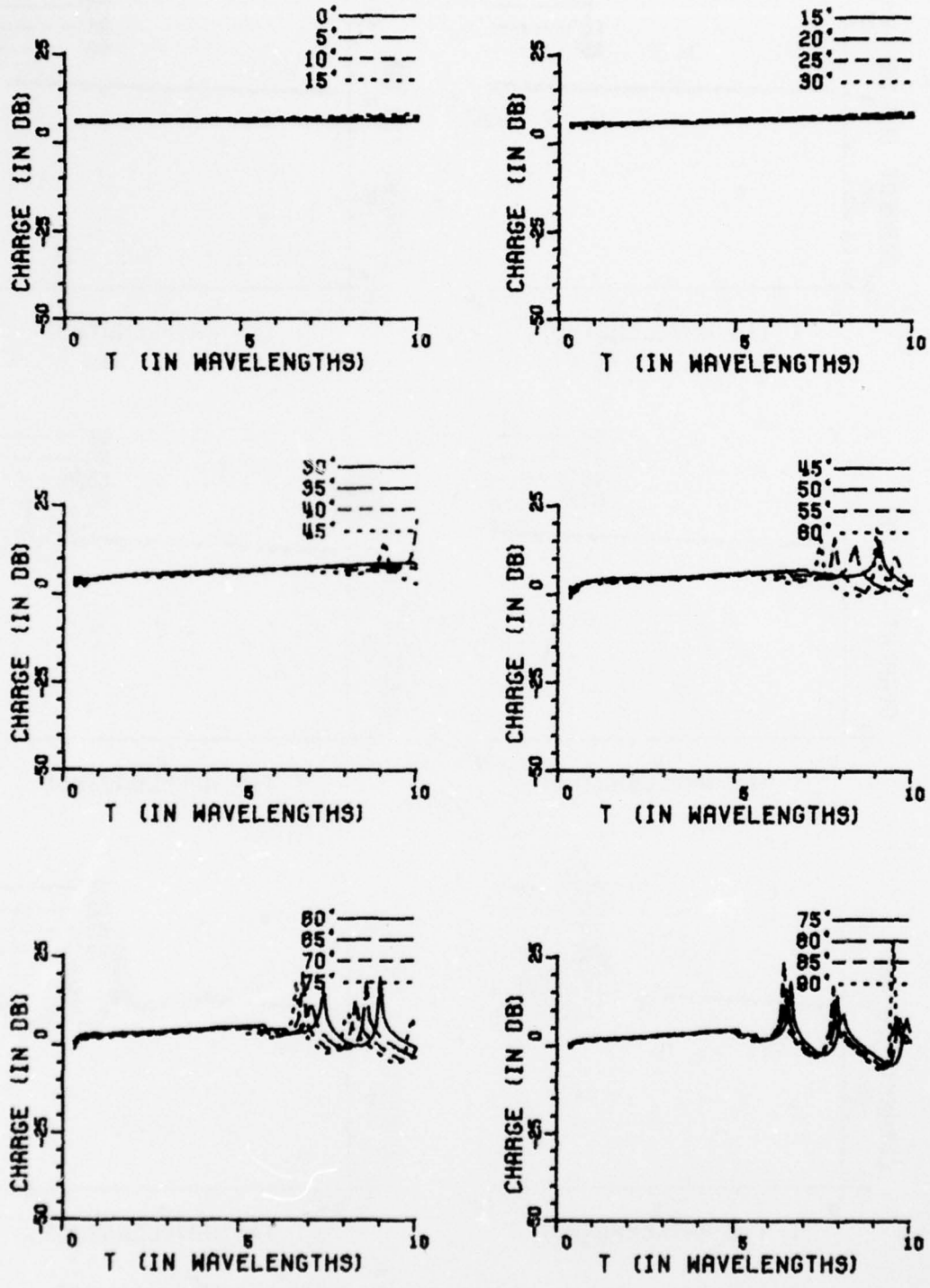

Figure 40b. Surface charge density with a=0.25 wavelength and r_1/a=20.0.

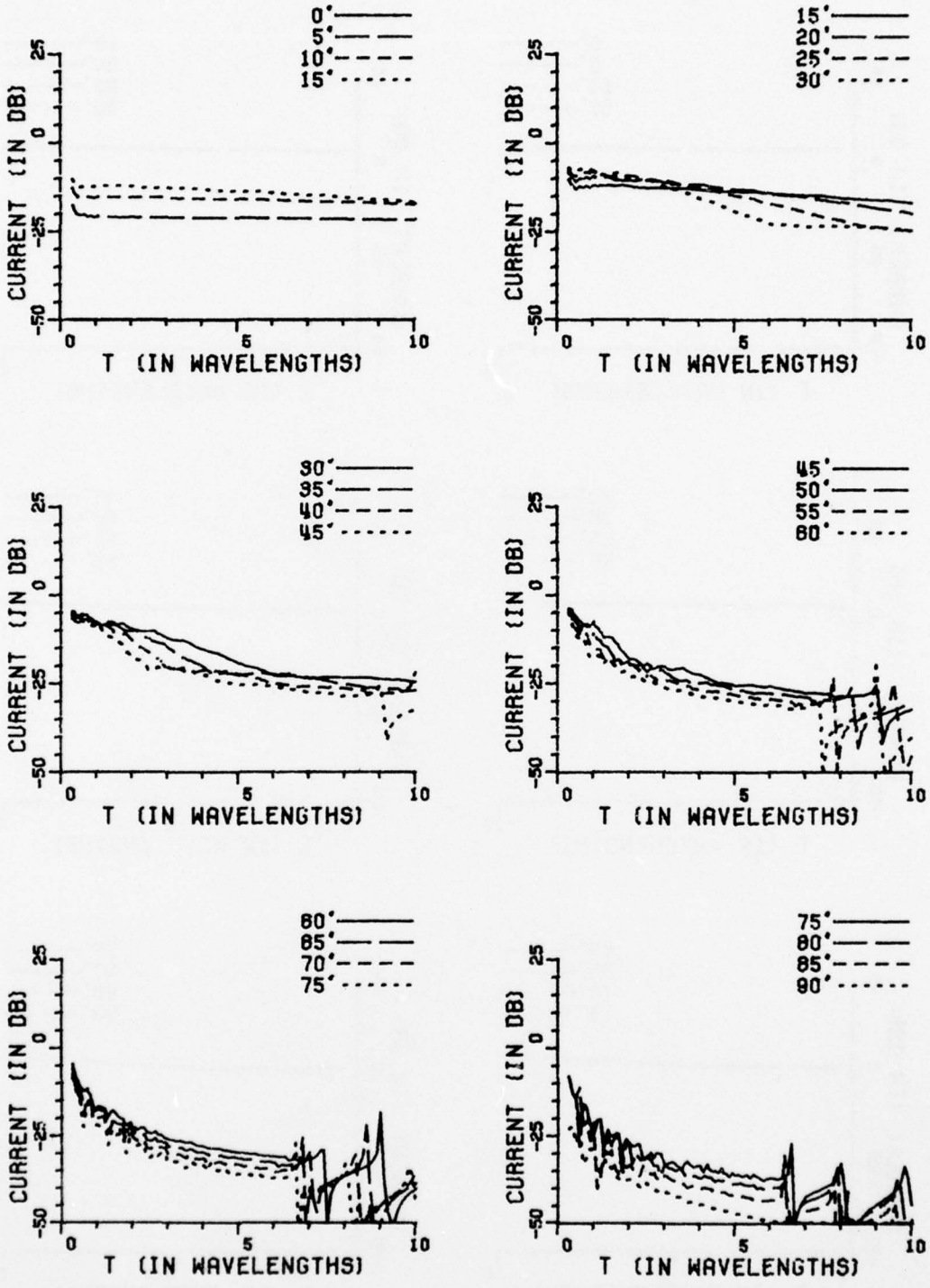

Figure 40c. Circumferential current density with a=0.25 wavelength and r_1/a=20.0.

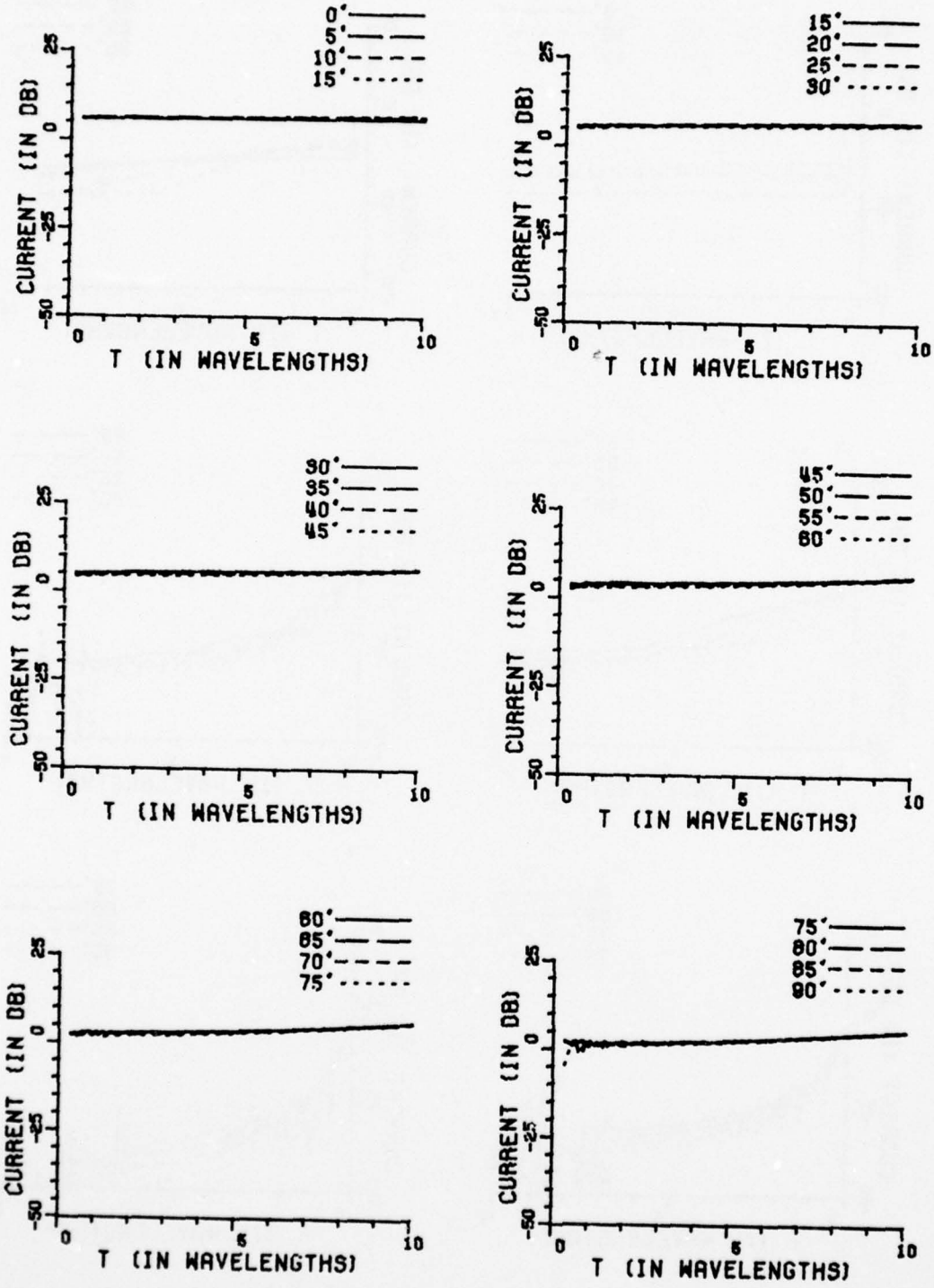

Figure 41a. Axial current density with a=0.25 wavelength and r_1/a=40.0.

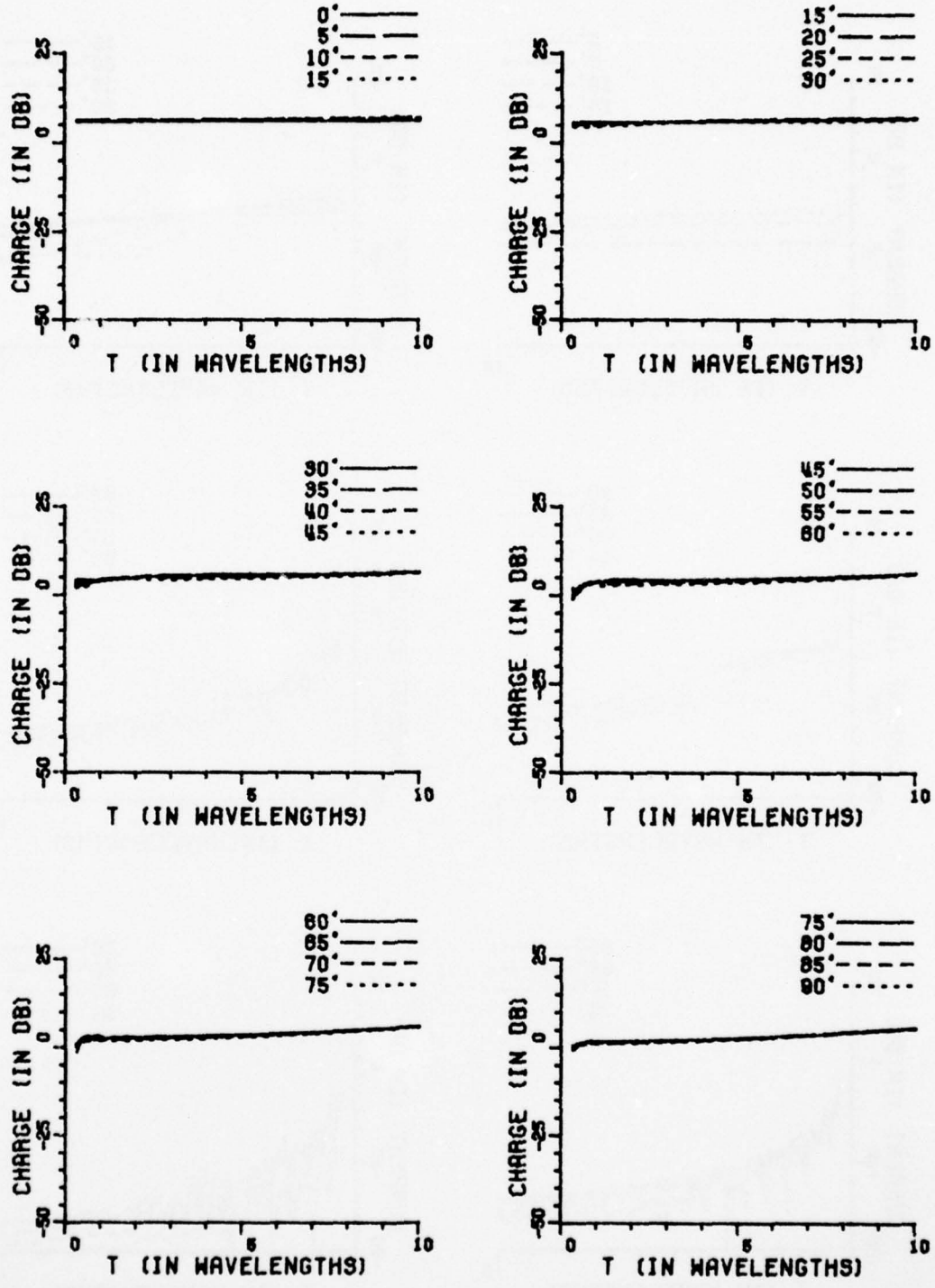

Figure 41b. Surface charge density with a=0.25 wavelength and r_1/a=40.0.

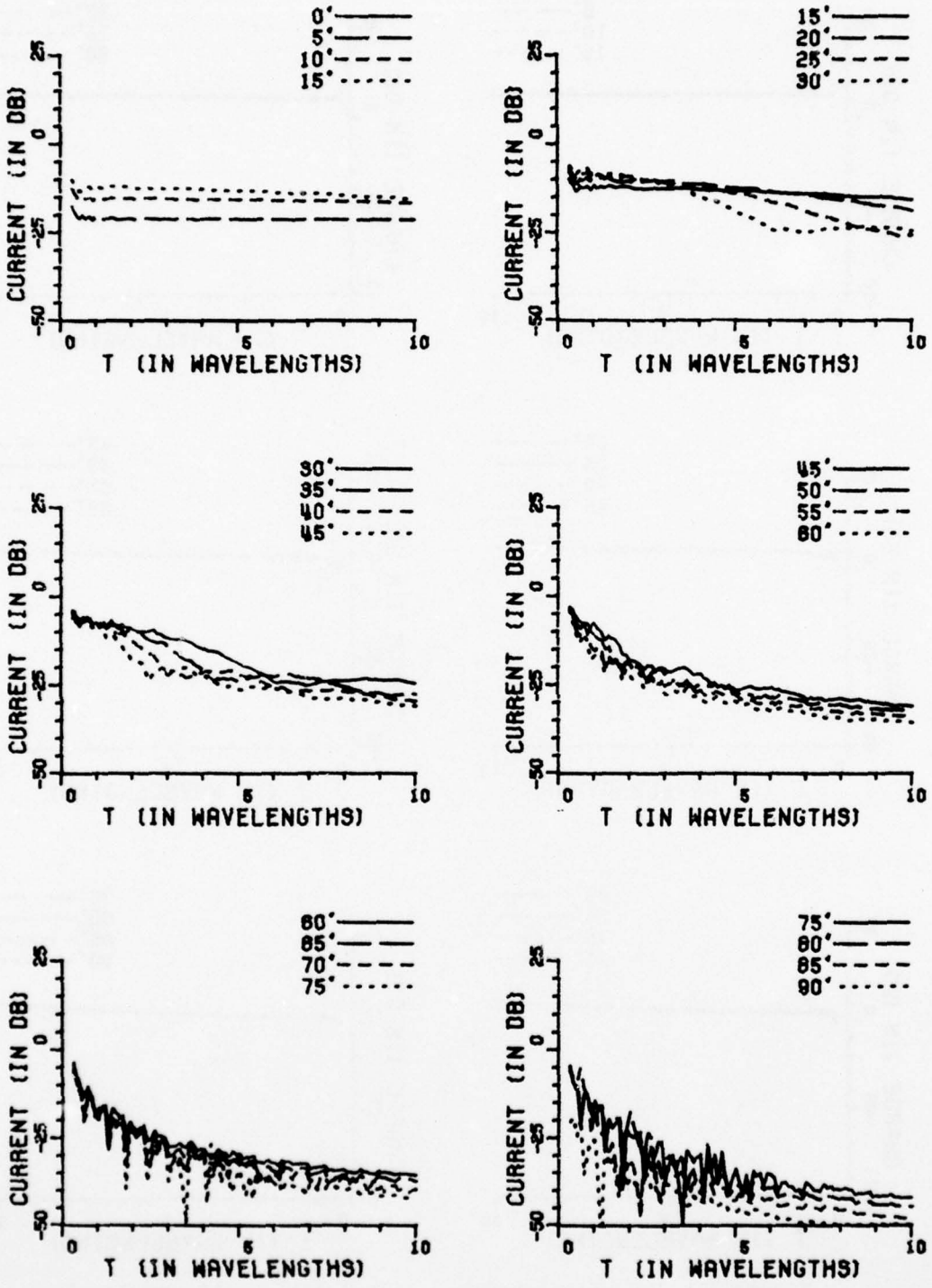

Figure 41c. Circumferential current density with a=0.25 wavelength and r_1/a=40.0.

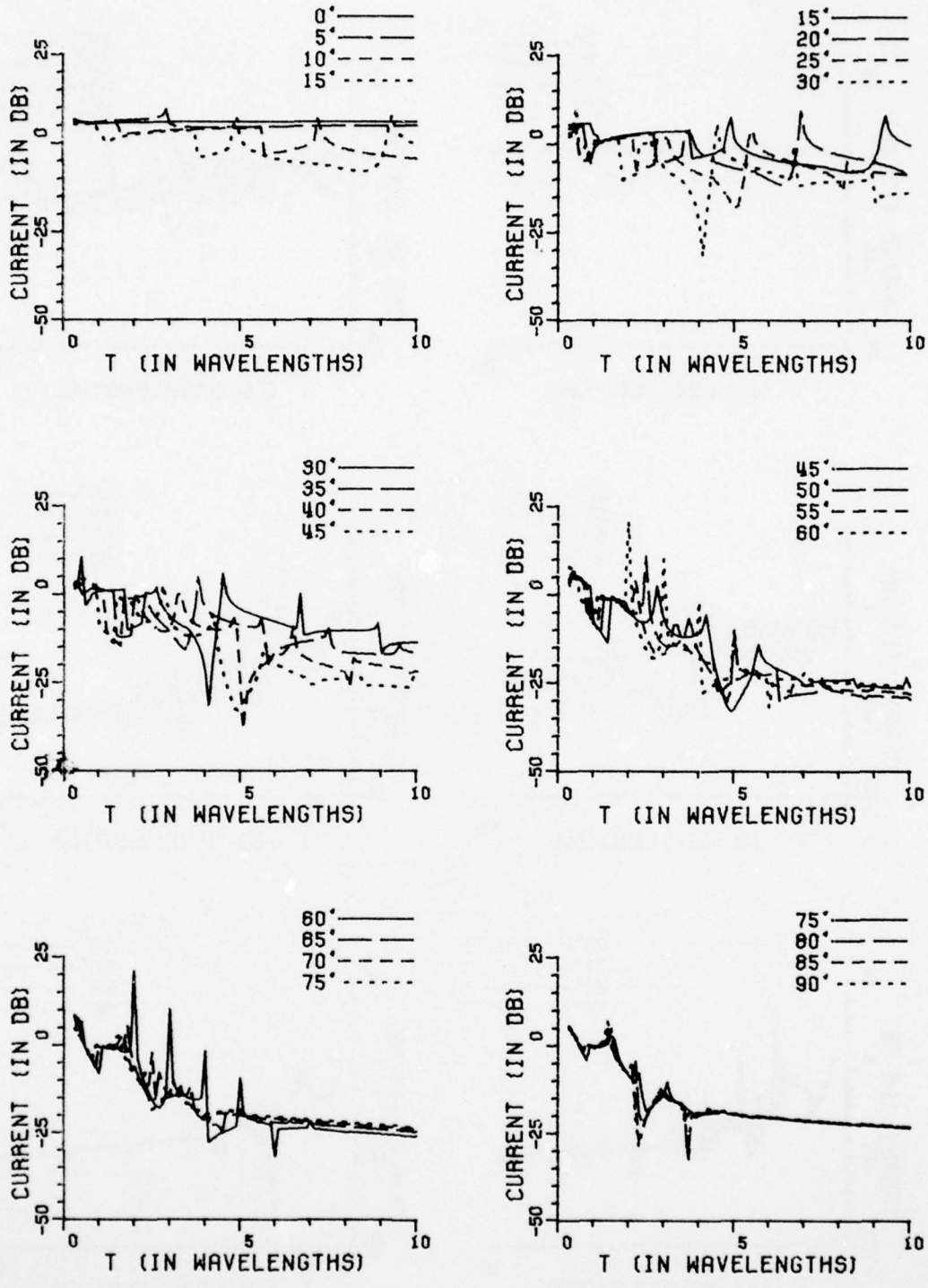

Figure 42a. Axial current density with a=0.5 wavelength and r_1/a=0.5.

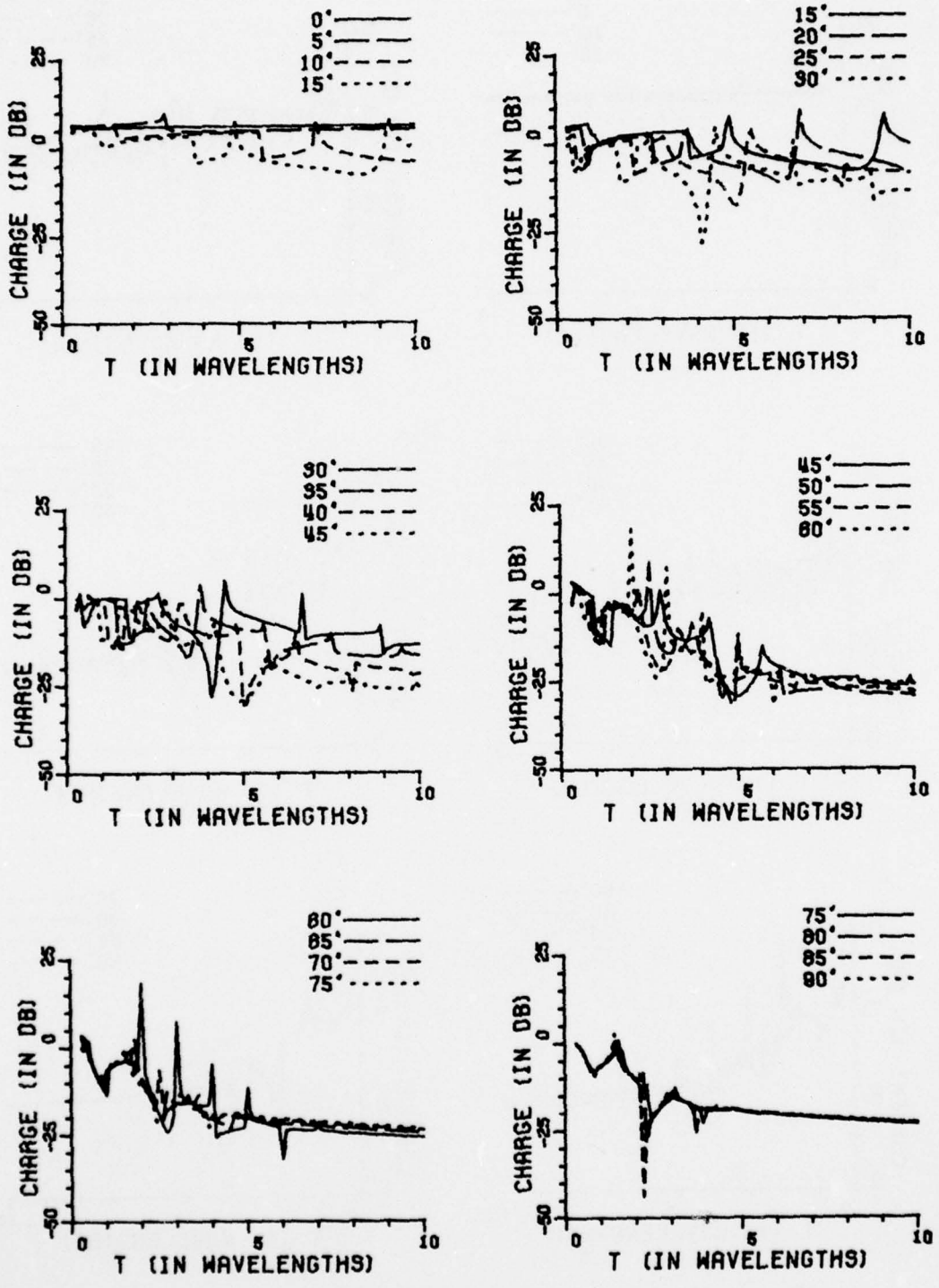

Figure 42b. Surface charge density with a=0.5 wavelength and r_1/a=0.5.

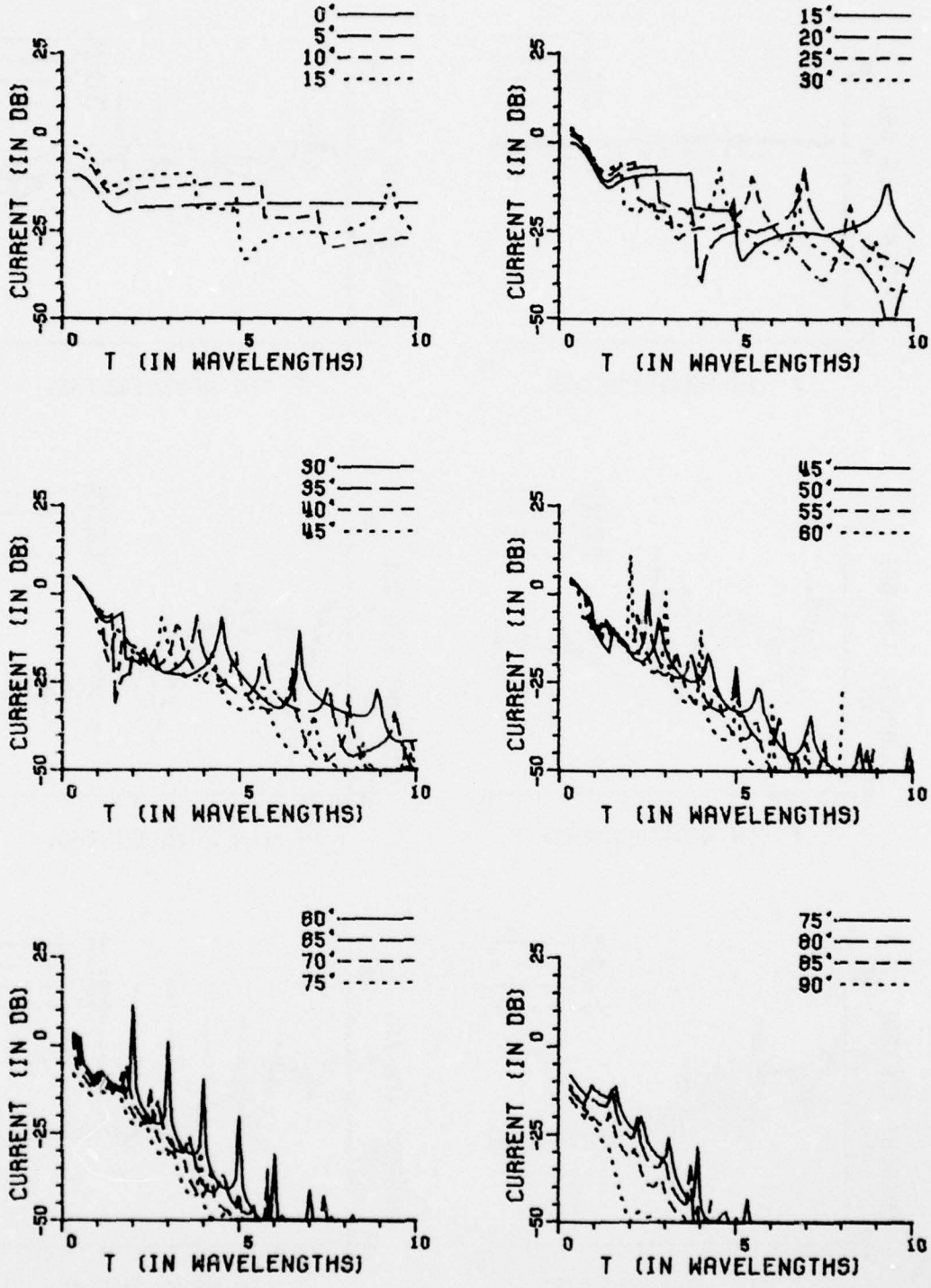

Figure 42c. Circumferential current density with a=0.5 wavelength and $r_1/a=0.5$.

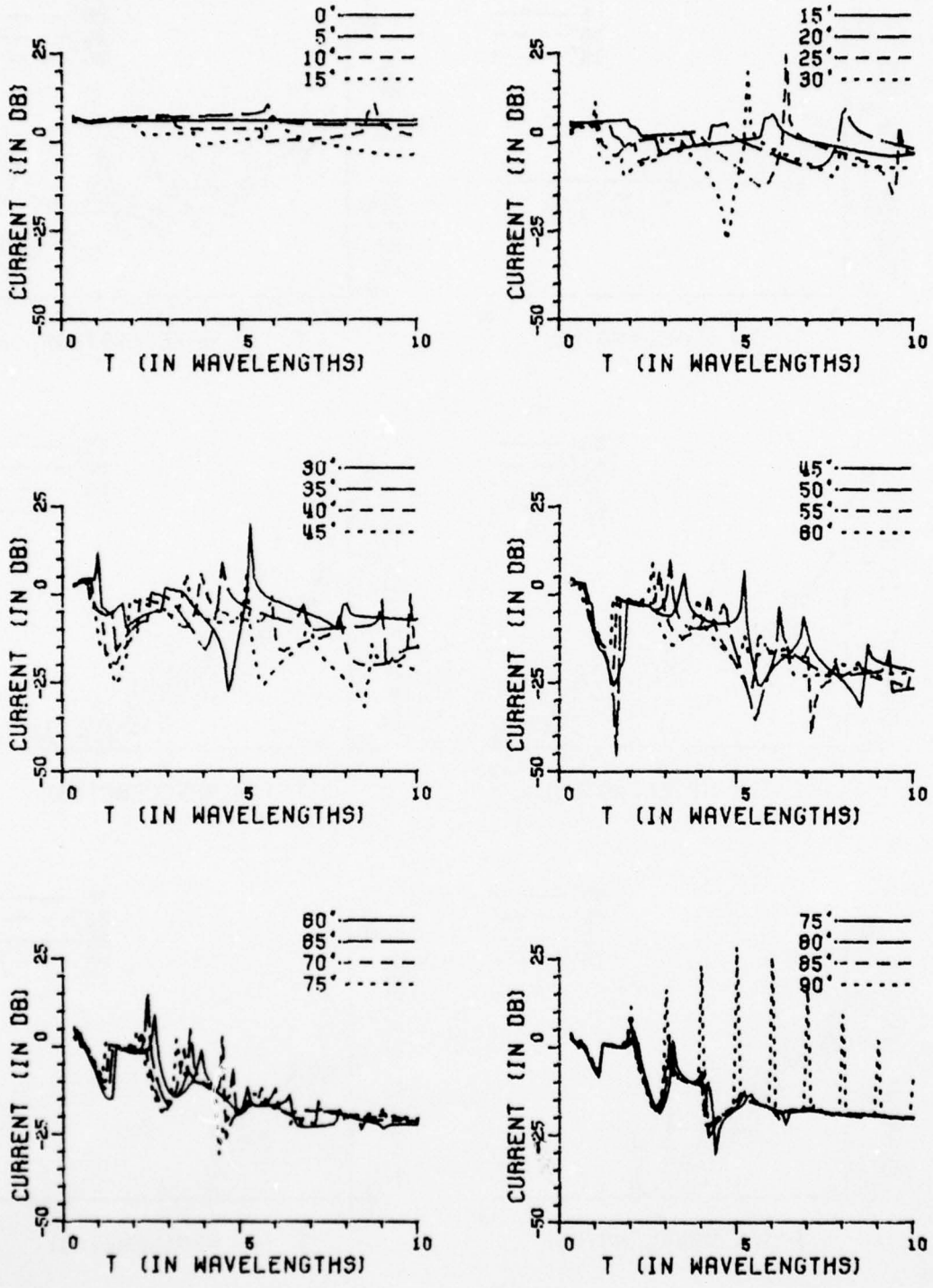

Figure 43a. Axial current density with a=0.5 wavelength and $r_1/a=1.0$.

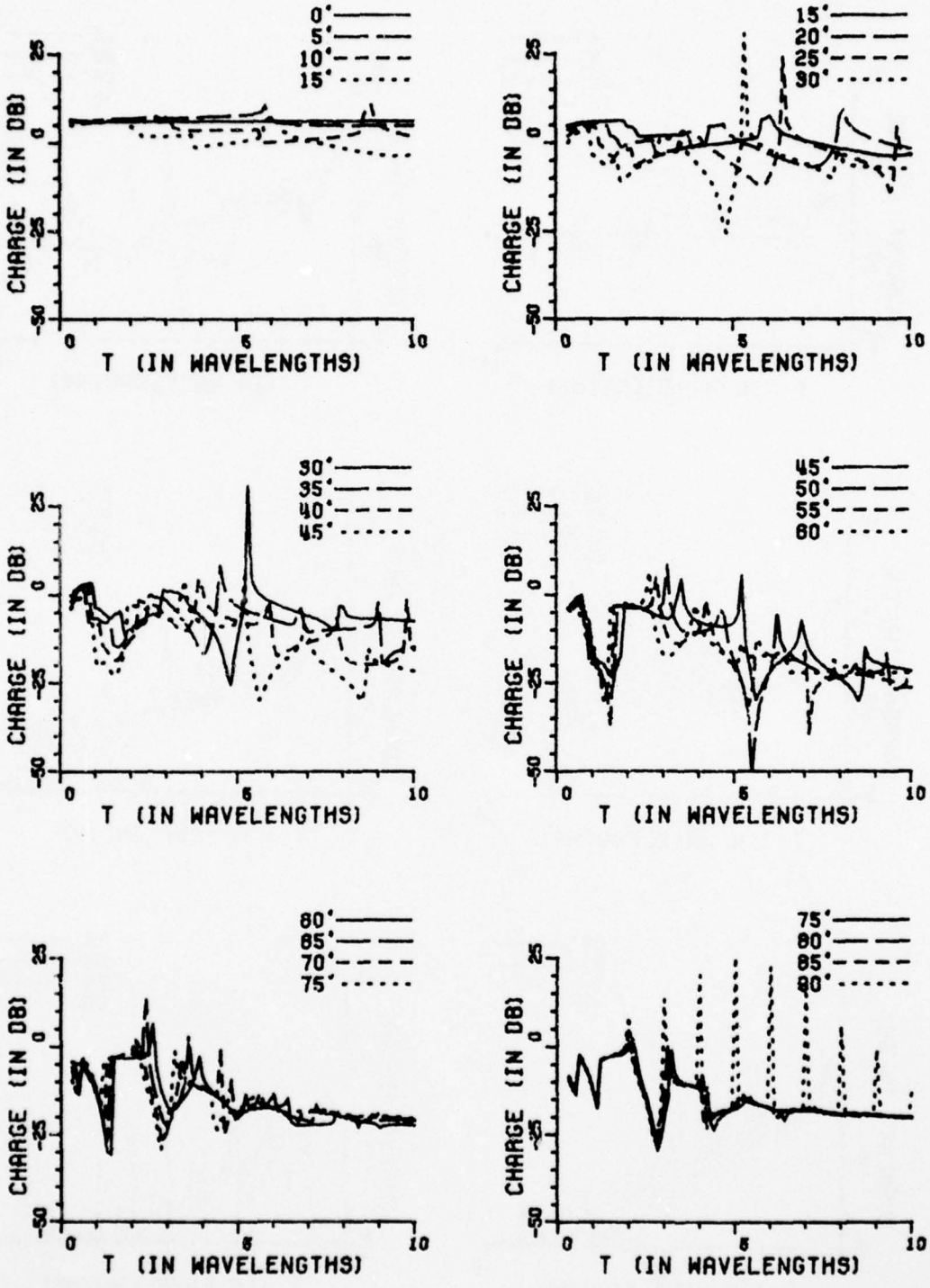

Figure 43b. Surface charge density with a=0.5 wavelength and $r_1/a=1.0$.

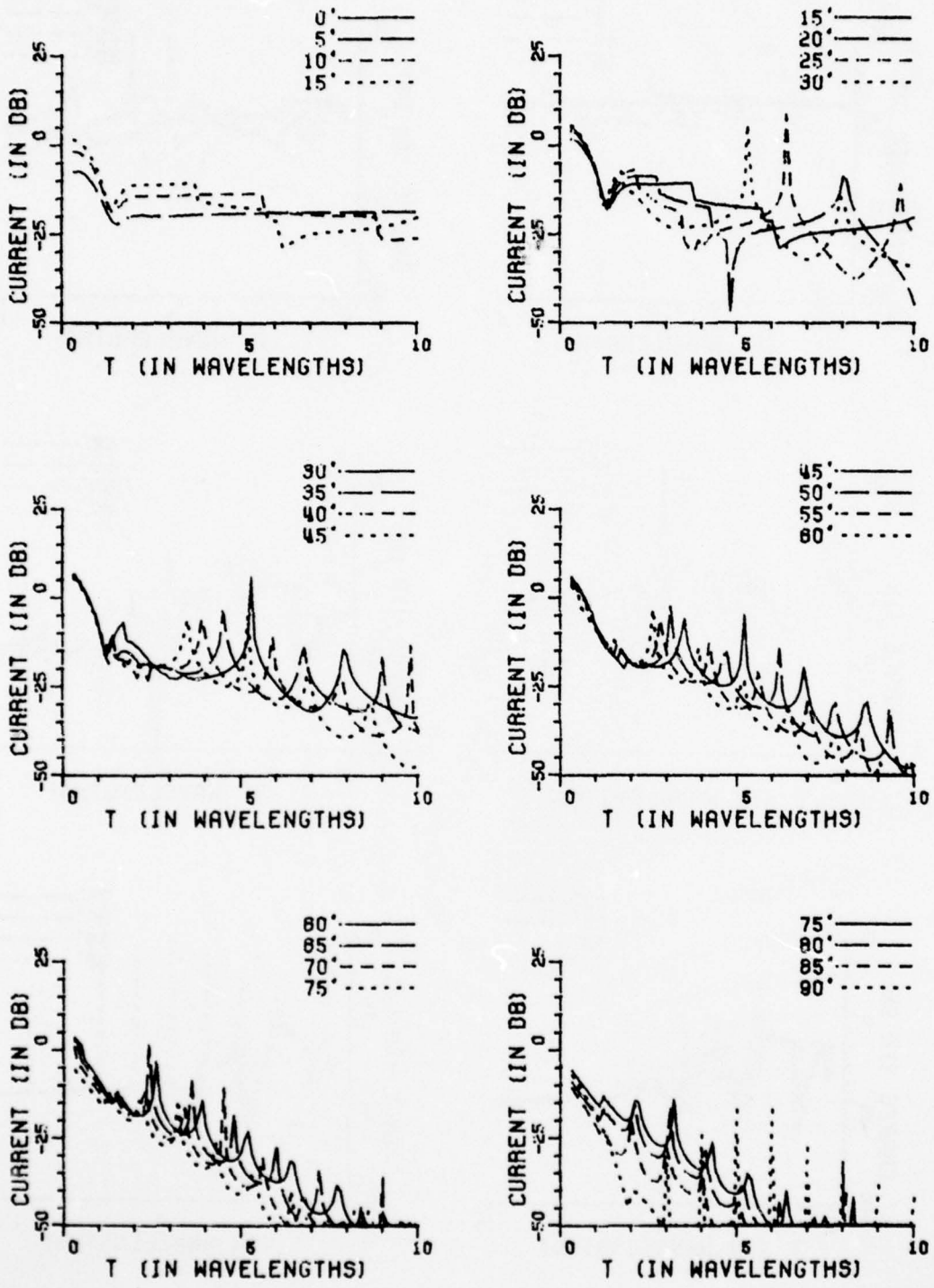

Figure 43c. Circumferential current density with a=0.5 wavelength and $r_1/a=1.0$.

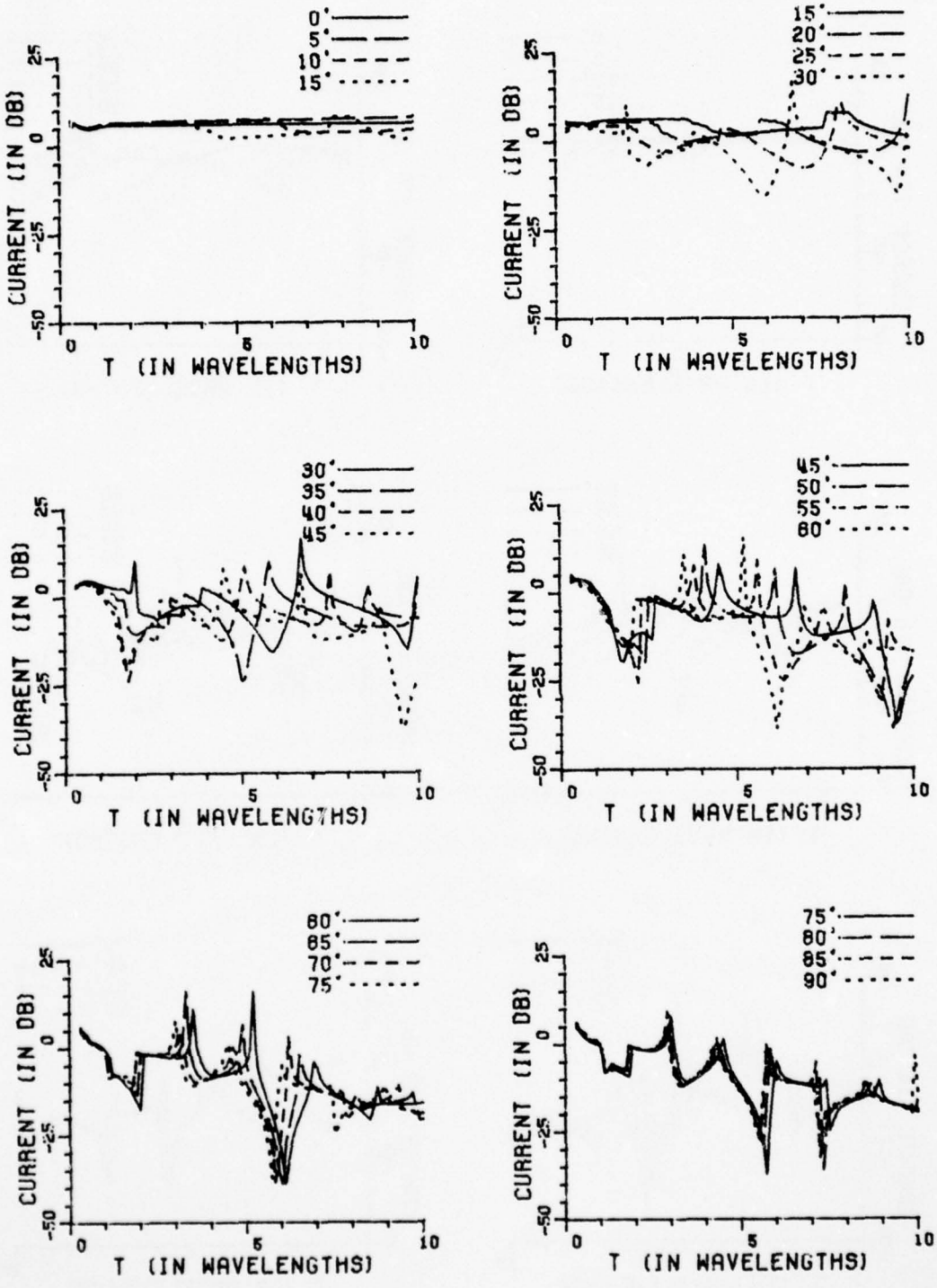

Figure 44a. Axial current density with a=0.5 wavelength and $r_1/a=2.0$.

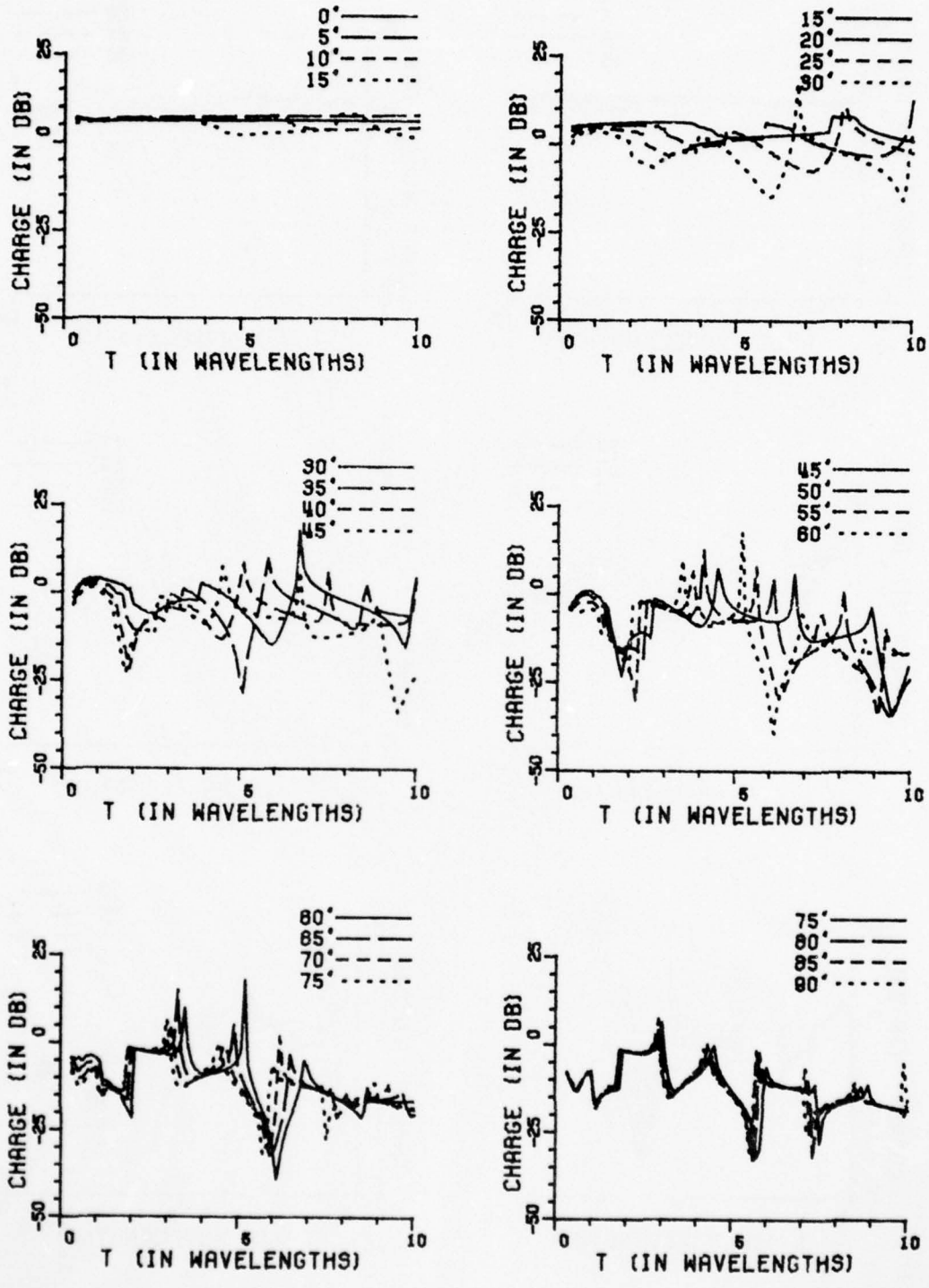

Figure 44b. Surface charge density with a=0.5 wavelength and r_1/a=2.0.

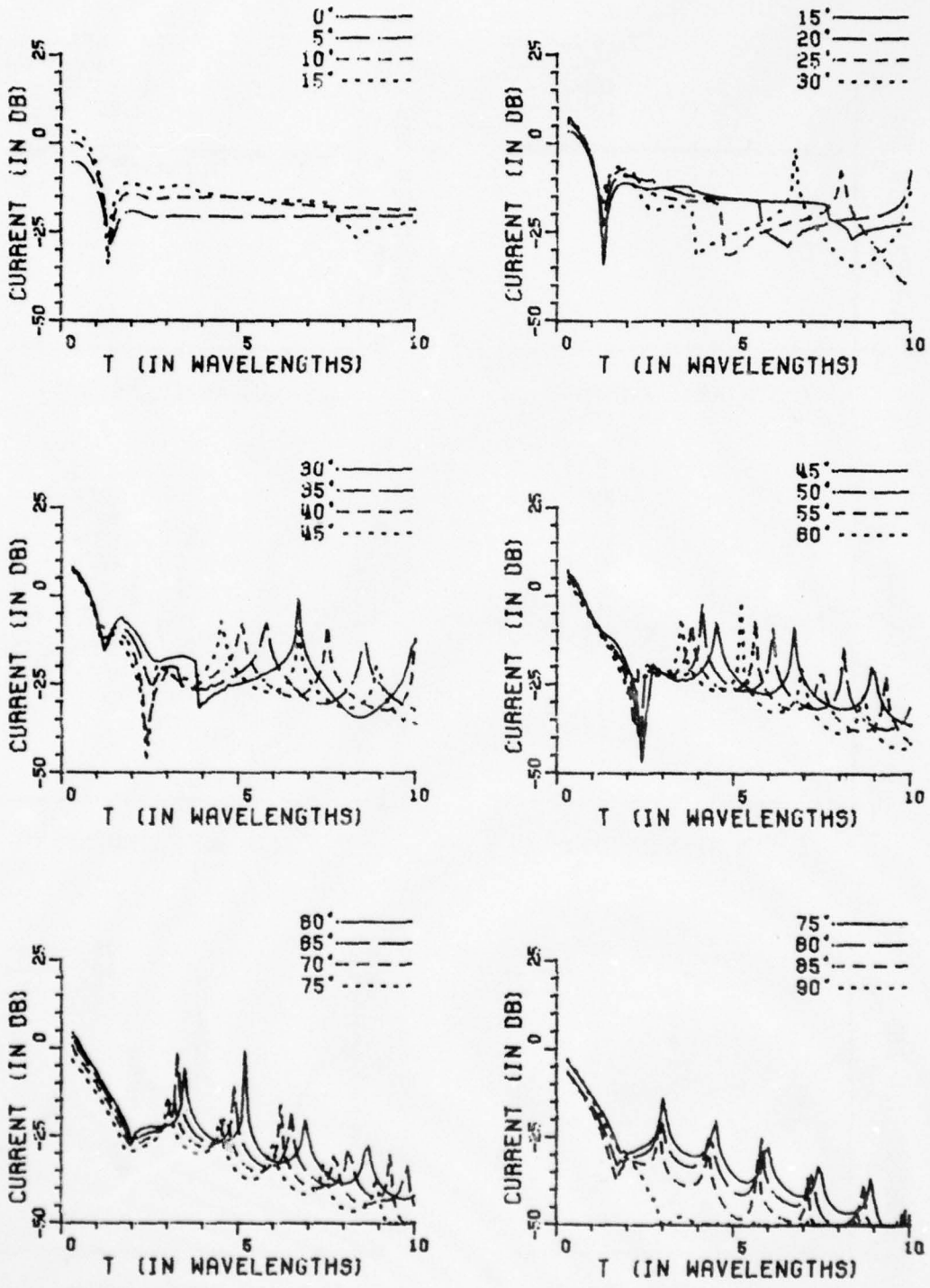

Figure 44c. Circumferential current density with a=0.5 wavelength and r_1/a=2.0.

AD-A064 828 OHIO STATE UNIV COLUMBUS ELECTROSCIENCE LAB F/G 20/3
THE SURFACE CURRENT AND CHARGE DENSITY INDUCED ON FINITE CYLIND--ETC(U)
OCT 78 E D GREER, W D BURNSIDE AFOSR-77-3324
UNCLASSIFIED ESL-784713-1 AFOSR-TR-79-0029 NL

2 OF 2
ADA
064828

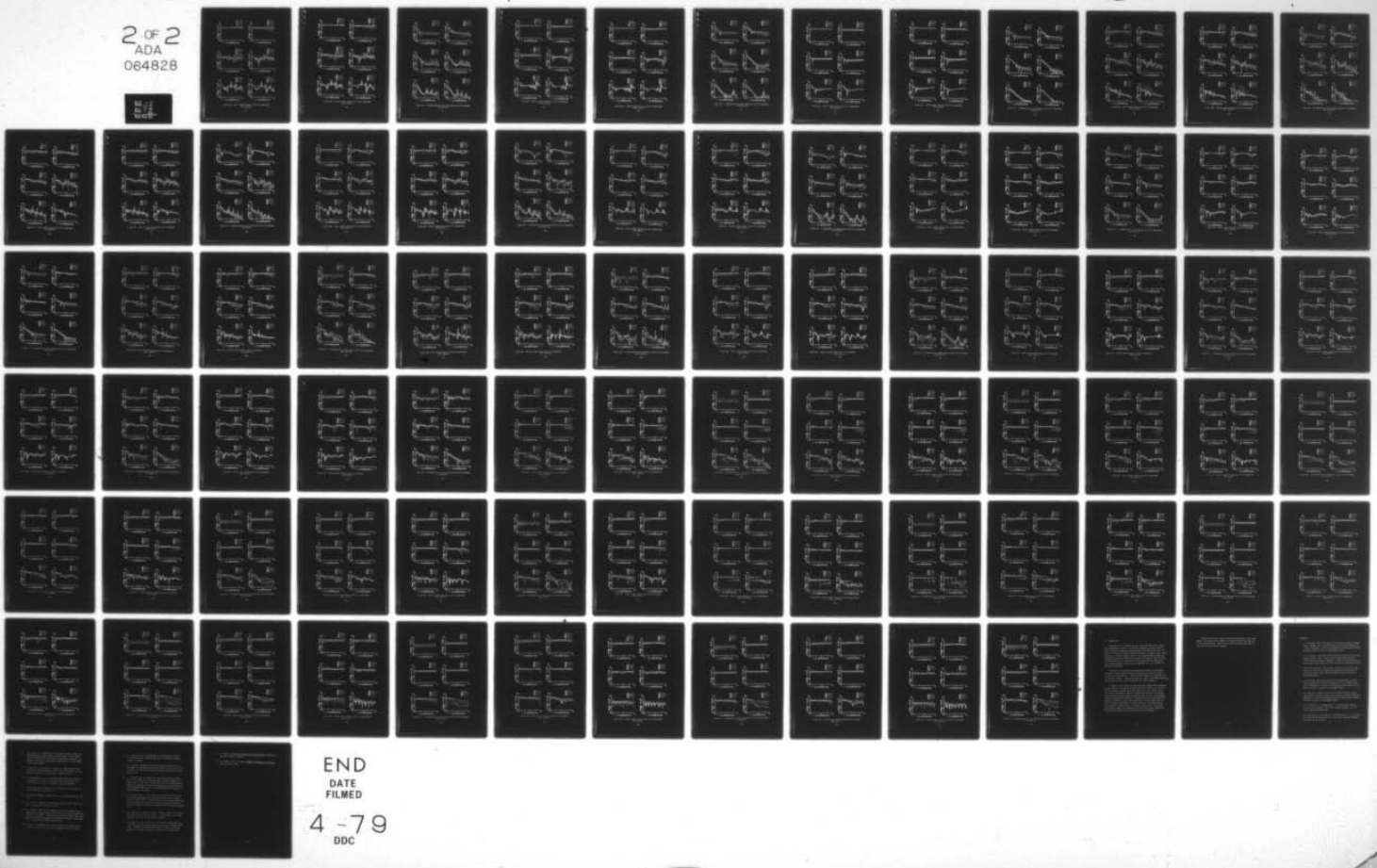

END
DATE
FILMED
4-79
DDC

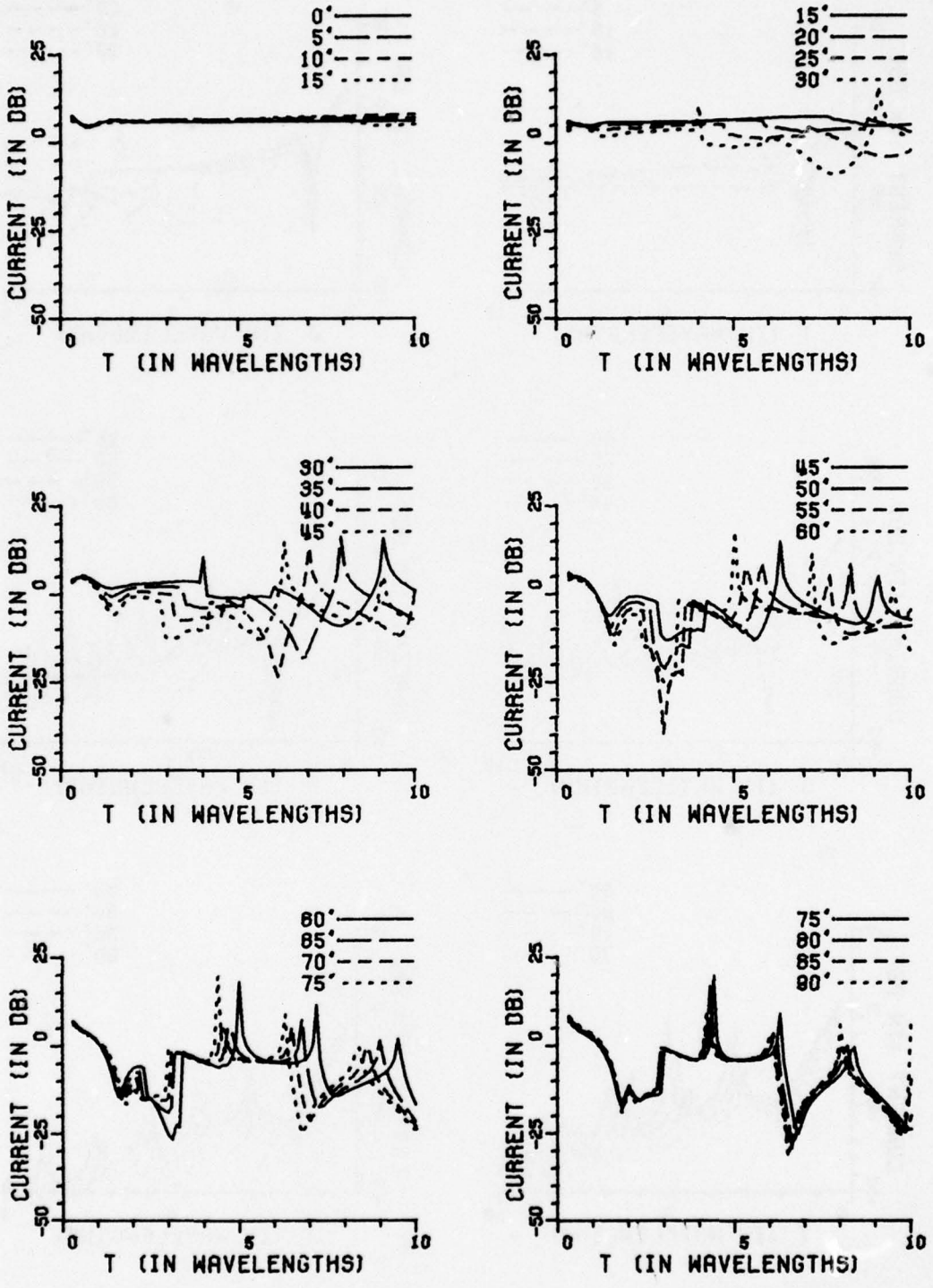

Figure 45a. Axial current density with a=0.5 wavelength and r_1/a=4.0.

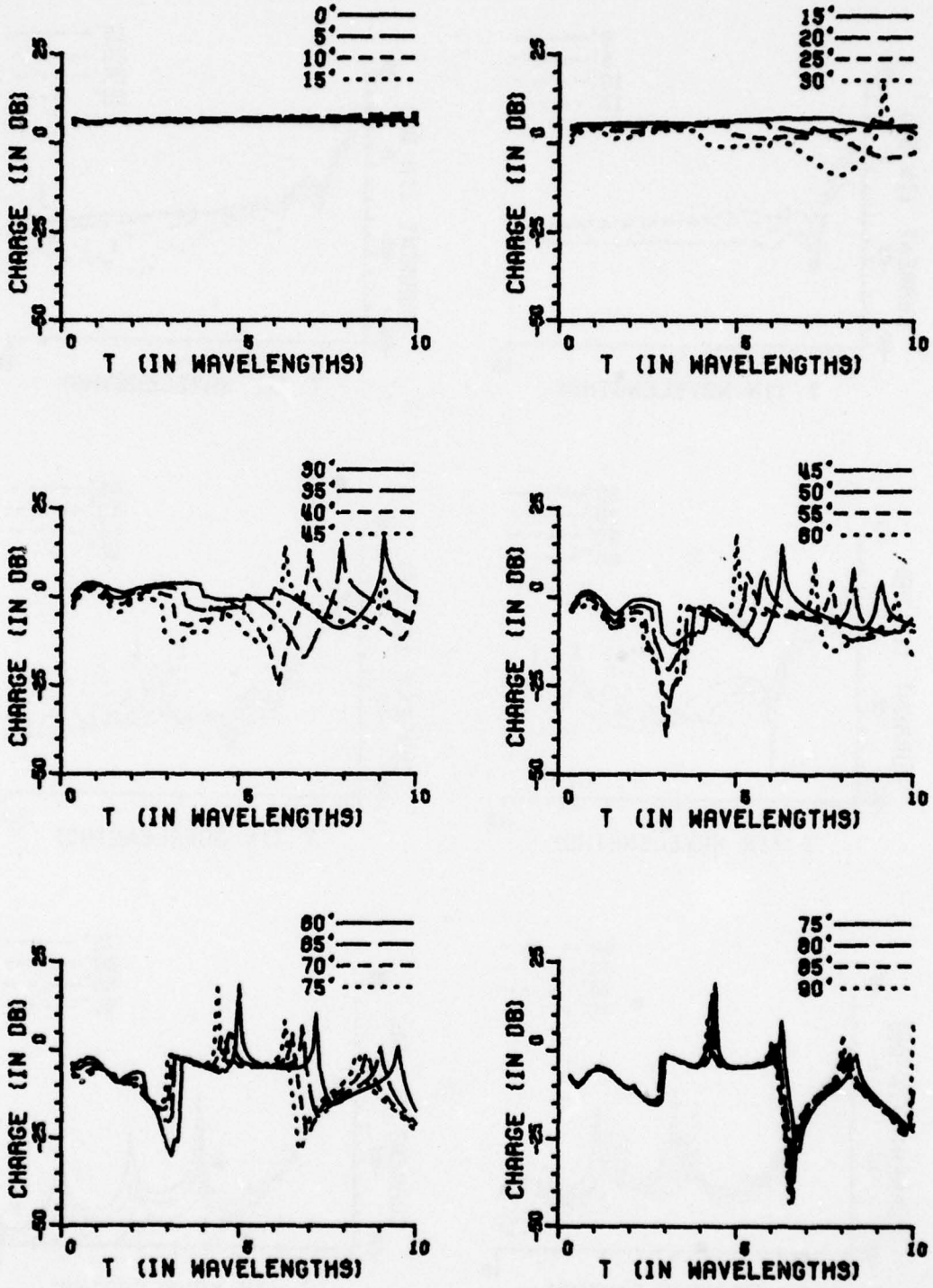

Figure 45b. Surface charge density with a=0.5 wavelength and r_1/a=4.0.

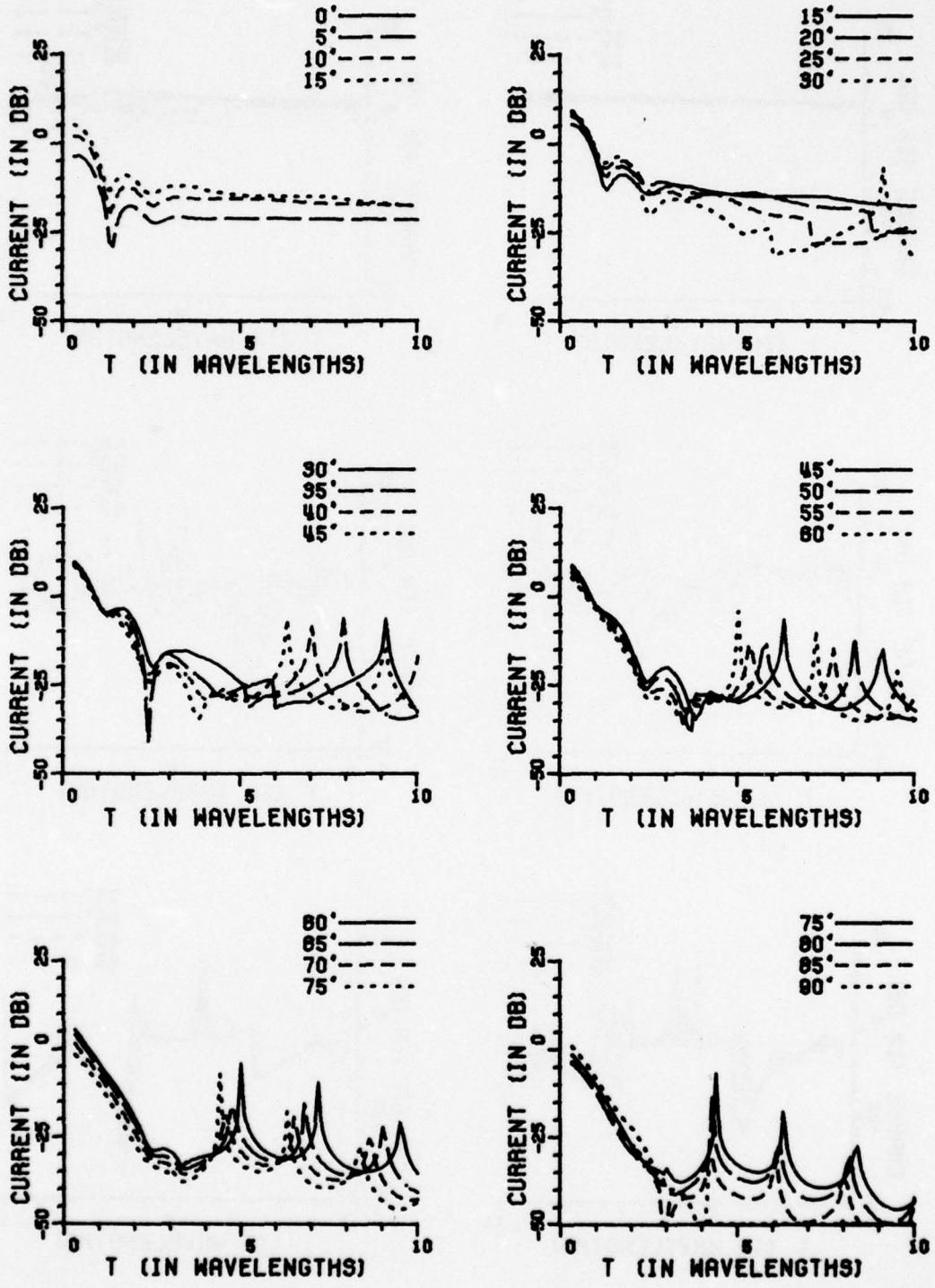

Figure 45c. Circumferential current density with a=0.5 wavelength and $r_1/a=4.0$.

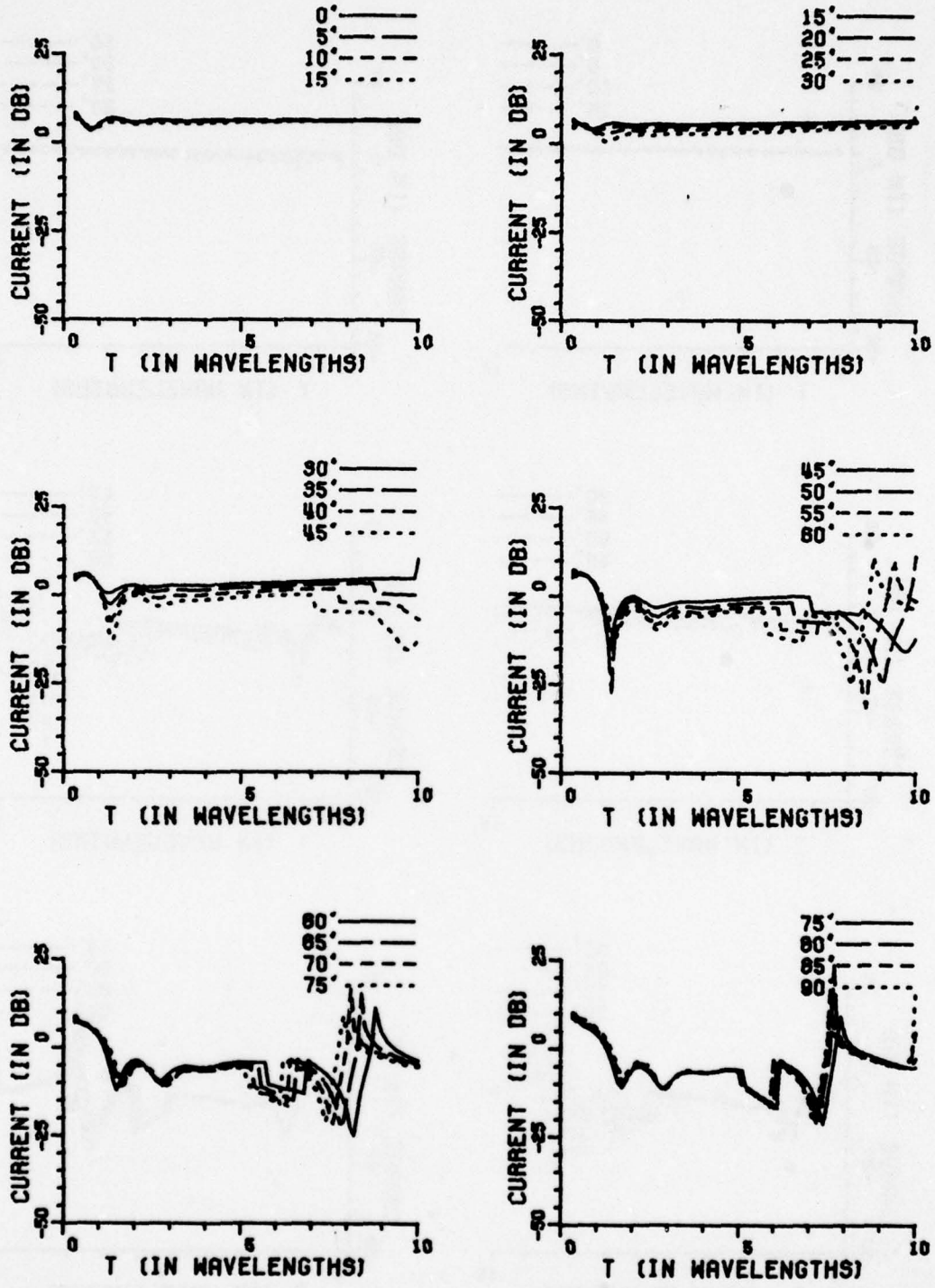

Figure 46a. Axial current density with a=0.5 wavelength and r_1/a=10.0.

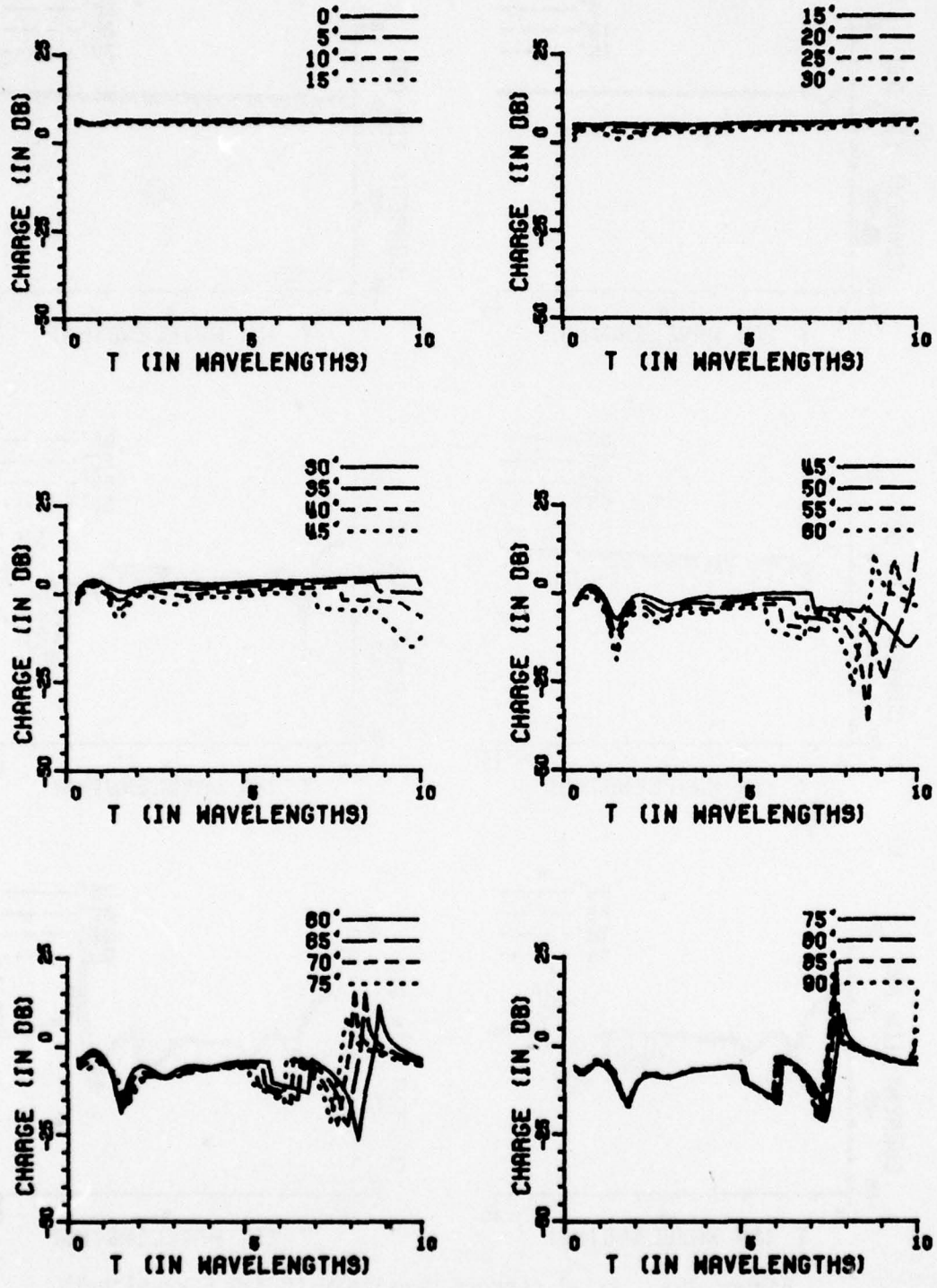

Figure 46b. Surface charge density with a=0.5 wavelength and r_1/a=10.0.

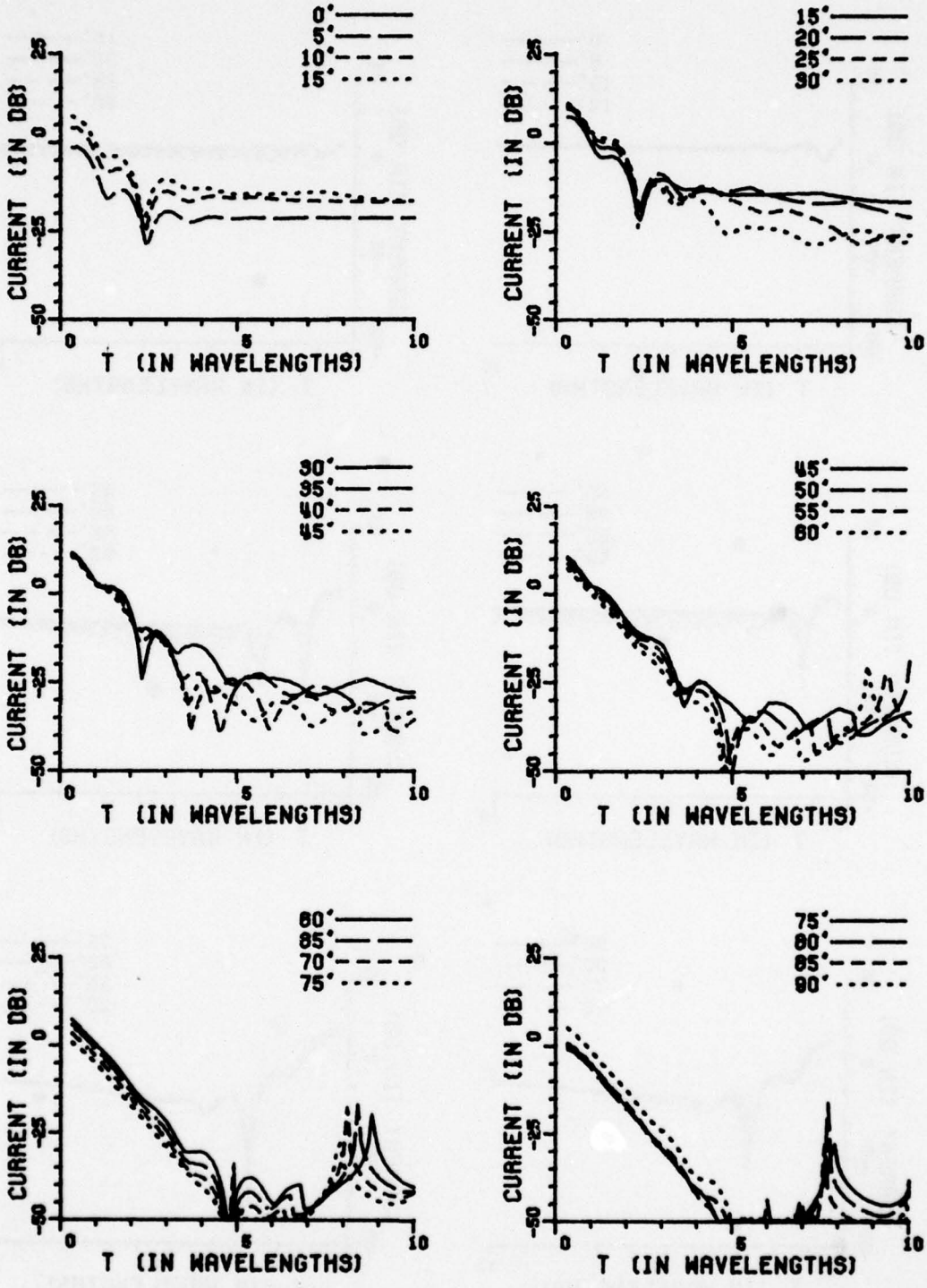

Figure 46c. Circumferential current density with a=0.5 wavelength and r_1/a=10.0.

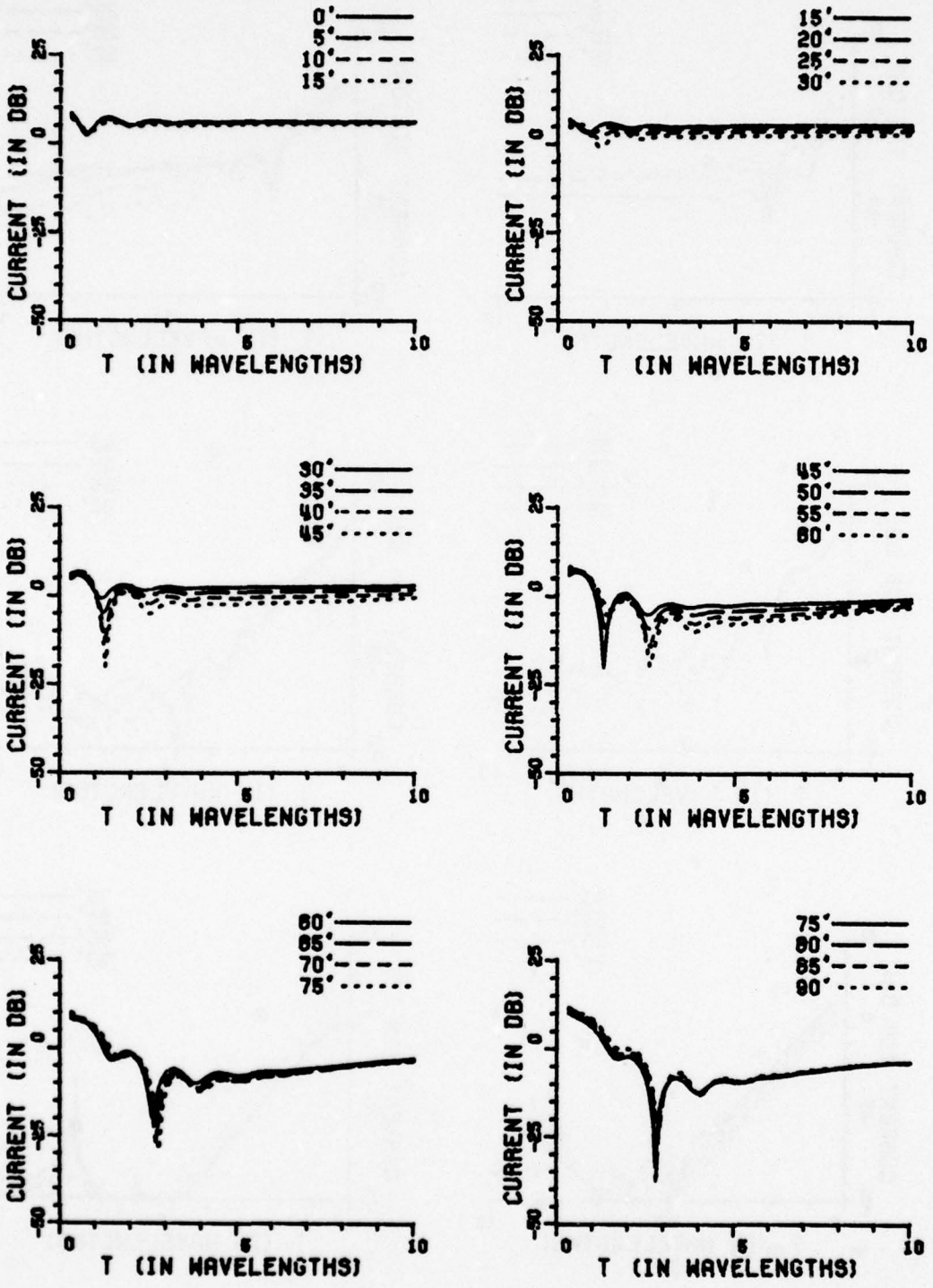

Figure 47a. Axial current density with a=0.5 wavelength and r_1/a=20.0.

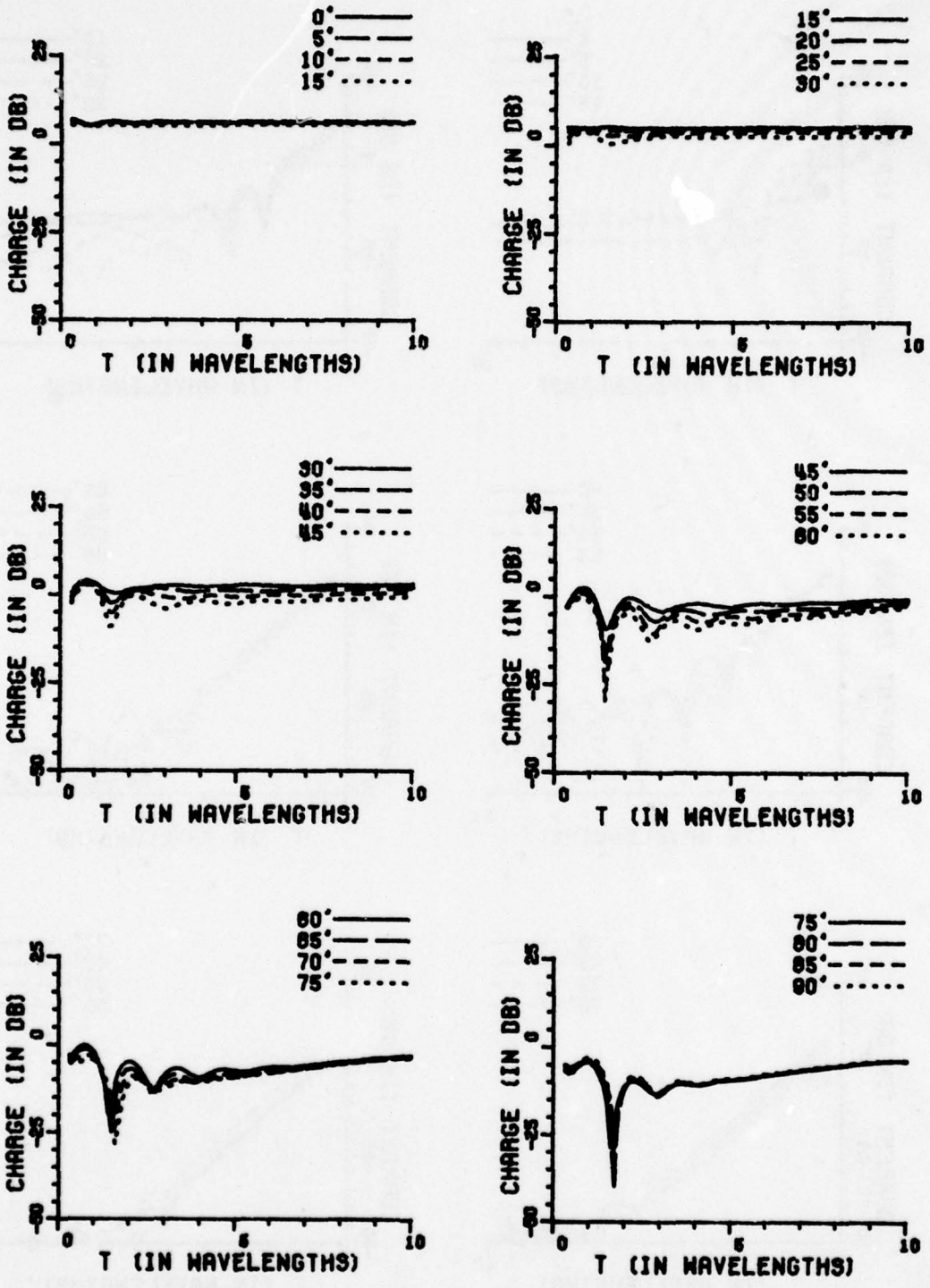

Figure 47b. Surface charge density with a=0.5 wavelength and r_1/a=20.0.

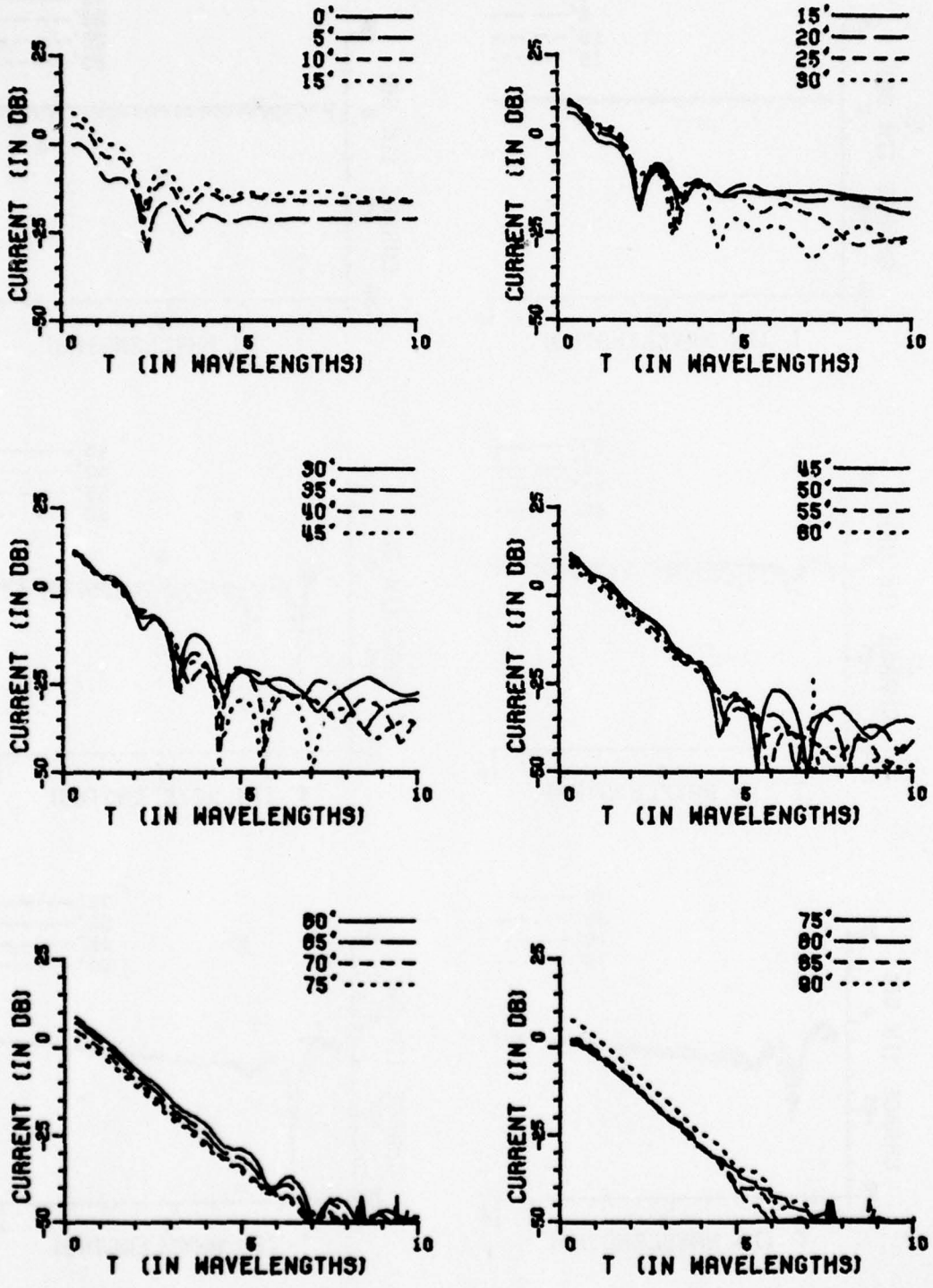

Figure 47c. Circumferential current density with a=0.5 wavelength and r_1/a=20.0.

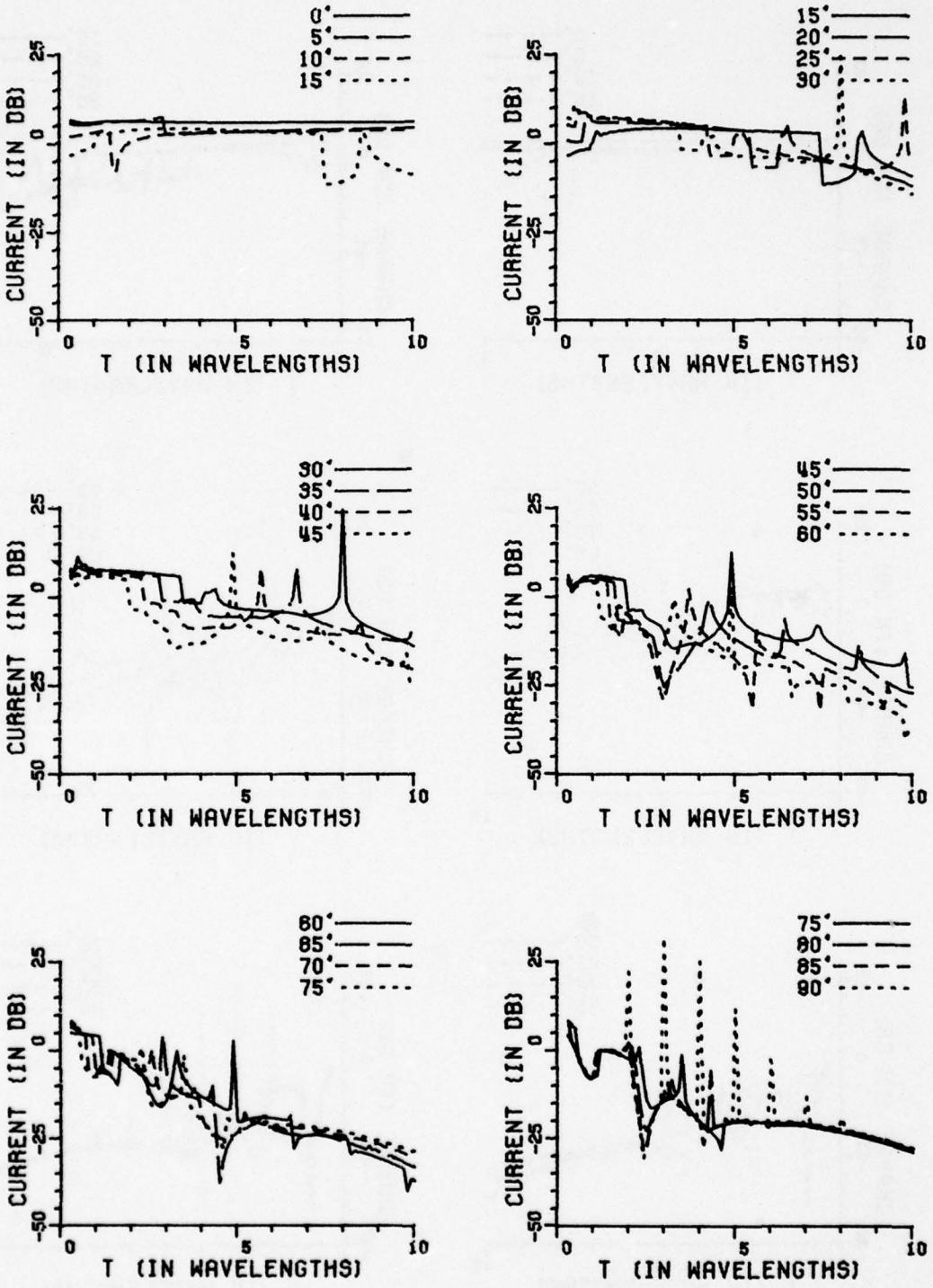

Figure 48a. Axial current density with a=1.0 wavelength and r_1/a=0.25.

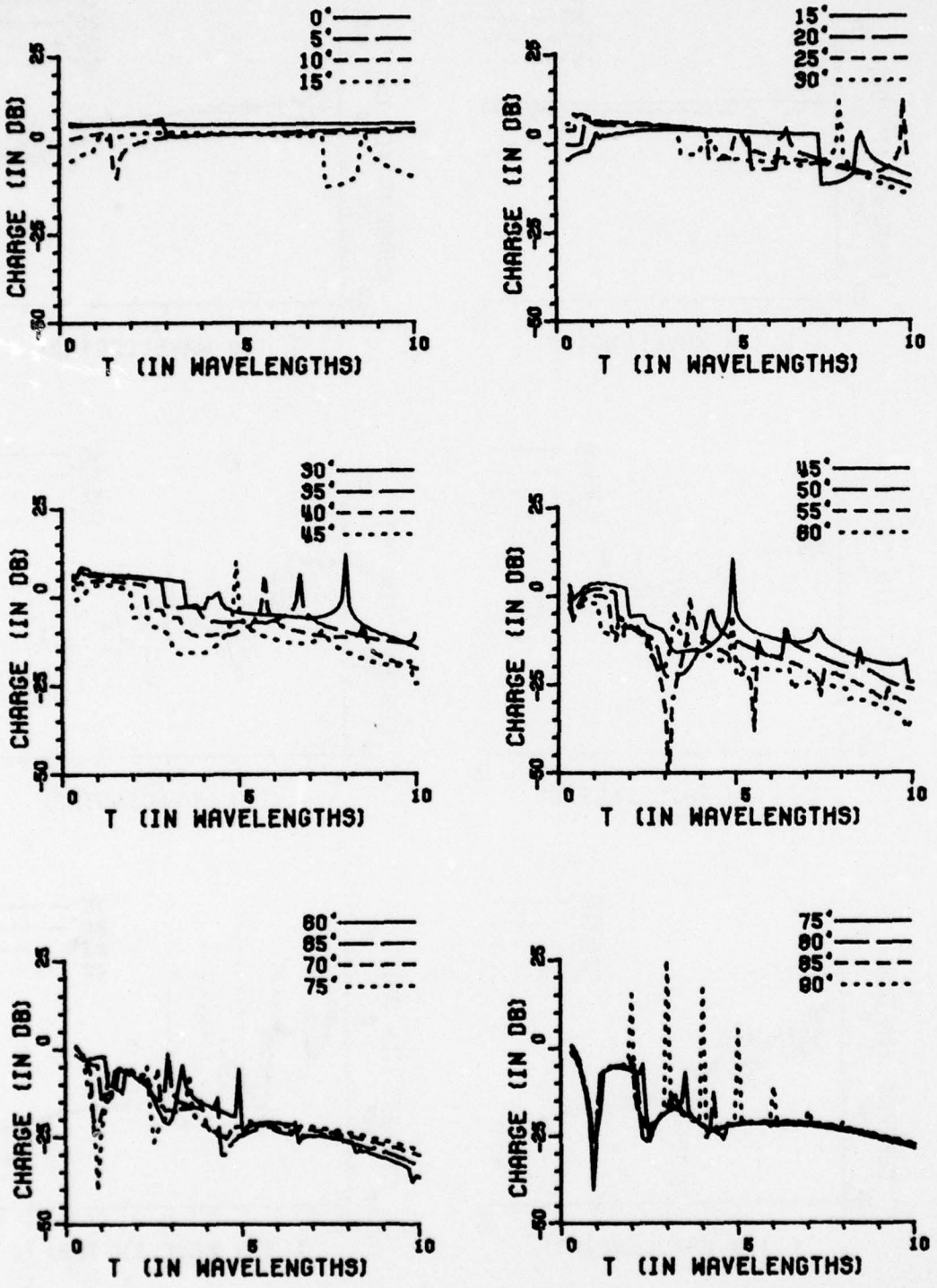

Figure 48b. Surface charge density with a=1.0 wavelength and r_1/a=0.25.

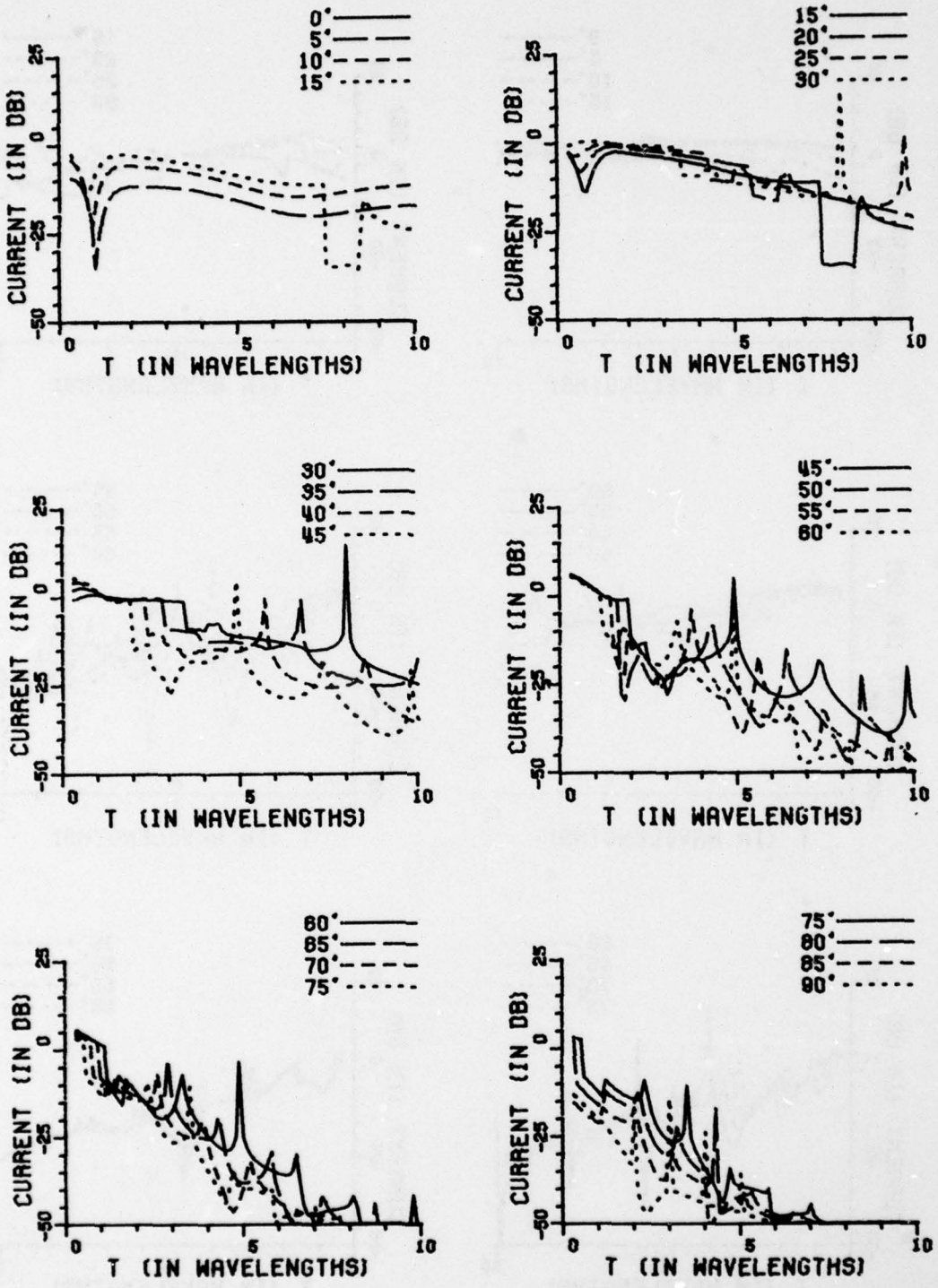

Figure 48c. Circumferential current density with a=1.0 wavelength and r_1/a=0.25.

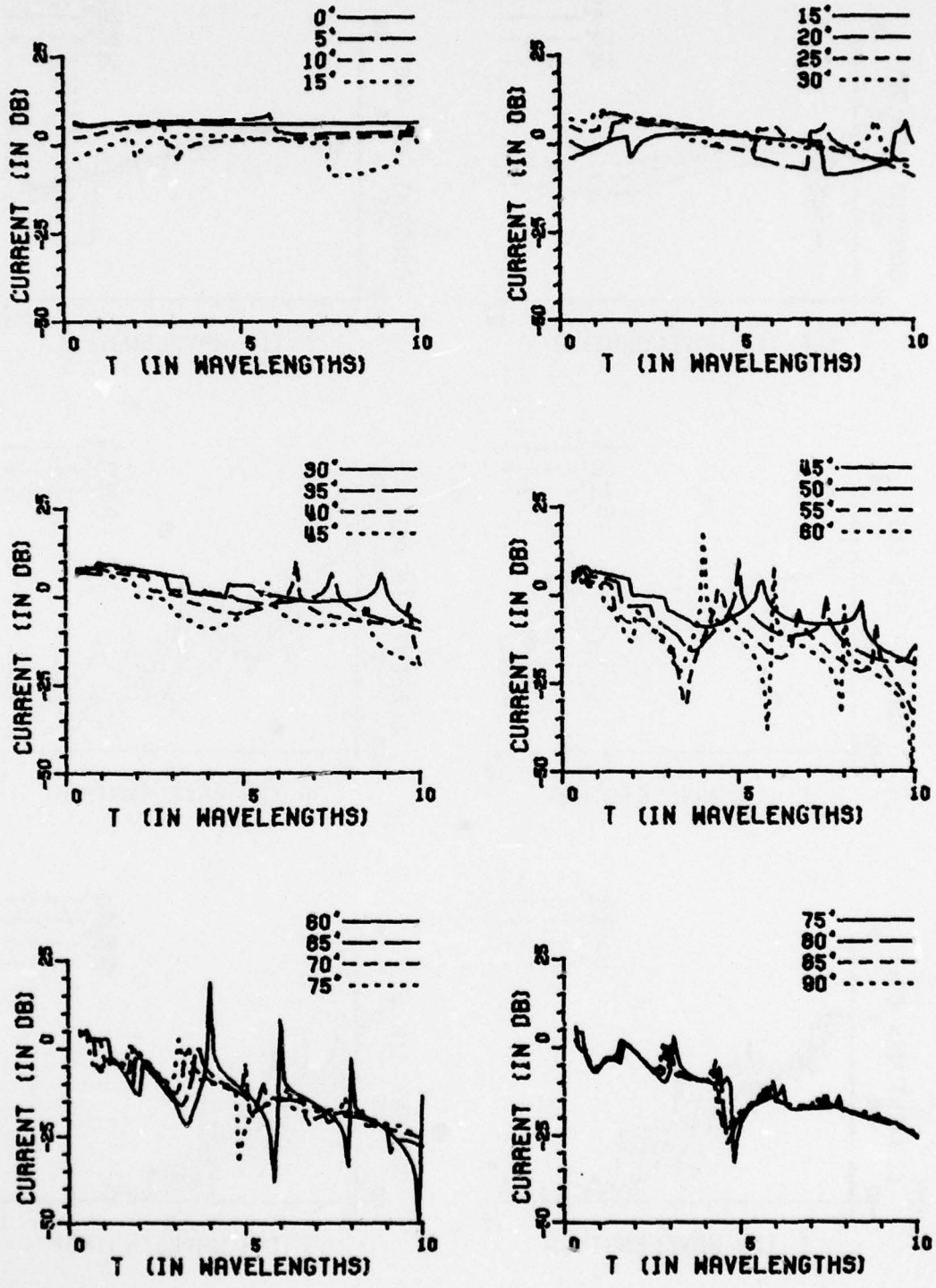

Figure 49a. Axial current density with a=1.0 wavelength and r_1/a=0.5.

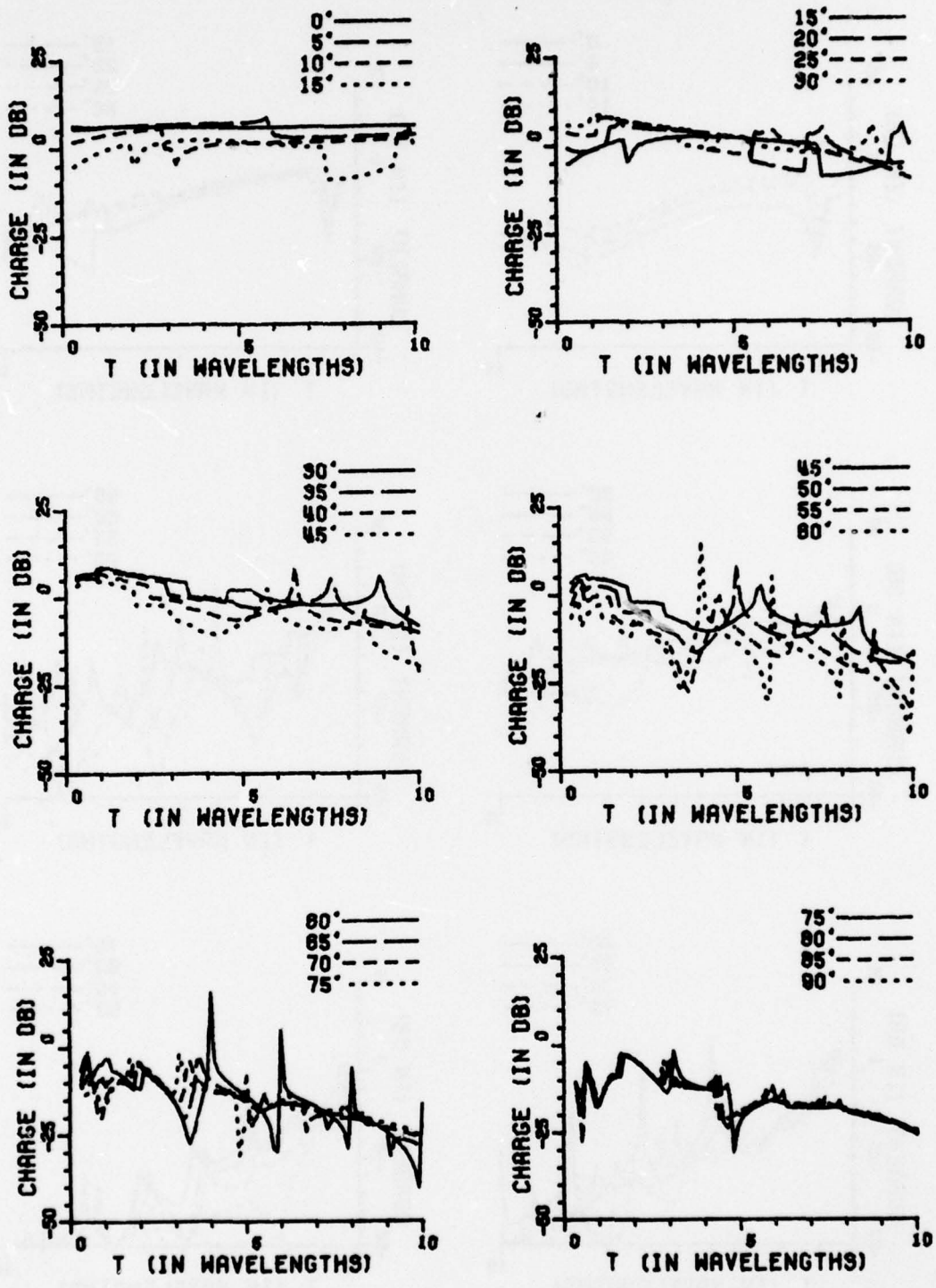

Figure 49b. Surface charge density with a=1.0 wavelength and r_1/a=0.5.

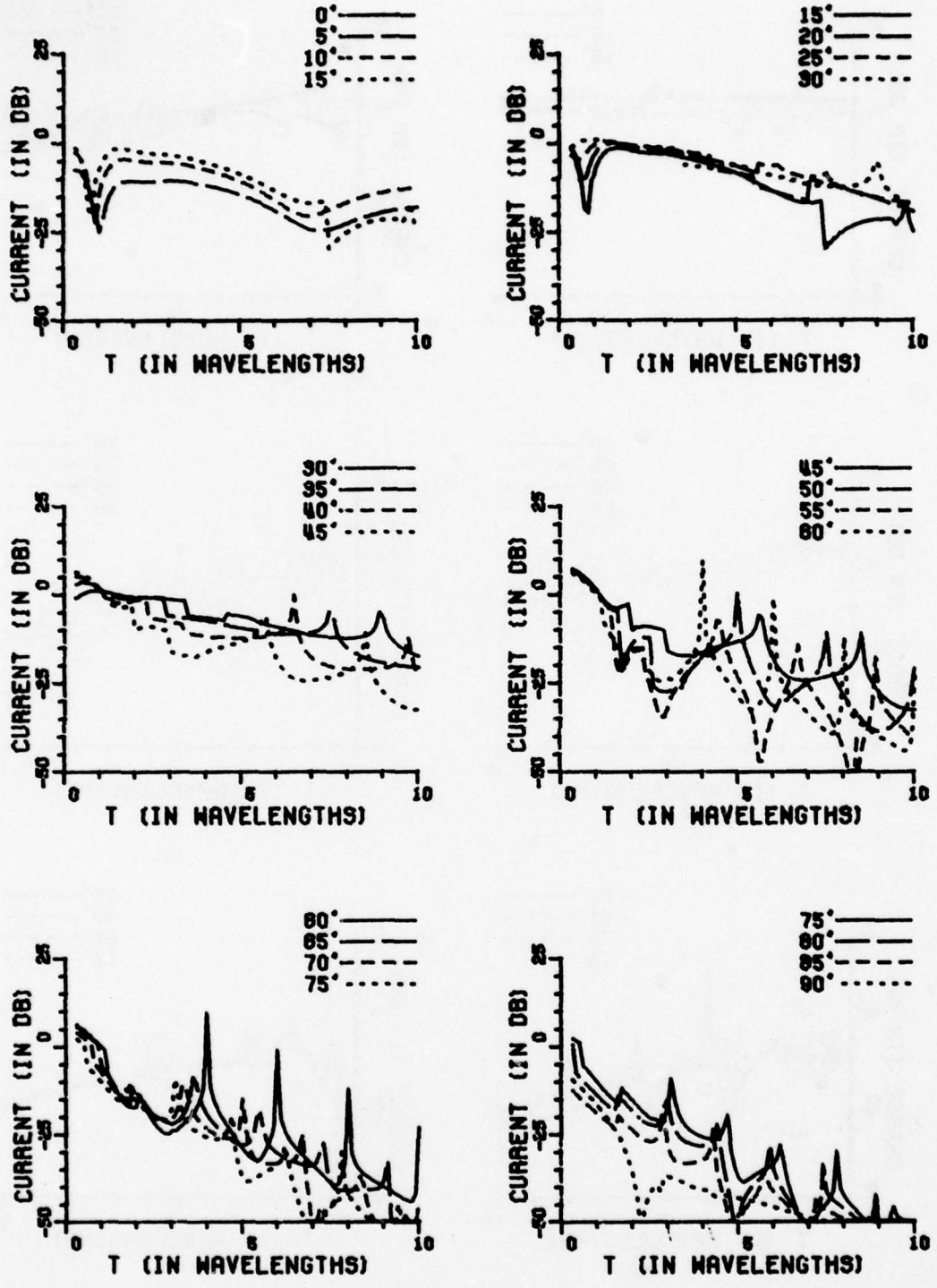

Figure 49c. Circumferential current density with a=1.0 wavelength and $r_1/a=0.5$.

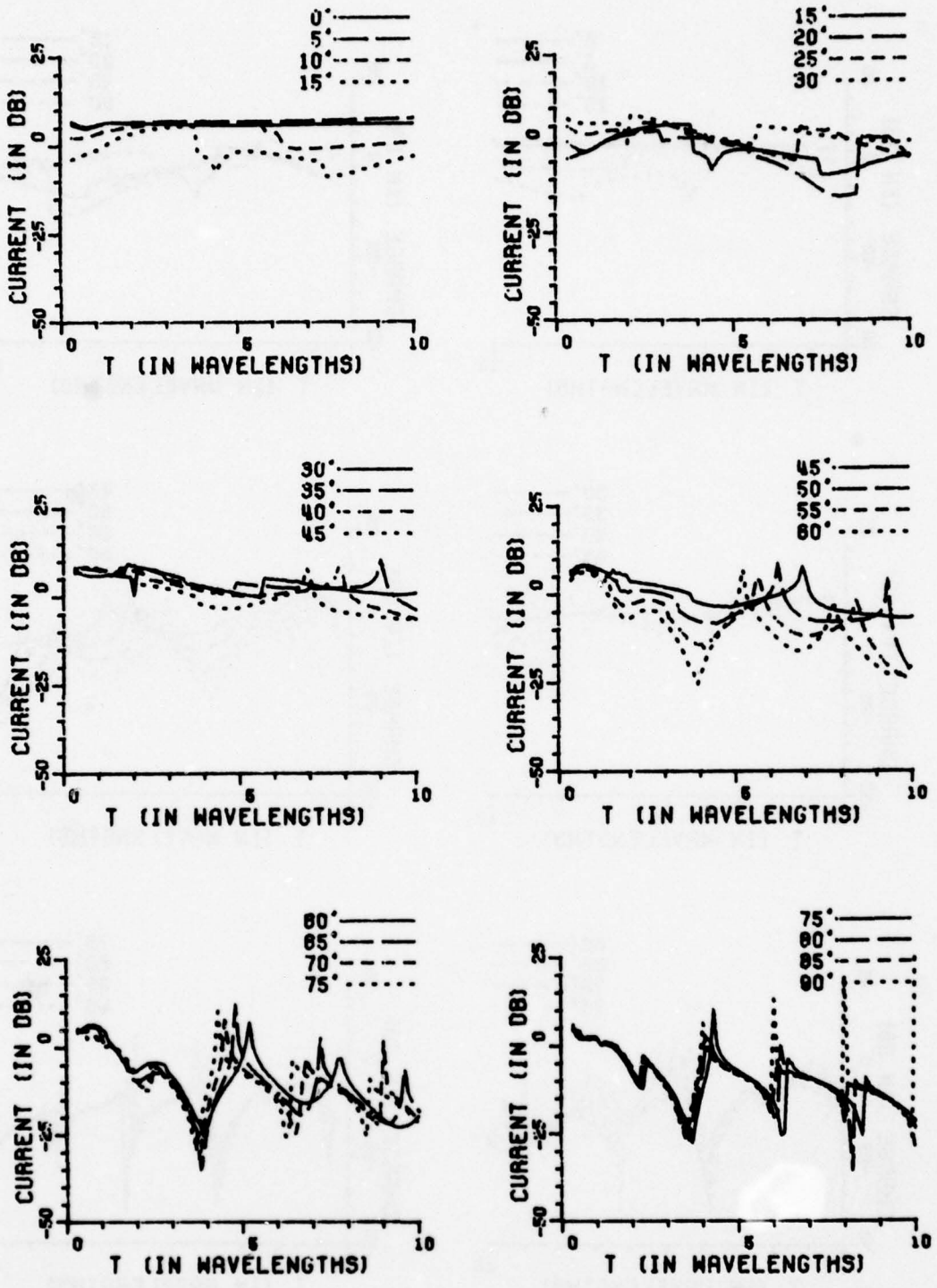

Figure 50a. Axial current density with a=1.0 wavelength and r_1/a=1.0.

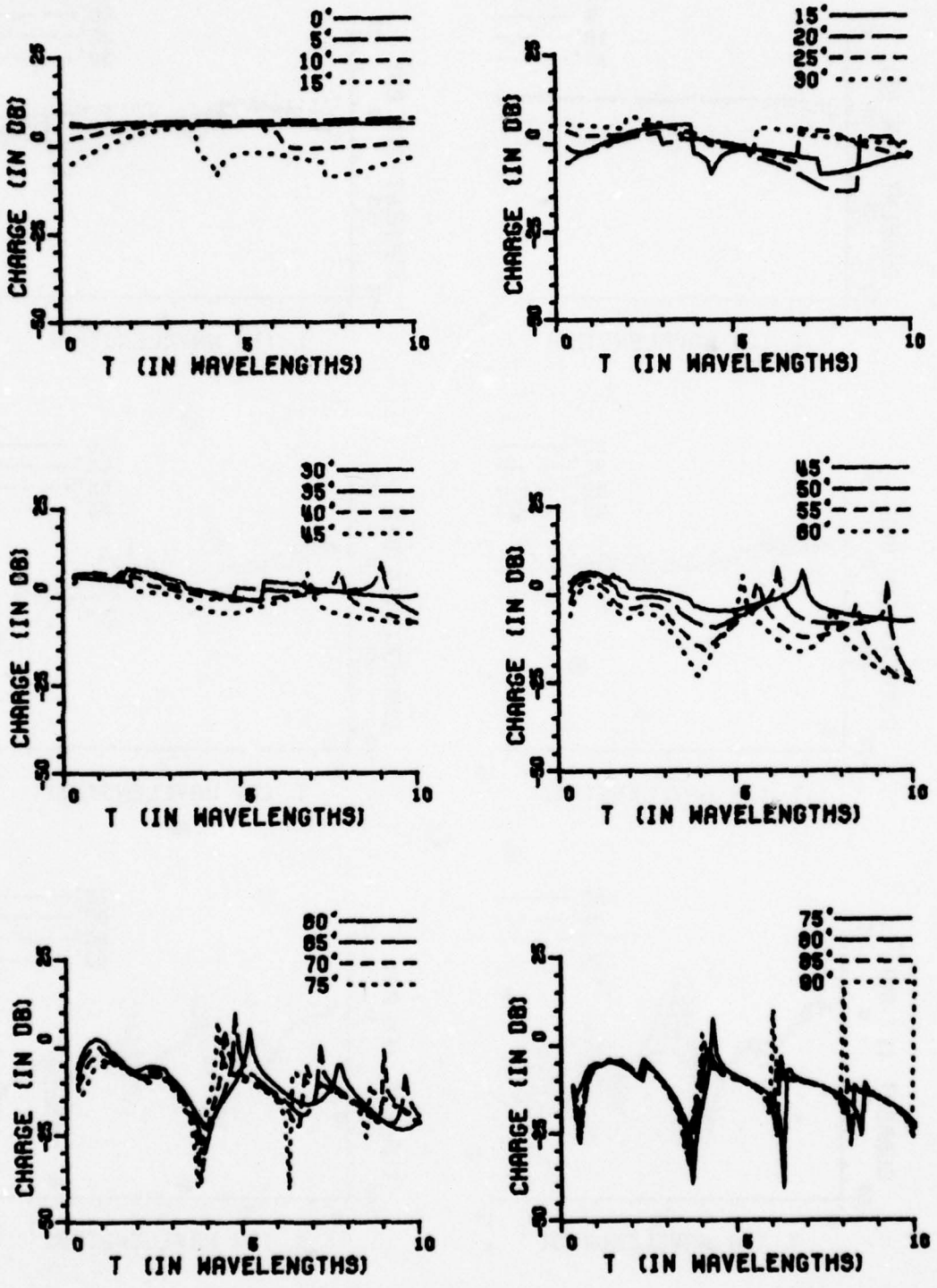

Figure 50b. Surface charge density with a=1.0 wavelength and $r_1/a=1.0$.

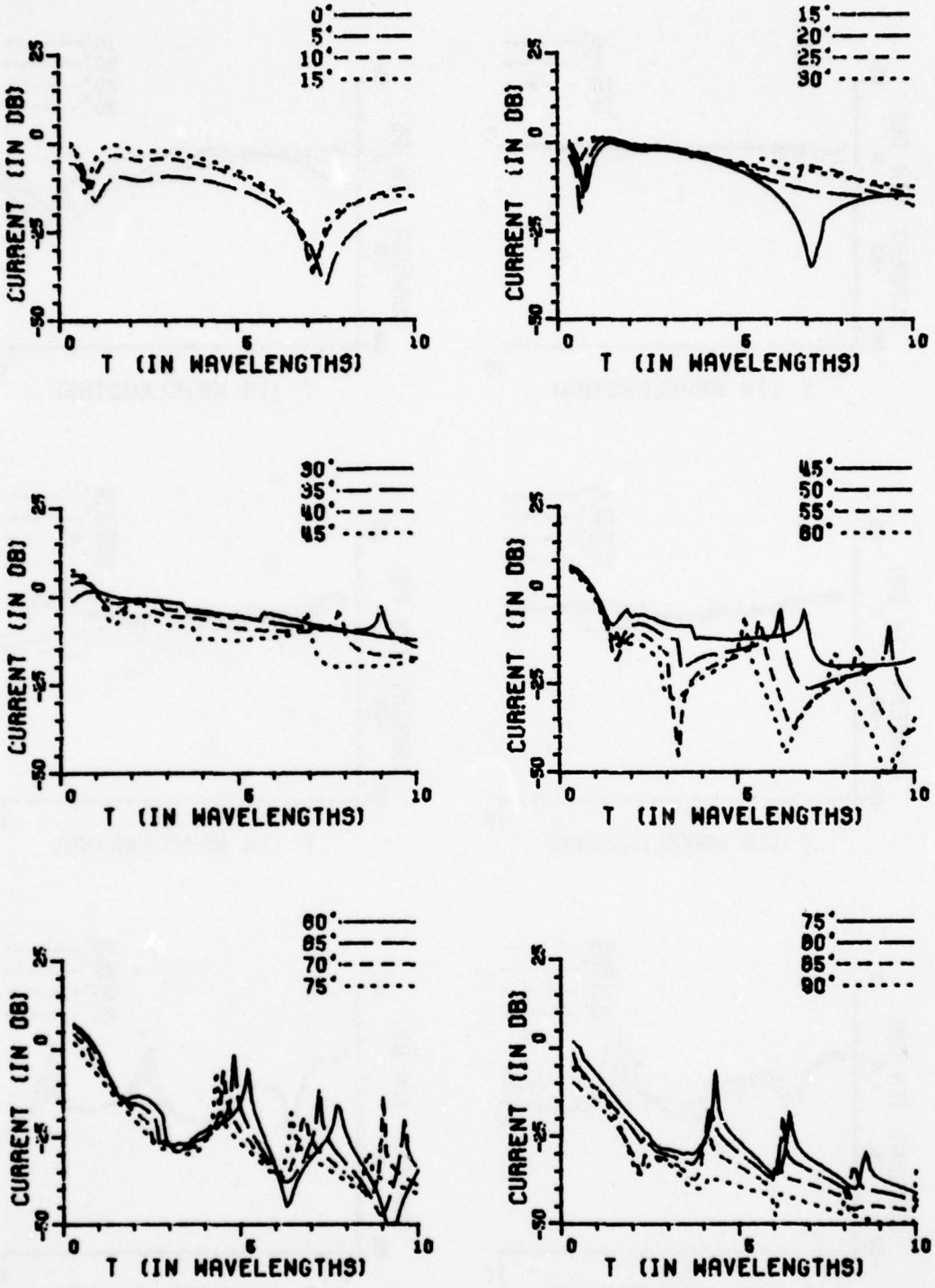

Figure 50c. Circumferential current density with a=1.0 wavelength and r_1/a=1.0.

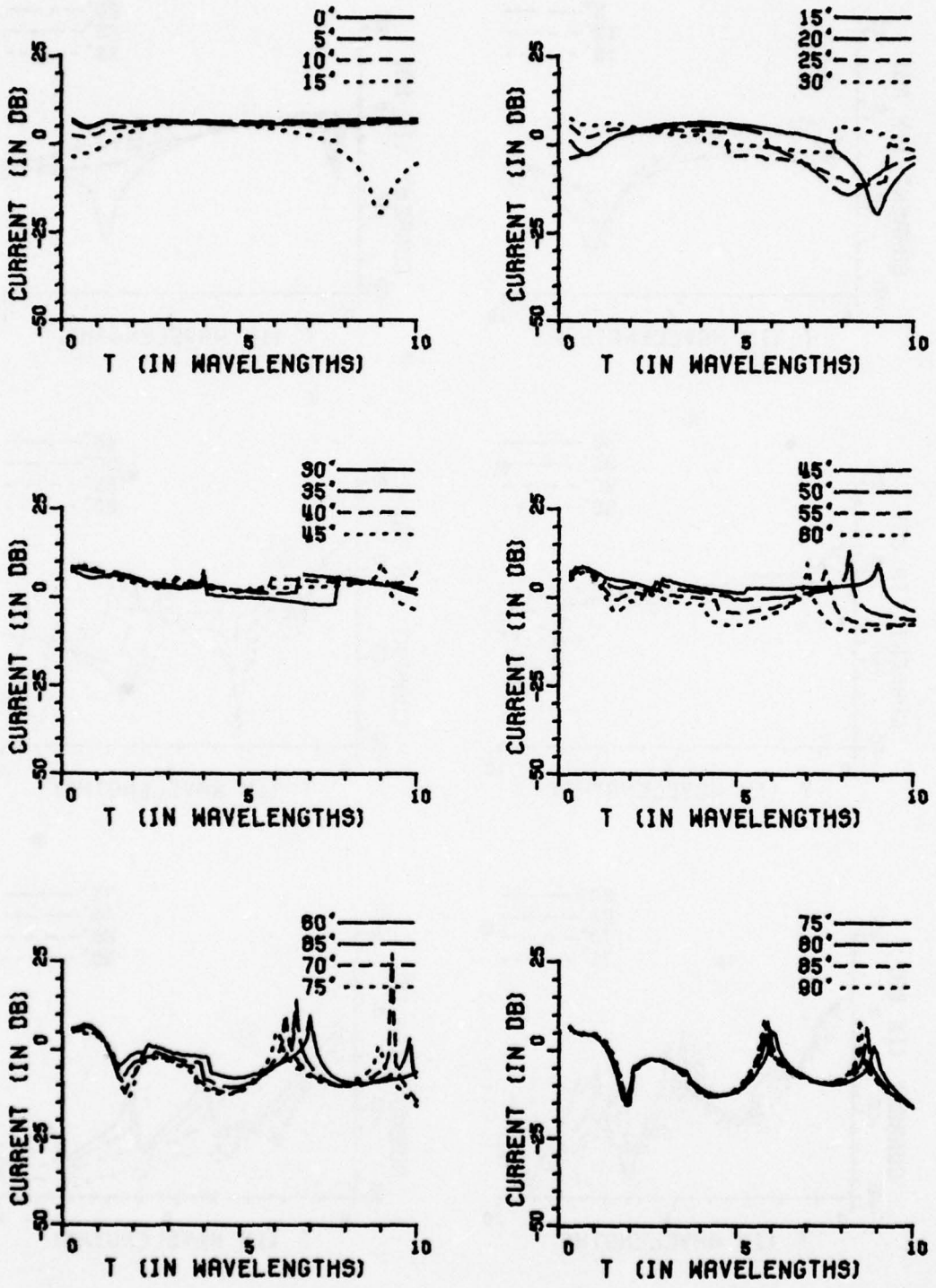

Figure 51a. Axial current density with a=1.0 wavelength and $r_1/a=2.0$.

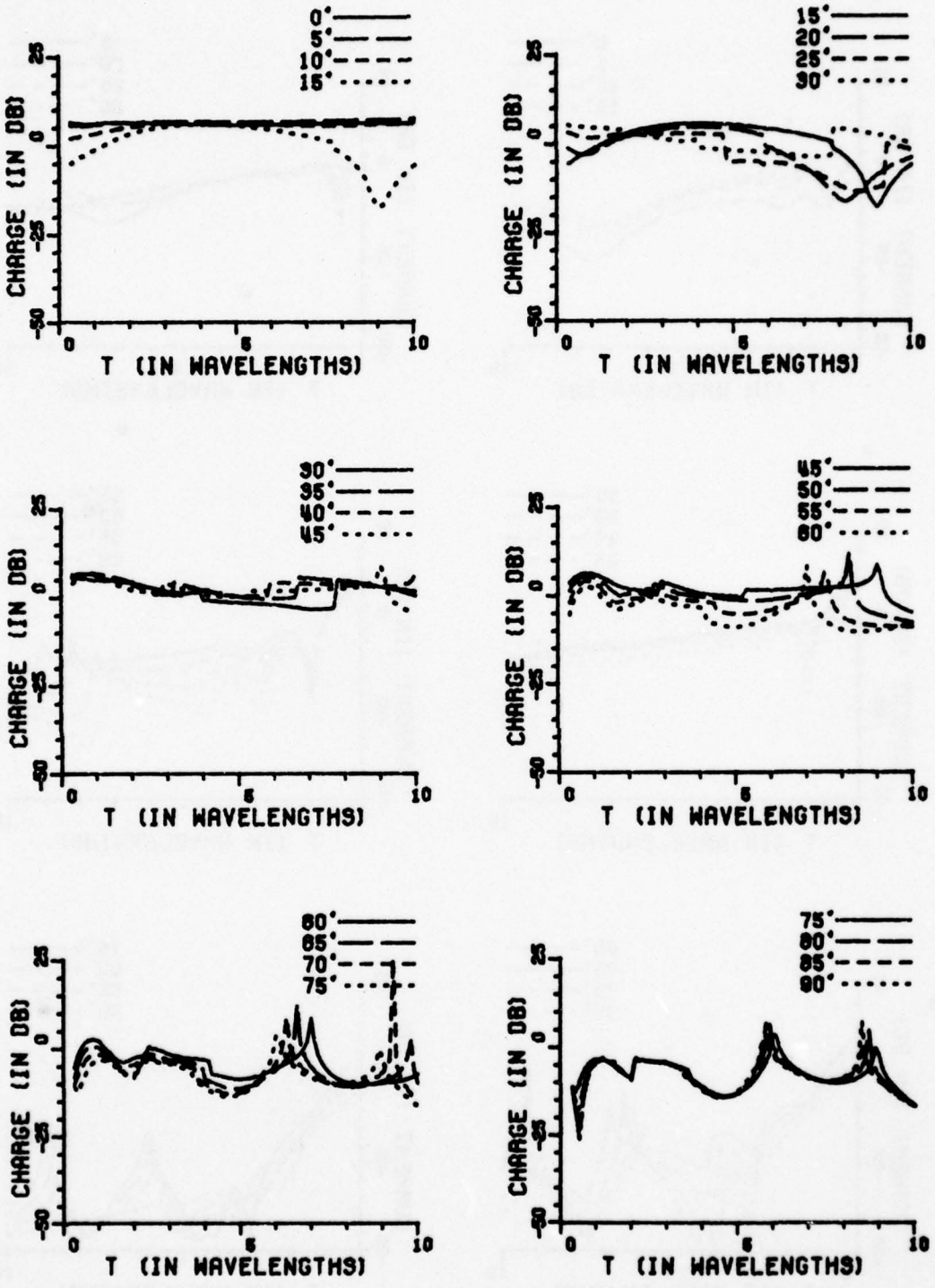

Figure 51b. Surface charge density with a=1.0 wavelength and r_1/a=2.0.

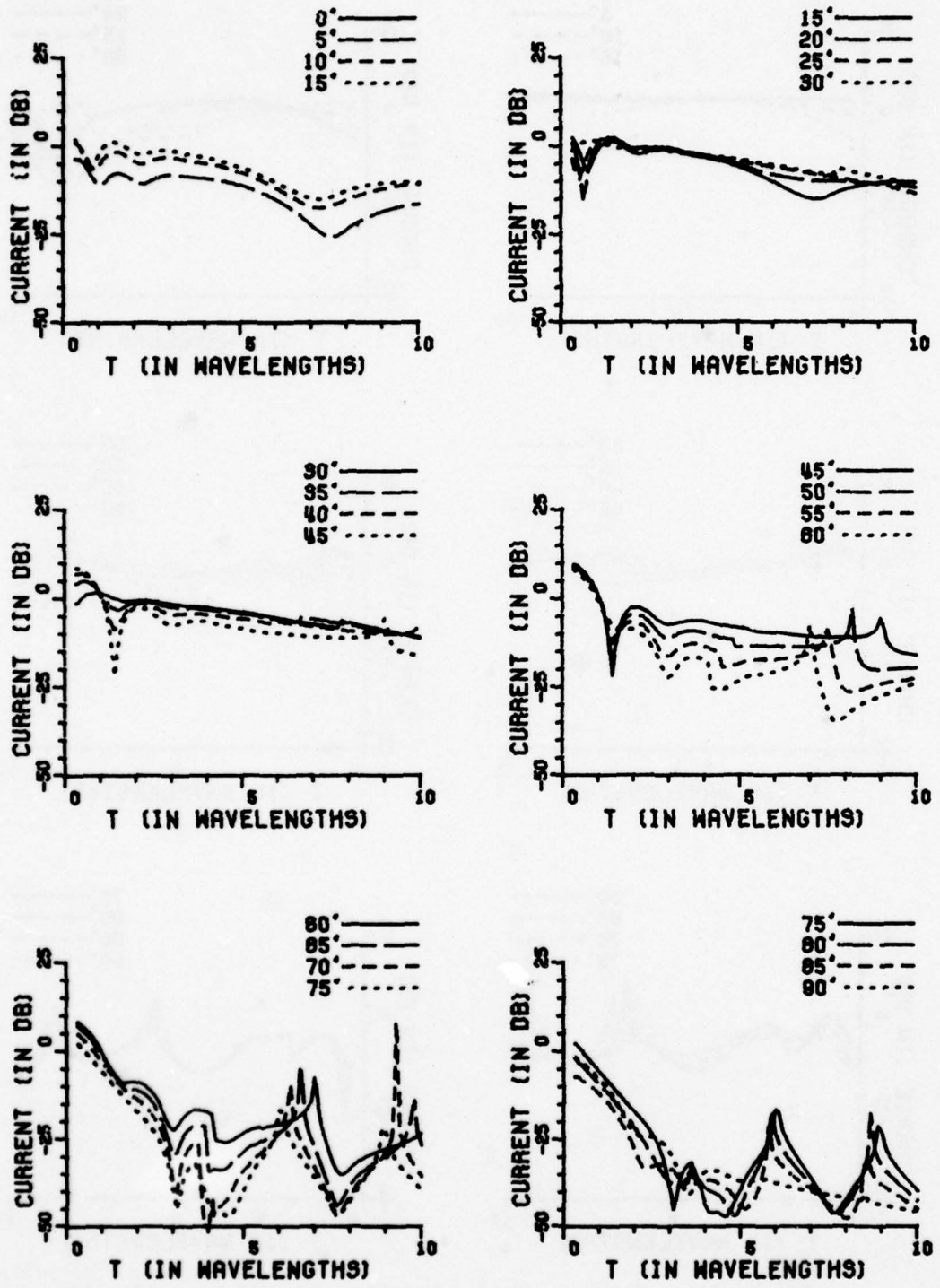

Figure 51c. Circumferential current density with a=1.0 wavelength and $r_1/a=2.0$.

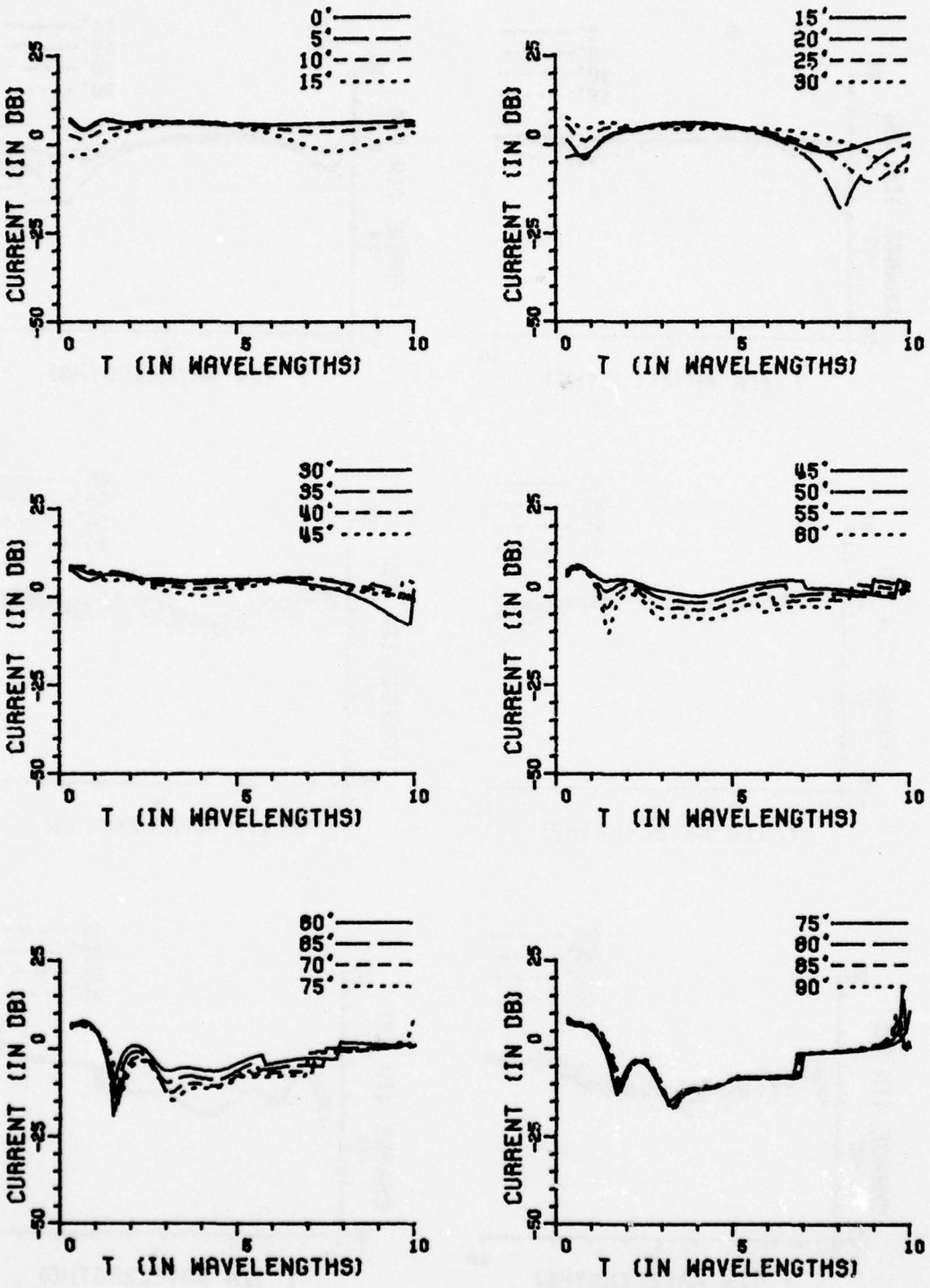

Figure 52a. Axial current density with a=1.0 wavelength and r_1/a=5.0.

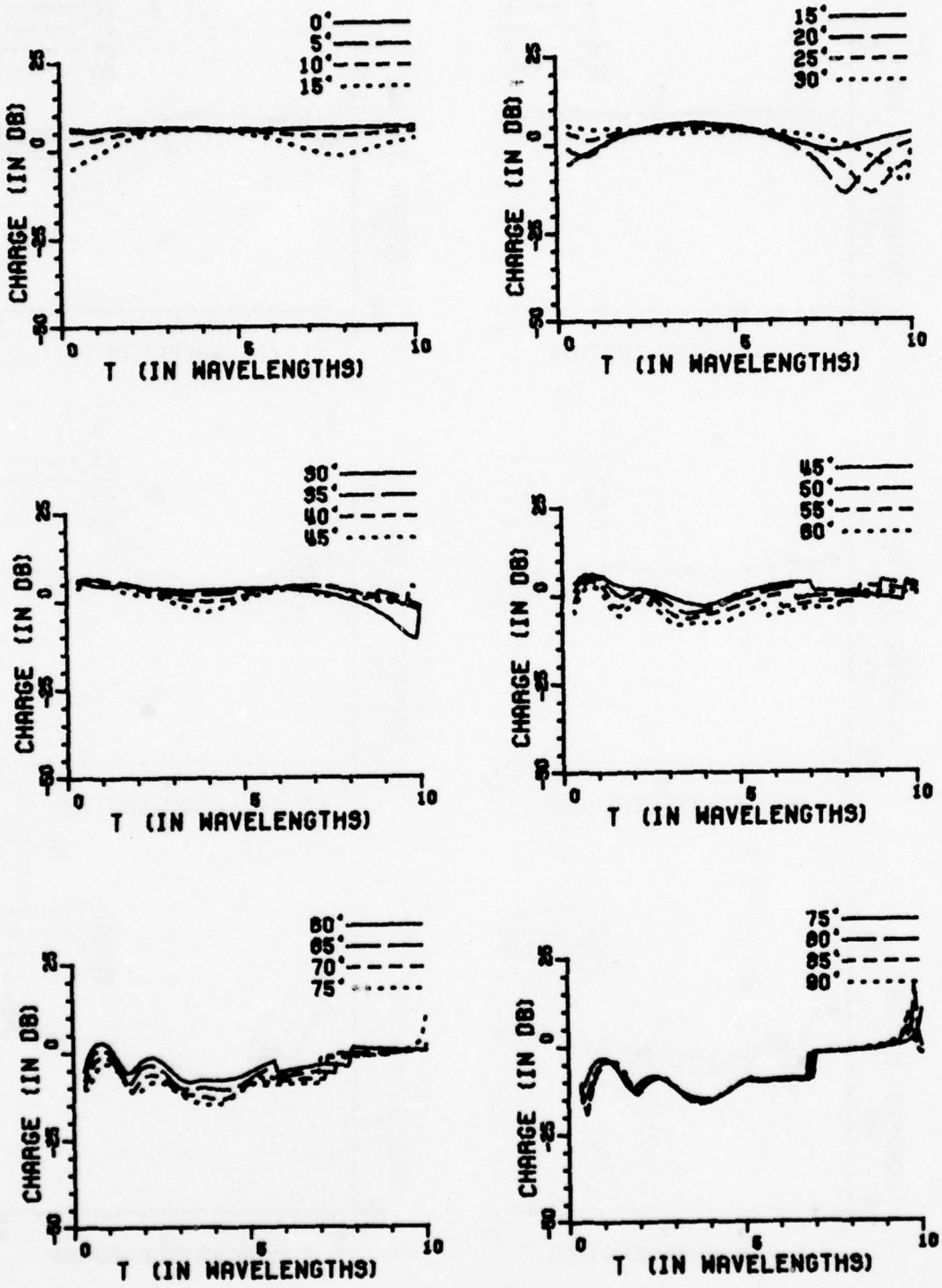

Figure 52b. Surface charge density with a=1.0 wavelength and $r_1/a=5.0$.

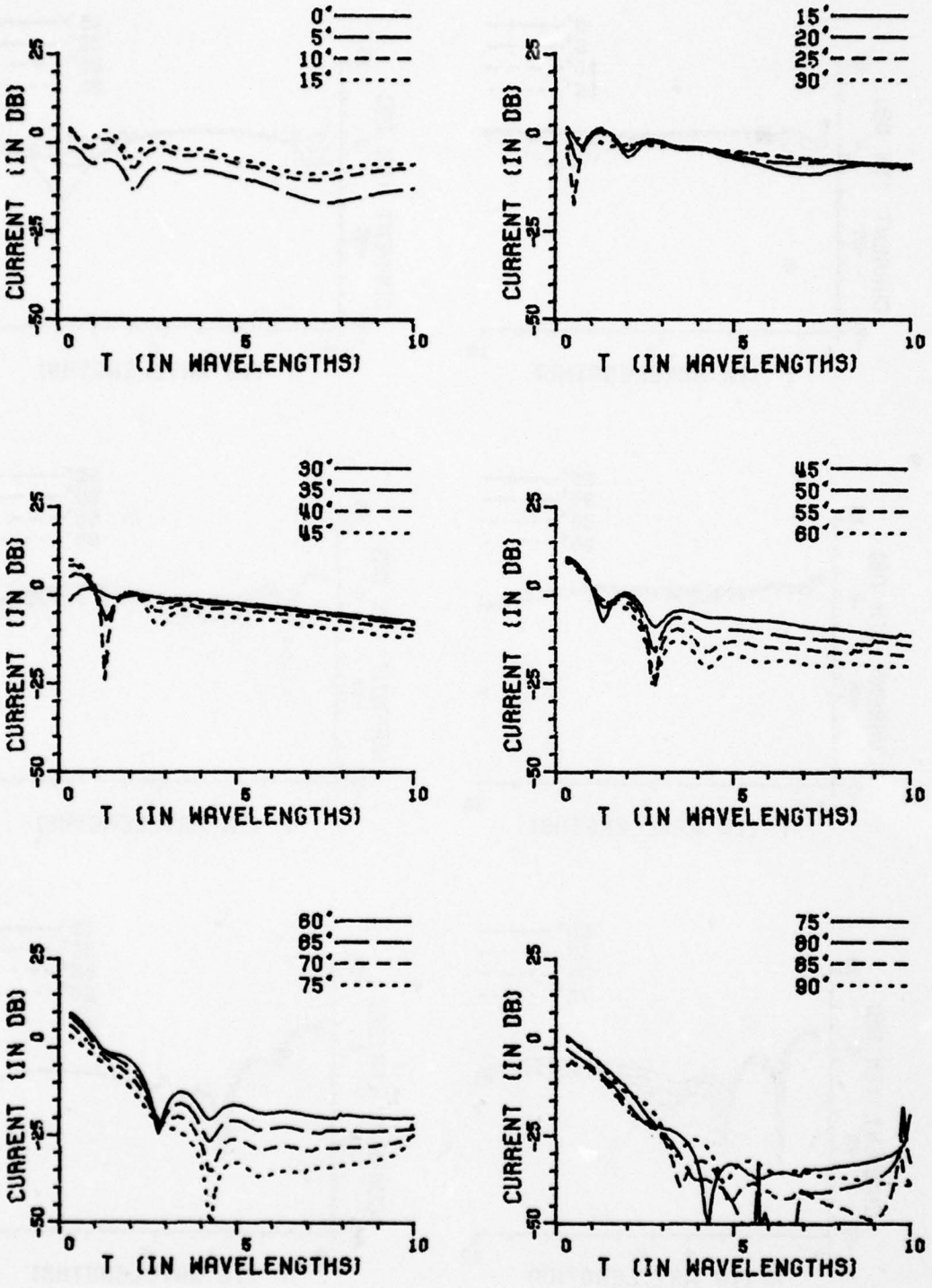

Figure 52c. Circumferential current density with a=1.0 wavelength and r_1/a=5.0.

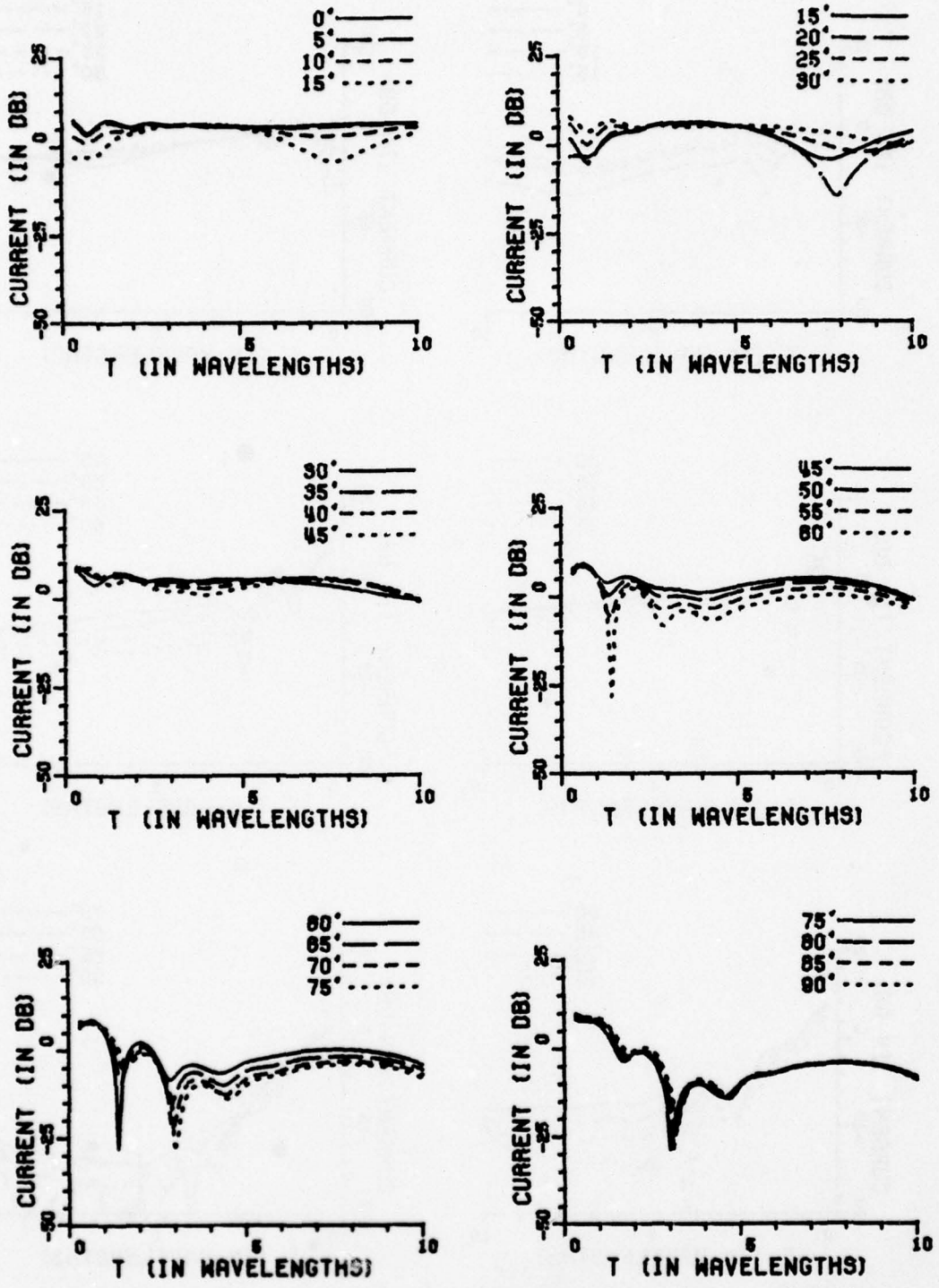

Figure 53a. Axial current density with a=1.0 wavelength and r_1/a=10.0.

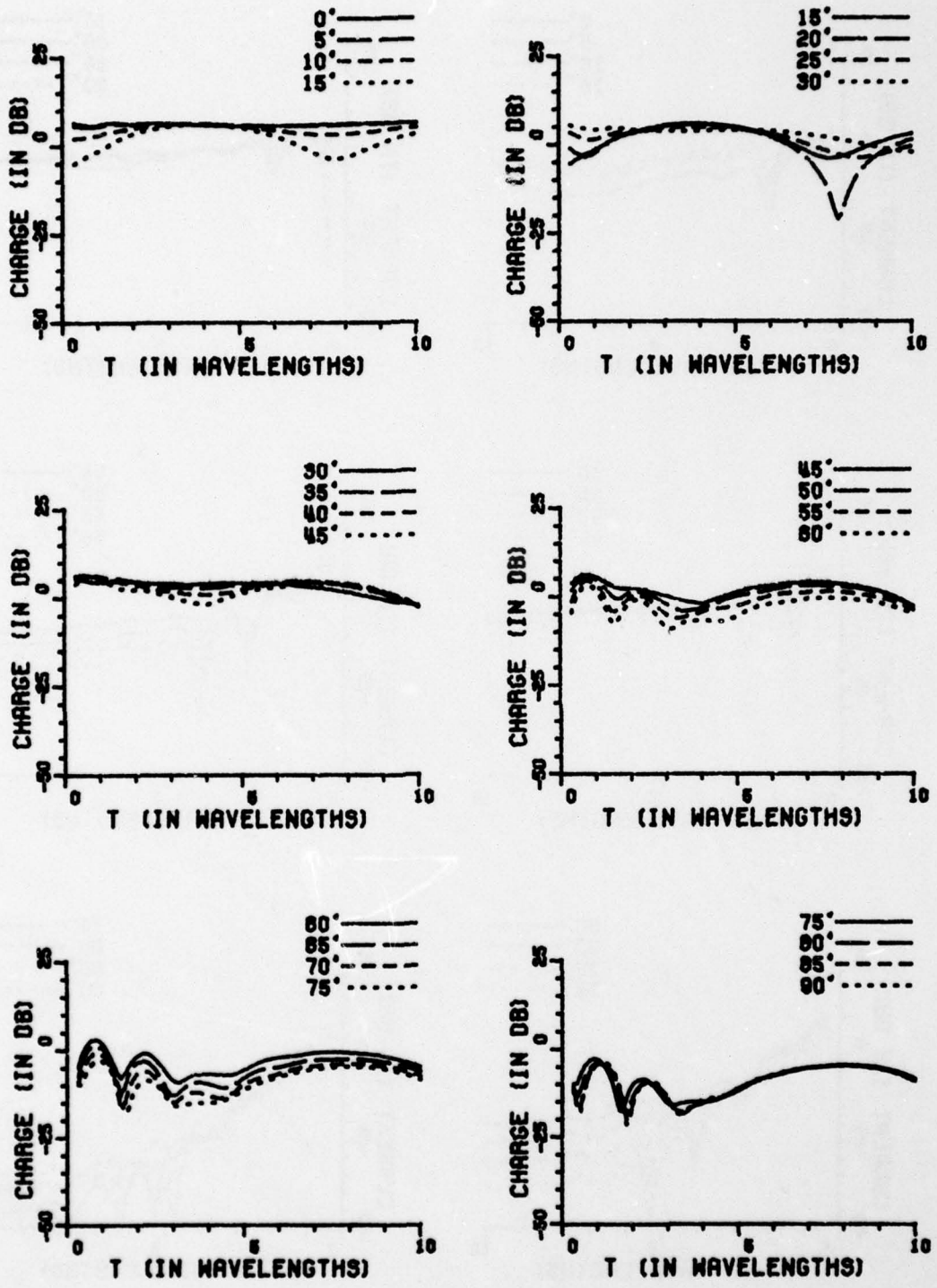

Figure 53b. Surface charge density with a=1.0 wavelength and r_1/a=10.0.

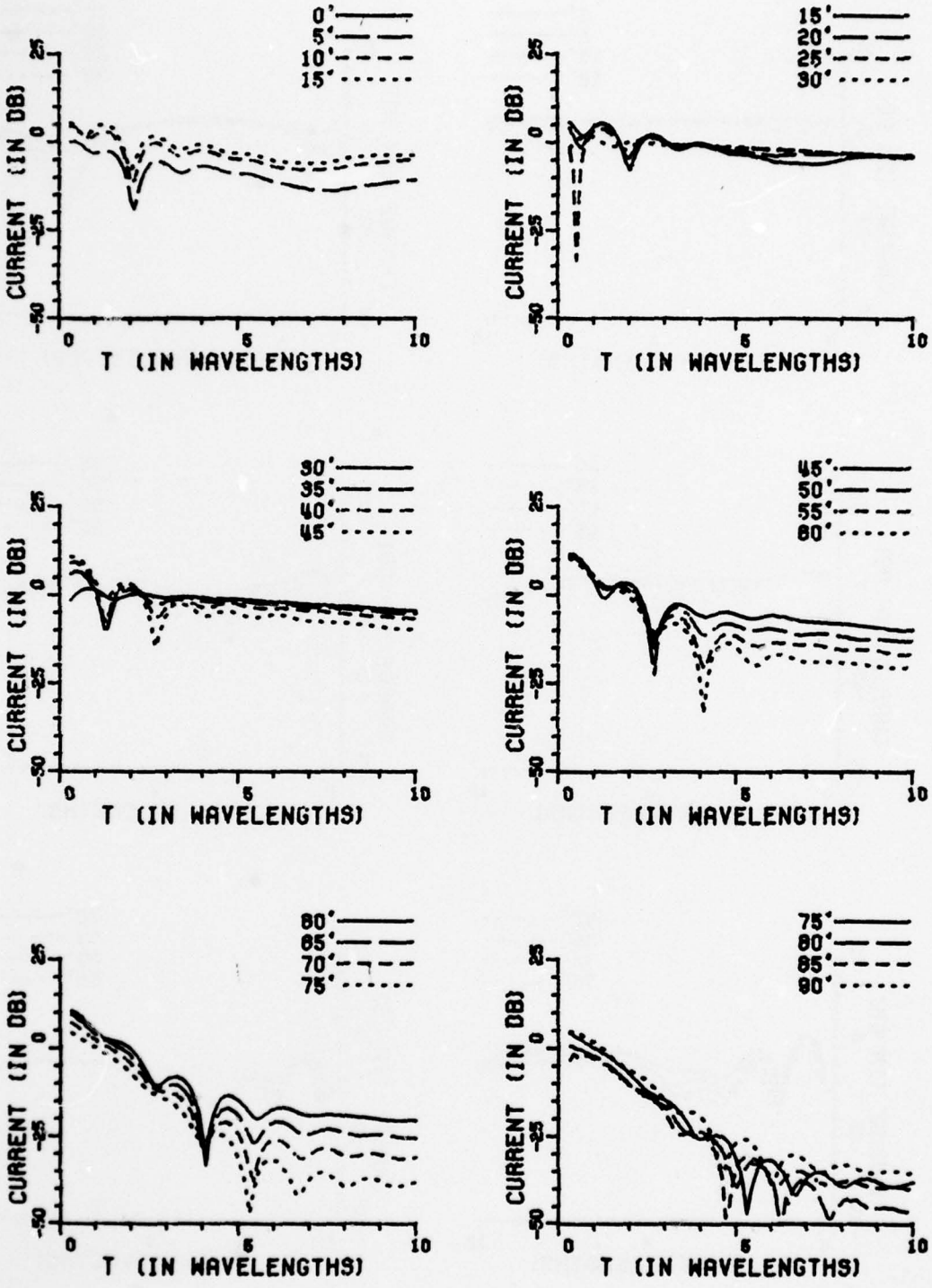

Figure 53c. Circumferential current density with a=1.0 wavelength and r_1/a=10.0.

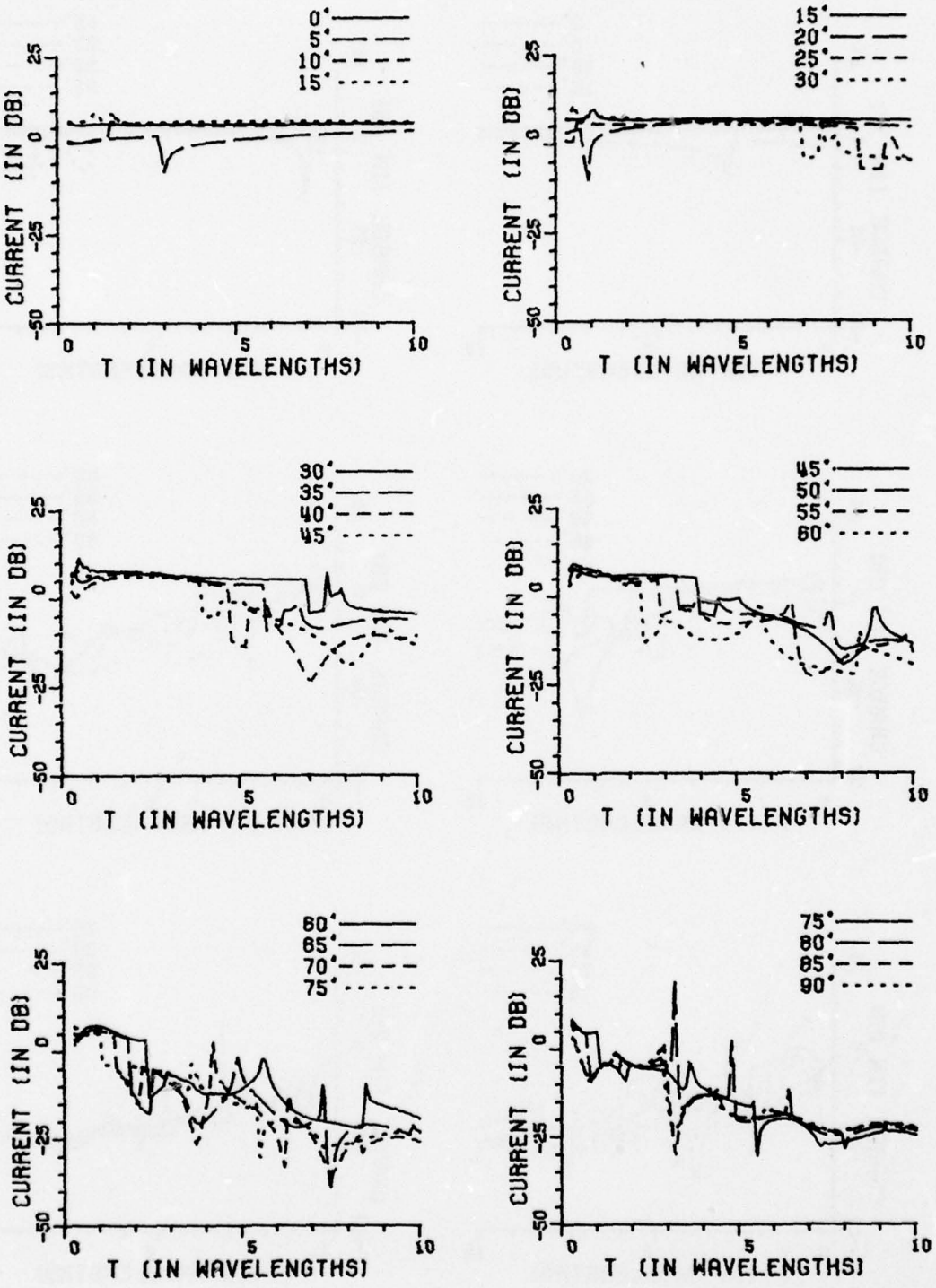

Figure 54a. Axial current density with a=2.0 wavelength and r_1/a=0.125.

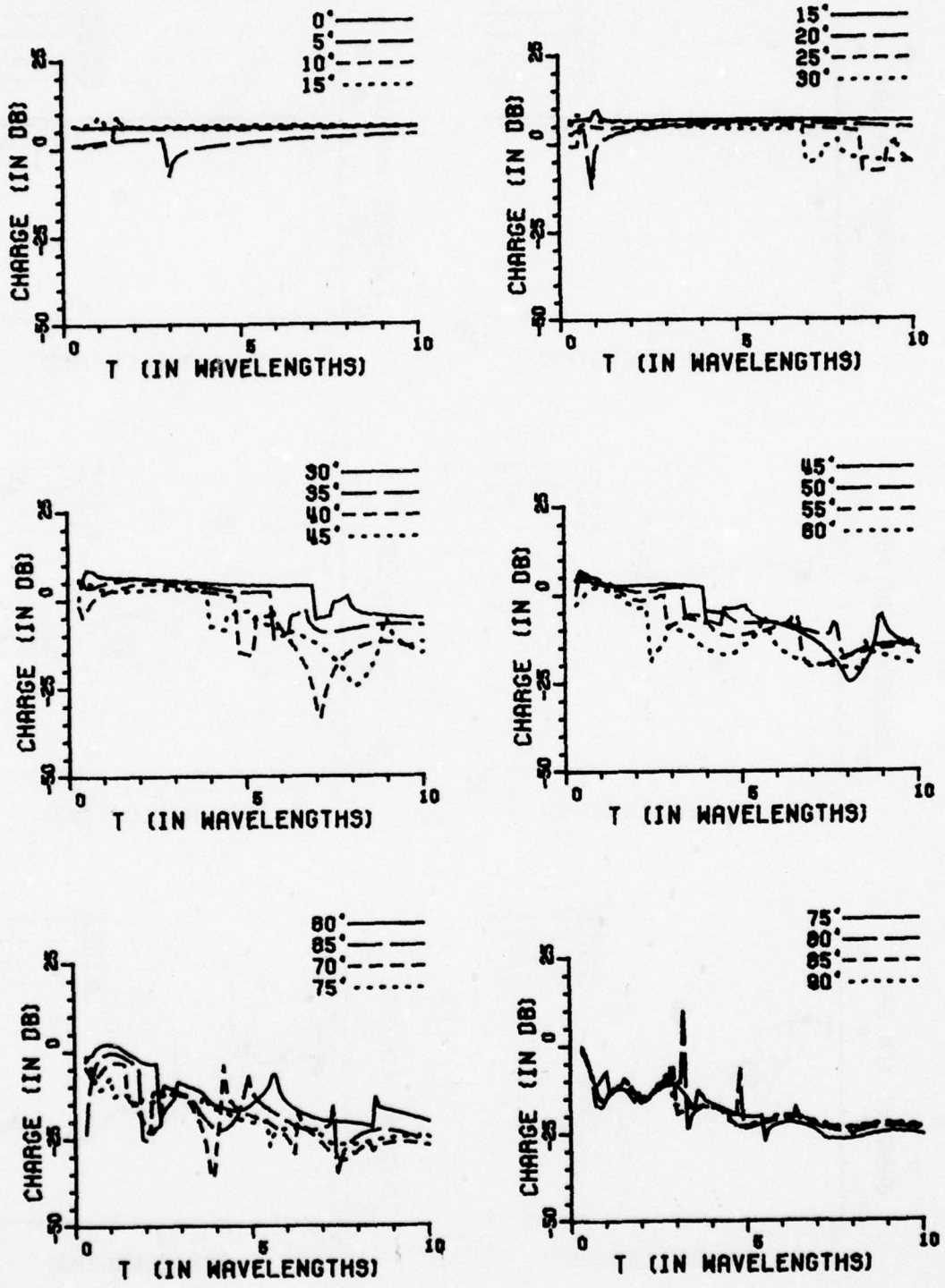

Figure 54b. Surface charge density with 2.0 wavelength and $r_1/a=0.125$.

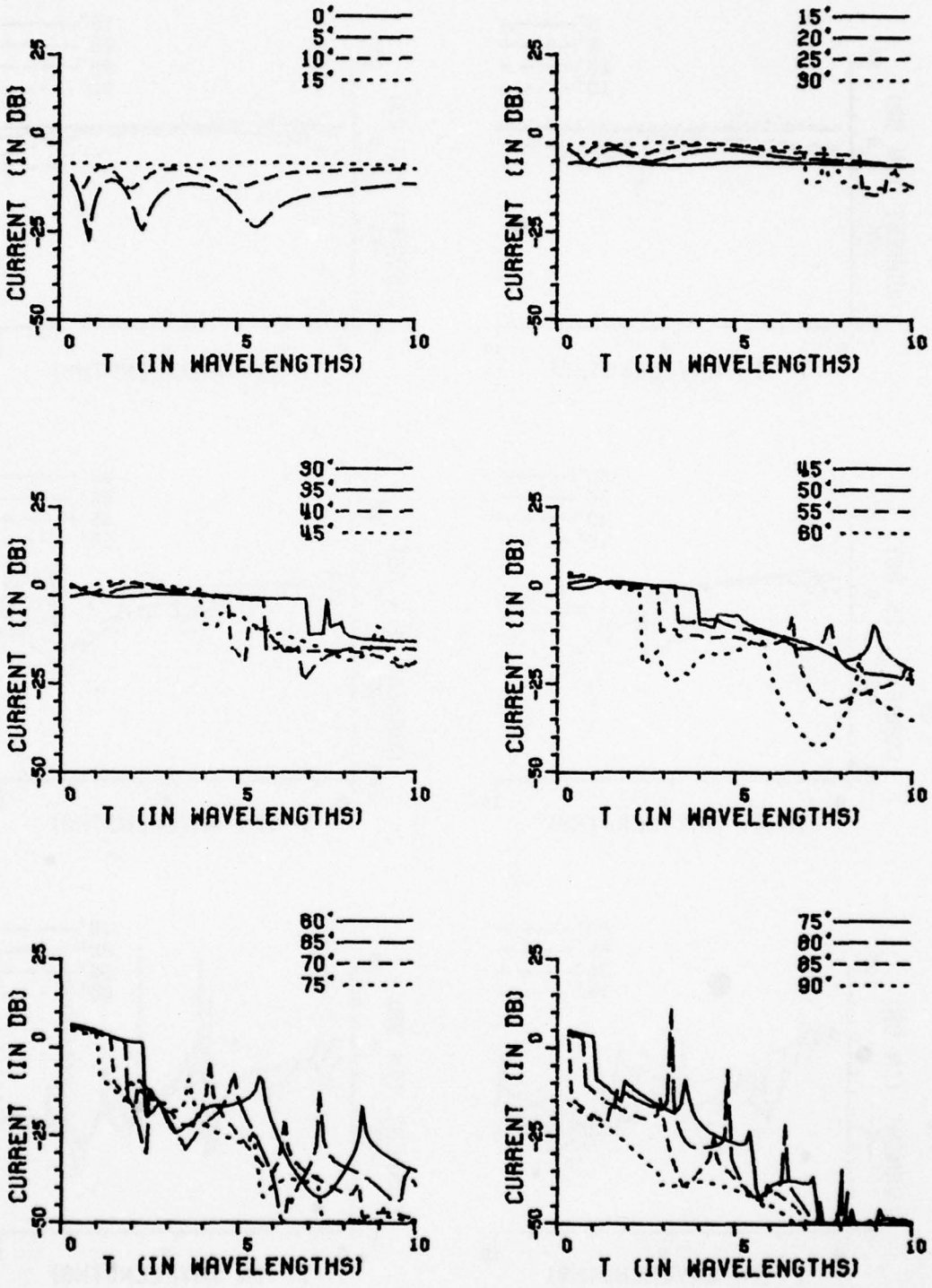

Figure 54c. Circumferential current density with a=2.0 wavelength and r_1/a=0.125.

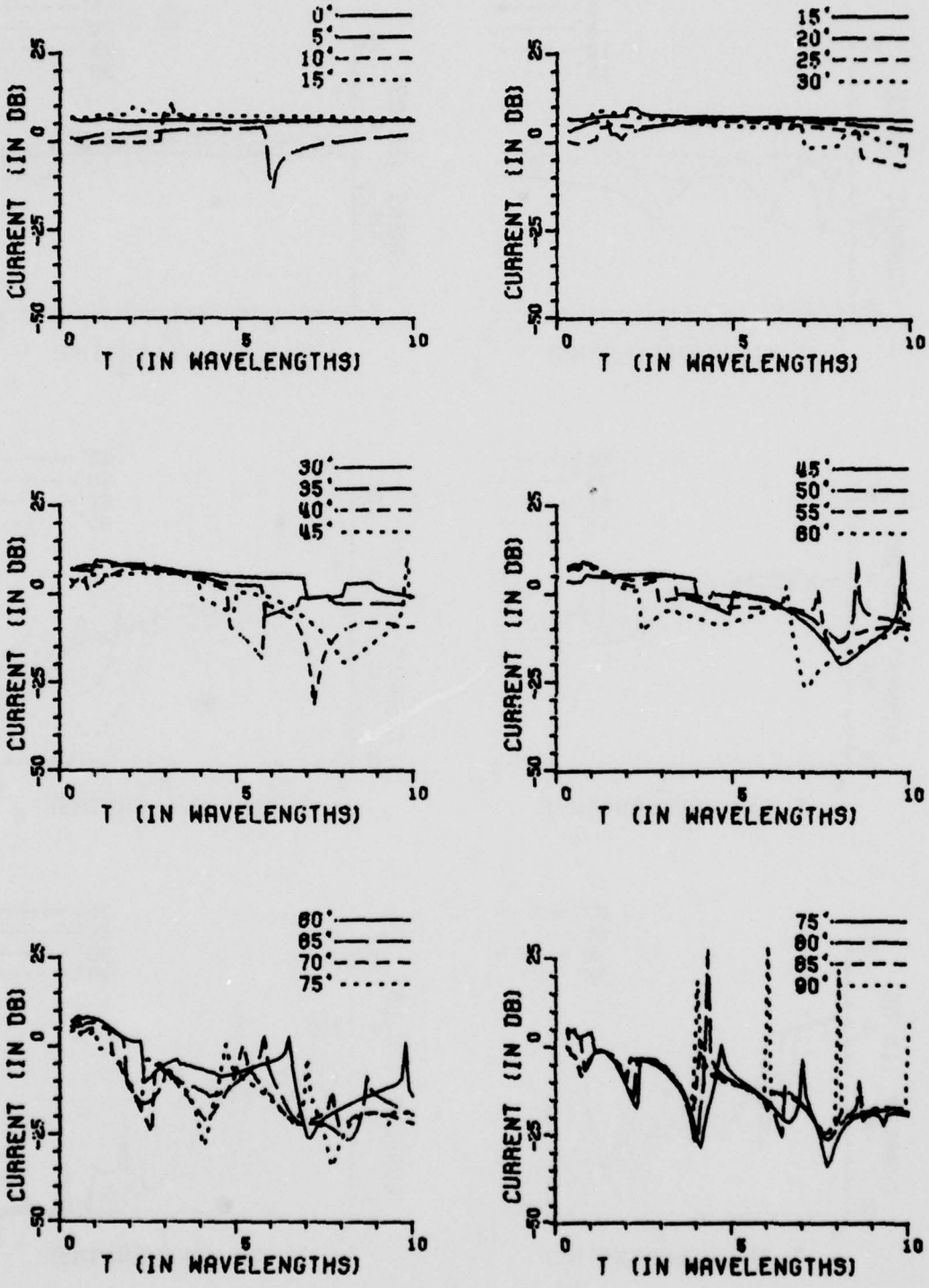

Figure 55a. Axial current density with a=2.0 wavelength and r_1/a=0.25.

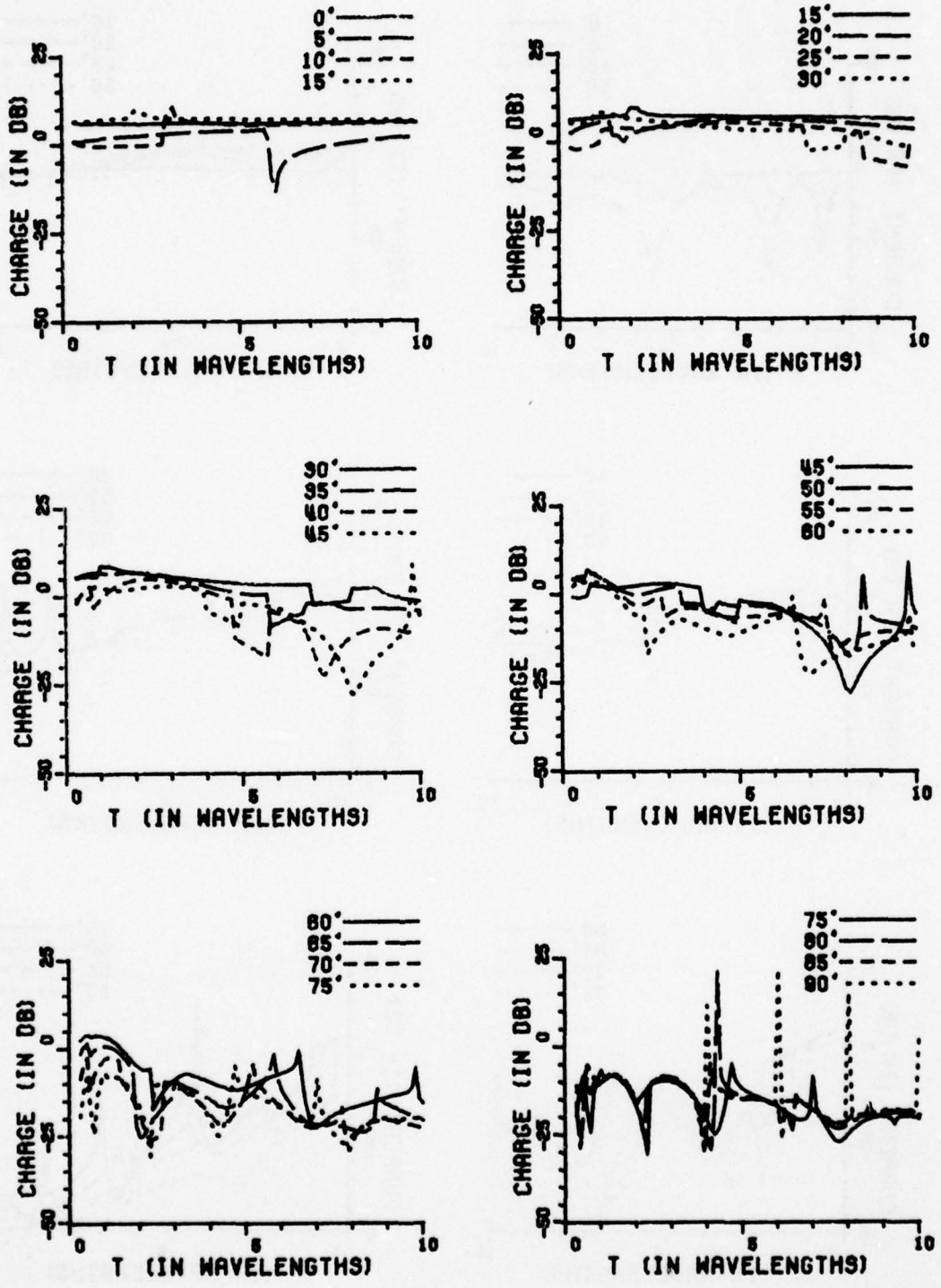

Figure 55b. Surface charge density with 2.0 wavelength and $r_1/a=0.25$.

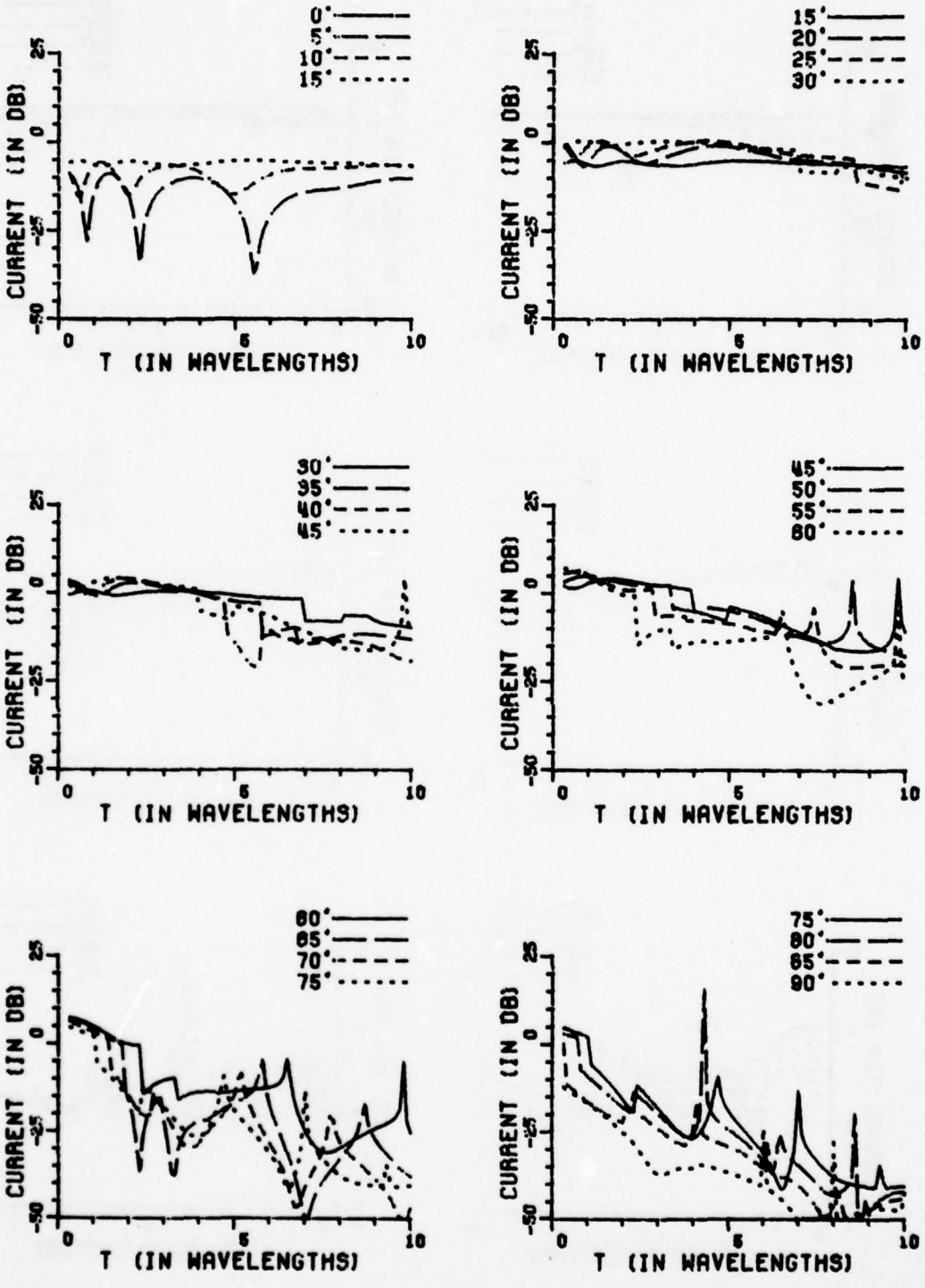

Figure 55c. Circumferential current density with a=2.0 wavelength and $r_1/a=0.25$.

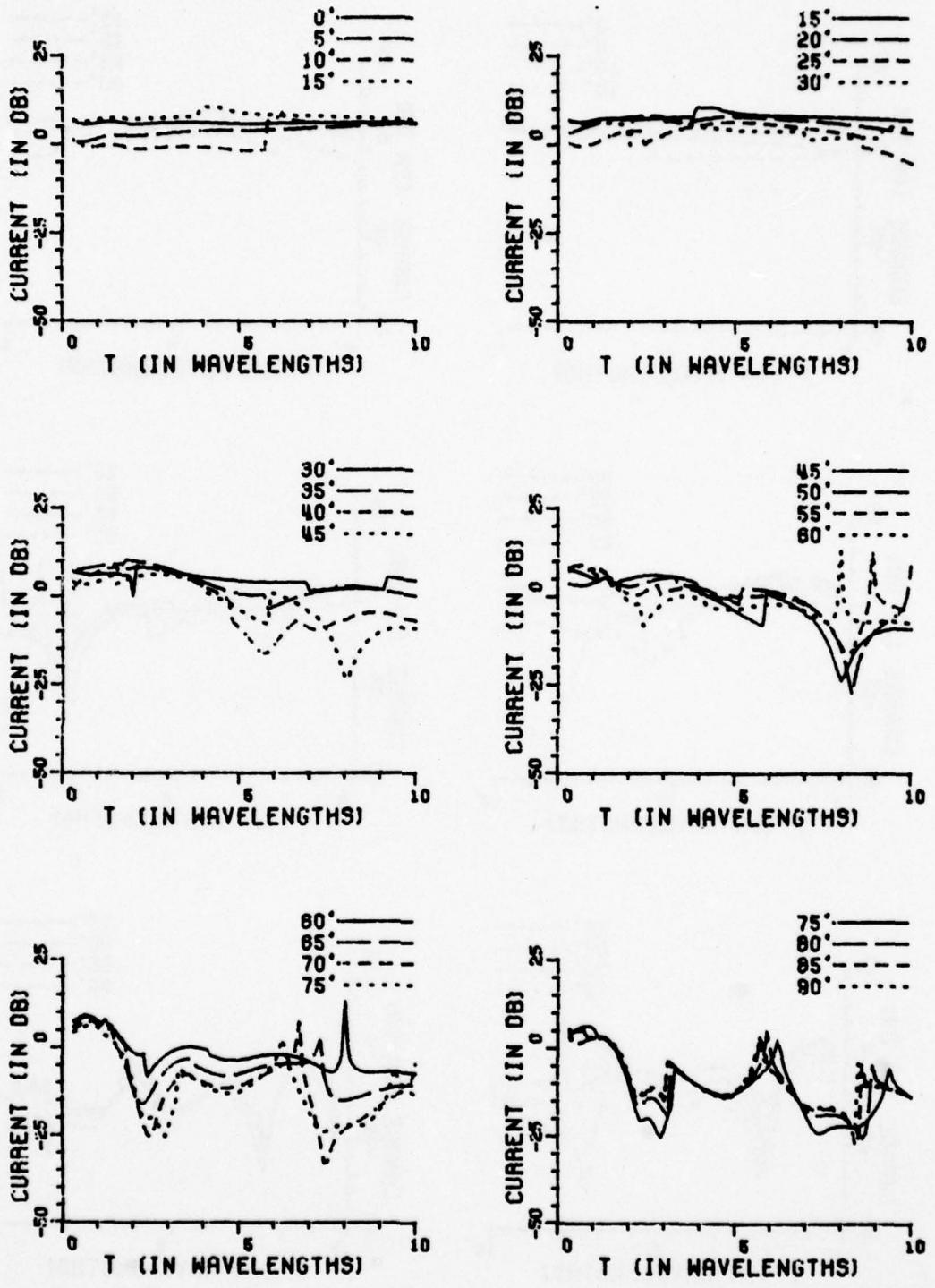

Figure 56a. Axial current density with a=2.0 wavelength and r_1/a=0.5.

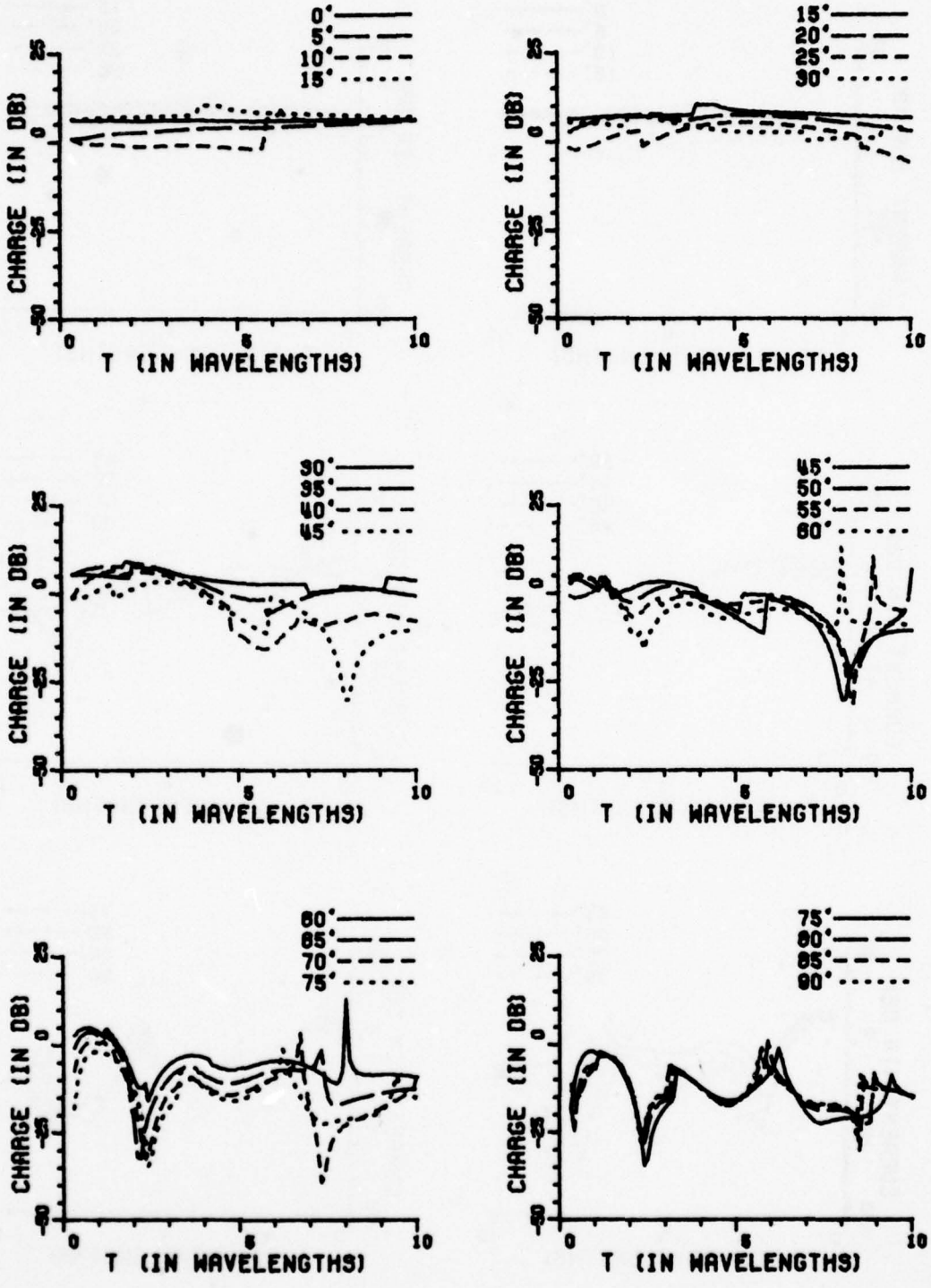

Figure 56b. Surface charge density with 2.0 wavelength and $r_1/a=0.5$.

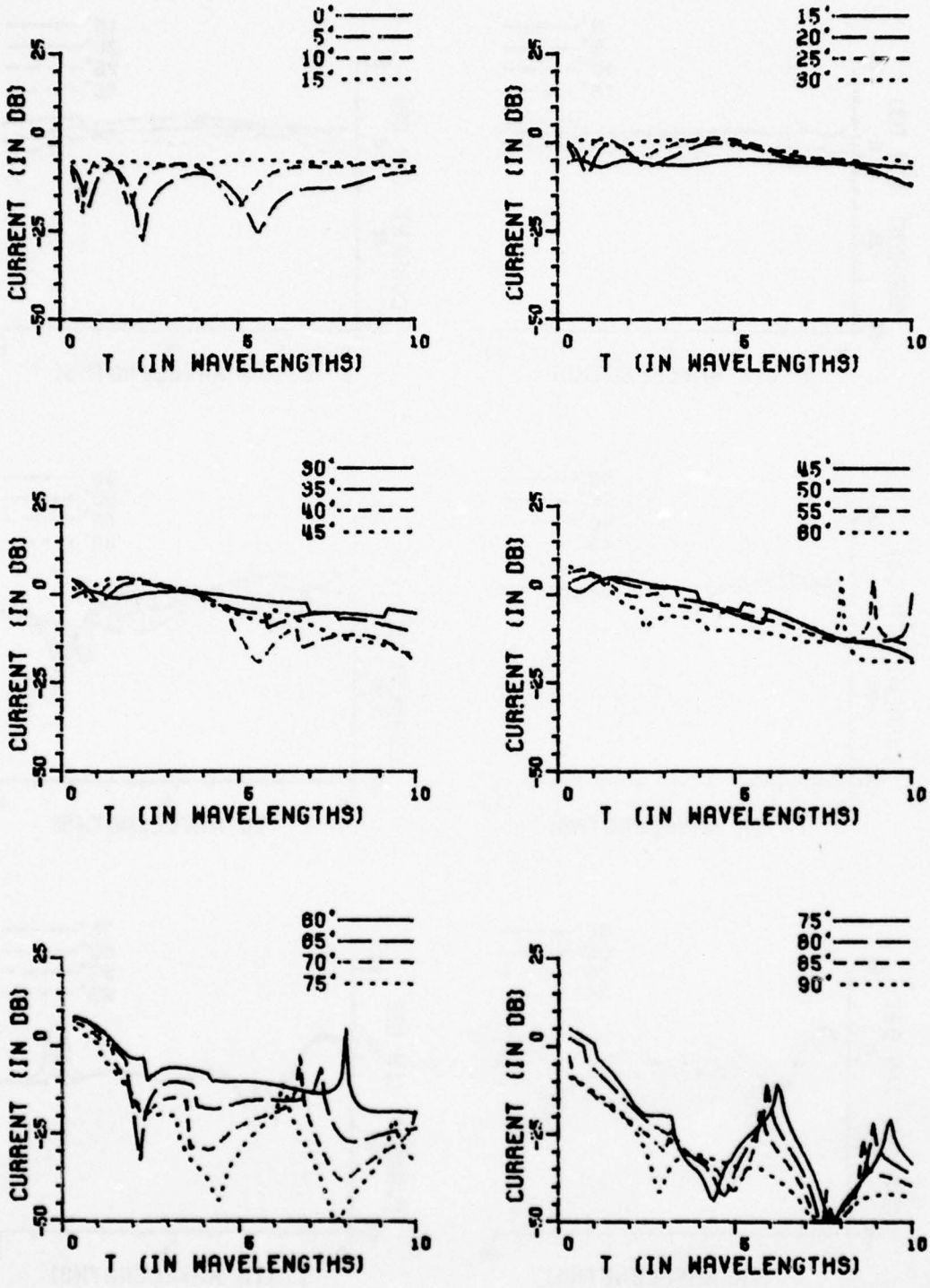

Figure 56c. Circumferential current density with a=2.0 wavelength and r_1/a=0.5.

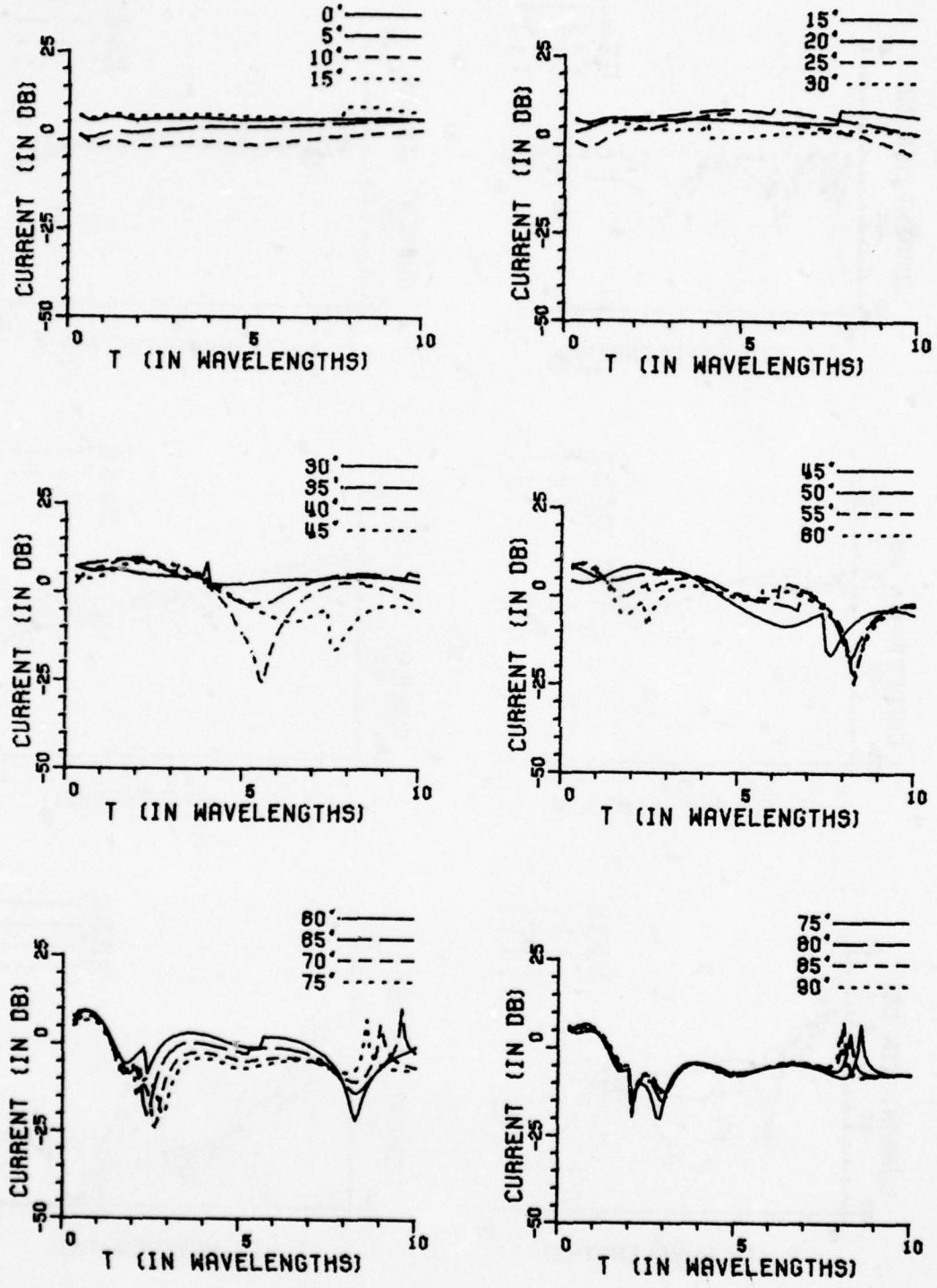

Figure 57a. Axial current density with a=2.0 wavelength and $r_1/a=1.0$.

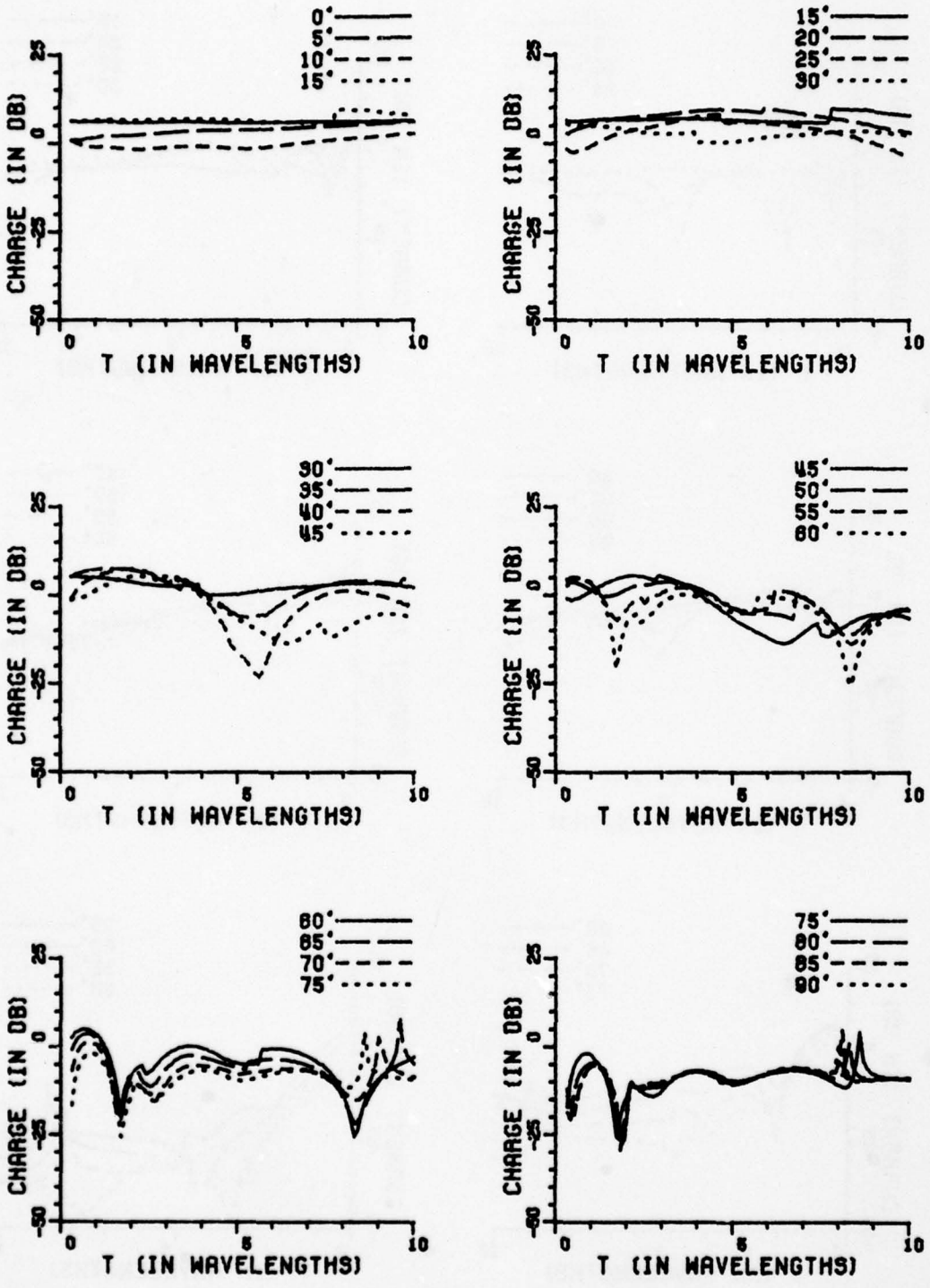

Figure 57b. Surface charge density with 2.0 wavelength and r_1/a=1.0.

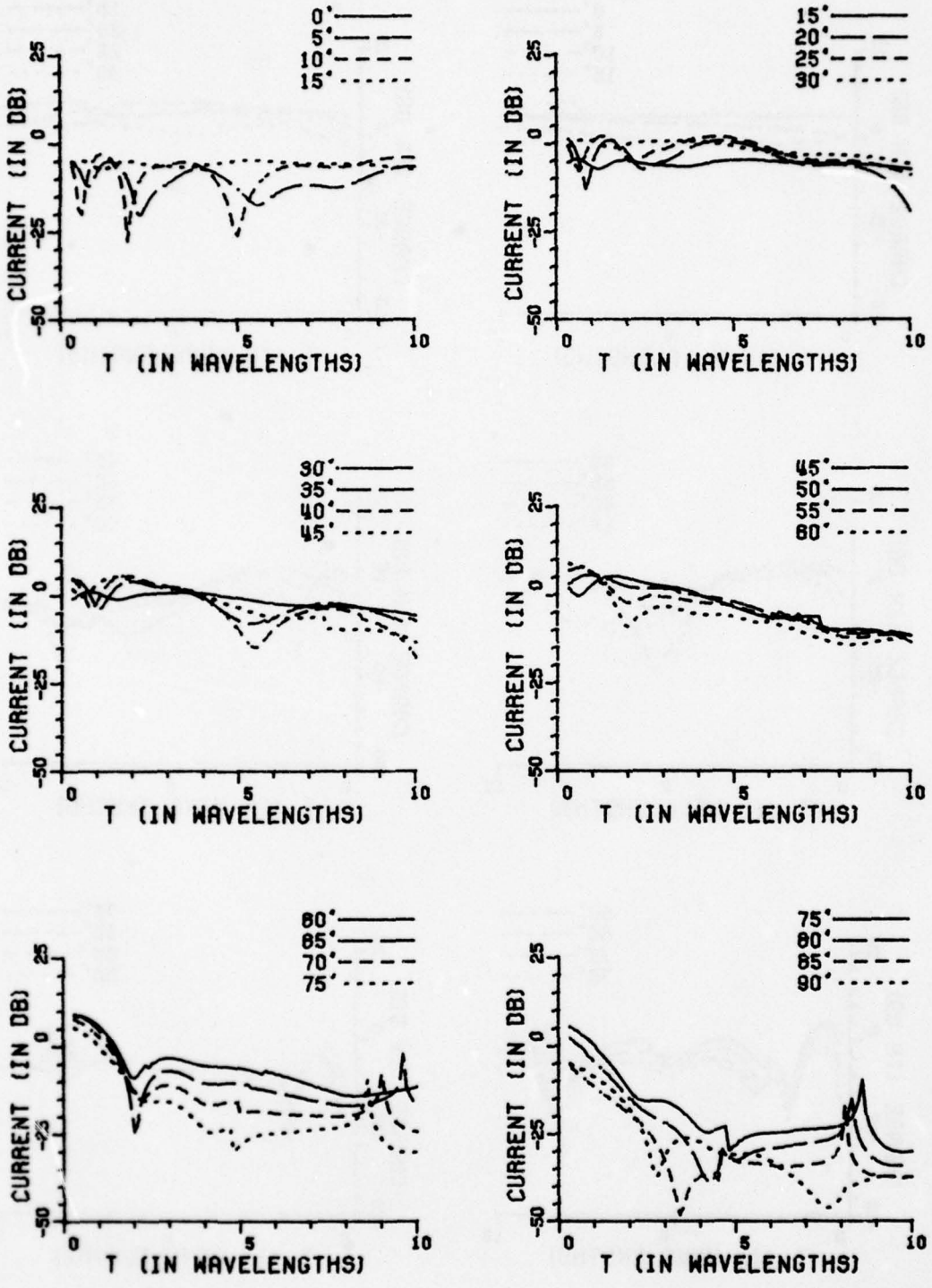

Figure 57c. Circumferential current density with a=2.0 wavelength and r_1/a=1.0.

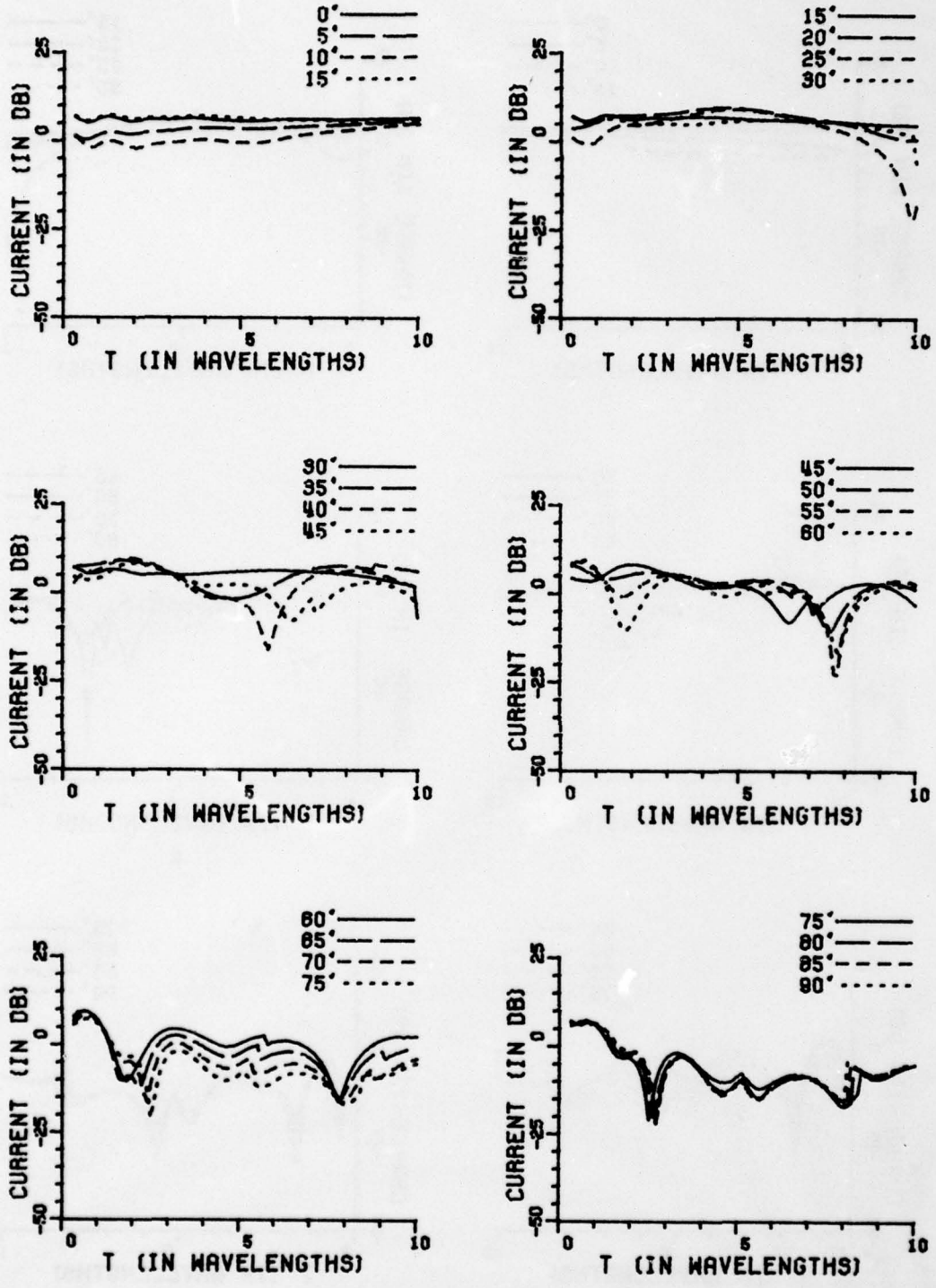

Figure 58a. Axial current density with a=2.0 wavelength and $r_1/a=2.5$.

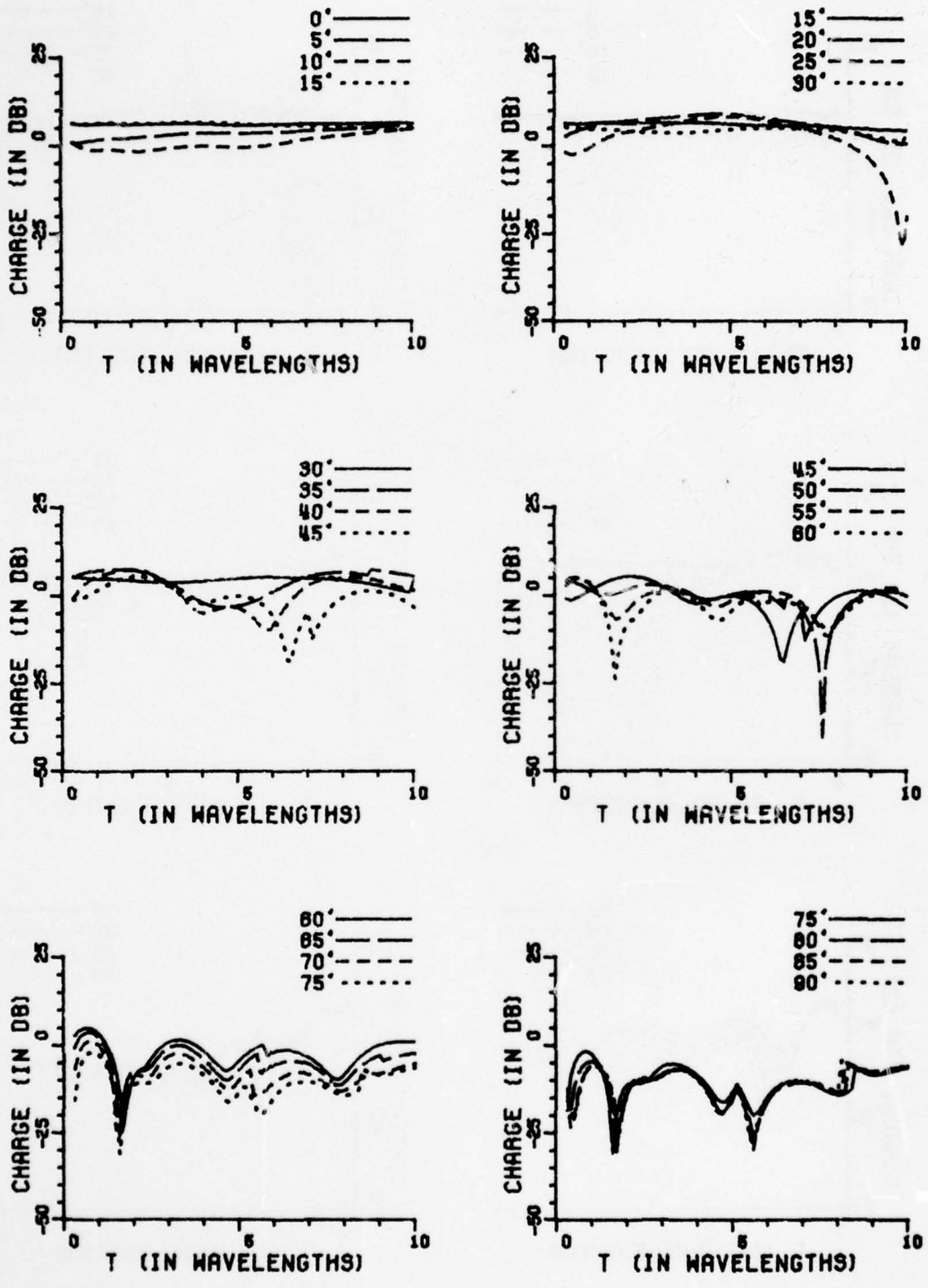

Figure 58b. Surface charge density with 2.0 wavelength and $r_1/a=2.5$.

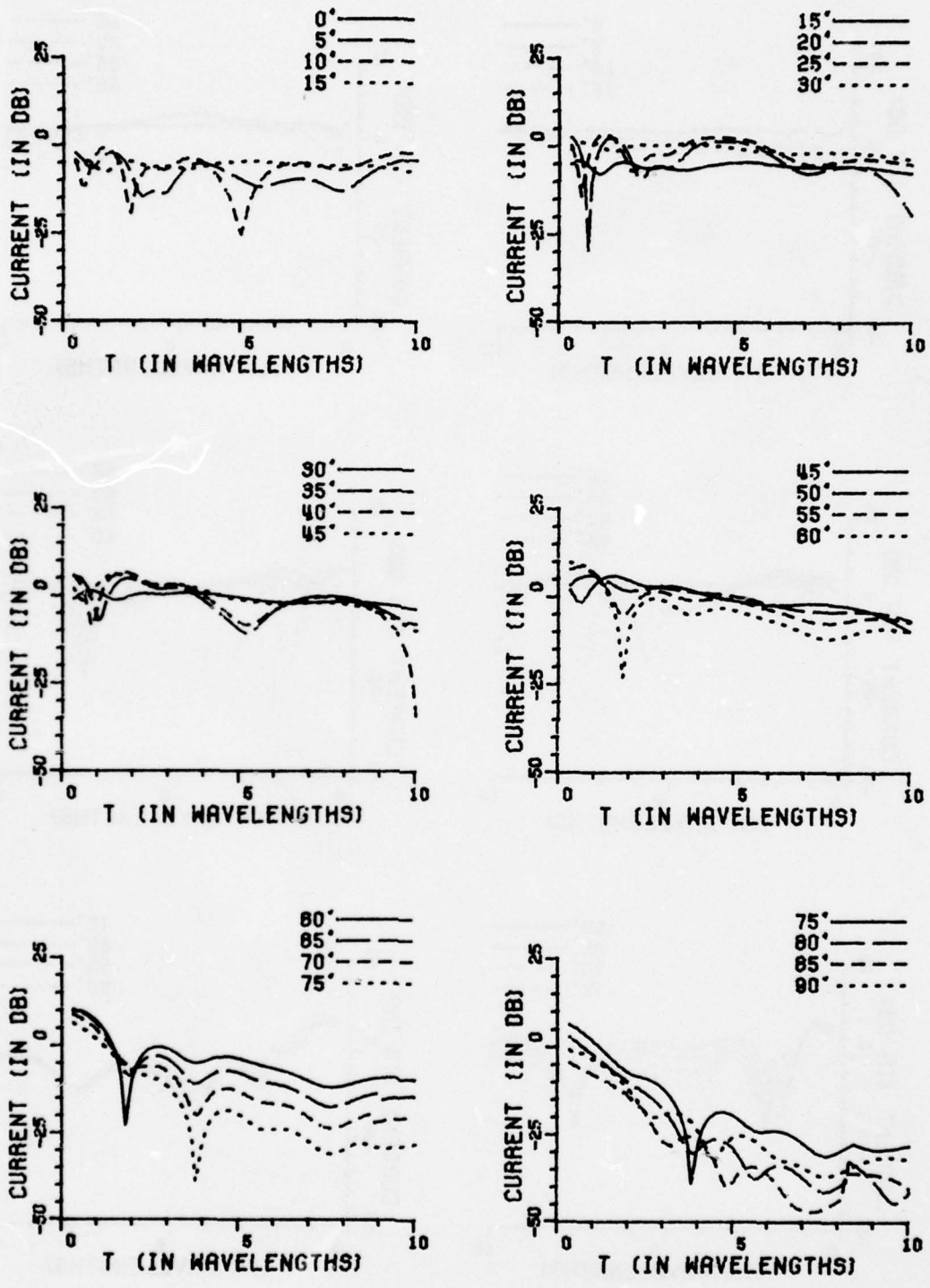

Figure 58c. Circumferential current density with a=2.0 wavelength and r_1/a=2.5.

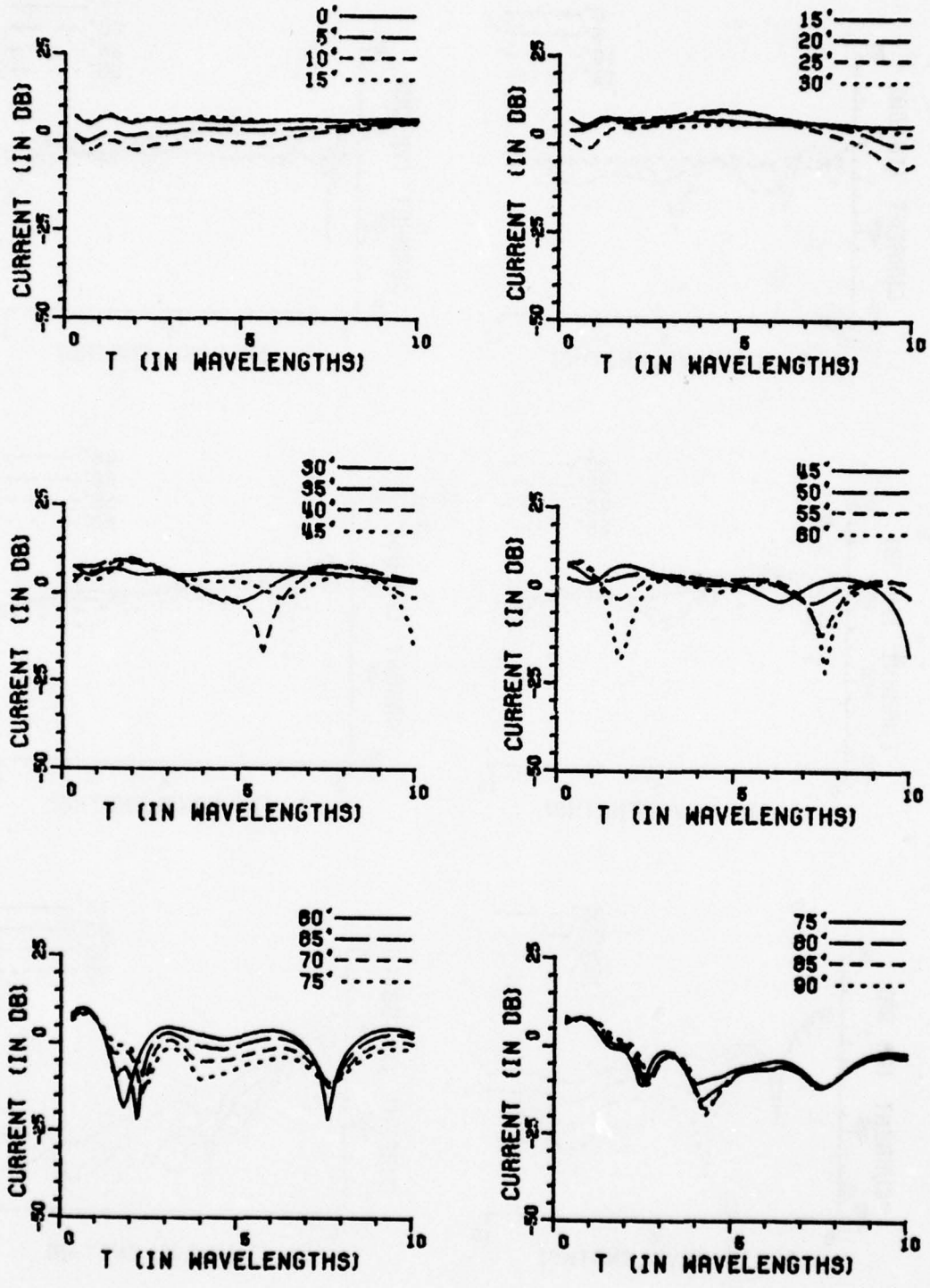

Figure 59a. Axial current density with a=2.0 wavelength and r_1/a=5.0.

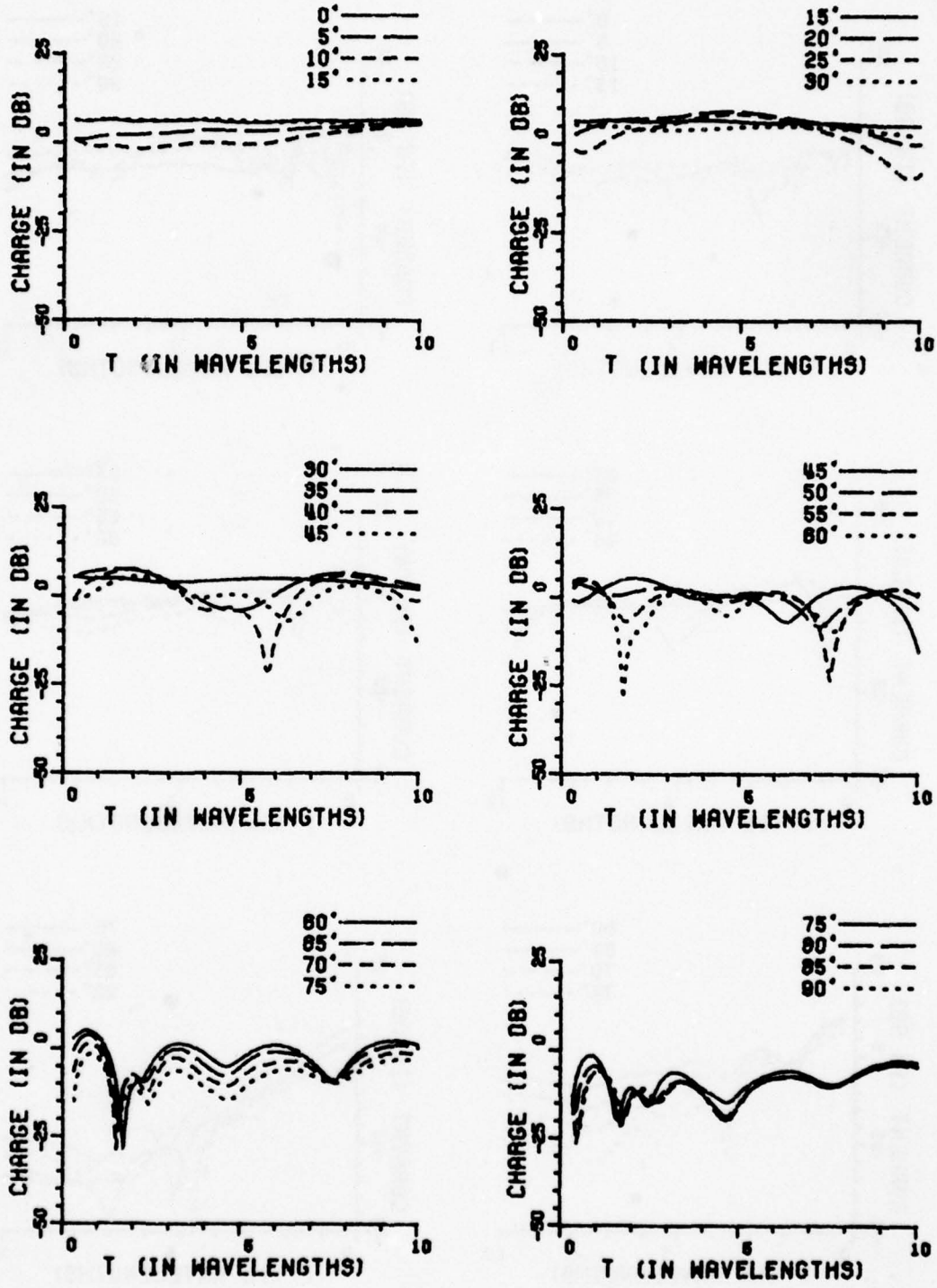

Figure 59b. Surface charge density with 2.0 wavelength and $r_1/a=5.0$.

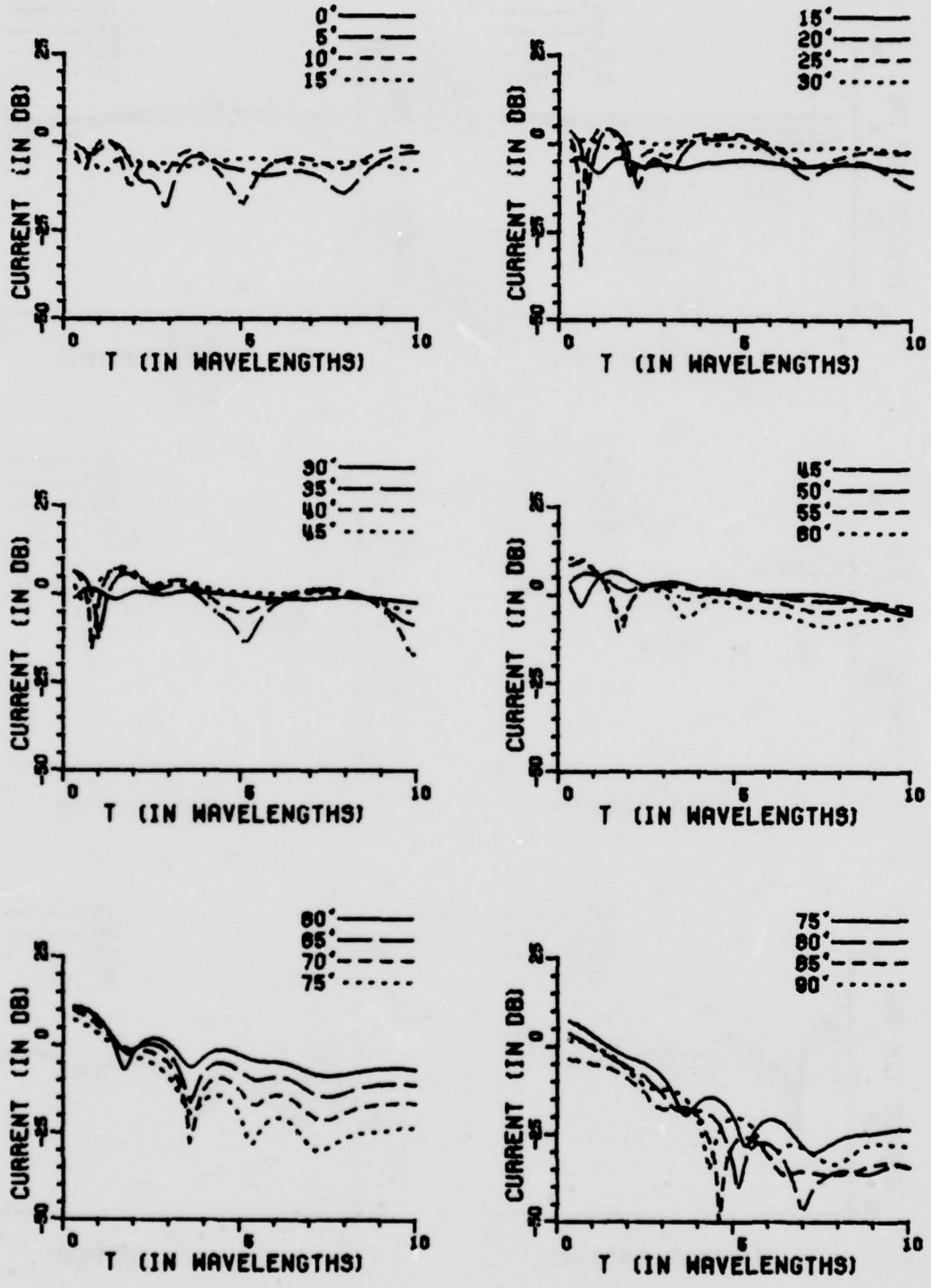

Figure 59c. Circumferential current density with a=2.0 wavelength and $r_1/a=5.0$.

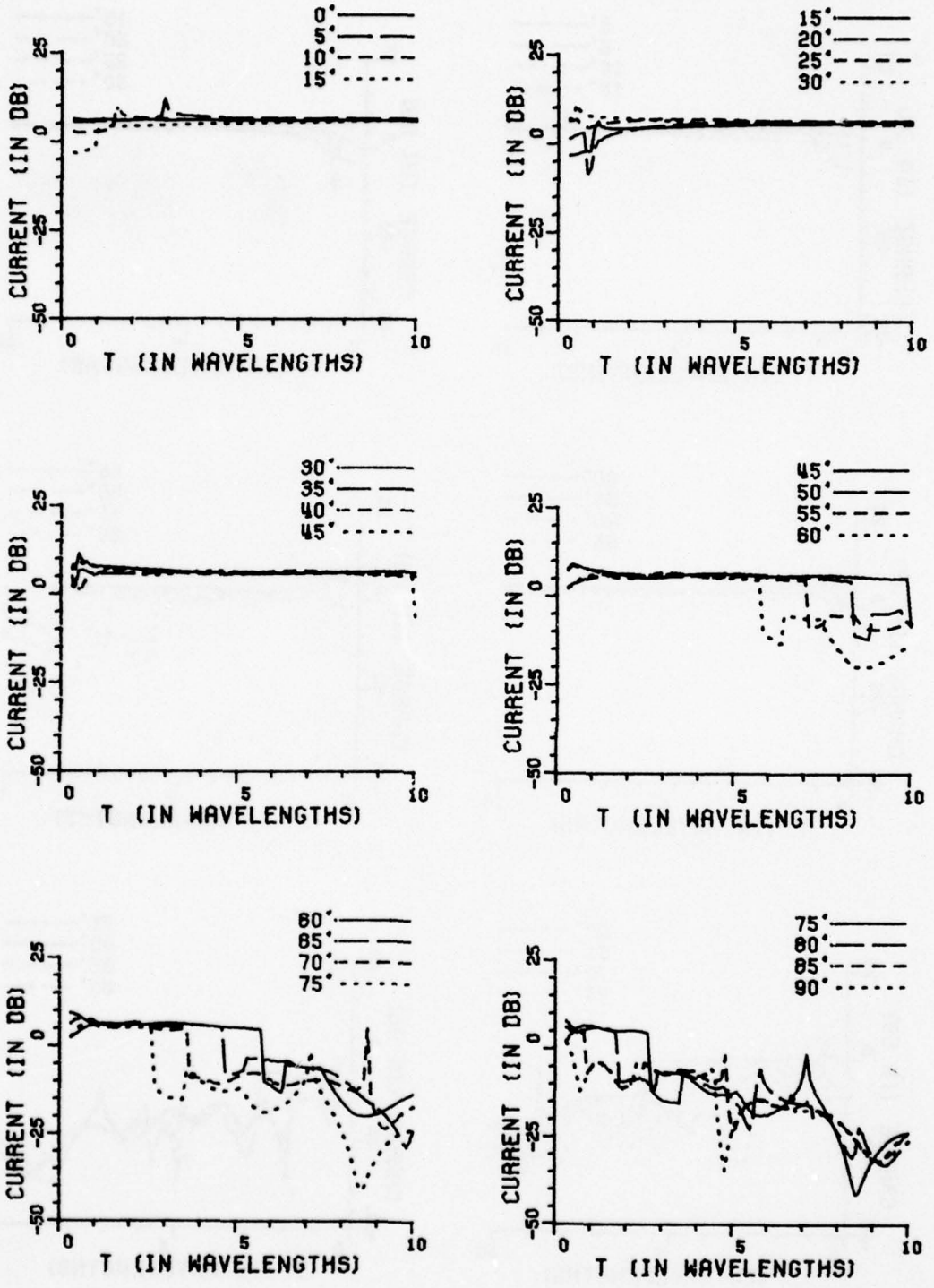

Figure 60a. Axial current density with a=5.0 wavelength and r_1/a=0.05.

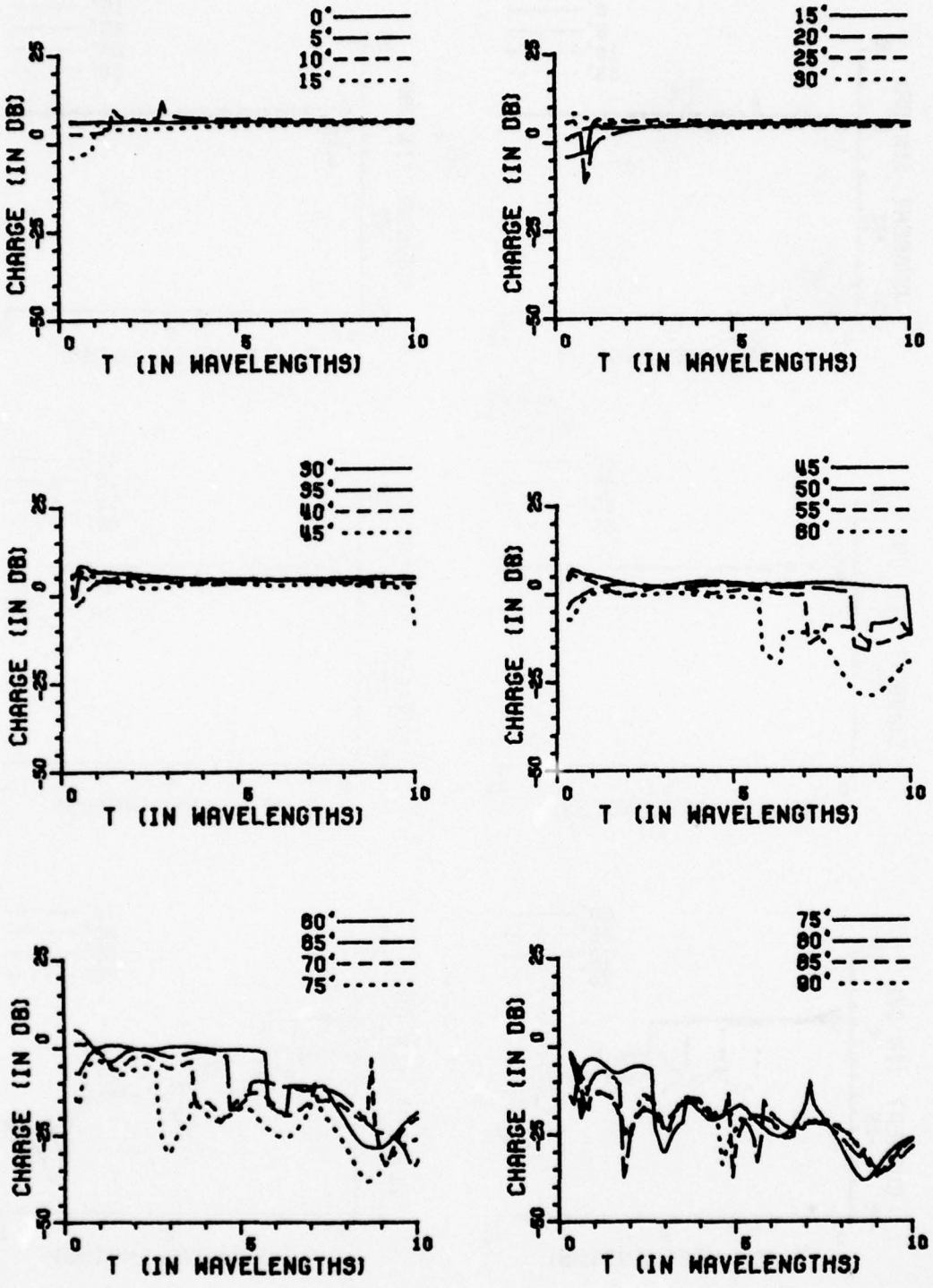

Figure 60b. Surface charge sensity with a=5.0 wavelength and r_1/a=0.05.

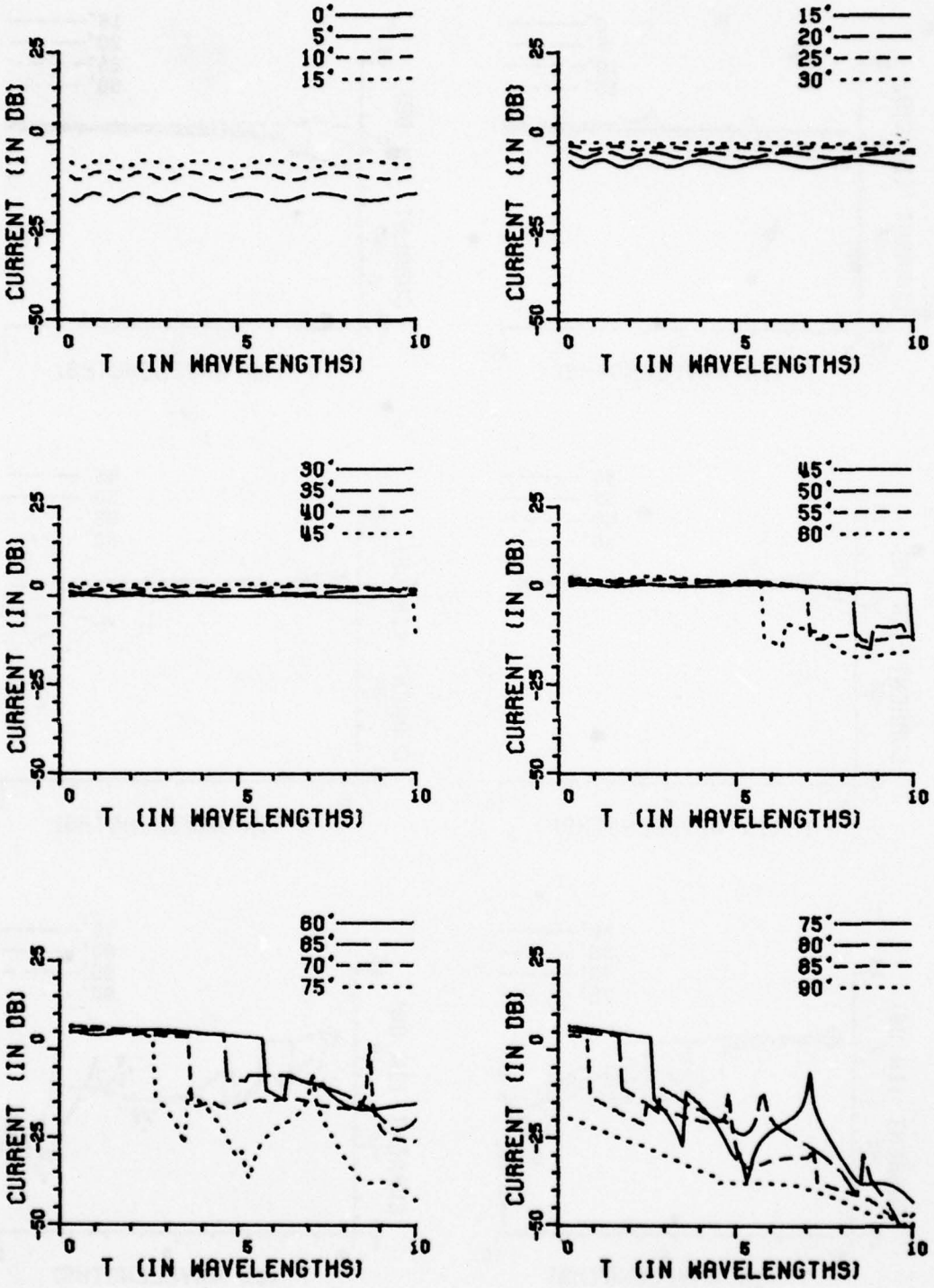

Figure 60c. Circumferential current density with a=5.0 wavelength and r_1/a=0.05.

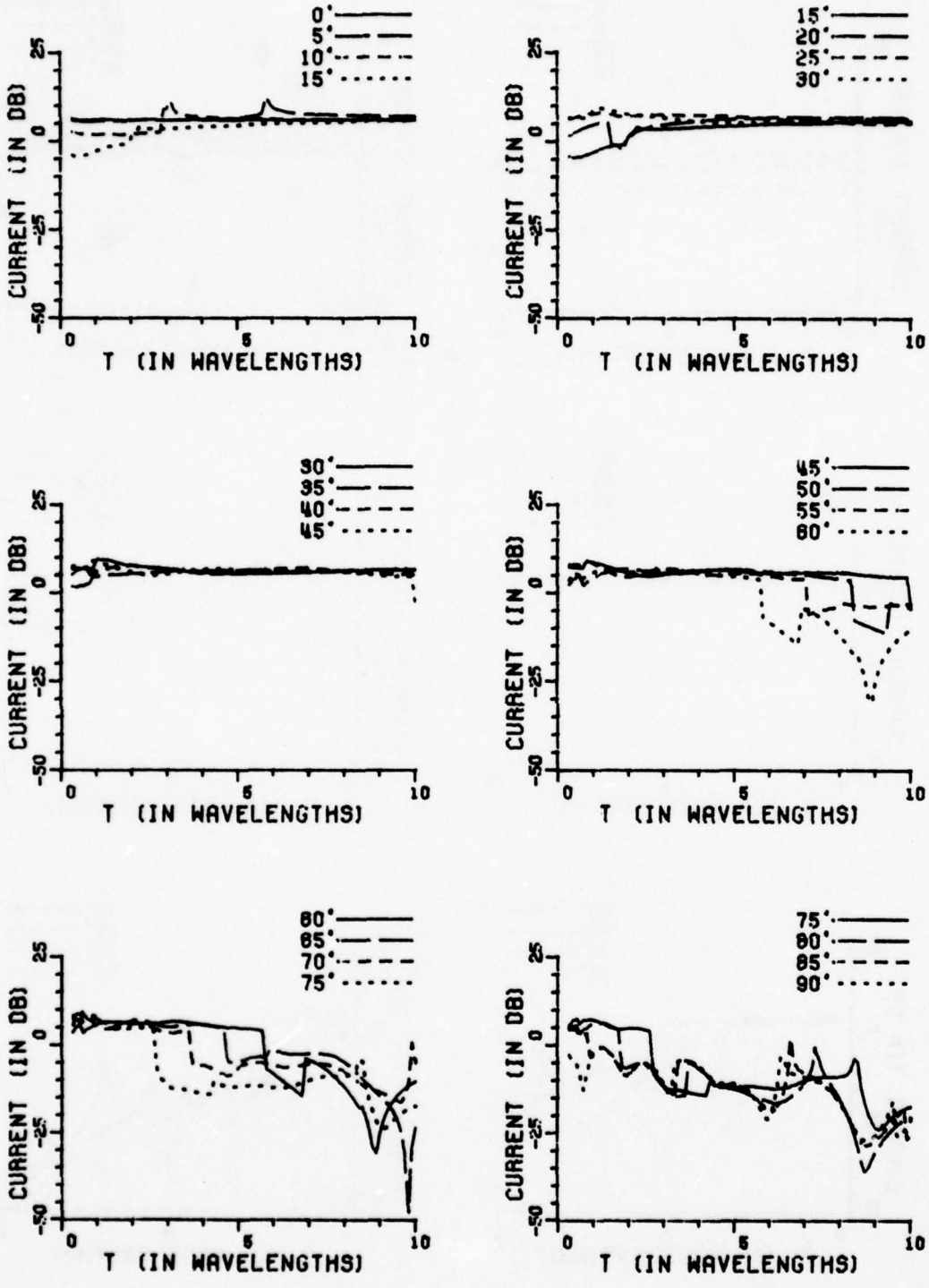

Figure 61a. Axial current density with a=5.0 wavelength and $r_1/a=0.1$.

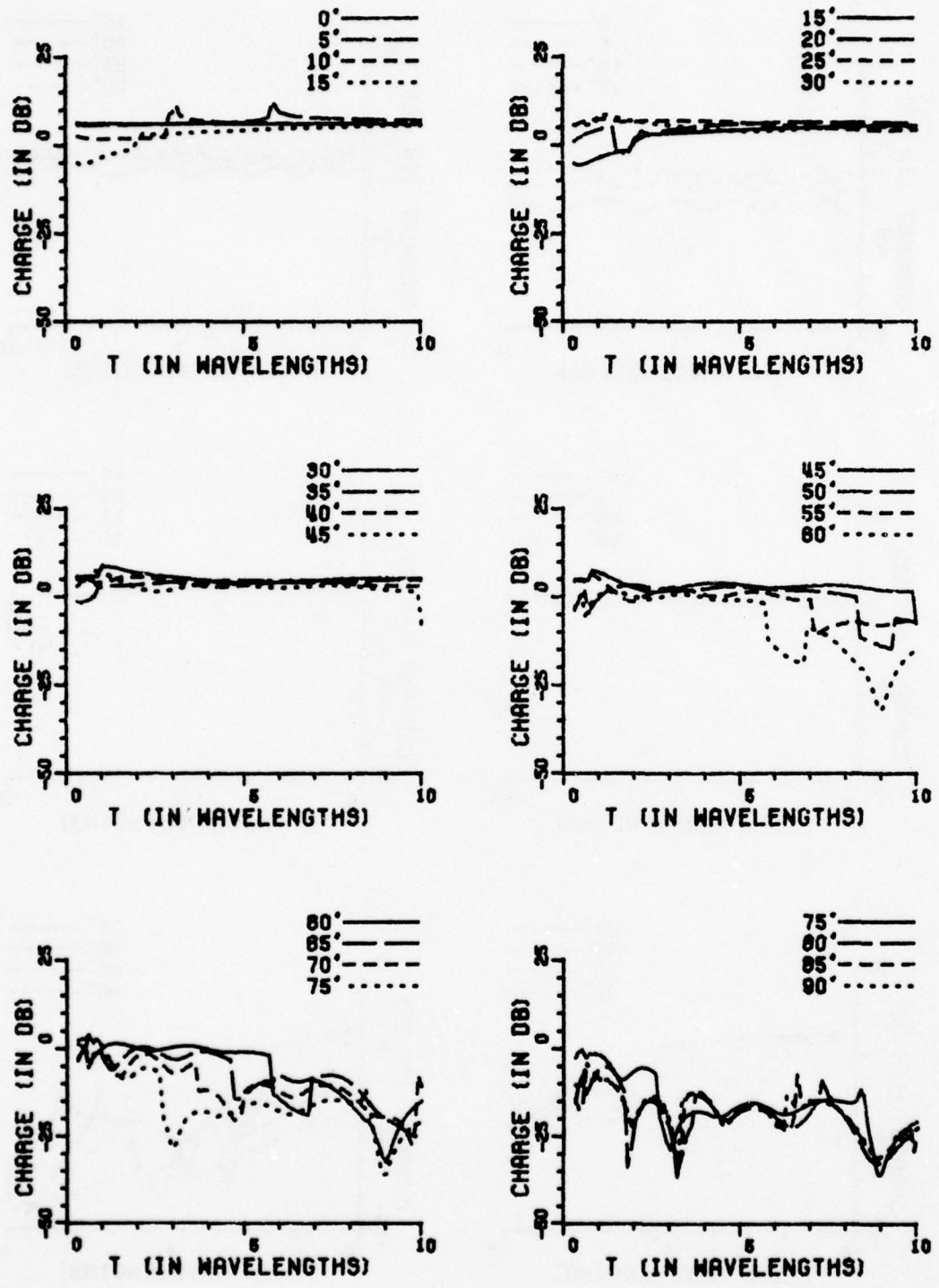

Figure 61b. Surface charge sensity with a=5.0 wavelength and r_1/a=0.1.

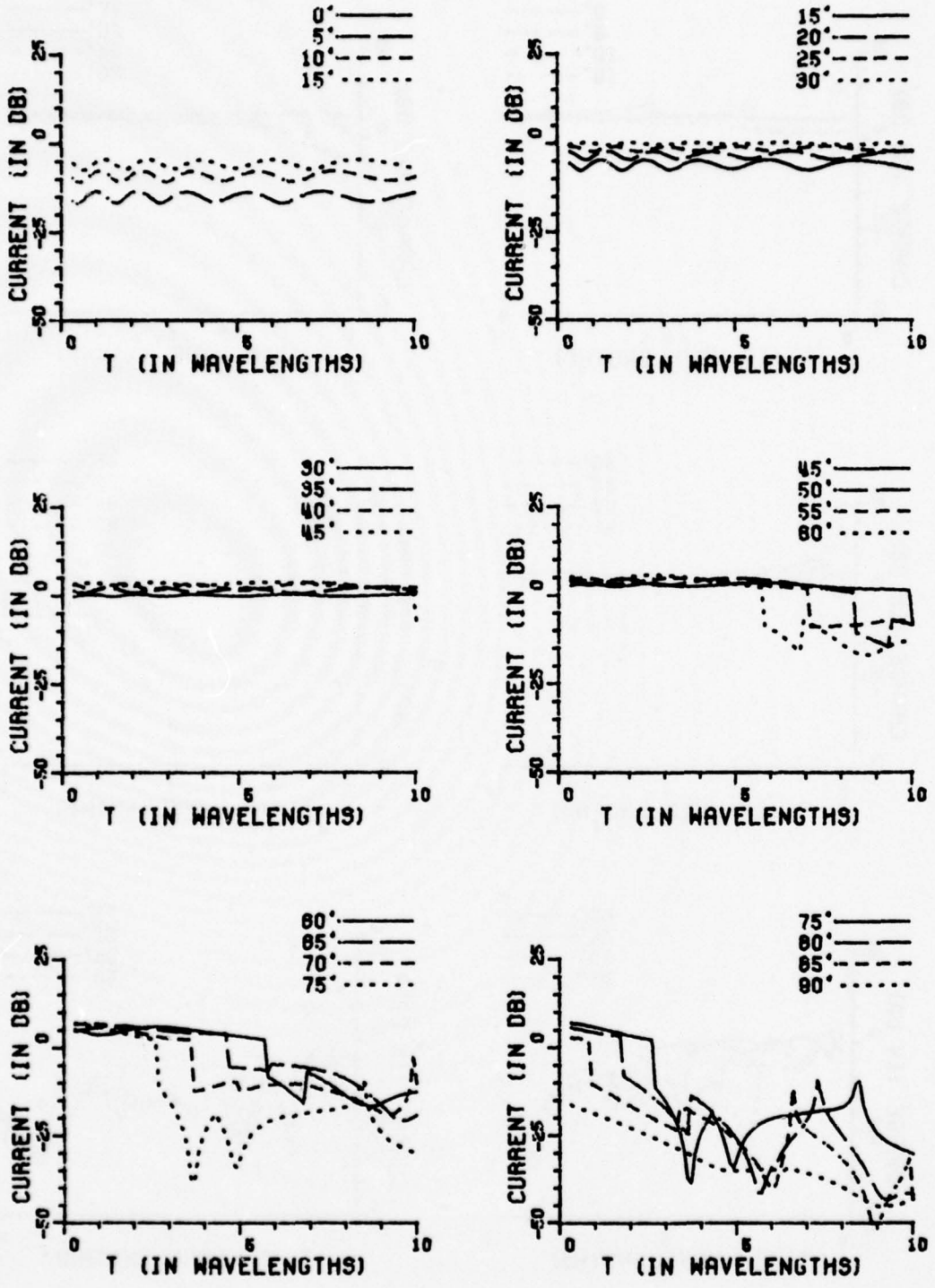

Figure 61c. Circumferential current density with a=5.0 wavelength and $r_1/a=0.1$.

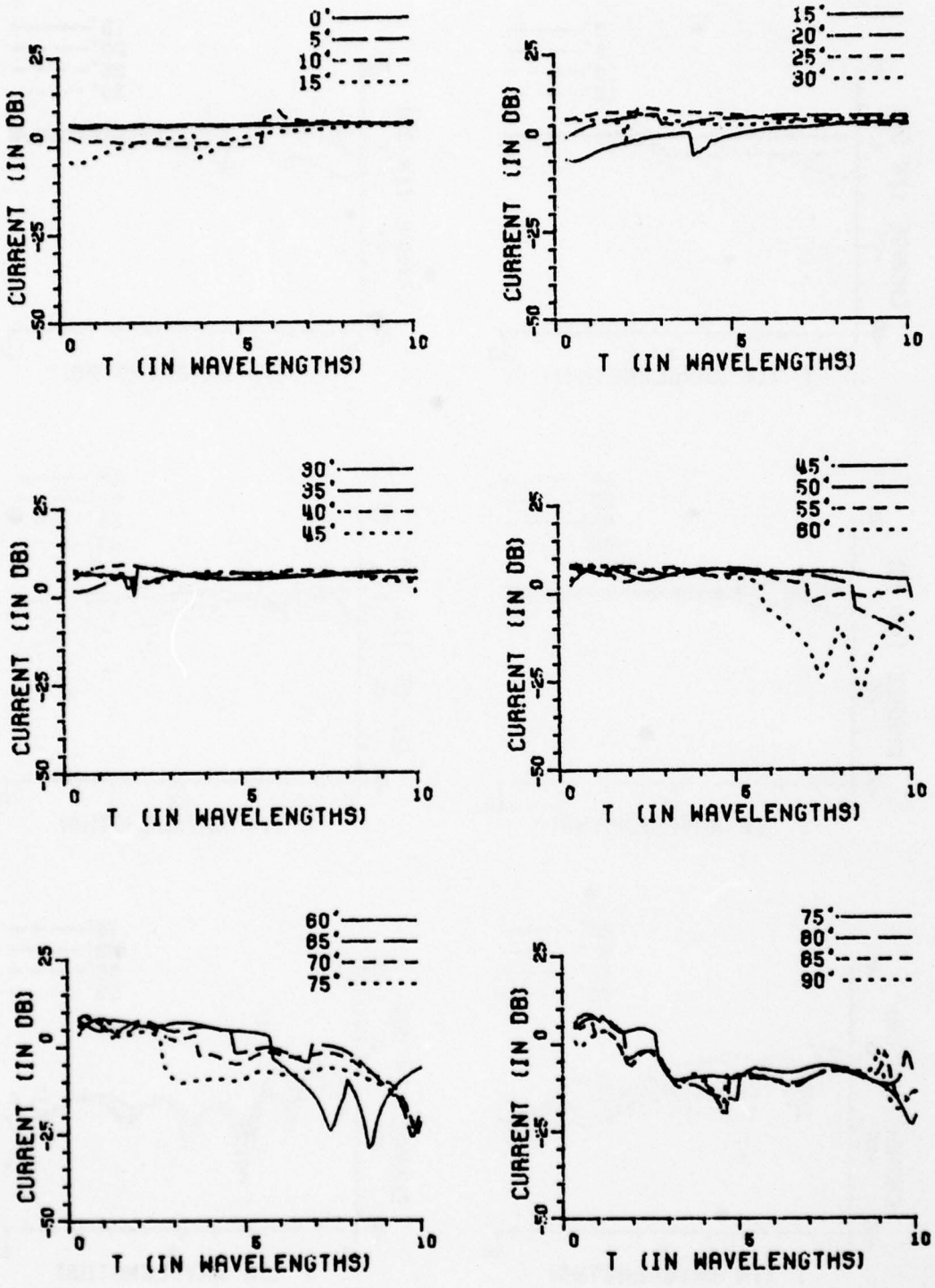

Figure 62a. Axial current density with a=5.0 wavelength and $r_1/a=0.2$.

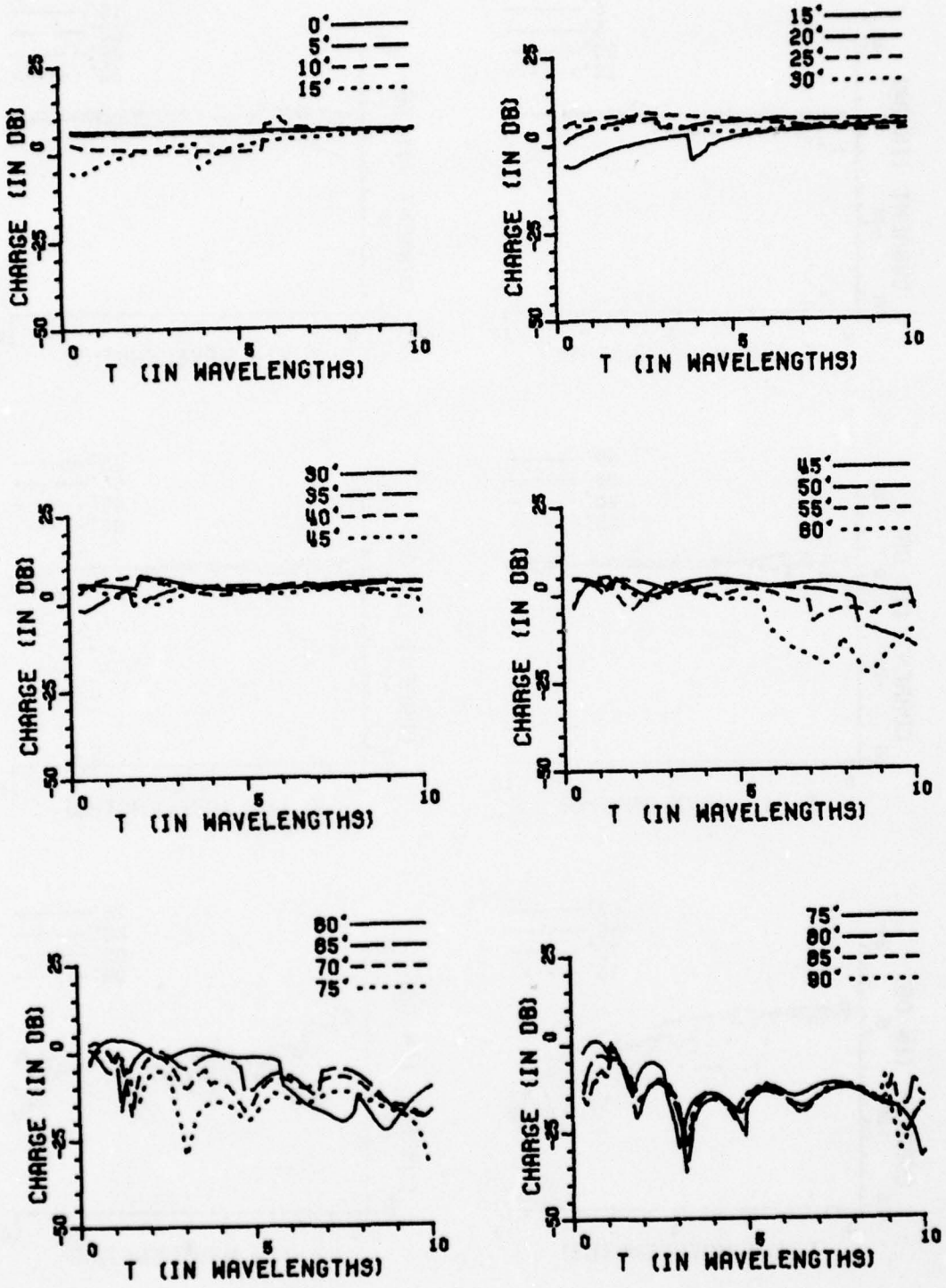

Figure 62b. Surface charge sensity with a=5.0 wavelength and $r_1/a=0.2$.

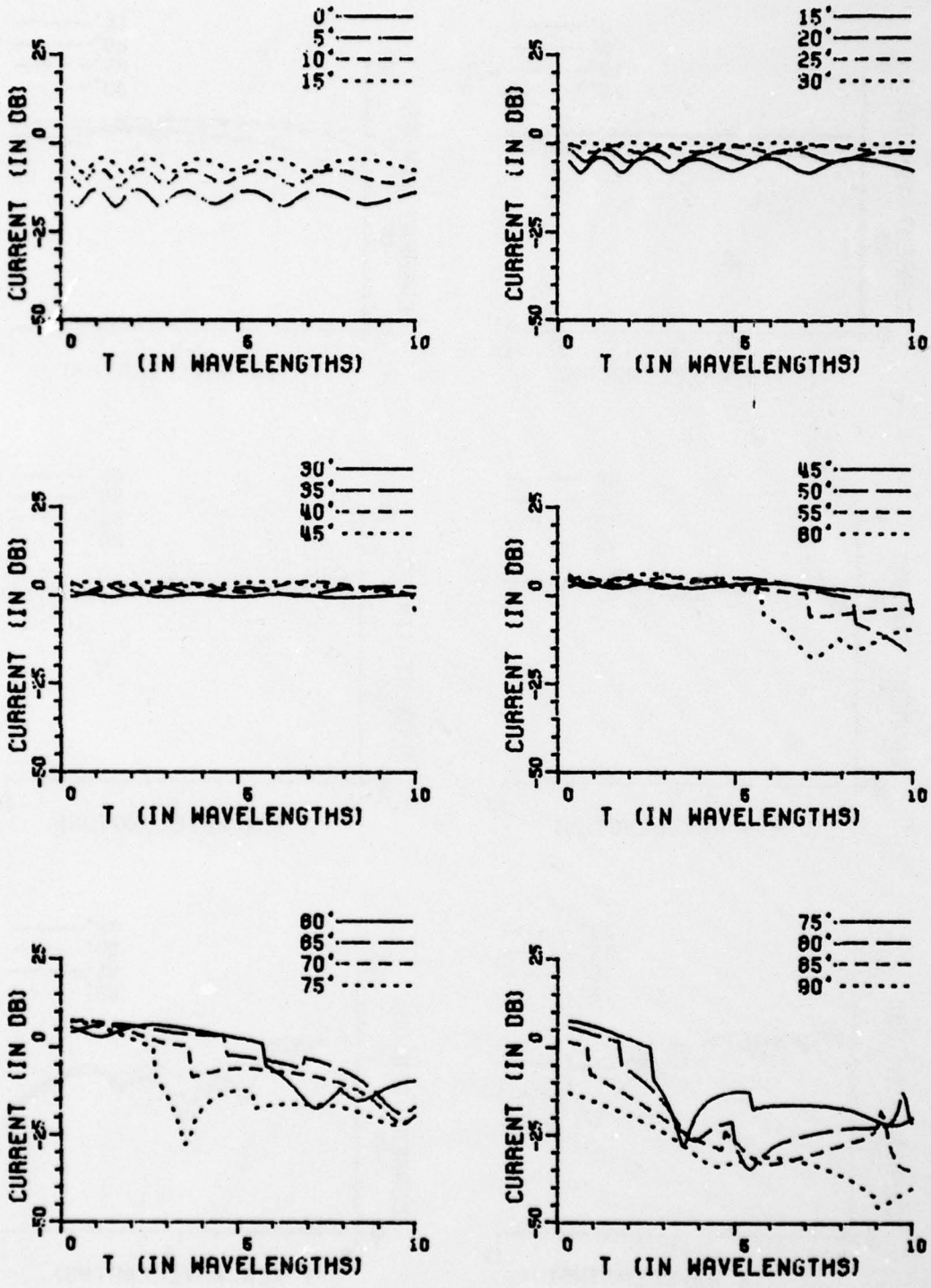

Figure 62c. Circumferential current density with a=5.0 wavelength and r_1/a=0.2.

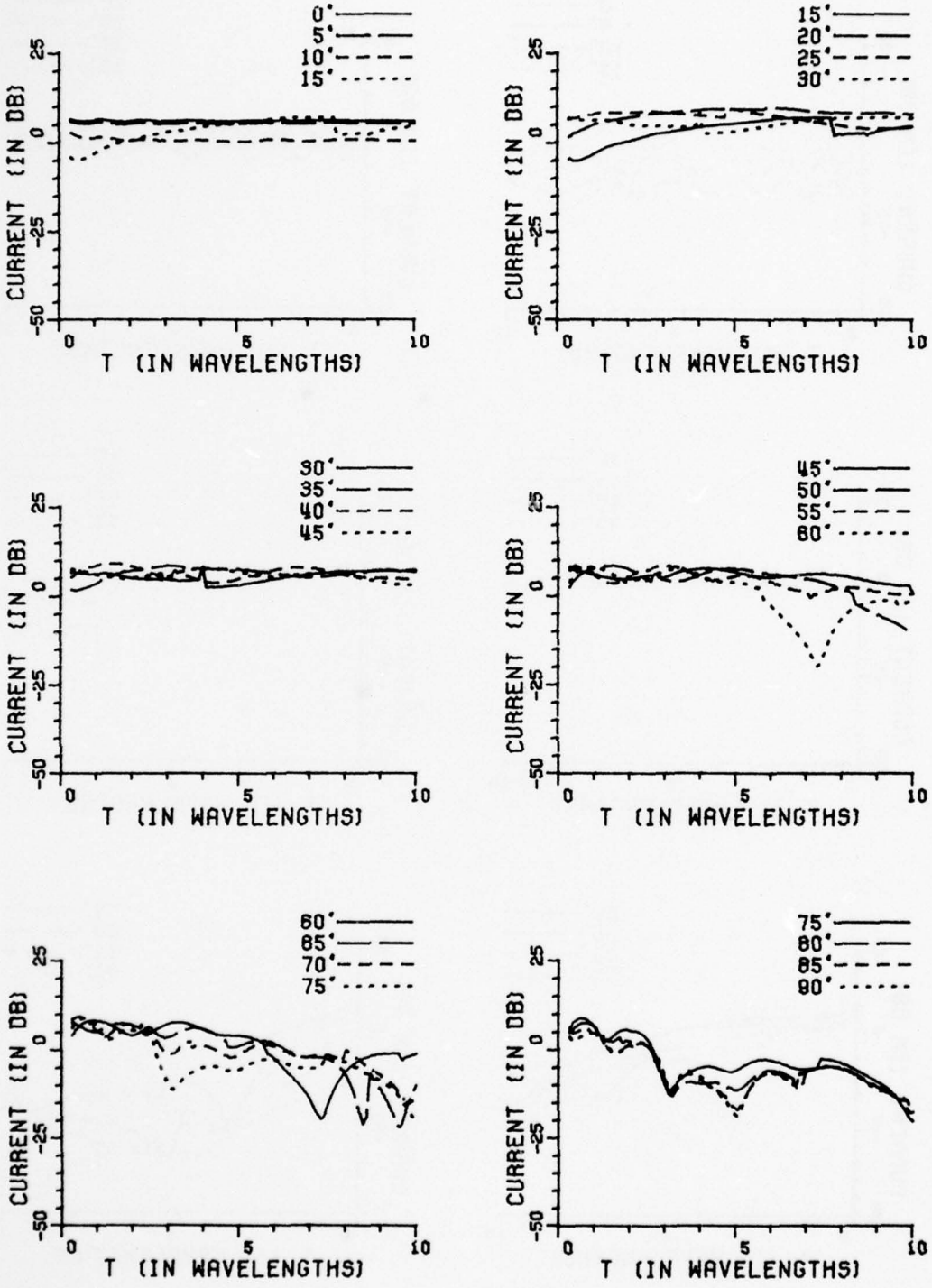

Figure 63a. Axial current density with a=5.0 wavelength and r_1/a=0.4.

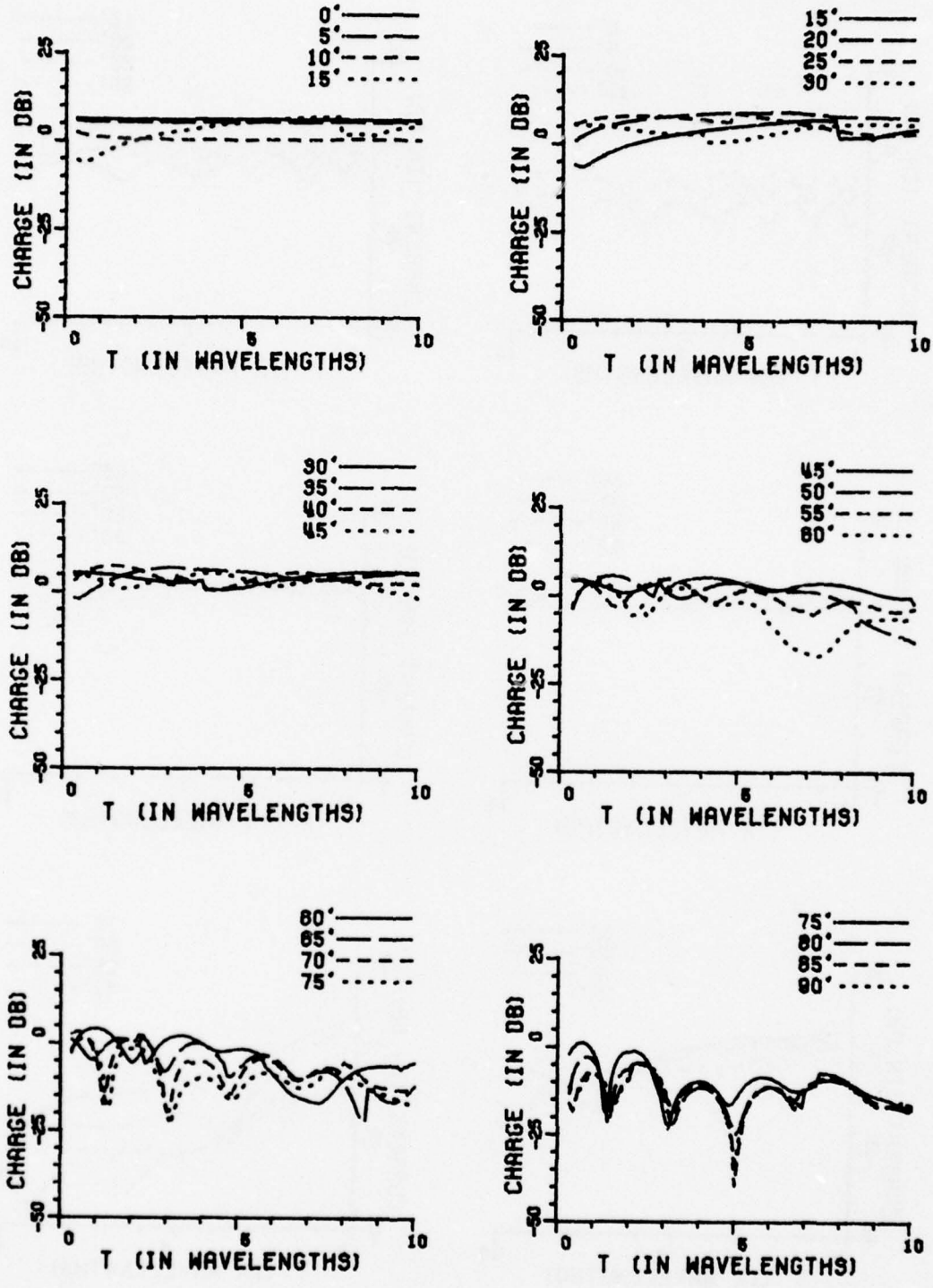

Figure 63b. Surface charge sensity with a=5.0 wavelength and $r_1/a=0.4$.

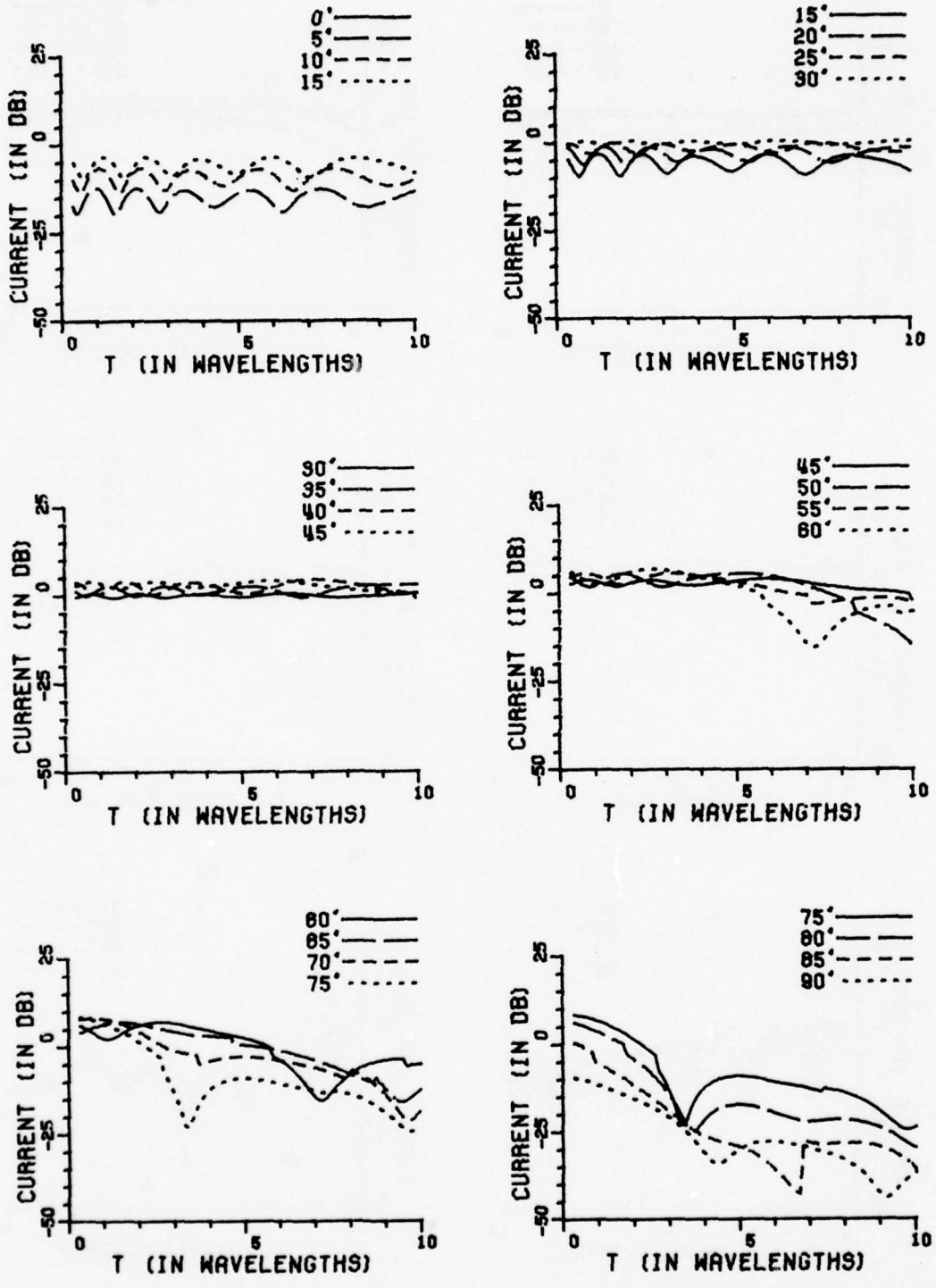

Figure 63c. Circumferential current density with a=5.0 wavelength and $r_1/a=0.4$.

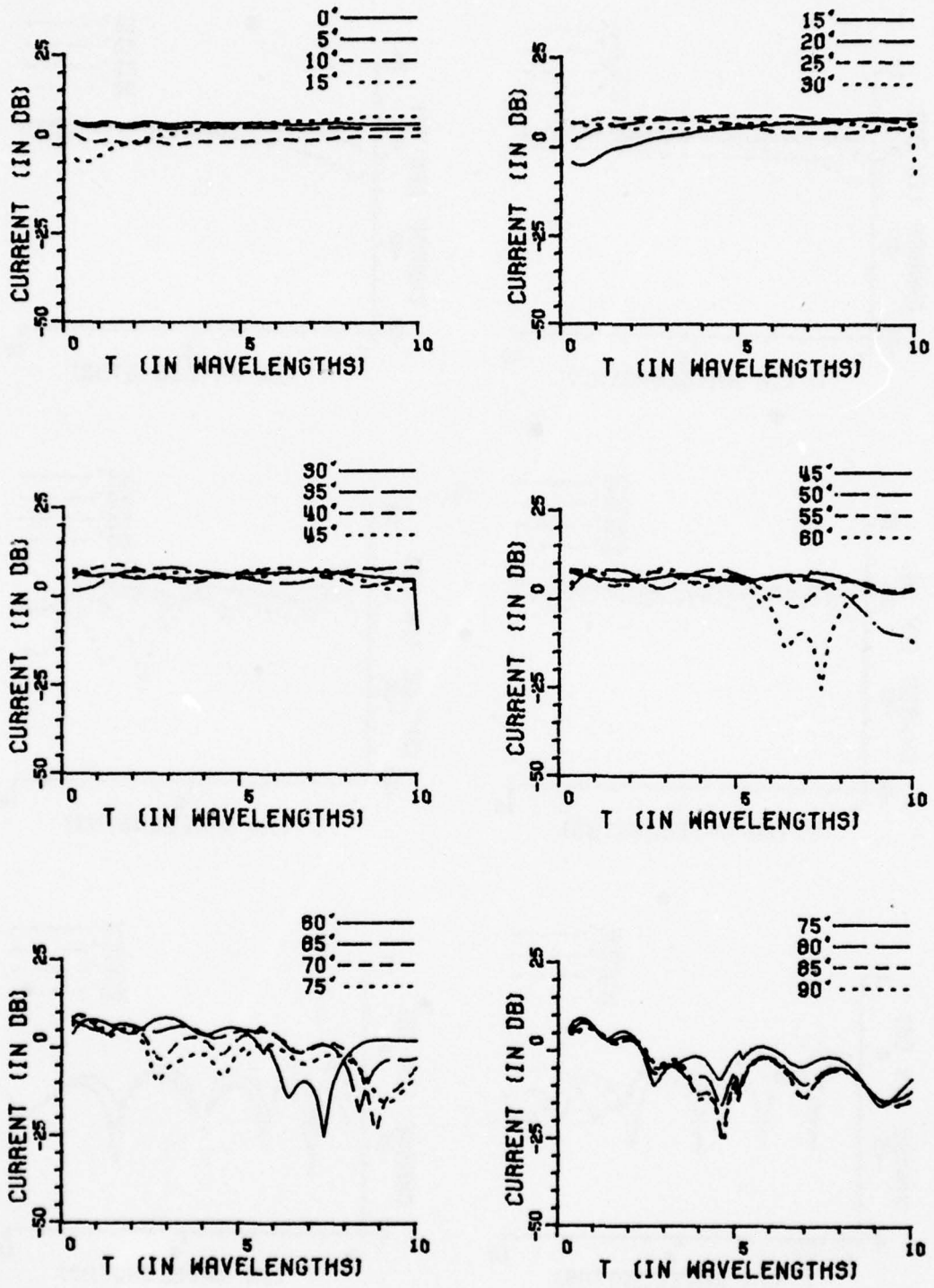

Figure 64a. Axial current density with a=5.0 wavelength and r_1/a=1.0.

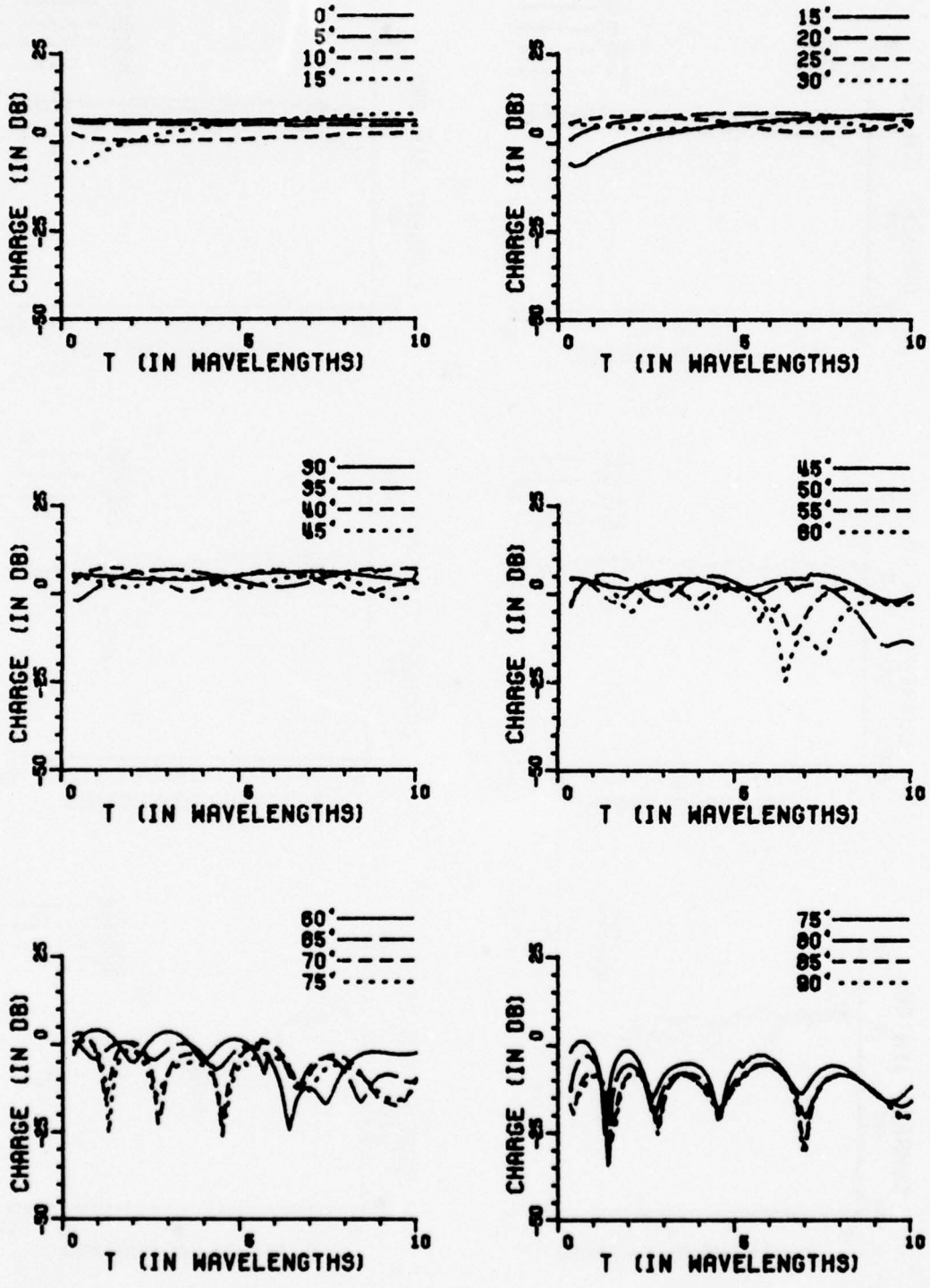

Figure 64b. Surface charge sensity with a=5.0 wavelength and r_1/a=1.0.

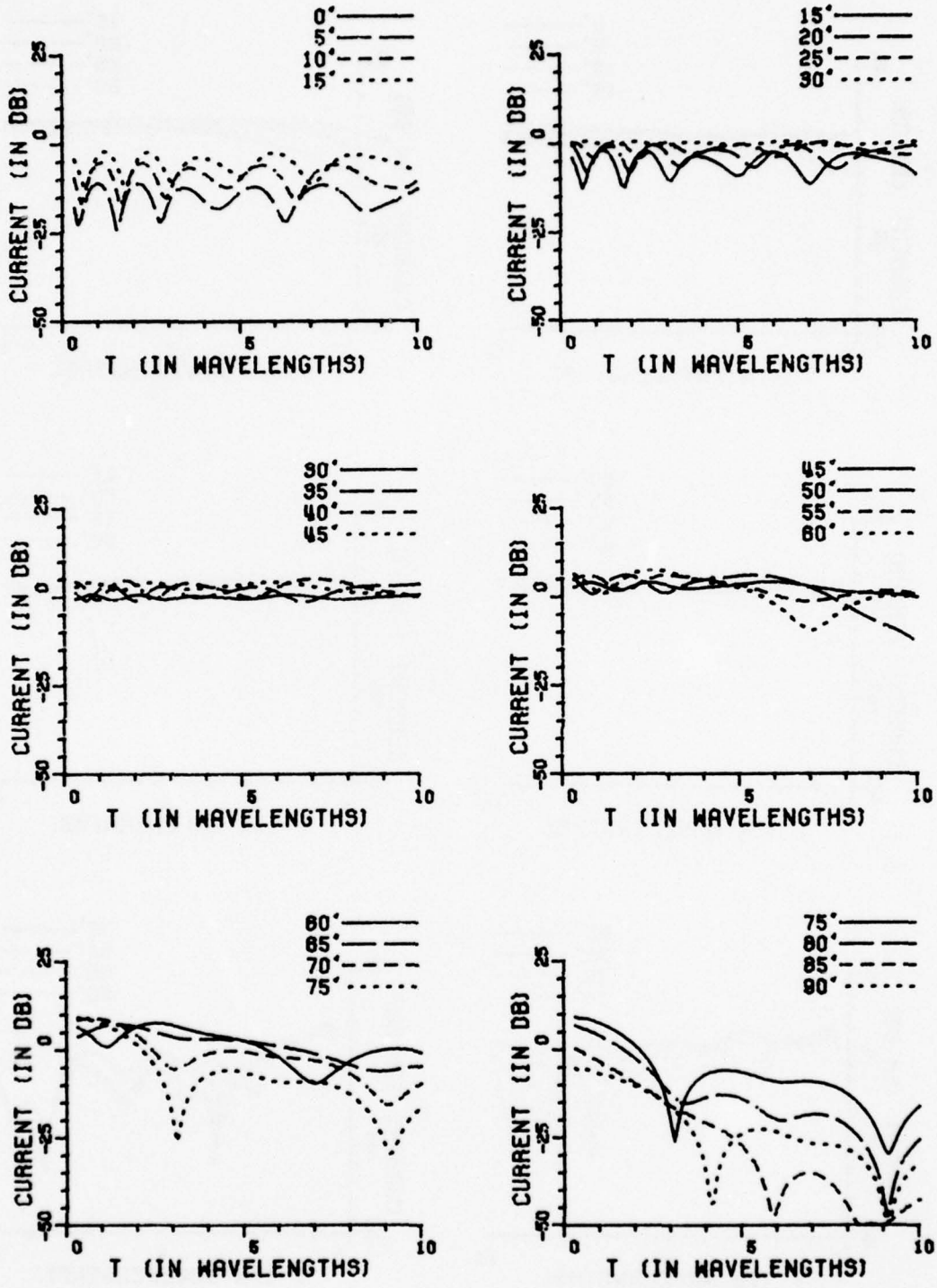

Figure 64c. Circumferential current density with a=5.0 wavelength and $r_1/a=1.0$.

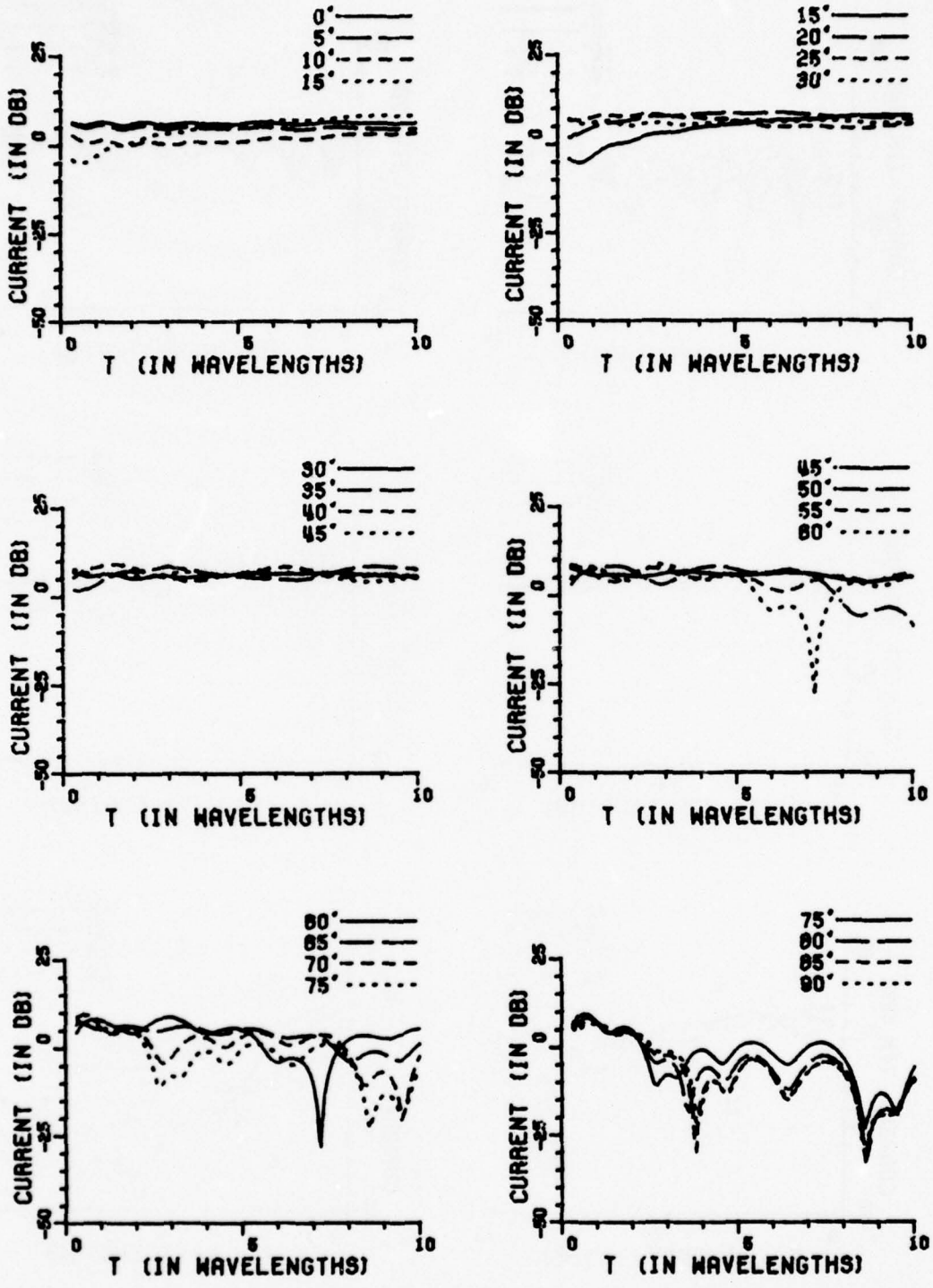

Figure 65a. Axial current density with a=5.0 wavelength and r_1/a=2.0.

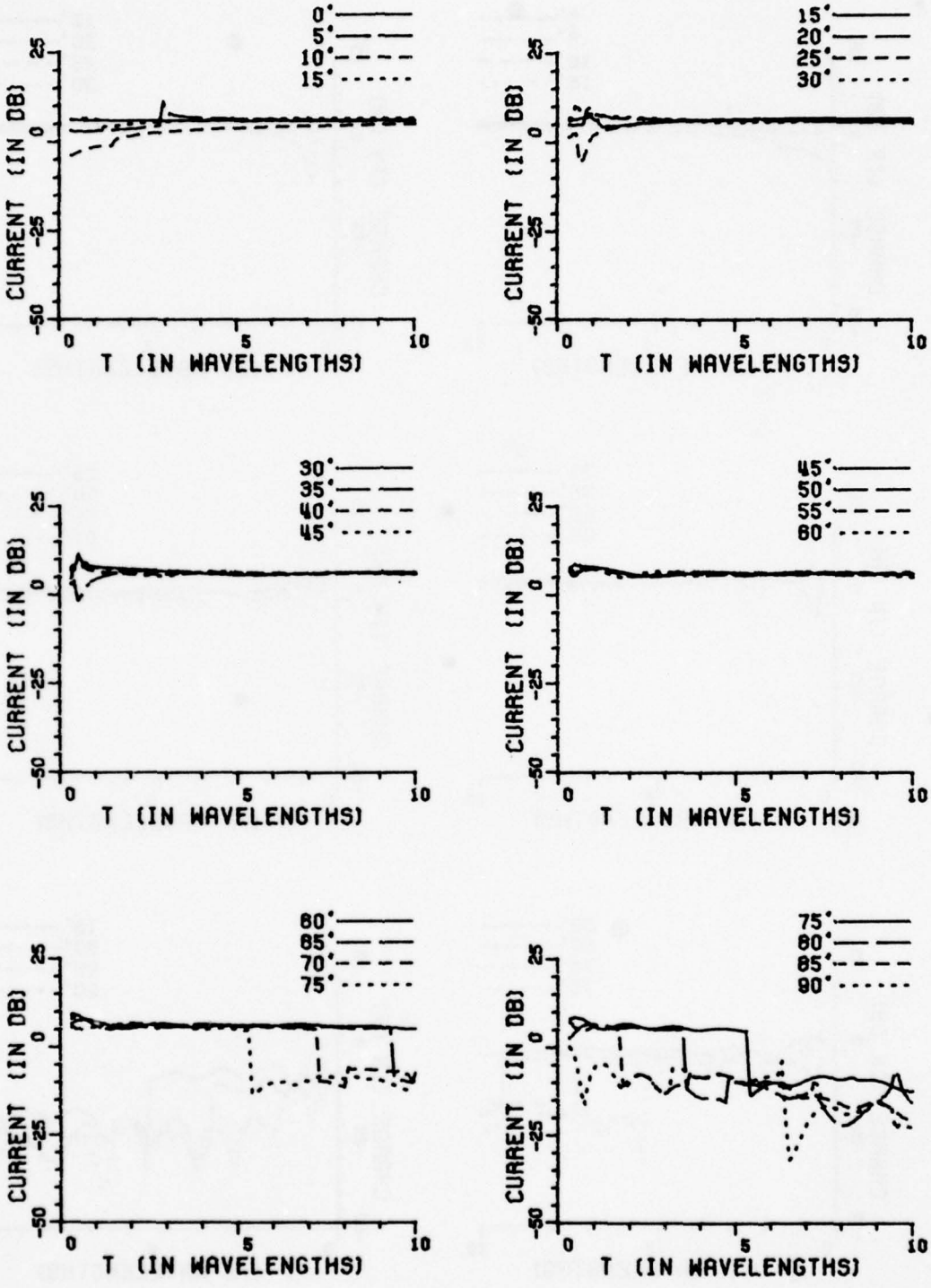

Figure 66a. Axial current density with a=10.0 wavelength and r_1/a=0.025.

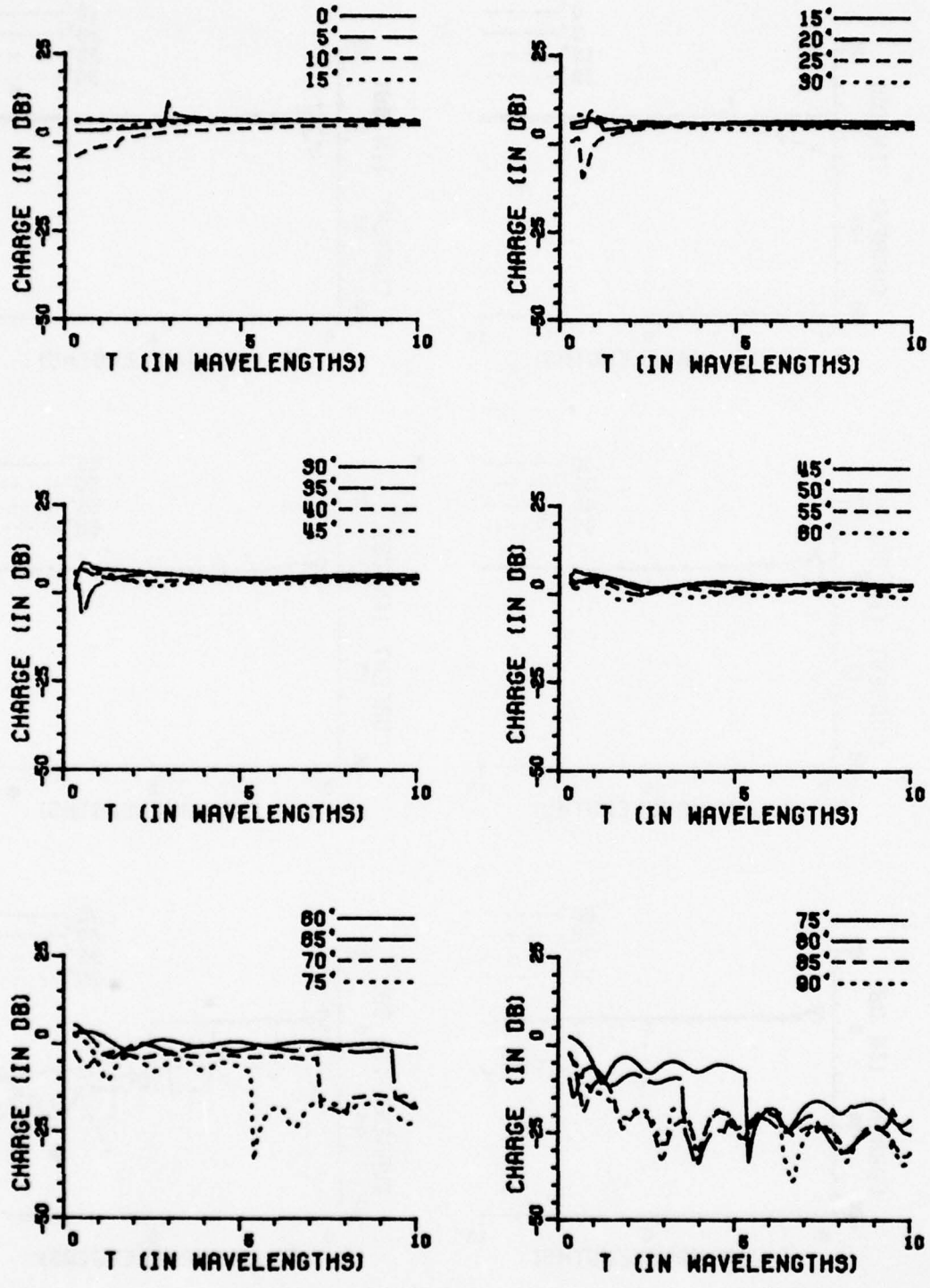

Figure 66b. Surface charge density with a=10.0 wavelength and r_1/a=0.025.

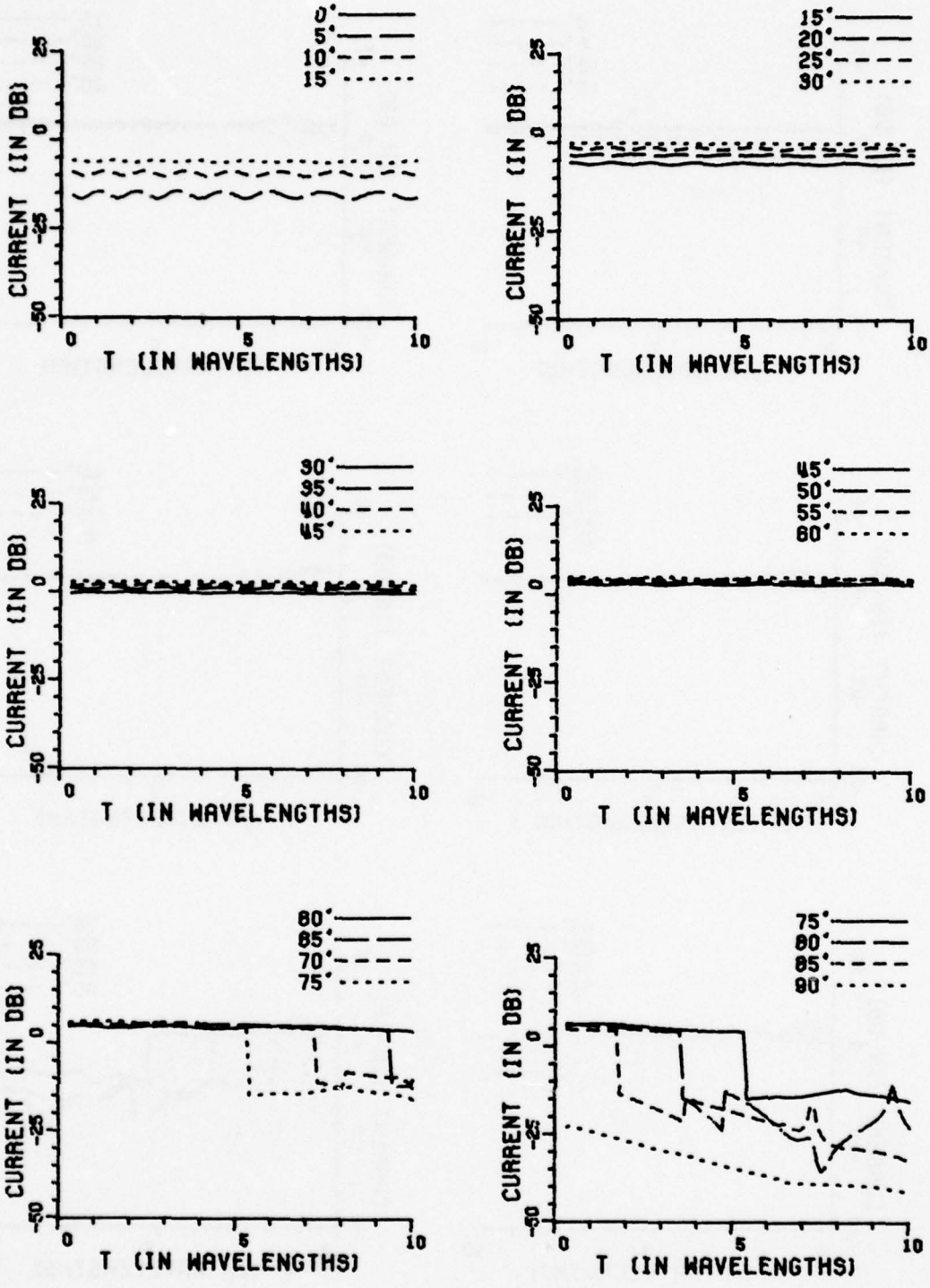

Figure 66c. Circumferential current density with a=10.0 wavelength and r_1/a=0.025.

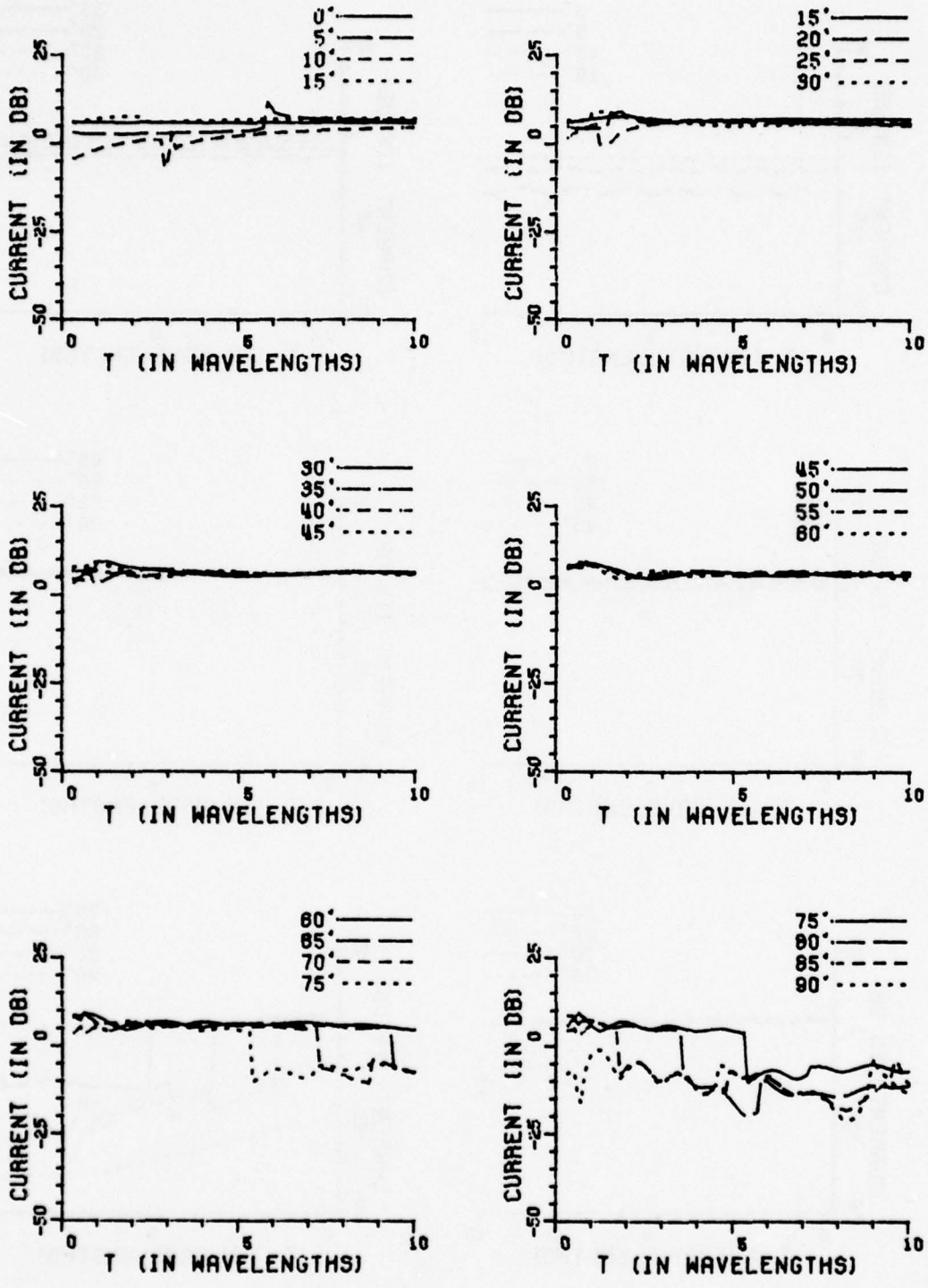

Figure 67a. Axial current density with a=10.0 wavelength and r_1/a=0.05.

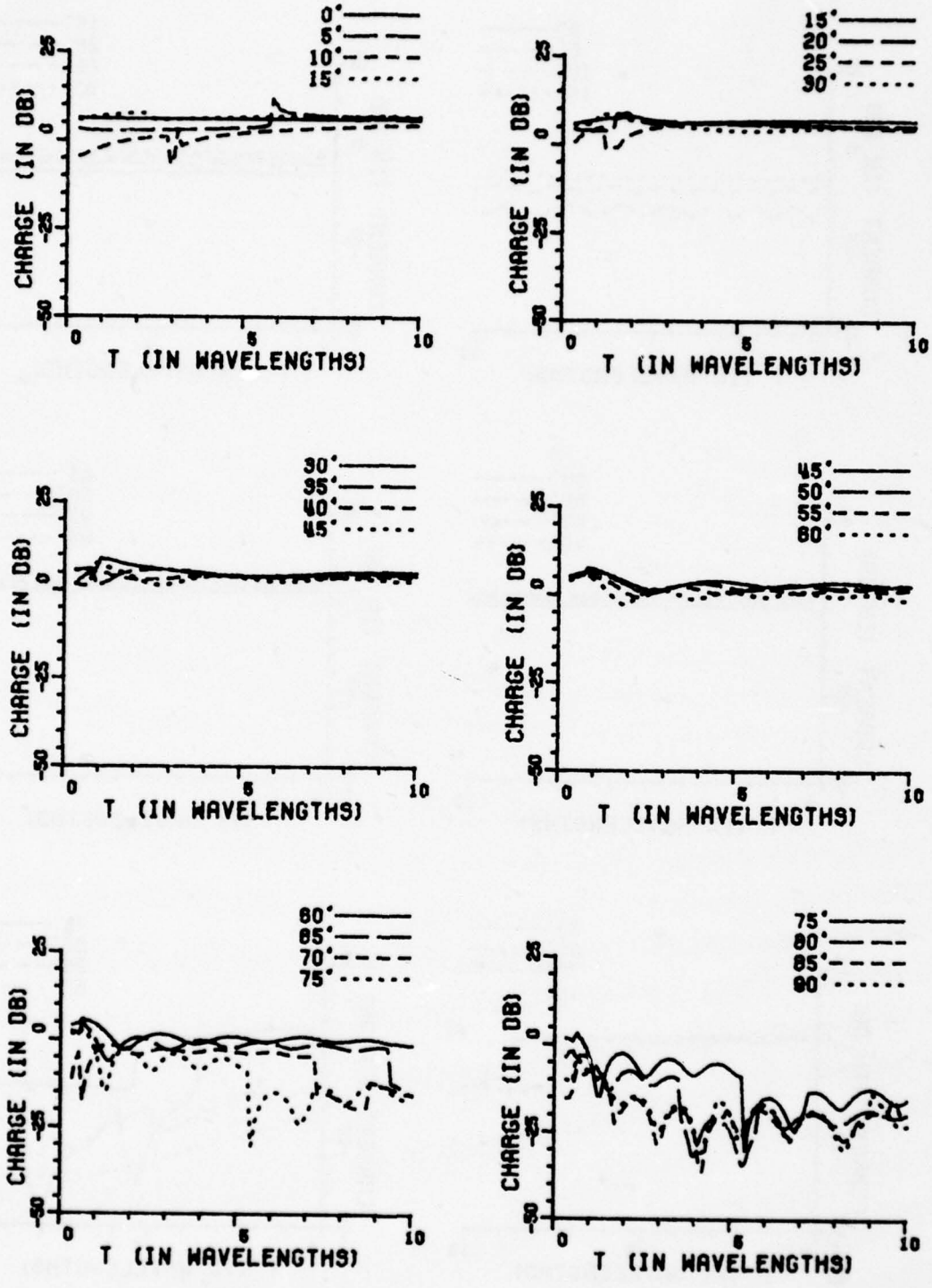

Figure 67b. Surface charge density with a=10.0 wavelength and r_1/a=0.05.

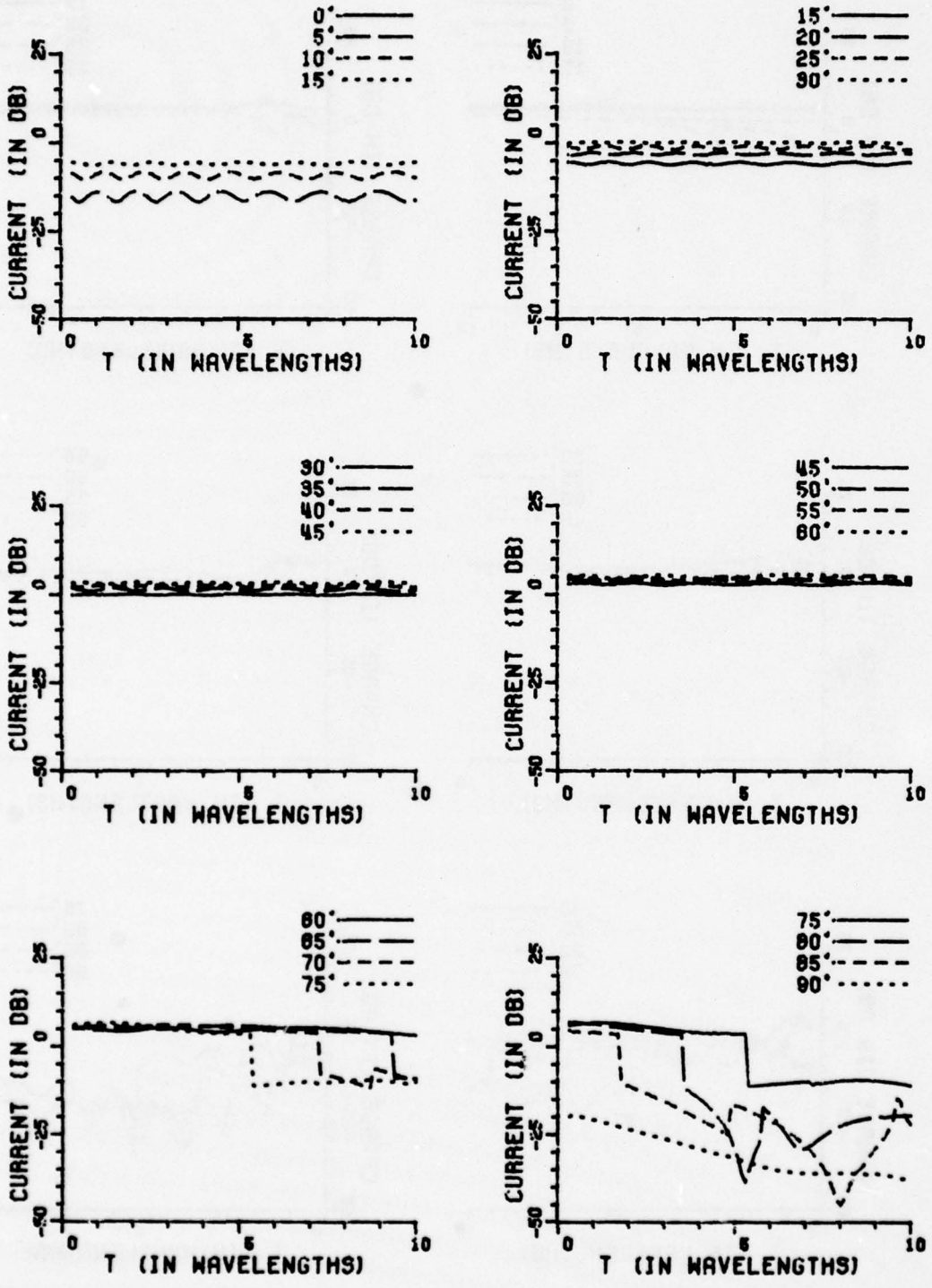

Figure 67c. Circumferential current density with a=10.0 wavelength and r_1/a=0.05.

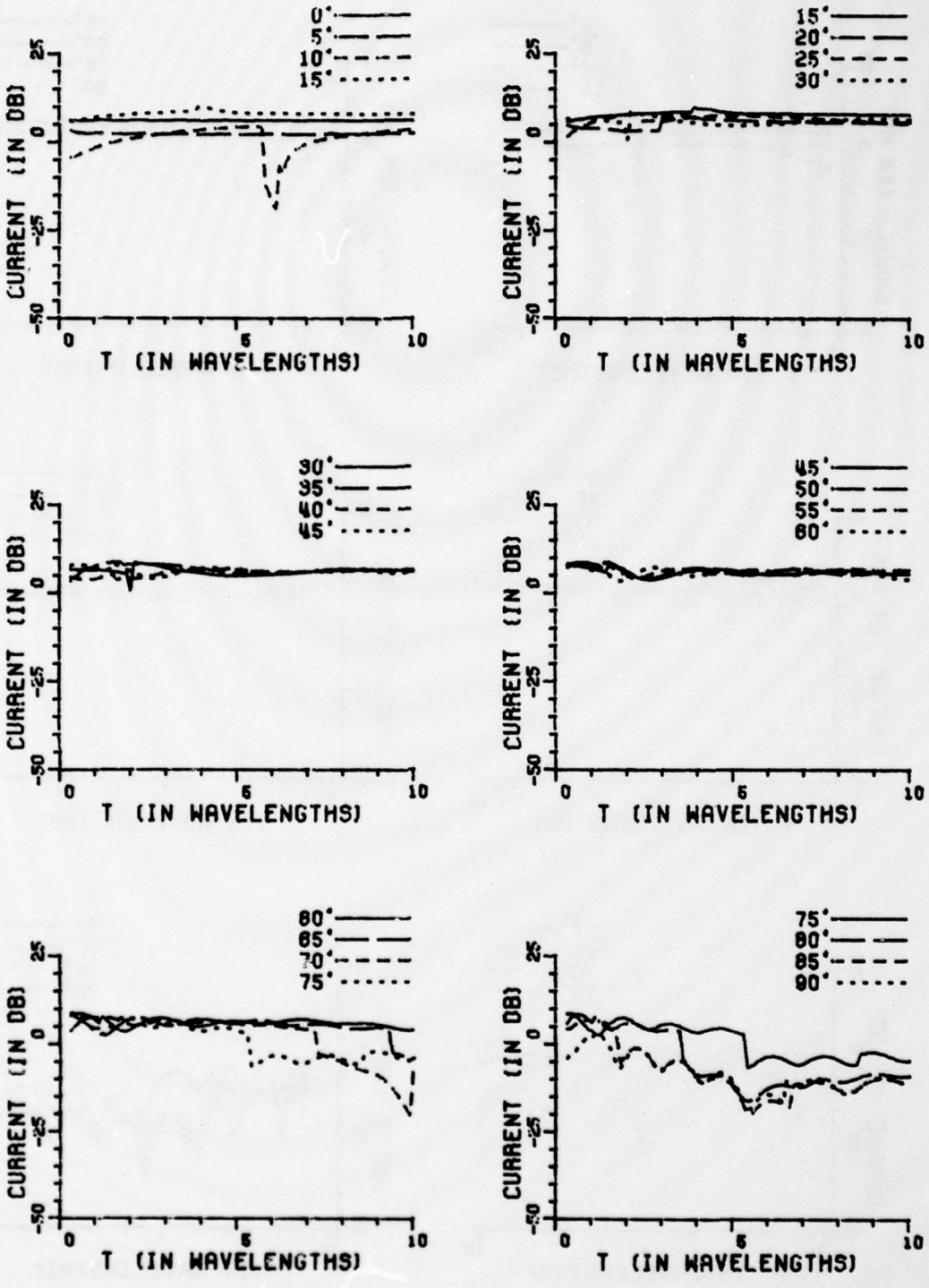

Figure 68a. Axial current density with a=10.0 wavelength and $r_1/a=0.1$.

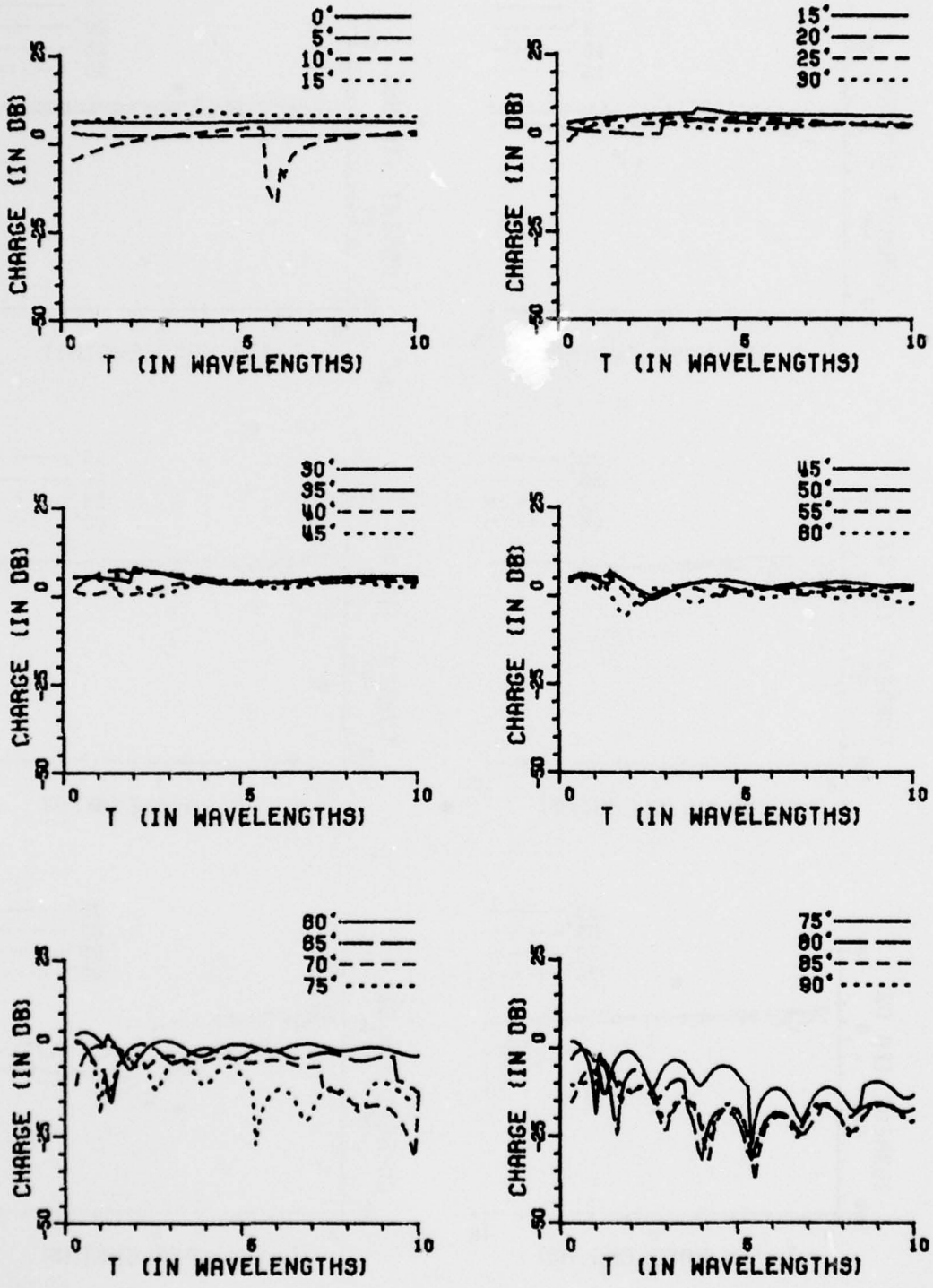

Figure 68b. Surface charge density with a=10.0 wavelength and r_1/a=0.1.

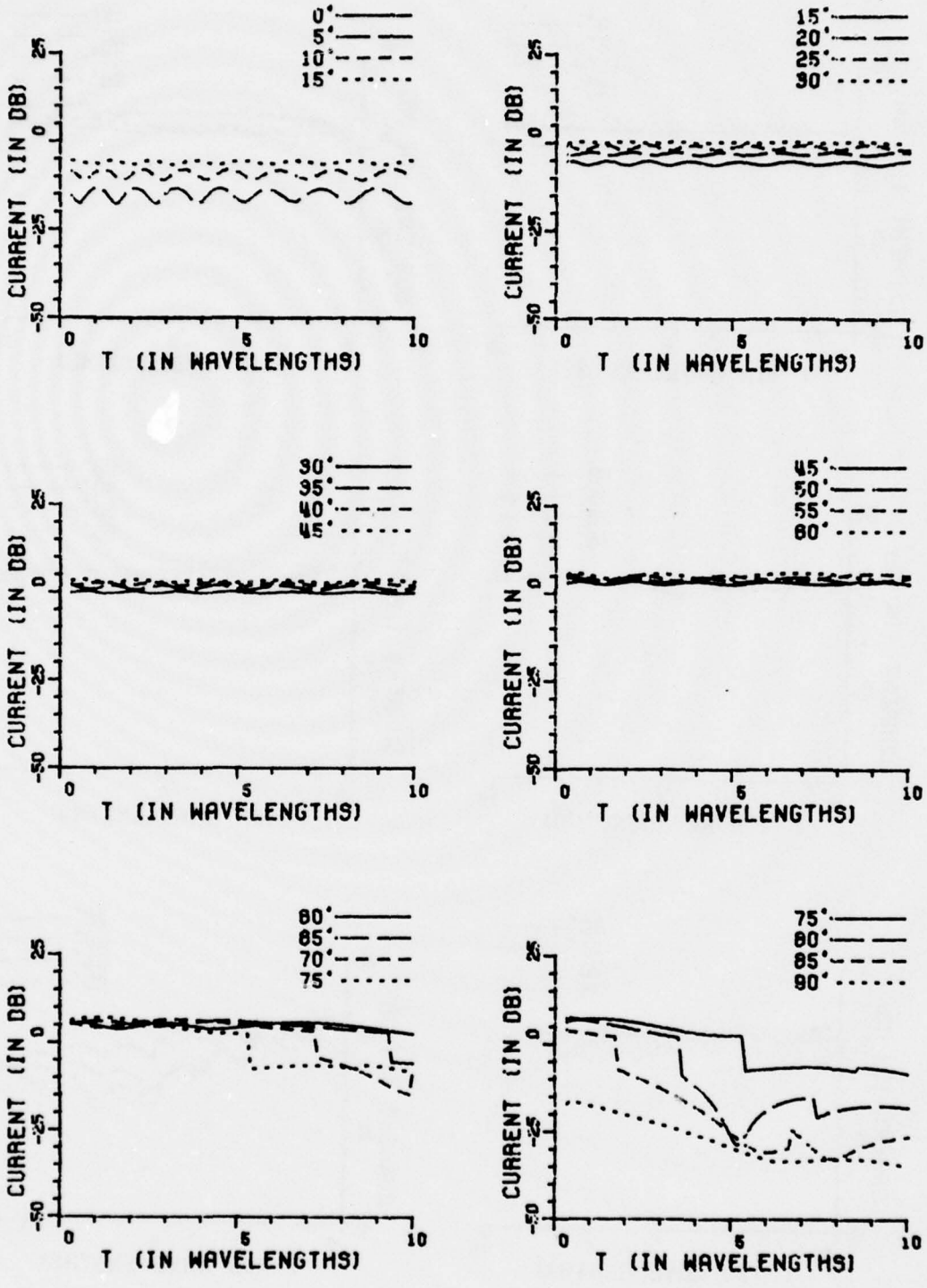

Figure 68c. Circumferential current density with a=10.0 wavelength and $r_1/a=0.1$.

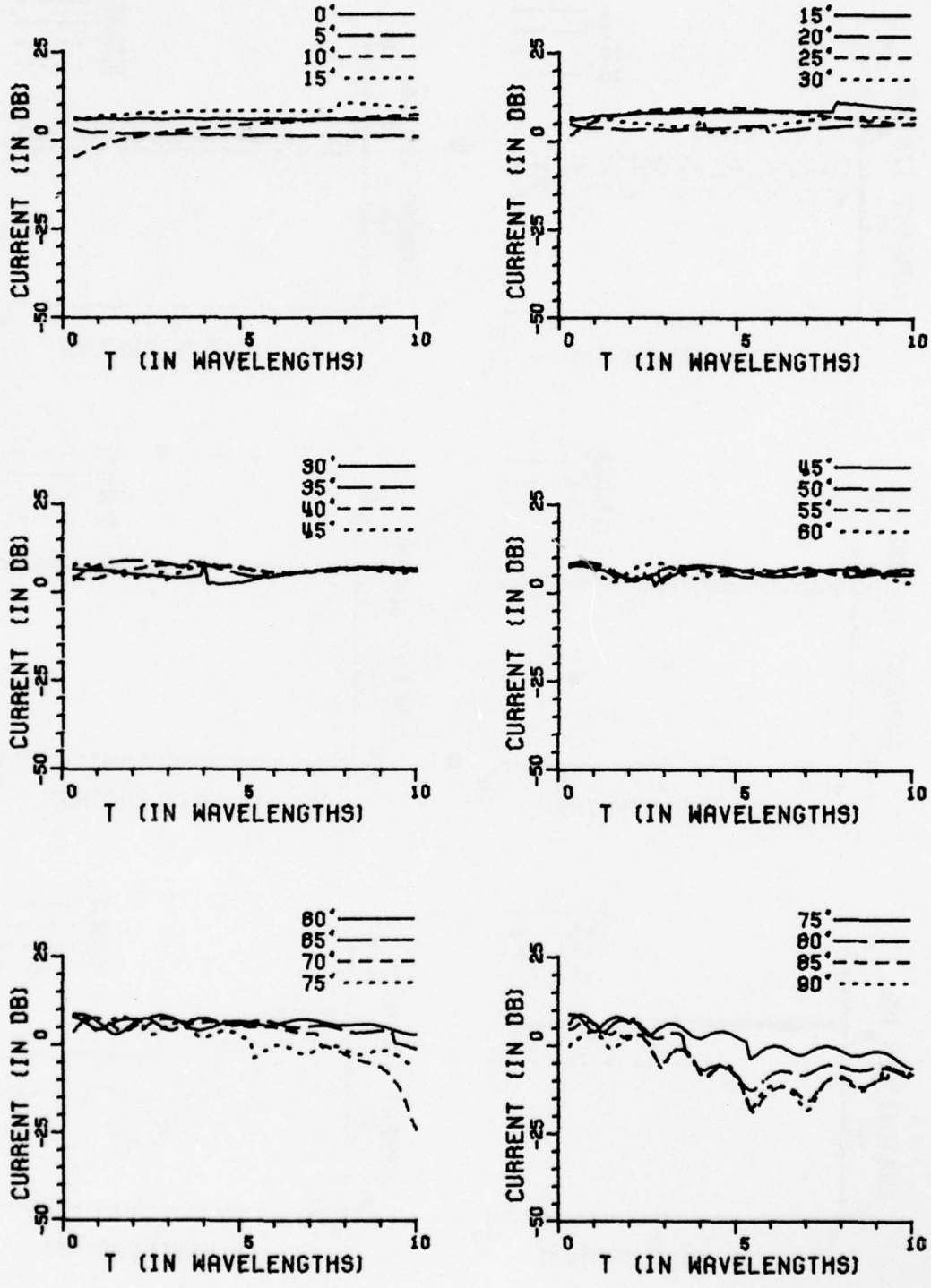

Figure 69a. Axial current density with a=10.0 wavelength and r_1/a=0.2.

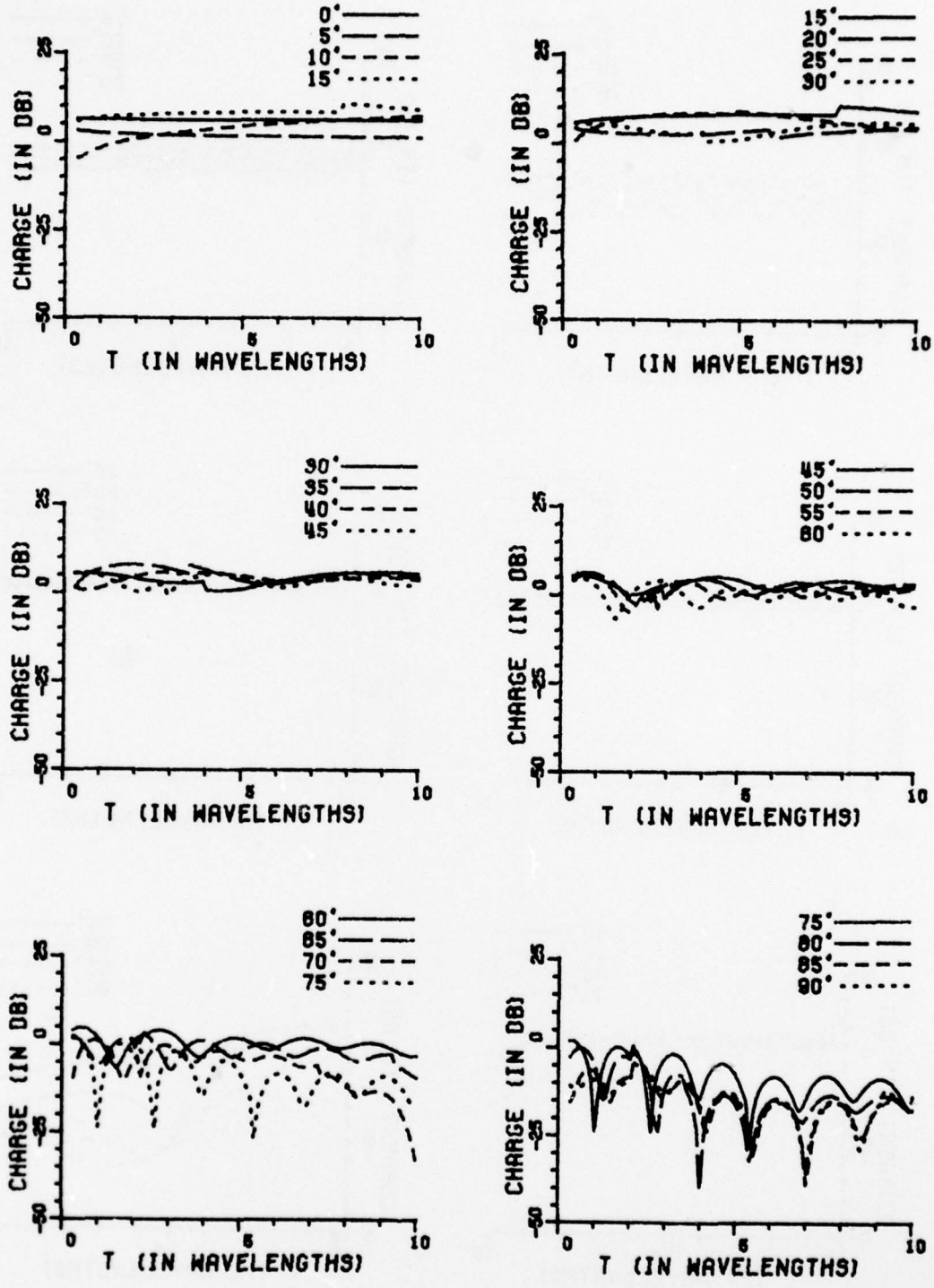

Figure 69b. Surface charge density with a=10.0 wavelength and r_1/a=0.2.

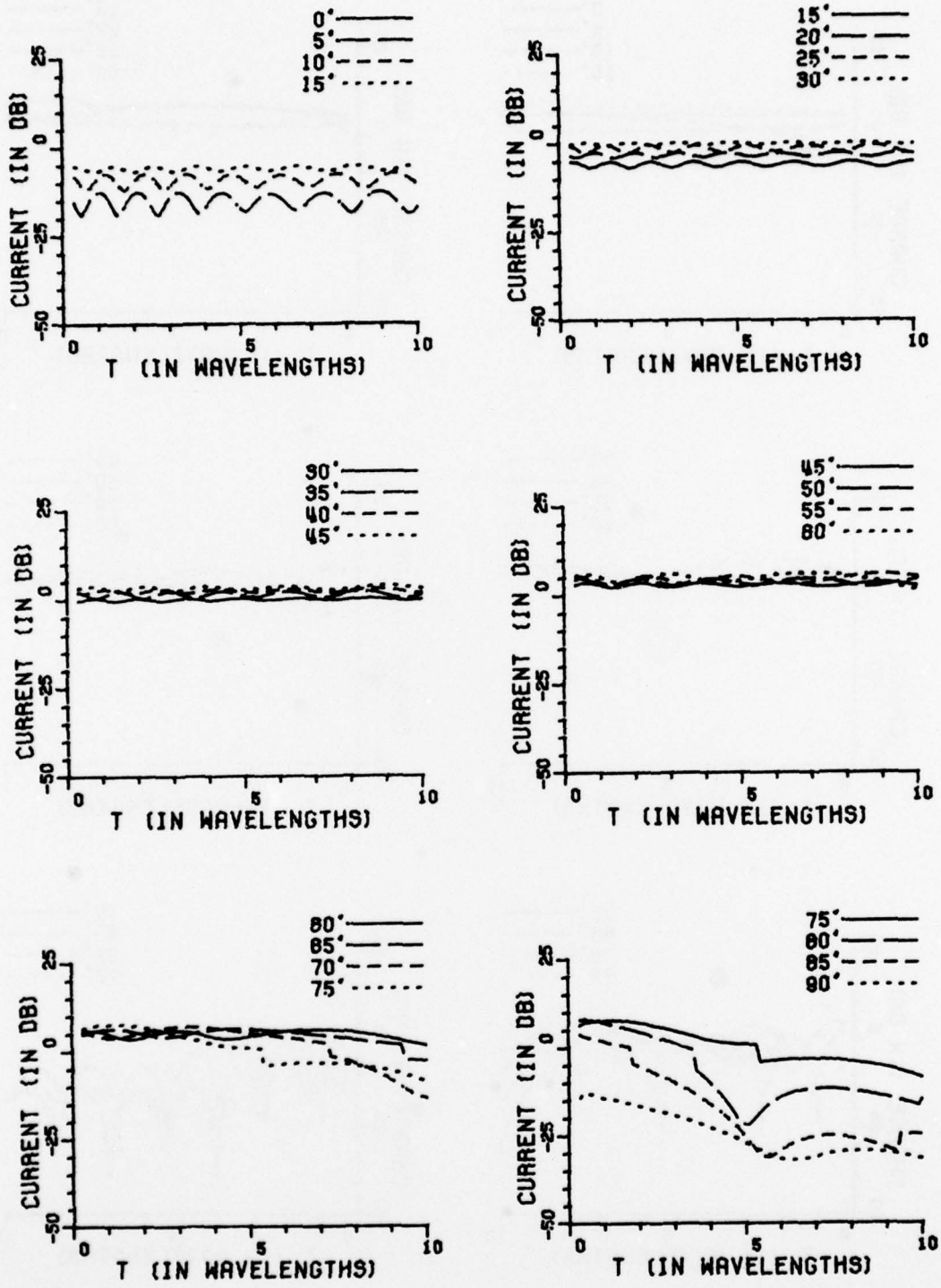

Figure 69c. Circumferential current density with a=10.0 wavelength and $r_1/a=0.2$.

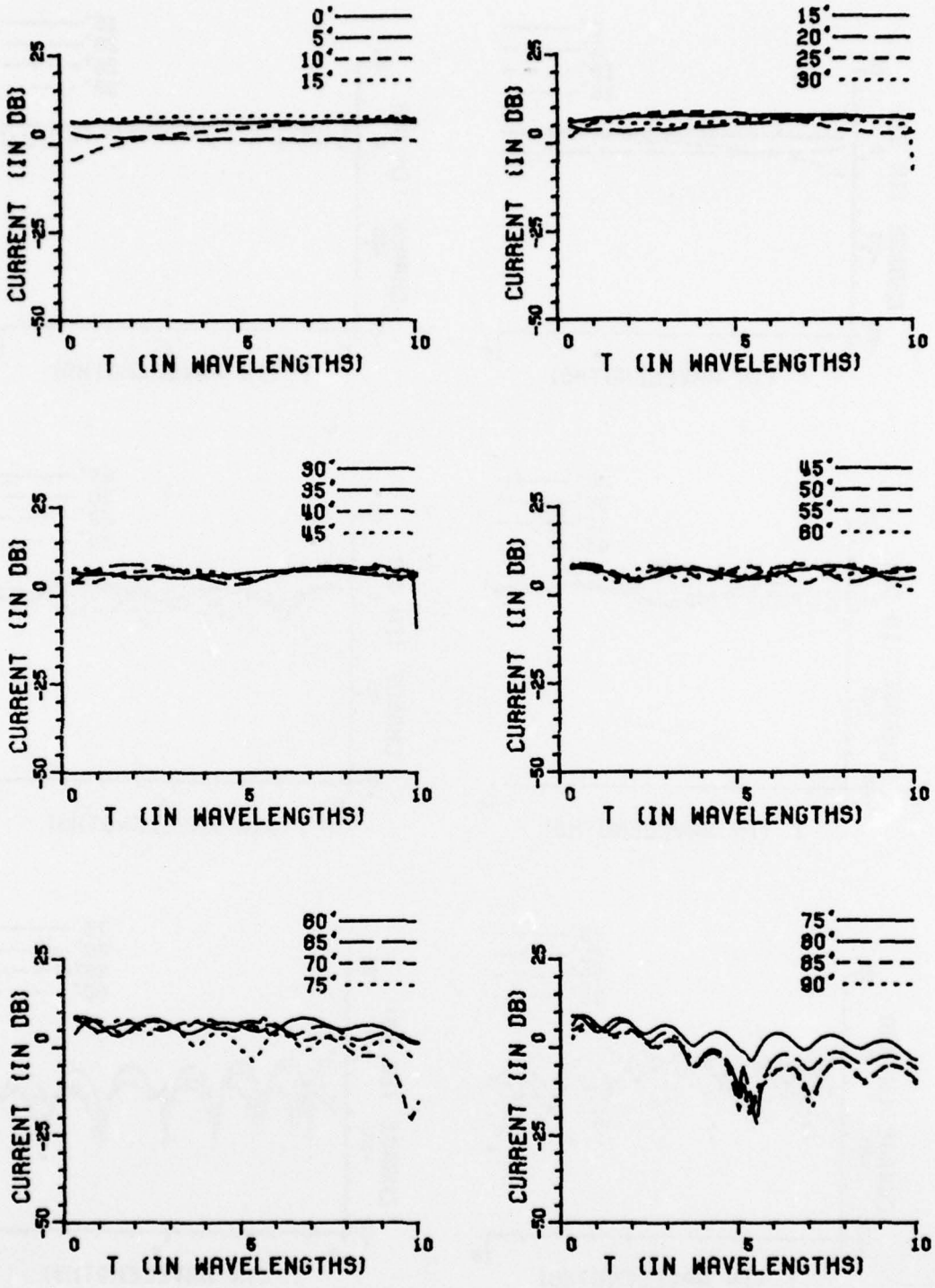

Figure 70a. Axial current density with a=10.0 wavelength and r_1/a=0.5.

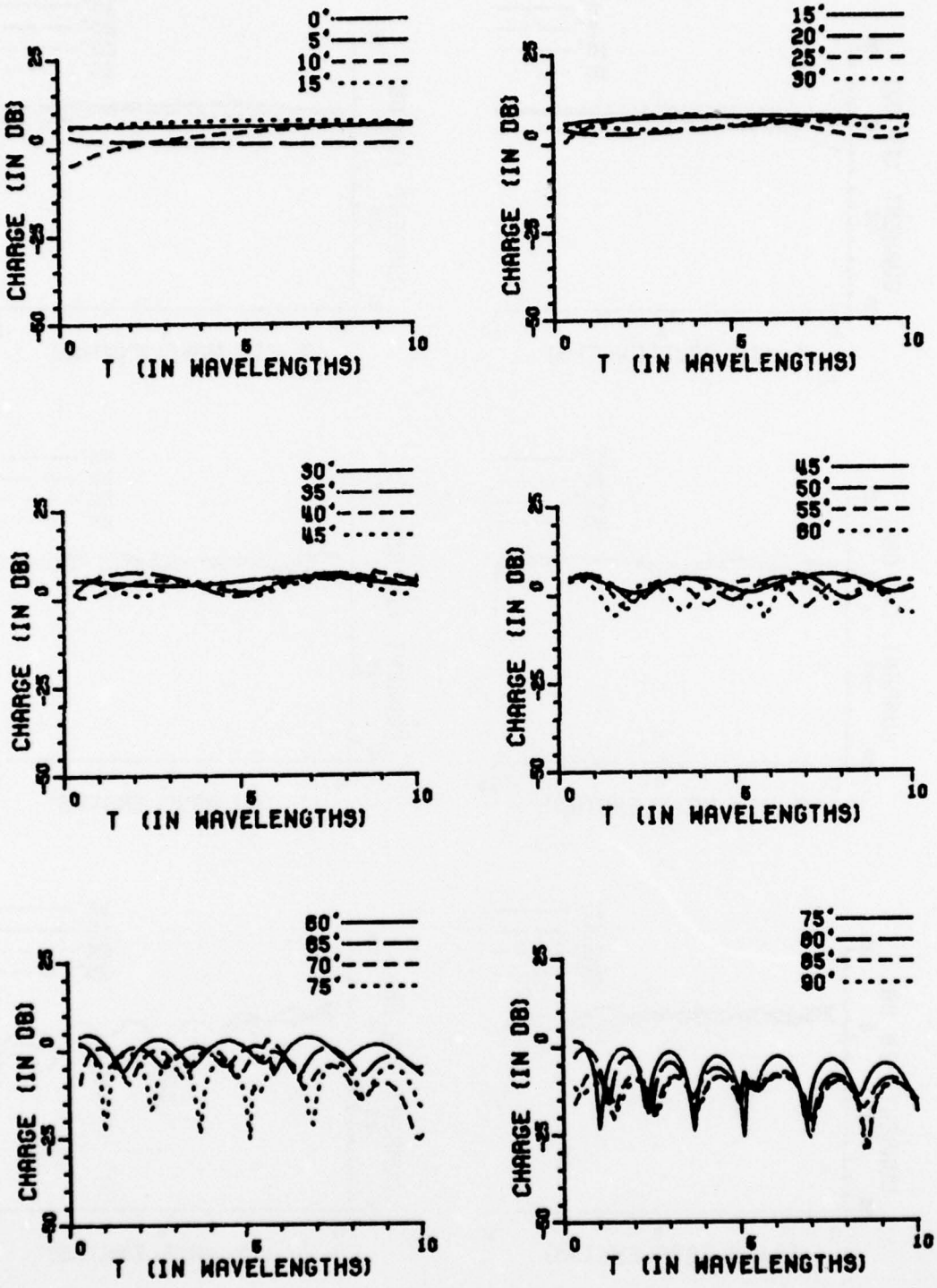

Figure 70b. Surface charge density with a=10.0 wavelength and $r_1/a=0.5$.

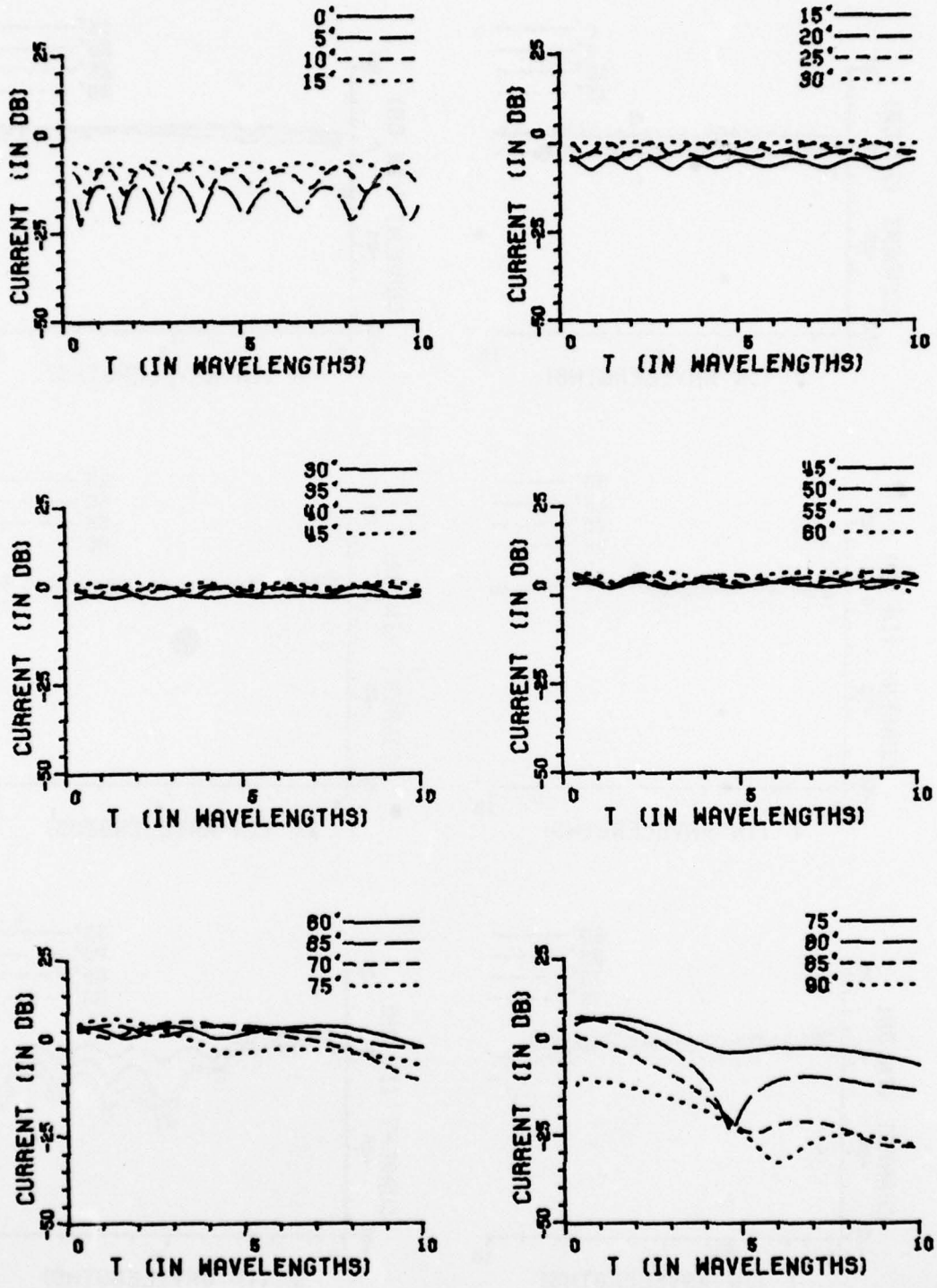

Figure 70c. Circumferential current density with a=10.0 wavelength and $r_1/a=0.5$.

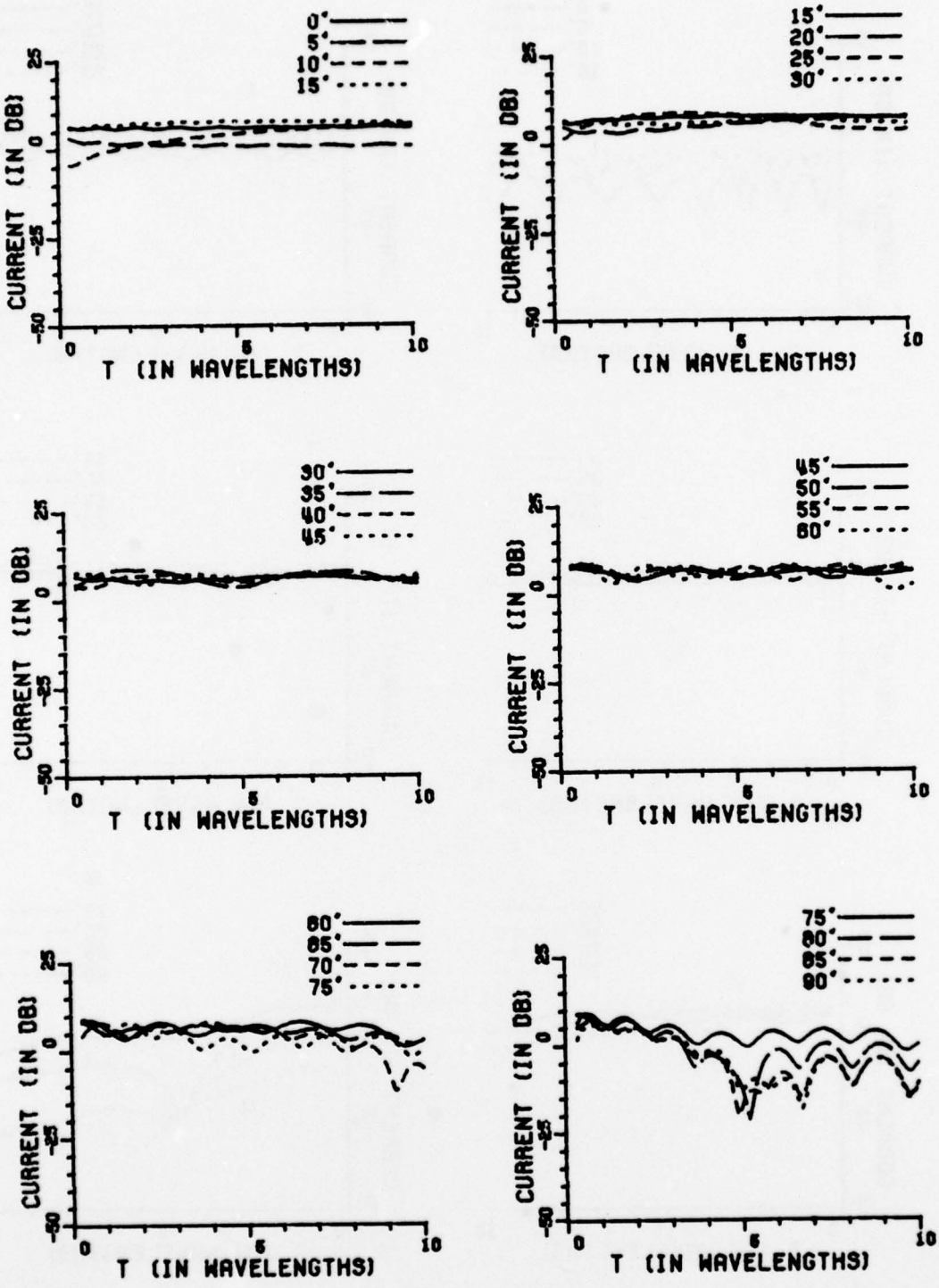

Figure 71a. Axial current density with a=10.0 wavelength and r_1/a=1.0.

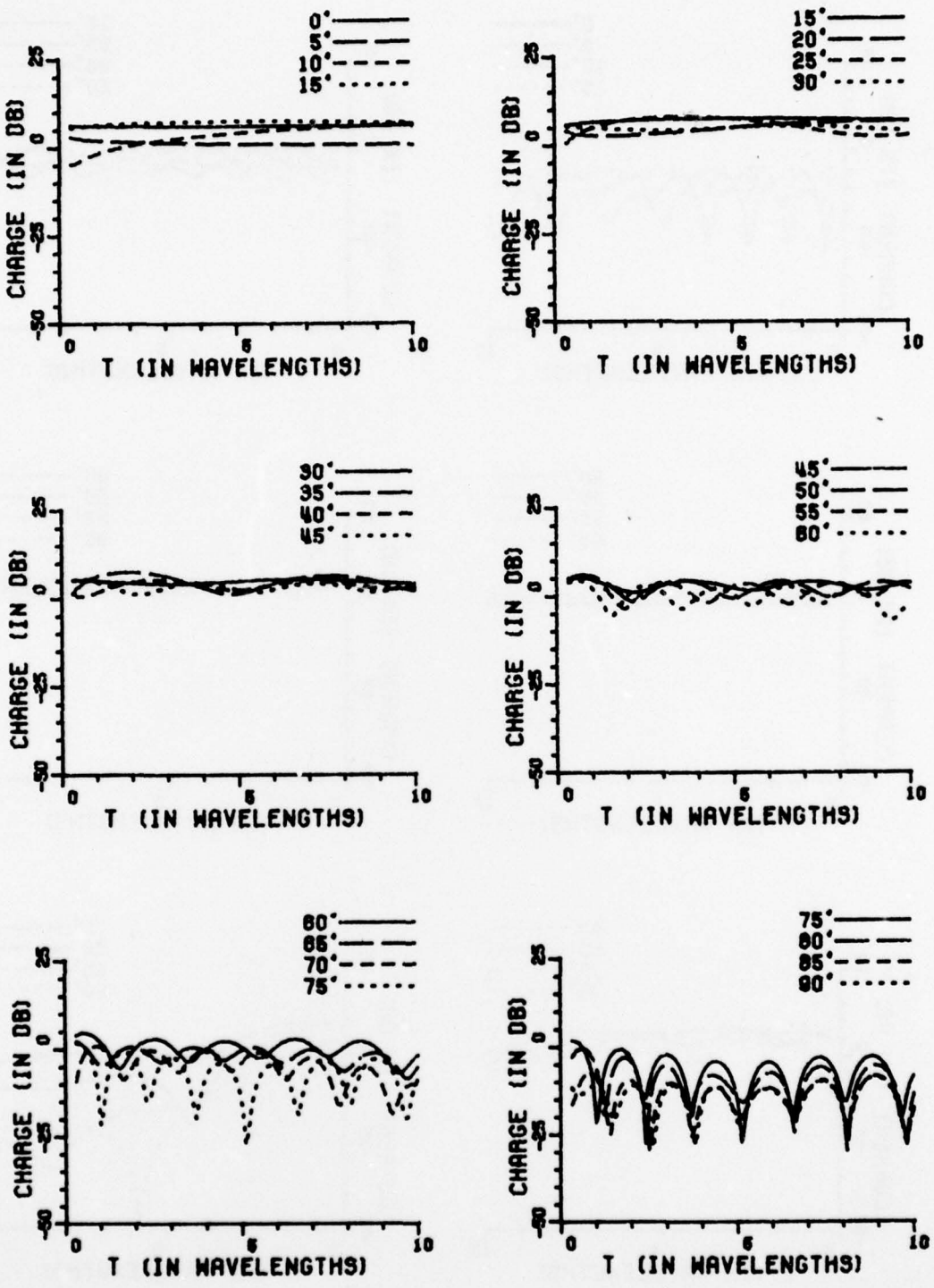

Figure 71b. Surface charge density with a=10.0 wavelength and r_1/a=1.0.

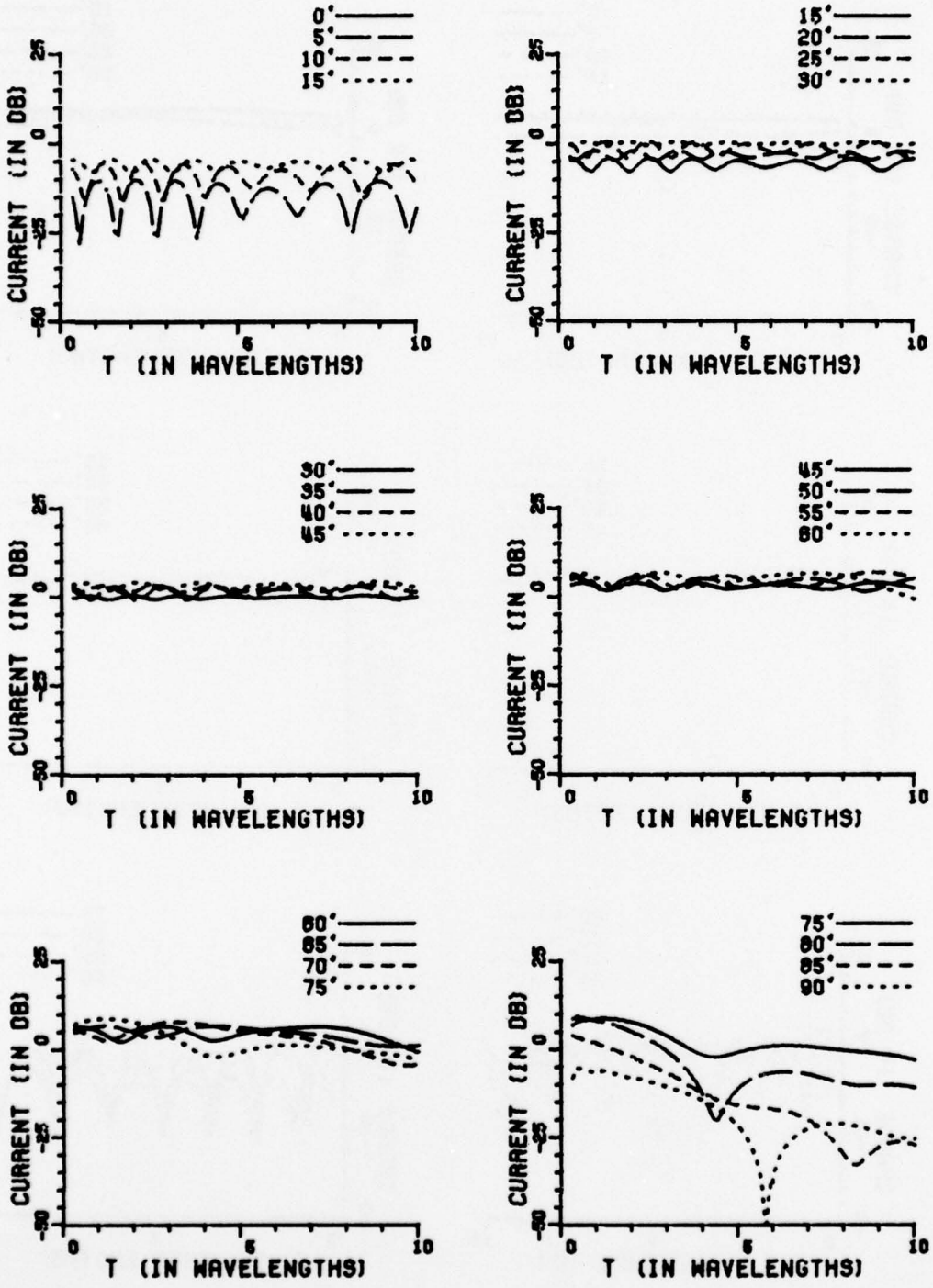

Figure 71c. Circumferential current density with a=10.0 wavelength and r_1/a=1.0.

VI. CONCLUSIONS

The object of this research has been to analyze the surface current and charge density induced on a perfectly conducting cylinder situated above a perfectly conducting ground plane by an incident plane wave. This model can be used to simulate a parked aircraft on a runway or other similar structures. The basic approach used in this study has been to apply the Geometrical Theory of Diffraction to analyze this problem. Thus, the solution presented here for surface current and charge density induced on a finite cylinder above a ground plane is applicable for radii as small as one quarter wavelength.

In Chapter III the parallel plate aperture problem was investigated in order to indicate where the GTD ray picture was valid and to verify the accuracy of the solution. The GTD results compare very favorably with a modal type solution. Current densities for a variety of aperture spacings, and current locations along the waveguide walls were presented.

In Chapter IV the results for the cylindrical geometry were presented. In this section the charge and current density were plotted as a function of the cylinder's distance above the ground plane, the cylinder radius, the incoming plane wave's angle of incidence with respect to the ground plane, and the distance from the observation point to the cylinder endcap along the bottom of the cylinder. In general the results have shown that caustics can appear in the solution especially if the cylinder radius is small in terms of wavelengths. A partial correction for these caustics was discussed in Chapter V and is included in the results. The caustic correction procedure is not complete since using the current theory only the principal diffraction point can be used in the procedure.

Incident plane waves in the principal plane were used in this study. However, the theory can be extended to include incident plane waves out of the principal plane. There is also a need for experimental data in this area to verify results obtained.

REFERENCES

1. R. J. Marhefka, "Roll Plane Analysis of On-Aircraft Antennas," Report 3188-1, December 1971, The Ohio State University ElectroScience Laboratory, Department of Electrical Engineering; prepared under Contract N62269-71-C-0296 for Naval Air Development Center.

2. C. L. Yu and W. D. Burnside, "Elevation Plane Analysis of On-Aircraft Atennas," Report 3188-2, January 1972, The Ohio State University ElectroScience Laboratory, Department of Electrical Engineering; prepared under Contract N62269-71-C-0296 for Naval Air Development Center.

3. "On Aircraft Antennas," Report 3188-3, January 1972, The Ohio State University ElectroScience Laboratory, Department of Electrical Engineering; prepared under Contract N62269-71-C-0296 for Naval Air Development Center.

4. W. D. Burnside, "Analysis of On-Aircraft Antenna Patterns," Report 3390-1, August 1972, The Ohio State University ElectroScience Laboratory, Department of Electrical Engineering; prepared under Contract N62269-72-C-0354 for Naval Air Development Center.

5. W. D. Burnside, "Analysis of On-Aircraft Antenna Patterns," Report 3390-2, May 1973, The Ohio State University ElectroScience Laboratory, Department of Electrical Engineering; prepared under Contract N62269-72-C-0354 for Naval Air Development Center.

6. W. D. Burnside, R. J. Marhefka and C. L. Yu, "Roll-plane Analysis of On-aircraft Antennas," IEEE Trans. Antennas Propagat., vol. AP-21, pp. 780-786, November 1973.

7. W. D. Burnside, M. C. Gilreath, R. J. Marhefka and C. L. Yu., "A Study of KC-135 Aircraft Antenna Patterns," IEEE Trans. Antennas Propagat., Vol. AP-23, No. 3, May 1975.

8. R. R. Lentz, P. H. Pathak and W. D. Burnside, "Surface Current and Surface Charge Density Induced on Aircraft Models," Report 3406-1, June 1972, The Ohio State University ElectroScience Laboratory, Department of Electrical Engineering; prepared under P. O. No. 901169 for the Boeing Company.

9. Y. Hwang, W. D. Burnside and L. Peters, Jr., "EMP-Induced Surface Charge and Current Densities on the B-1 and 747 Aircraft," Air Force Weapons Laboratory, Kirtland AFB, NM. (AFWL-TR-75-122).

10. R. G. Kouyoumjian, and P. Pathak, "A Uniform Geometrical Theory of Diffraction for an Edge of a Perfectly Conducting Surface," Proc. of the IEEE, Vol. 62, No. 11, November, 1974, pp. 1448-1461.

11. G. Deschamps, "Ray Techniques in Electromagnetics," Proc. IEEE, Vol. 60, pp. 1022-1035, September 1972.

12. A. Sommerfeld, Optics, Academic Press, Inc., New York, 1954, pp. 245-265.

13. J. B. Keller, "Geometrical Theory of Diffraction," Jour. Optical Soc. Amer., 52 (February 1962), pp. 116-130.

14. R. C. Rudduck, "Application of Wedge Diffraction to Antenna Theory," Report 1691-13, 30 June 1965, The Ohio State University ElectroScience Laboratory, Department of Electrical Engineering; prepared under Grant NSF-338 for National Aeronautics and Space Administration, Washington, D. C. Also published as NASA Report CR-372.

15. W. Pauli, "An Asymptotic Series for Functions in the Theory of Diffraction of Light," Phys. Rev., 54 (1 December 1938), pp. 924-931.

16. D. L. Hutchins, and R. G. Kouyoumjian, "A New Asymptotic Solution to the Diffraction by a Wedge," URSI 1967 Spring Meeting, Ottawa, Canada, pp. 154-155.

17. D. L. Hutchins, "Asymptotic Series Describing the Diffraction of a Plane Wave by a Two-Dimensional Wedge of Arbitrary Angle," Ph.D. Dissertation, The Ohio State University, Department of Electrical Engineering, 1967.

18. P. H. Pathak, and R. G. Kouyoumjian, "The Dyadic Diffraction Coefficient for a Perfectly Conducting Wedge," Scientific Report No. 5, Report 2183-4, 5 June 1970, The Ohio State University ElectroScience Laboratory, Department of Electrical Engineering; prepared under Contract AF19(628)-5929 for Air Force Cambridge Research Laboratories. (AFCRL-69-0546) (AD 707821)

19. R. C. Rudduck, and L. L. Tsai, "Aperture Reflection Coefficient of a Parallel-Plane Waveguide by Wedge Diffraction Analysis," Report 1691-20, 10 April 1967, The Ohio State University ElectroScience Laboratory, Department of Electrical Engineering; prepared under Grant NsG-448 for National Aeronautics and Space Administration, Washington, D. C.

20. N. C. Albertsen, P. Balling, and N. E. Jensen, "Caustics and Caustic Corrections to the Field Diffracted by a Curved Edge," Proc. of the IEEE, Vol. AP-25, No. 3, May 1977, pp. 297-303.

21. C. E. Ryan, Jr., and L. Peters, Jr., "Evaluation of Edge-Diffracted Fields Including Equivalent Currents for the Caustic Regions," IEEE Trans. on Antennas and Propagation Comm., Vol. AP-7, pp. 292-299, May 1969. (see also correction: Vol. AP-8, p. 275, March 1970.)

22. A. Papoulis, The Fourier Integral and Its Applications, McGraw-Hill, New York, 1962, pp. 139-143.

23. M. Abramowitz and I. A. Stegun, Handbook of Mathematical Functions, New York: Dover, 1965.